

# UC Santa Cruz

## UC Santa Cruz Electronic Theses and Dissertations

### Title

Design, Syntheses and Characterization of Transition Metal Complexes for Utilization in Therapeutic Applications

### Permalink

<https://escholarship.org/uc/item/0h75v4gq>

### Author

Stenger-Smith, Jenny

### Publication Date

2020

Peer reviewed|Thesis/dissertation

UNIVERSITY OF CALIFORNIA  
SANTA CRUZ

**DESIGN, SYNTHESIS AND CHARACTERIZATION OF TRANSITION  
METAL COMPLEXES FOR UTILIZATION IN THERAPEUTIC  
APPLICATIONS**

A dissertation submitted in partial satisfaction  
of the requirements for the degree of

DOCTOR OF PHILOSOPHY

in

CHEMISTRY

by

**Jenny R. Stenger-Smith**

December 2020

The Dissertation of Jenny R. Stenger-  
Smith is approved:

---

Professor Pradip K. Mascharak, Chair

---

Professor Scott R. J. Oliver

---

Professor Theodore R. Holman

---

Quentin Williams  
Acting Vice Provost and Dean of Graduate Studies



Copyright © by  
Jenny R. Stenger-Smith

2020

## Table of Contents

---

List of Figures.....	viii
List of Tables.....	xv
List of Schemes.....	xvi
Abstract.....	xvii
Acknowledgements.....	xx
Dedication.....	xxiii
<b>Chapter 1. Introduction.....</b>	<b>1</b>
<b>1.1 Background on Antibacterial and Anticancer Drug Development and Complications.....</b>	<b>1</b>
<b>1.2 General Direction of Research.....</b>	<b>6</b>
<b>1.3 References.....</b>	<b>7</b>
 <b>Chapter 2. Trackable Antimicrobial Silver Complexes.....</b>	 <b>10</b>
<b>2.1 Background on Medicinal silver.....</b>	<b>10</b>
2.1.1 Antimicrobial silver.....	11
<b>2.2 Trackable Antibacterial Silver Complexes With Aryl Benzothiazoles.....</b>	<b>16</b>
2.2.1 Synthesis and Spectroscopy.....	18
2.2.2 Crystal Structure, Binding Mode Discussion and Density Functional Theory.....	23
2.2.3 Antibacterial Action.....	30

2.2.4 Experimental Section.....	35
2.2.4.1 General Methods.....	35
2.2.4.2 Synthesis.....	35
2.2.4.3 X-ray Crystallography.....	36
2.2.4.4 Computational Methods.....	39
2.2.4.5 Bacterial Studies.....	39
2.3 References.....	40
2.4 Reprint of Publication and Permissions.....	45
 <b>Chapter 3. Antimicrobial Gold Complexes With the {Au(PPh<sub>3</sub>)}<sup>+</sup> Moiety.....</b>	<b>57</b>
3.1 Background on Medicinal Gold.....	57
3.1.1 Chemistry of Au(I) .....	59
3.1.2 Anticancer Activity of Au(I)PPh <sub>3</sub> .....	61
3.1.3 Antibacterial Activity Au(I)PPh <sub>3</sub> .....	62
3.1.4 Antimycobacterial Activity Au(I)PPh <sub>3</sub> .....	66
3.2 Trackable Antibacterial Gold Triphenylphosphine Complexes with Aryl Benzothiazoles.....	69
3.2.1 Synthesis and Spectroscopy.....	70
3.2.2 Crystal Structure and Binding Mode Discussion.....	76
3.2.3 Antibacterial Action and Interactions.....	83
3.2.4 Experimental Section.....	90
3.2.4.1 General Methods.....	90

3.2.4.2 <i>Synthesis</i> .....	90
3.2.4.3 <i>X-ray Crystallography</i> . ....	92
3.2.4.4 <i>Bacterial Studies</i> .....	95
<b>3.3 Antimycobacterial Activity of Gold Complexes with Pyrazinamide</b> .....	96
3.3.1 Synthesis and Spectroscopy.....	97
3.3.2 Crystal Structure Descriptions.....	102
3.3.3 Antimycobacterial Activity and Interactions.....	103
3.3.4 Experimental Section.....	113
3.3.4.1 <i>General Methods</i> .....	113
3.3.4.2 <i>Synthesis</i> .....	113
3.3.4.3 <i>X-ray Crystallography</i> .....	115
3.3.4.4 <i>Mycobacterial Studies</i> .....	117
<b>3.4 References</b> .....	118
<b>3.5 Reprints of Publications and Permissions</b> .....	127
 <b>Chapter 4. Manganese Carbonyl Complexes</b> .....	153
<b>4.1 Background on CO and photoCORMs</b> .....	153
<b>4.2 Manganese Based photoCORMs with Aryl Benzothiazoles</b> .....	157
4.2.1 Synthesis and Spectroscopy.....	158
4.2.2 Crystal Structure Descriptions.....	159
4.2.3 CO Release Properties and “Turn On” Fluorescence Tracking.....	161
4.2.4 Experimental Section.....	165

4.2.4.1 <i>General Methods</i> .....	165
4.2.4.2 <i>Synthesis</i> .....	166
4.2.4.3 <i>X-ray Crystallography</i> .....	167
<b>4.3 Single Photon Near IR active photoCORMs</b> .....	170
4.3.1 <i>Synthesis</i> .....	171
4.3.2 <i>Crystal Structure Description</i> .....	171
4.3.3 <i>Spectroscopy</i> .....	174
4.3.4 <i>CO Release Kinetics and Evaluation</i> .....	180
4.3.5 <i>Density Functional Studies</i> .....	188
4.3.6 <i>Experimental Section</i> .....	190
4.3.6.1 <i>General Methods</i> .....	190
4.3.6.2 <i>Synthesis</i> .....	190
4.3.6.3 <i>X-ray Crystallography</i> .....	192
4.3.6.4 <i>Computational Methods</i> .....	193
<b>4.4 References</b> .....	197
<b>4.5 Reprints of Publication and Permissions</b> .....	202
 <b>Chapter 5. Conclusions</b> .....	208
<b>5.1 Evaluation of Silver and Gold Complexes With Benzothiazoles as Antimicrobial Agents</b> .....	208
<b>5.2 Advantages of Gold(I)PPh<sub>3</sub> Complexes</b> .....	210
<b>5.3 Near IR Active photoCORMs</b> .....	212

<b>5.4 Overall Conclusions.....</b>	<b>212</b>
<b>5.5 References.....</b>	<b>212</b>

## List of Figures

---

<b>Figure 1.1.</b>	Structures of the clinically used metal-based drugs silver sulfadiazine (A), auranofin (B) and cisplatin(C).....	4
<b>Figure 2.1.</b>	NHC Ag <sup>+</sup> complexes showing antibacterial activity.....	14
<b>Figure 2.2.</b>	Silver(I) complexes that show antibacterial activity.....	15
<b>Figure 2.3.</b>	The two benzothiazole moieties (top) and their complexes with silver (bottom).....	17
<b>Figure 2.4.</b>	The FT-IR spectrum of Agpbt(top) and Agqbt(bottom) in KBr.....	18
<b>Figure 2.5.</b>	The <sup>1</sup> H NMR of Agpbt (top trace) and Agqbt (bottom trace) in CDCl <sub>3</sub> at 298K.....	19
<b>Figure 2.6.</b>	Absorption spectra of Agpbt (black), Agqbt (blue), pbt (red) and qbt (yellow) in DCM.....	20
<b>Figure 2.7.</b>	Emission spectra of Agpbt (black), Agqbt (blue), pbt (red) and qbt (yellow) in DCM (λ <sub>ex</sub> at 330, 350, 310 and 335 nm respectively).....	20
<b>Figure 2.8.</b>	The turn on fluorescence signaling Ag <sup>+</sup> deligation from pbt (red trace) upon additions of 0.2eq of Bu <sub>4</sub> NCl to Agpbt (black trace, 40μM) in DCM.....	22
<b>Figure 2.9.</b>	The turn on fluorescence signaling Ag <sup>+</sup> deligation from qbt (yellow trace) upon additions of 0.2eq of Bu <sub>4</sub> NCl to Agpbt (blue trace, 40 μM) in DCM.....	22
<b>Figure 2.10.</b>	The perspective view of Agpbt with thermal ellipsoids are shown at 50% probability level with H atoms and BF <sub>4</sub> <sup>-</sup> counterion omitted for clarity.....	23
<b>Figure 2.11.</b>	The perspective view of Agqbt with thermal ellipsoids are shown at 50% probability level with H atoms and BF <sub>4</sub> <sup>-</sup> counterion omitted for clarity.....	24

<b>Figure 2.12.</b> The perspective view of the ligands pbt (right panel) and qbt (left panel) with thermal ellipsoids are shown at 50% probability level with H atoms omitted for clarity.....	24
<b>Figure 2.13.</b> The isomer confirmations of the qbt ligand.....	26
<b>Figure 2.14.</b> The Kohn-Sham orbitals in the frontier region of L1 (qbt).....	27
<b>Figure 2.15.</b> The Kohn-Sham orbitals in the frontier region of Agqbt.....	29
<b>Figure 2.16.</b> The total spin density for the T1 state of Agqbt.....	29
<b>Figure 2.17.</b> <i>P. aeruginosa</i> lawns (top row) with KBr (left), 2% qbt (center), and 2% Agqbt and <i>S. aureus</i> lawns (bottom row) with KBr (left), 2% qbt (center), and 2% Agqbt.....	31
<b>Figure 2.18.</b> The bztpy ligand and its structure with Ag <sup>+</sup> and Cu <sup>2+</sup> .....	33
<b>Figure 2.19.</b> Clearing of bacterial growth of <i>Acinetobacter baumannii</i> (top row): plate (a) KBr pellet 2% (w/w) with Agbztpy (left side) and AgNO <sub>3</sub> (right side); plate (b) KBr pellet 2% (w/w) with Cubztpy (left side) and Agbztpy (right side); plate (c) KBr pellet 2% (w/w) with bztpy (left side) and blank pellet (right side). <i>Staphylococcus epidermidis</i> (bottom row): plate (a) KBr pellet 2% (w/w) with Agbztpy (left side) and AgNO <sub>3</sub> (right side); plate (b) KBr pellet 2% (w/w) with Agbztpy (left side) and Cubztpy (right side); plate (c) KBr pellet 2% (w/w) with bztpy (left side) and blank pellet (right side).....	34
<b>Figure 3.1.</b> Auranofin and examples of linear arrangement of [L-Au(PPh <sub>3</sub> )] complexes.....	57
<b>Figure 3.2.</b> Complexes of [L-Au(PPh <sub>3</sub> )] that show activity towards Gram-positive bacteria.....	63
<b>Figure 3.3.</b> Antibacterial Au(I) complexes.....	65
<b>Figure 3.4.</b> Complexes with antimycobacterial action.....	68
<b>Figure 3.5.</b> The complexes AuPpbt (left) and AuPqbt (right) studied in this chapter.....	70
<b>Figure 3.6.</b> FT-IR Spectra of AuPpbt (top) and AuPqbt (bottom) in KBr.....	72
<b>Figure 3.7.</b> NMR spectra of AuPpbt (top) and pbt (bottom) in CDCl <sub>3</sub> at 298K.....	73



<b>Figure 3.8.</b> NMR spectra of AuPqbt (top) and qbt (bottom) in CDCl <sub>3</sub> at 298K.....	73
<b>Figure 3.9.</b> Absorption spectra of AuPpbt (black), AuPqbt (blue), pbt (red) and qbt (yellow) in DCM.....	74
<b>Figure 3.10.</b> Emission spectra of AuPpbt (black), AuPqbt (blue), pbt (red) and qbt (yellow) in DCM ( $\lambda_{\text{ex}}$ at 330, 350, 310 and 335 nm respectively).....	75
<b>Figure 3.11.</b> Perspective view of the cation of complex AuPpbt (top) and AuPqbt (bottom) with the atom-labeling scheme. The thermal ellipsoids are shown at 50% probability level. Only one of the two crystallographically independent molecules in the asymmetric unit is shown for AuPpbt.....	77
<b>Figure 3.12.</b> The packing patterns for complexes AuPpbt (top) and AuPqbt (bottom) along <i>a</i> axis.....	80
<b>Figure 3.13.</b> Representation of intermolecular $\pi$ - $\pi$ stacking and C---S non-bonded interactions in complex AuPpbt.....	81
<b>Figure 3.14.</b> Different modes of binding of pbt and aryl-benzothiazole.....	82
<b>Figure 3.15.</b> Bacterial lawns after 18 h incubation with KBr pellets of KBr, pbt and qbt (top panel, left to right) and ClAu(PPh <sub>3</sub> ), AuPpbt and AuPqbt (bottom panel, left to right).....	85
<b>Figure 3.16.</b> <sup>19</sup> F NMR spectrum of the mixture of AuPpbt and F <sub>3</sub> CC <sub>6</sub> H <sub>4</sub> SH (top trace), PPh <sub>3</sub> Au–SC <sub>6</sub> H <sub>4</sub> CF <sub>3</sub> synthesized independently (middle trace) and F <sub>3</sub> CC <sub>6</sub> H <sub>4</sub> SH (bottom trace) in CDCl <sub>3</sub> . F <sub>3</sub> CC <sub>6</sub> H <sub>4</sub> S–SC <sub>6</sub> H <sub>4</sub> CF <sub>3</sub> was present in the thiol as an impurity.....	87
<b>Figure 3.17.</b> <sup>31</sup> P NMR spectra of complex AuPpbt (top trace) and PPh <sub>3</sub> Au–SC <sub>6</sub> H <sub>10</sub> NO <sub>3</sub> (bottom trace, formed upon addition of HSC <sub>6</sub> H <sub>10</sub> NO <sub>3</sub> to AuPpbt) in CDCl <sub>3</sub> (the ppm values are w.r.t free PPh <sub>3</sub> in CDCl <sub>3</sub> ).....	88
<b>Figure 3.18.</b> Dramatic rise in luminescence upon addition of CF <sub>3</sub> C <sub>6</sub> H <sub>4</sub> SH to AuPqbt in chloroform. Left: CHCl <sub>3</sub> solution of AuPqbt; right: a mixture of AuPqbt and CF <sub>3</sub> C <sub>6</sub> H <sub>4</sub> SH in CHCl <sub>3</sub> .....	89
<b>Figure 3.19.</b> Circular clearing ring in <i>P. aeruginosa</i> lawn upon application of AuPpbt.....	90

<b>Figure 3.20.</b> The gold complexes AuPpza (left), Au3pza (middle) and Au3pzo (right) evaluated for their antimycobacterial activity.....	97
<b>Figure 3.21.</b> FT-IR spectrum of AuPpza in KBr, cm <sup>-1</sup> .....	98
<b>Figure 3.22.</b> H-NMR spectrum of AuPpza in CD <sub>3</sub> OD at 298K.....	98
<b>Figure 3.23.</b> FT-IR spectra of the precursor complex (top) and Au3pza (bottom)...	100
<b>Figure 3.24.</b> <sup>1</sup> H NMR (in CD <sub>3</sub> CN) spectra of Au3pza (top), the precursor compound (middle) and pza (bottom).....	101
<b>Figure 3.25.</b> FT-IR spectrum of Au3pzo in KBr.....	102
<b>Figure 3.26.</b> <sup>1</sup> H NMR spectra of Au3pzo in CD <sub>3</sub> CN at 298K.....	102
<b>Figure 3.27.</b> The structure of AuPpza with water and OTf anion omitted for clarity. Ellipsoids are shown at the 50% probability level.....	103
<b>Figure 3.28.</b> Crystal structure of Au3pza with thermal ellipsoids at 50% probability.....	105
<b>Figure 3.29.</b> Crystal structure of Au3pzo with thermal ellipsoids at 50% probability.....	105
<b>Figure 3.30.</b> <i>M. tuberculosis</i> OD <sub>600</sub> values of initial (day 0) and after 24h (day 1) incubation with test compounds at 80μM. Column C has no additional compound or acetone.....	109
<b>Figure 3.31.</b> F <sup>19</sup> NMR spectra of HSC <sub>6</sub> H <sub>4</sub> CF <sub>3</sub> (top), ClAuPPh <sub>3</sub> + HSC <sub>6</sub> H <sub>4</sub> CF <sub>3</sub> (middle), and AuPpza + HSC <sub>6</sub> H <sub>4</sub> CF <sub>3</sub> (bottom).....	112
<b>Figure 3.32.</b> Reaction of ClAuPPh <sub>3</sub> (left) and AuPpza (right) after addition of N-acetyl-L-cysteine-methyl-ester.....	112
<b>Figure 4.1.</b> Examples of photoCORMs that exhibit release of CO upon illumination of UV or visible light.....	155
<b>Figure 4.2.</b> TPE active manganese carbonyl complexes that exhibit loss of CO upon irradiation with an 800 nm laser.....	156
<b>Figure 4.3.</b> Mn(I) pbt and qbt based visible light active photoCORMs.....	157
<b>Figure 4.4.</b> FT-IR spectra of Mnpbt (top) and Mnqbt (bottom) in KBr matrix....	158

<b>Figure 4.5.</b> The $^1\text{H}$ NMR spectra of Mnpbt (top) and Mnqbt (bottom) in $\text{CD}_3\text{CN}$ at 298K.....	159
<b>Figure 4.6.</b> A perspective view of Mnpbt showing the atom-labeling scheme with ellipsoids at the 50% probability level.....	160
<b>Figure 4.7.</b> A perspective view of Mnqbt showing the atom-labeling scheme with ellipsoids at the 50% probability level.....	160
<b>Figure 4.8.</b> Changes in the electronic absorption spectrum of Mnpbt in acetonitrile upon exposure to intervals of visible light in MeCN.....	162
<b>Figure 4.9.</b> Changes in the electronic absorption spectrum of Mnqbt in acetonitrile upon exposure to intervals of visible light in MeCN.....	162
<b>Figure 4.10.</b> The $\ln[\text{C}]$ vs time plot for Mnpbt indicating $k_{\text{CO}}$ value of $0.98 \pm 0.02$ (concentration $7.76 \times 10^{-5} \text{ M}$ ).....	163
<b>Figure 4.11.</b> The $\ln[\text{C}]$ vs time plot for Mnqbt indicating $k_{\text{CO}}$ value of $2.51 \pm 0.02$ (concentration $6.87 \times 10^{-5} \text{ M}$ ).....	163
<b>Figure 4.12.</b> Enhancement of emission intensity for Mnpbt in acetonitrile upon exposure to visible light ( $\lambda_{\text{ex}} = 345 \text{ nm}$ , $\lambda_{\text{em}} = 390 \text{ nm}$ ).....	164
<b>Figure 4.13.</b> Enhancement of emission intensity for Mnqbt in acetonitrile upon exposure to visible light ( $\lambda_{\text{ex}} = 345 \text{ nm}$ , $\lambda_{\text{em}} = 405 \text{ nm}$ ).....	165
<b>Figure 4.14.</b> Near IR active photoCORMs.....	171
<b>Figure 4.15.</b> Molecular structure of MnNIR1 with atom labeling scheme. The thermal ellipsoids are shown at 50% probability level.....	173
<b>Figure 4.16.</b> Structures of previously reported photoCORMs.....	173
<b>Figure 4.17.</b> Molecular structure of MnNIR2. The thermal ellipsoids are shown at 50% probability level.....	174
<b>Figure 4.18.</b> FT-IR spectrum of MnNIR1 (top) and MnNIR2(bottom) in KBr matrix.....	175
<b>Figure 4.19.</b> $^1\text{H}$ NMR spectrum of NIR1 (top trace) and MnNIR1 (bottom trace) in $\text{CDCl}_3$ at 298K (not shown; 3.07 ppm, s, 6H for NIR1 and 3.25 ppm, s, 6H for MnNIR1).....	176

<b>Figure 4.20.</b> $^1\text{H}$ NMR spectrum of NIR2 (top trace) and MnNIR2 (bottom trace) in $\text{CDCl}_3$ at 298K (not shown; 3.02 ppm, s, 6H for NIR2 and 3.08 ppm, s, 6H for MnNIR2).....	177
<b>Figure 4.21.</b> Electronic absorption spectrum of MnNIR1 (black trace) and NIR1 (black dashed trace) in $\text{CHCl}_3$ .....	178
<b>Figure 4.22.</b> Electronic absorption spectrum of MnNIR2 (black trace) and NIR2 (black dashed trace) in $\text{CHCl}_3$ .....	179
<b>Figure 4.23.</b> Electronic absorption spectrum of MnNIR1 in 1%DMSO/PBS.....	179
<b>Figure 4.24.</b> Changes in the electronic spectrum of MnNIR1 (solid traces) upon illumination of 730 nm light in $\text{CHCl}_3$ at 298K. The absorption spectrum of NIR1 is also shown (dashed trace).....	181
<b>Figure 4.25.</b> UV-vis traces from the Myoglobin assay with a $\text{CHCl}_3$ solution of MnNIR1 at 298K: blue trace, oxidized Mb; black trace, reduced Mb; red trace, COMb.....	182
<b>Figure 4.26.</b> Spectral Changes of MnNIR2 (solid traces) upon exposure to 730 nm light in 2 min intervals and MIR2 (blue dashed trace) in $\text{CHCl}_3$ .....	182
<b>Figure 4.27.</b> The $\ln[\text{MnNIR1}]$ vs Time plot used to determine $k_{\text{CO}}$ at 100% (black trace), 75% (green trace), 50% (blue trace) and 25% (red trace) power of 730nm light.....	184
<b>Figure 4.28.</b> The $\ln[\text{MnNIR2}]$ vs time plot used to the find the $k_{\text{CO}}$ of MnNIR2 ( $0.0566 \pm 0.0008$ ) in $\text{CHCl}_3$ .....	184
<b>Figure 4.29.</b> Comparison of $k_{\text{CO}}$ release rates for MnNIR1 compared to power of light source output. Proportionality constant = $1.04 \pm 0.09$ .....	185
<b>Figure 4.30.</b> The $\ln[\text{MnNIR1}]$ vs time plot used to the find the $k_{\text{CO}}$ of MnNIR1 ( $0.0088 \pm 0.0006$ ) in 1%DMSO/PBS.....	186
<b>Figure 4.31.</b> $\text{CHCl}_3$ solutions of MnNIR1 (green) and after irradiation with 730nm light (blue).....	187
<b>Figure 4.32.</b> The FT-IR spectrum of MnNIR1 (black trace) and MnNIR1 after irradiation with 730 nm light (red trace) in KBr. A solution of MnNIR1	

in CHCl <sub>3</sub> was irradiated and further removal of the solvent afforded the photolyzed solid (red trace). .....	187
<b>Figure 4.33.</b> The EPR spectrum of photolyzed MnNIR1 in MeCN.....	188
<b>Figure 4.34.</b> Calculated energy diagram of MnNIR1 with the MOs involved in the HOMO to LUMO transition.....	189
<b>Figure 4.35.</b> Relative Gibbs free energy (in kcal/mol), fraction of molecules in the ground state ensemble for the conformation (%), excitation wavelength (oscillator strength), C1-C2-N-C3 torsion angle (in °) of the conformers of (a) NIR1 and (b) MnNIR1.....	195
<b>Figure 5.1.</b> Comparison of the bacterial rings of clearing from Agqbt (left) and AuPpbt (right) of <i>P. aeruginosa</i> .....	209

## List of Tables

---

<b>Table 2.1.</b> Crystal data and refinement parameters for Agpbt and Agqbt .....	38
<b>Table 3.1.</b> Selected bond distances (Å) and angles (°) for complex AuPpbt · CH <sub>2</sub> Cl <sub>2</sub> and AuPqbt.....	78
<b>Table 3.2.</b> Crystal data and structure refinement parameters for AuPpbt and AuPqbt.....	94
<b>Table 3.3.</b> Selected bond lengths and angles for AuPpza•H <sub>2</sub> O, Au3pza and Au3pzo.....	104
<b>Table 3.4.</b> MIC (μM) values for activity against <i>M. Smegmatis</i> .....	107
<b>Table 3.5.</b> Refinement parameters for AuPpza, Au3pza and Au3pzo.....	116
<b>Table 4.1.</b> Crystal data and structure refinement experimental details of Mnpbt and Mnqbt.....	168
<b>Table 4.2.</b> Selected bond lengths and angles for Mnpbt.....	169
<b>Table 4.3.</b> Selected bond lengths and angles for Mnqbt.....	169
<b>Table 4.4.</b> Rates of CO release from MnNIR1 calculated from various power of NIR light.....	185
<b>Table 4.5.</b> Crystal data and structure refinement parameters for <b>MnNIR1</b> and <b>MnNIR1</b> .....	193
<b>Table 4.6.</b> TD-DFT results of MnNIR1 and NIR1.....	196

---

## List of Schemes

---

<b>Scheme 3.1.</b> Typical synthetic routes for [L-Au(PPh <sub>3</sub> )] complexes.....	60
<b>Scheme 3.2.</b> Synthetic Route for AuPpbt and AuPqbt.....	71
<b>Scheme 3.3.</b> Suggested ligand binding mode rearrangement from the precursor complex (left) to Au <sub>3</sub> pza.....	100

# **DESIGN, SYNTHESIS AND CHARACTERIZATION OF TRANSITION METAL COMPLEXES FOR UTILIZATION IN THERAPEUTIC APPLICATIONS**

**Jenny Stenger-Smith**

## **ABSTRACT**

The use of metal complexes for therapeutic applications has been valuable in the treatment of diseases such as cancer and microbial infections. These metal complexes can be purposefully designed with ligands and metal centers that produce favorable properties for advancing the treatment of these diseases. In both microbial infections and cancer, resistance to commonly prescribed drugs is observed and new therapeutic methods with differing mechanisms of action is needed to further treat these diseases.

Both gold and silver complexes have shown potent activity towards microbial infections. These metals are known to have multiple mechanism of actions which together produce the bactericidal activity. This is a particular advantage in the treatment of multi-drug resistant microbes and considering traditional organic based antibiotics typically have only one specific mechanism of action. In Chapter 2, silver complexes with benzothiazoles are evaluated for their antimicrobial activity using a skin and soft tissue infection (SSTI) model and proved to be potent bactericidal agents. The use of benzothiazoles as a ligand for silver is important in that they are members of a class of



antibacterial agents and these ligands also exhibit fluorescence quenching when coordinated to the silver center. The interactions of the silver complexes with biological molecules (potentially leading to the bactericidal activity) is thus accompanied by the gradual turn on of fluorescence and provides a convenient means to track the release of  $\text{Ag}^+$ .

Chapter 3 utilizes gold complexes bearing triphenylphosphine for the treatment of bacterial and mycobacterial infections. Gold complexes with the same benzothiazoles used in Chapter 2 showed potent bactericidal activity with the SSTI model. Experiments indicated that the overall charge and structure of the gold complexes synthesized was important for the effectiveness of these species. Considering the results obtained from the antibacterial activity of the gold(I) triphenylphosphine ( $\{\text{Au}(\text{PPh}_3)\}^+$ ) complexes, the second part of Chapter 3 focuses on the utility of this moiety towards mycobacterial infections. Mycobacterium are known to have very thick, hydrophobic and waxy outer membranes which are linked to their difficulty of treatment (*Mycobacterium tuberculosis* is responsible for Tuberculosis (TB) disease). Utilizing a complex with the  $\{\text{Au}(\text{PPh}_3)\}^+$  unit and the clinically used TB drug pyrazinamide showed better antimicrobial activity compared to other gold species lacking this unit (likely brought about from the enhanced lipophilicity provided from the  $\{\text{Au}(\text{PPh}_3)\}^+$  unit).

The work described in Chapter 4 discusses light activated carbon monoxide (CO) releasing molecules (photoCORM) which have shown important therapeutic effects towards the eradication of cancer. The design strategy of extending the  $\pi$

conjugation of the ligand framework lead us to identify the first single photon excitation activation of manganese carbonyl photoCORMs with low power near IR light. While release of CO has been observed in this type of species with two photon excitations with near IR light, this two photon process requires expensive high power lasers. By using light in this region with low power as needed for single photon excitation, better penetration into tissues can be observed with less damage and allows for improved therapeutic effects.

The transition metal complexes used in this work were designed to achieve specific results pertinent to the treatment of disease. The studies and experiments done with the complexes prove that these design principles are a useful tool to enhance the effectiveness of metal complexes for biological implementations.

## Acknowledgements

I would like to thank my thesis advisor Professor Pradip K. Mascharak for his support and guidance throughout my time working towards my doctorate degree. His scientific knowledge and discussions has really helped me to develop into the scientist I am today. I am deeply grateful for the time and energy he put in to ensuring I was on track to reach my goals.

I would also like to thank my committee members Professor Scott R. J. Oliver and Professor Theodore R. Holman for their guidance through all the milestones to receiving a PhD. I had the pleasure of being a TA for both them and enjoyed my time doing so.

When I first arrived to UCSC, Dr. Indranil Chakraborty showed me the ropes in lab and has since provided enormous support. He was always willing to run a crystal or help me in any scientific way. I would like to thank him not only for his scientific support, but also for his friendship. There have been a number of lab mates who have been there to discuss ideas with me or to help me solve a problem. I would like to thank, Dr. Miguel Pinto, Brian Kawahara, Dr. Jorge Jimenez and John Wenger for both their entertainment and knowledge throughout my time in lab. I also wish to thank Rama Ouattara, Binu Dhukuchhu, and Jorge Martinez Gonzales, the undergraduate students who worked closely with me and helped me greatly in lab.

I would also like to thank my friends Ariel Kuhn and Pamela Schleissner for all their love, support, and discussions both inside and outside chemistry. I could not have

gone through graduate school without you two by my side. I want to acknowledge many of my chemistry friends Victor, Duy, David, Bia, Anam, Jocelyn, Kaitlyn, Jerah, Tommy and Pat for their friendship and fun times throughout grad school.

I am very grateful for the help of Dr. Mireille Kamariza who collaborated with me on a major project. Also for the mentorship provided by Dr. Alejandro Briseno during my NREIP internship. A special thanks to Dr. Samantha Carrington for teaching me DFT and always being available for practice talks and support.

I would like to thank all of the chemistry faculty for their guidance and knowledge as well as the staff, especially Karen Meece and Katie Crampton who have also been extremely helpful with any request or question I have.

I appreciate the friendship and knowledge from my high school chemistry teacher, John Cosner, who after taking his class I decided to pursue chemistry. I would also like to thank Dr. Chad Immoos who prepared me for graduate school in undergrad research at Cal Poly SLO.

I wish to thank my friends Amy Long, Morgan and Callie Stickney, Sarah Prittie, and Erin Splendorio who have been there for me for so many years. I also would like to thank Toni and Jamie Kelly for welcoming me into their family and always supporting my goals.

Last, but not least I wish to thank my amazing family for their love and dedication. My father, Dr. John D. Stenger-Smith who has been and still is an inspiration, an invaluable resource and friend. My mom, Lisa, who has always been there to listen to me, offer advice and keep me going no matter what. My two sisters

Julie and Jazz who are my best friends and distractions when I needed them. My husband Mackie Kelly, who I met in the first few months of grad school and has been my rock and number one supporter. I also wish to thank Ma, who taught me how to be a strong independent woman and never give up.

## **Dedication**

I dedicate this thesis to my amazing family, friends and especially to Ma.

## **Chapter 1. Introduction**

### **1.1 Background on Antibacterial and Anticancer Drug Development and Complications**

There is no question that cancer and microbial infections are some of the major ominous diseases in the world today. In fact, antimicrobial resistance is now considered to be a global healthy emergency and cancer is the second leading cause of death.<sup>1,2</sup> These maladies have been studied extensively but still remain serious challenges despite the enormous effort from scientists. Antibiotics like penicillin and other “wonder drugs” were not developed until the 1950s. However, their use was so substantial and effective that many people thought infectious microbes were largely conquered and suggested researchers focus on other diseases like cancer.<sup>3</sup> Cancer chemotherapy research started in the early 1900s when drugs like 5-fluorouracil were studied, but initial treatments showed little promising results due to severe side effects.<sup>4</sup> The development of cisplatin used in combination with other drugs significantly increased the cure rate of testicular cancer and further prompted combination therapy research.<sup>4</sup> While early drug discoveries towards the treatment of these diseases had been moving in the right direction, the problem of emerging resistance has appeared as a major obstacle in both cancer chemotherapy and bacterial infections.

The mechanisms of resistance towards antibiotics and chemotherapy drugs are vastly different, but the overall problem remains the same: traditional drugs are no longer able to effectively treat the disease.<sup>5,6</sup> Bacterial resistance to sulfonamides,

trimethoprim, and penicillins are widely known and the CDC has identified numerous species as urgent and serious threats.<sup>7,8</sup> The cause of the wide spread antibiotic resistance crisis is thought to be from overuse, inappropriate prescribing, extensive agricultural use, availability of few new antibiotics and regulatory barriers. One of the most popular and deadly species, Methicillin resistant *Staphylococcus Aureus* (MRSA), killed more people than HIV/AIDS, Parkinson's disease, emphysema and homicide combined. There are numerous other multi-drug resistant (MDR) pathogens including *Streptococcus pneumonia*, *Pseudomonas Aeruginosa*, and *Mycobacterium tuberculosis* which add to the antibiotic crisis. This same effect is becoming prevalent in cancer treatment and chemotherapeutic resistance is thought to be responsible for 90% of cancer related deaths. Resistance to many common chemotherapy drugs like Methotrexate, Cisplatin, Doxorubicin, Taxol and Vinblastine has been observed and even multi-drug resistance in cancer chemotherapy is apparent.<sup>9</sup> Both chemotherapeutic and antibiotic resistance can be acquired or intrinsic. Regardless of the nature of resistance, it is generally believed that part of the resistance problem could be solved by the development of new and/or combination of therapeutics to treat these diseases.<sup>5,10</sup> To move a new drug past clinical trials and into market is a slow and expensive process.<sup>5</sup> Despite the hurdles, drug discovery for the treatment of these diseases is a highly important and emerging area if we are to continue to effectively cure and treat diseases.

In recent years, research on drug discovery has broadened to include areas such as machine learning, nanoparticles, novel metal complexes, antibodies, and use of



radioactive elements. One particular area of interest in our laboratory is to design and isolate metal complexes and explore their applications in medicine. Scientists have been exploring medicinal inorganic molecules as novel drugs with different mechanisms of action compared to traditional clinically used drugs.<sup>11</sup> Inorganic elements play an important role in biological systems and have been used in the medicinal world as diagnostic agents, enzyme inhibitors, radiopharmaceuticals, and therapeutic agents in chelation therapy.<sup>11</sup> Metallic complexes of Ag, Au, Cu, Ni, Co have been studied for their antimicrobial properties<sup>12,13</sup> and Pt, Au, Ru, Re and Cu have been exploited in cancer therapy.<sup>14,15</sup> Specifically in this report, complexes of Ag and Au for antibacterial treatment and Mn for cancer treatment will be discussed.

Silver has been the most popular metal for use as antimicrobial agents and has been in use clinically as silver sulfadiazine (**Figure 1.1, A**) to treat burn wound infections. The antibacterial activity of silver sulfadiazine has been strongly correlated to the  $\text{Ag}^+$  ion rather than the sulfadiazine ligand.<sup>16</sup> While the exact mechanism of action of silver complexes is not entirely known, research suggests that there are multiple pathways by which it can exert its antibacterial action.<sup>17</sup> One of the recent findings is the ability of  $\text{Ag}^+$  ions to bind to essential cysteine containing enzymes which could play a role in its antimicrobial action.<sup>18,19</sup> The disruption of bacterial cell walls, binding to peptides and cofactors, DNA damage and ROS formation have also been identified as possible mechanisms of actions in general for silver compounds.<sup>17</sup> These offer alternate routes to traditional organic antibiotics and may be useful in combating MDR bacteria. Many antimicrobial silver complexes have been identified

and extensively studied, but efforts have and need to be made to fine tune selective uptake for better activity and lower toxicity.<sup>17,20</sup> Ligands chosen to complex silver can influence stability, lipophilicity and therefore play a crucial role in selectivity and action.

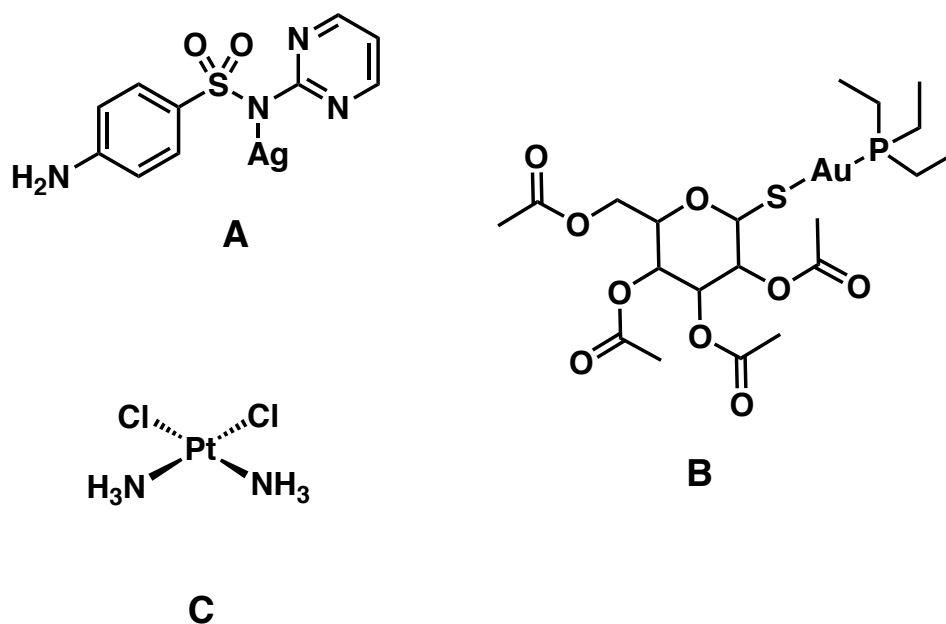


**Figure 1.1.** Structures of the clinically used metal-based drugs silver sulfadiazine (A), auranofin (B) and cisplatin (C).

Like silver, gold has been recognized for its antimicrobial activity but has gained significant attention in the anticancer realm as well.<sup>19,21,22</sup> In late 1800s, Gold therapy was popularized by Robert Koch who investigated the activity of  $\text{KAu}(\text{CN})_2$  towards *M. tuberculosis*.<sup>23</sup> The study of gold complexes eventually led to the introduction of the FDA approved drug auranofin (**Figure 1.1, B**) in 1985 for the treatment of

rheumatoid arthritis. A huge effort to find new and improved gold drugs has since ensued, even the repurposing of auranofin for potential treatment of cancer, bacterial infections, parasites and HIV/AIDS.<sup>24</sup> Much like silver, the specific mechanism of action of gold drugs is not understood, however some identified targets for anticancer properties are inhibition of thioredoxin reductase (TrxR) and inhibition of the ubiquitin-proteasome system.<sup>24</sup> In bacteria, gold has been identified to inhibit formation of cell wall and biosynthetic pathways involved in DNA and protein production.<sup>25</sup> The effectiveness of gold complexes is also influenced by the ligands on the gold center which ultimately influence uptake, binding targets and overall toxicity. Research into new gold and silver complexes could offer an answer to infections by MDR bacteria.

Cisplatin (**Figure 1.1, C**), a platinum based inorganic chemotherapeutic, has been used to treat cancer since the late 1970s.<sup>26</sup> While this drug has aided in increasing the life expectancy of cancer patients, there are severe side effects and resistance to this drug is a common occurrence. New therapeutic drugs that offer different mechanisms to combat resistance and fewer off target effects are important for the continuing development of cancer drugs. One area that has gained much attention in the anticancer field is carbon monoxide releasing molecules (CORMs). The human body endogenously produces carbon monoxide (CO) and it plays an important role in cell signaling and recently it has been discovered that CO can be exploited in other therapeutic applications.<sup>27</sup> Exogenous carbon monoxide is known to show anti-proliferative and pro-apoptotic effects in cancer cells and has been studied for its use in cancer treatment.<sup>27</sup> One challenge researchers have faced is controlling the release

of CO to the particular area of interest so as not to cause adverse side effects in healthy tissues. For this purpose, systems which release CO when exposed to light (photoCORMs) have been extensively studied. Usually photoCORMs involve metal carbonyl complexes which release CO upon exposure of light in the UV-visible range.<sup>28</sup> Research in this area has focused towards using light within the phototherapeutic window (650-1000nm) to allow for deeper penetration and less damage to cells.<sup>29,30</sup> Development of new CO releasing molecules which are fine-tuned in their CO release ability may provide leads towards valuable new cancer drugs.

Research on new therapeutic treatments, regardless of disease, is important for the developing world. Because drug resistance in both bacteria and cancer cells will make traditional drugs irrelevant and out of date, discovery of new drugs and how they work (along with their side effects) will provide valuable insight into new generation of therapeutic agents.

## **1.2 General Direction of Research**

The need for new and improved treatment methods to combat drug resistance for both bacterial infections and cancer is growing rapidly. A number of different directions could be taken in developing these new therapeutics and most believe new drugs or drug combinations could help to reduce the impact of resistance. The goal of this current research is to use the understanding of what we know about current metal containing drugs to further design and investigate new drugs that may be useful in the treatment of resistant infections and diseases.

Chapter 2 will focus on complexes of silver and how their structure influences antibacterial action. Fluorescent properties will be linked to the trackability of the Ag<sup>+</sup> delivery. Chapter 3 describes the versatility of gold complexes for their use as various antimicrobial agents. The importance of ligand influence and oxidation state will be highlighted and compared. In chapter 4 the development of photoCORMs with CO activation in the phototherapeutic region will be described. Each chapter highlights a different metal and thus background information for the specific goal will be extensively outlined within each chapter.

### 1.3 References

- (1) Toner, E.; Adalja, A.; Gronvall, G. K.; Cicero, A.; Inglesby, T. V. Antimicrobial Resistance Is a Global Health Emergency. *Heal. Secur.* **2015**, *13* (3), 153–155.
- (2) Heron, M. Deaths: Leading Causes for 2017. *Natl. Vital Stat. Reports* **2019**, *68* (6).
- (3) Lederberg, J. Infectious History. *Science*. **2000**, *288* (5464), 287-293
- (4) DeVita, V. T.; Chu, E. A History of Cancer Chemotherapy. *Cancer Res.* **2008**, *68* (21), 8643–8653.
- (5) Gold, H. S.; Moellering Jr., R. C. Antimicrobial-Drug Resistance. *Drug Ther. (NY)*. **1996**, *335* (19), 1445–1453.
- (6) Alfarouk, K. O.; Stock, C. M.; Taylor, S.; Walsh, M.; Muddathir, A. K.; Verduzco, D.; Bashir, A. H. H.; Mohammed, O. Y.; Elhassan, G. O.; Harguindey, S.; Reshkin, S. J.; Ibrahim, M. E.; Rauch, C. Resistance to Cancer Chemotherapy: Failure in Drug Response from ADME to P-Gp. *Cancer Cell Int.* **2015**, *15* (71).
- (7) Sköld, O. Resistance to Trimethoprim and Sulfonamides. *Vet. Res.* **2001**, *32* (3–4), 261–273.
- (8) Ventola, L. Antibiotic Resistance Crisis. *Pharm. Ther.* **2015**, *40* (4), 277–283.

- (9) Mansoori, B.; Mohammadi, A.; Davudian, S.; Shirjang, S.; Baradaran, B. The Different Mechanisms of Cancer Drug Resistance: A Brief Review. *Adv. Pharm. Bull.* **2017**, *7* (3), 339–348.
- (10) Wang, X.; Zhang, H.; Chen, X. Drug Resistance and Combating Drug Resistance in Cancer. *Cancer Drug Resist.* **2019**, *2*, 141–160.
- (11) Sadler, P. J.; Guo, Z. Metals in Medicine. *Angewandte* **1999**, *38*, 1512–1531.
- (12) Rizzotto, M. Metal Complexes as Antimicrobial Agents. In *A Search for Antibacterial Agents*; Varaprasad Bobbarala, IntechOpen, 2012, pp 73–88.
- (13) Glišić, B.; Djuran, M. I. Gold Complexes as Antimicrobial Agents: An Overview of Different Biological Activities in Relation to the Oxidation State of the Gold Ion and the Ligand Structure. *Dalt. Trans.* **2014**, *43* (16), 5950–5969.
- (14) Ndagi, U.; Mhlongo, N.; Soliman, Metal Complexes in Cancer Therapy an-Update from Drug Design Perspective. *Drug Des. Devel. Ther.* **2017**, *11*, 599–616.
- (15) Fricker, S. P. Metal Based Drugs: From Serendipity to Design. *Dalt. Trans.* **2007**, No. 43, 4903–4917.
- (16) Fox, C. L.; Modak, S. M. Mechanism of Silver Sulfadiazine Action on Burn Wound Infections. *Antimicrob. Agents Chemother.* **1974**, *5* (6), 582–588.
- (17) Medici, S.; Peana, M.; Crisponi, G.; Nurchi, V. M.; Lachowicz, J. I.; Remelli, M.; Zoroddu, M. A. Silver Coordination Compounds: A New Horizon in Medicine. *Coord. Chem. Rev.* **2016**, *327–328*, 349–359.
- (18) Wang, H.; Wang, M.; Yang, X.; Xu, X.; Hao, Q.; Yan, A.; Hu, M.; Lobinski, R.; Li, H.; Sun, H. Antimicrobial Silver Targets Glyceraldehyde-3-Phosphate Dehydrogenase in Glycolysis of: E. Coli. *Chem. Sci.* **2019**, *10* (30), 7193–7199.
- (19) Frei, A. Metal Complexes, an Untapped Source of Antibiotic Potential? *Antibiotics* **2020**, *9* (90).
- (20) Liang, X.; Luan, S.; Yin, Z.; He, M.; He, C.; Yin, L.; Zou, Y.; Yuan, Z.; Li, L.; Song, X.; Lv, C.; Zhang, W. Recent Advances in the Medical Use of Silver Complex. *Eur. J. Med. Chem.* **2018**, *157*, 62–80.
- (21) Dominelli, B.; Correia, J. D. G.; Kühn, F. E. Medicinal Applications of Gold(I/III)-Based Complexes Bearing N-Heterocyclic Carbene and Phosphine

- Ligands. *J. Organomet. Chem.* **2018**, *866*, 153–164.
- (22) Mora, M.; Gimeno, M. C.; Visbal, R. Recent Advances in Gold-NHC Complexes with Biological Properties. *Chem. Soc. Rev.* **2019**, *48*, 447–462.
  - (23) Koch, R. Über Bakteriologische Forschung. *Detsch. Med. Wochenschr.* **1890**, *16*, 756–757.
  - (24) Roder, C.; Thomson, M. J. Auranofin: Repurposing an Old Drug for a Golden New Age. *Drugs R D* **2015**, *15*, 13–20.
  - (25) Thangamani, S.; Mohammad, H.; Abushahba, M. F. N.; Sobreira, T. J. P.; Hedrick, V. E.; Paul, L. N.; Seleem, M. N. Antibacterial Activity and Mechanism of Action of Auranofin against Multi-Drug Resistant Bacterial Pathogens. *Sci. Rep.* **2016**, *6* (October 2015), 1–13.
  - (26) Dasari, S.; Bernard Tchounwou, P. Cisplatin in Cancer Therapy: Molecular Mechanisms of Action. *Eur. J. Pharmacol.* **2014**, *740*, 364–378.
  - (27) Motterlini, R.; Otterbein, L. E. The Therapeutic Potential of Carbon Monoxide. *Nat. Rev. Drug Discov.* **2010**, *9*, 728–743.
  - (28) Wright, M. A.; Wright, J. A. PhotoCORMs: CO Release Moves into the Visible. *Dalt. Trans.* **2016**, *45* (16), 6801–6811.
  - (29) Smith, A. M.; Mancini, M. C.; Nie, S. Second Window for in Vivo Imaging. *Nat. Nanotechnol.* **2009**, *4* (11), 710–711.
  - (30) Plaetzer, K.; Krammer, B.; Berlanda, J.; Berr, F.; Kiesslich, T. Photophysics and Photochemistry of Photodynamic Therapy: Fundamental Aspects. *Lasers Med. Sci.* **2009**, *24* (2), 259–268.

## **Chapter 2. Trackable Antimicrobial Silver Complexes**

### **2.1 Background on Medicinal Silver**

Silver has been used for its antimicrobial purposes for thousands of years; in containers to keep water fresh, for wound healing and the treatment of ulcers.<sup>1</sup> It eventually became medical practice for the prevention of infection by the use of silver foil in wound dressings, silver structures in surgical implants or silver nitrate as eye drops. In the early 1900s colloidal silver was ingested or given intravenously for the treatment of sepsis, tonsillitis, epidermitis and other infections. Silver sulfadiazine was developed and approved for clinical use in the late 1900s and was widely used as a topical agent to control bacterial infections particularly in burn victims.<sup>2</sup> Since then, other complexes of silver in the forms of ionic complexes and nanoparticles have been extensively studied and developed for their antimicrobial activity.<sup>3</sup>

On top of direct use for treatment of infection in humans, silver has been gaining increasing popularity for its preventative use in medical devices. Silver coatings or incorporation into these medical devices or the packaging of such devices has been shown to prevent microbes from growth on these surfaces.<sup>3</sup> Patents containing applications of antimicrobial silver in the past decade have increased and even expanded into water filtration systems and food storage containers.

Silver is typically well tolerated in the body, however misuse can cause some further complications. The most common side effect is argyria, the deposition of silver particles under the skin causing a blue-grey tint.<sup>4</sup> The degree of argyria observed is



dependent on the method of application (topical, ingestion, eye drops), the frequency of use and other factors. Agyria can go away on its own or can be permanent, but in general does not have severe side effects unless extensive use or misuse is the cause. When proper use is observed silver exhibits low toxicity within the body and its use associated with medical devices is considered relatively low risk for adverse side effects. For these reasons the applications of silver in various areas has been successfully explored, is considered relatively safe and is commonly used.<sup>5</sup>

### **2.1.1 Antimicrobial Silver**

Silver has been used for extensive medical applications due to the significantly lower toxicity to human cells than to bacteria.<sup>6</sup> There are a number of different forms of silver which can be useful for antimicrobial properties including ionic complexes of silver or silver nanoparticles. Silver is a  $d^{10}$  metal, most commonly as the charged species  $Ag^+$  (as an ionic complex) or  $Ag^0$  (as nanoparticles). Complexes with silver carrying a  $1^+$  charge can vary in geometry with common linear and tetrahedral coordination environments however 3, 5 and 6 coordinate complexes have been identified. The ligand environment surrounding the metal center is typically composed of S, P, N, O, halide, carbene, or a combination of multiple ligands.<sup>7</sup> The coordination flexibility of these complexes provide seemingly unlimited possibilities for the development of silver complexes with different properties arising from the influence of the ligand.

The exact mechanism of action of silver has not been fully elucidated, but it is generally believed to involve the release of  $\text{Ag}^+$  from the coordination environment and subsequent interactions with biological molecules that disrupt cellular functions.<sup>8</sup> Silver ions have been identified to interact strongly with bacterial membranes as well as with internal components of the bacteria. The binding of silver ions with thiol groups occurs rapidly and has led to the identification of deactivation of the succinate dehydrogenase and aconitase membrane respiratory chain enzymes in some bacteria.<sup>9</sup> This leads to the observed production of reactive oxygen species (ROS) and DNA damage, all of which contribute to the mechanism of antimicrobial action for silver ions. Damage to bacterial membranes causing the cell wall to degrade and release its contents have also been identified to play a role in the activity.<sup>10</sup> The mechanism of action of silver nanoparticles seems to be similar to that of  $\text{Ag}^+$  due to the life cycle of the nanoparticles eventual transformation into silver ions, however the exact mechanism still remains unclear.<sup>11,12</sup> The use of silver nanoparticles has been extensively studied, however the risk of increased silver released into the environment has not yet been fully elucidated.<sup>13</sup> For this reason, we wanted to avoid the use of silver nanoparticles and their potential negative effect on the ecosystem and rather focus on the efficacy of discrete ionic complexes.

Considering the mechanism of action of these complexes arises from the release of the  $\text{Ag}^+$  ion from the native ligand environment, specific design strategies to control release of silver ions have been evaluated. More strongly coordinating ligands will release ions slower and may allow for a much lower silver content to be effective than

the clinically used silver sulfadiazine which loses silver ions rapidly.<sup>8</sup> Of the types of silver complexes evaluated for their antimicrobial action, silver N-heterocyclic carbenes (NHC) have been one of the most developed due to the relatively strong silver carbon bond. This functionalization of the NHC core allows varying physiochemical properties of the silver complexes that can be tailored for specific uses.<sup>7</sup> NHC compound **1** (**Figure 2.1**) showed potent activity towards the respiratory infectious pathogen *Pseudomonas aeruginosa* and *in vivo* activity with *P. aeruginosa* infected mice.<sup>14</sup> The silver complex showed minimal cytotoxic activity while lowering bacterial loads within the lung indicating this type of complex may be useful in the treatment of pulmonary infections. Complex **2** (**Figure 2.1**) also containing the NHC core showed *in vivo* activity towards *Galleria mellonella* larvae infected with *Staphylococcus aureus* and the yeast *Candida albicans*.<sup>15</sup> Administration of **2** in the infected larvae showed an increased rate of survival compared to untreated larvae and no immune response was identified unlike similar experiments with AgNO<sub>3</sub>. The lipid nature of **2** may be better tolerated by the insects own immune system and therefore the antimicrobial properties were concluded to be from **2** and not a non-specific immune response induced by administration. Further bis NHC complexes of type **3** (**Figure 2.1**) have been identified to have potent *in vitro* activity towards *S. aureus* and *Escherichia coli* with MIC's ranging from 12.5 to 100 µg/mL.<sup>16</sup> Complexes of this type were able to degrade both DNA and RNA and this mechanism likely plays a role in their antibacterial activity. Many more NHC containing species have been evaluated, but overall the structure

activity relationship of this type of silver complexes seems to be correlated to the bioavailability of  $\text{Ag}^+$  and the lipophilicity.<sup>7</sup>

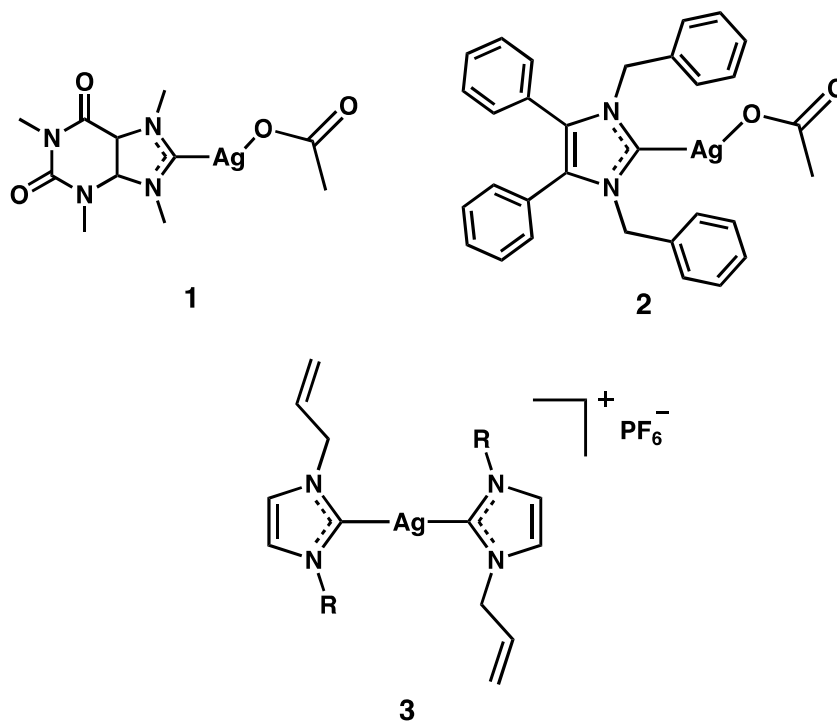


**Figure 2.1.** NHC  $\text{Ag}^+$  complexes showing antibacterial activity.

Silver carboxylate complexes have also been extensively evaluated for their antimicrobial activity. Complex **4** (**Figure 2.2**) showed potent activity towards the Gram-negative species *E.coli* and *P. aeruginosa* as well as Gram-positive species *S. aureus* and *Enterococcus faecalis*.<sup>17</sup> The bimetallic complex **5** (**Figure 2.2**) was evaluated for its activity towards *S. epidermitis* and *S. aureus* showing increased activity compared to  $\text{AgNO}_3$  and potent antibiofilm activity. These and other results in this study show important implications for wound healing using a hydrogel-cream with

complex **5**.<sup>18</sup> Further, complex **6** (**Figure 2.2**) with carboxylate and N donor ligands were evaluated against *E.coli*, *C. albicans*, *S. aureus*, *Bacillus subtilis* and *Salmonella glostrup* with MIC's ranging between 0.1 and 50  $\mu\text{g/mL}$ .<sup>19</sup> The LD<sub>50</sub> of **6** was determined in mice to be 2.22 g/kg indicating low toxicity and good prospects for antimicrobial drugs of silver with amino acids. Other silver complexes with mixed ligands also show potent antibacterial activity. The tetrahedral complex **7** (**Figure 2.2**) and other similar complexes showed potent bactericidal activity towards methicillin resistant *S. aureus* (MRSA), *Klebsiella pneumonia*, *Salmonella typhimurium* and the yeast *C. albicans*.<sup>20</sup>

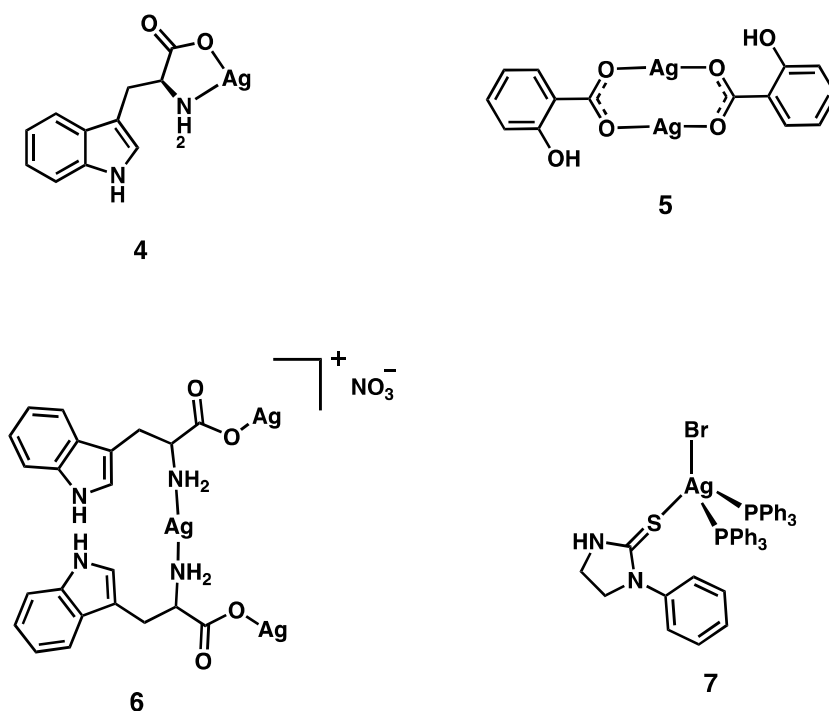


**Figure 2.2.** Silver(I) complexes that show antibacterial activity.

The antimicrobial properties of silver complexes have been extensively studied on numerous species of bacteria, yeast and even tumor cell lines.<sup>7</sup> The potent eradication of bacterial cells and low cytotoxicity identified for these species prove silver to be a useful tool in combating infections and is already commercially used in burn wound infections, textiles and medical device coatings. The  $\text{Ag}^+$  ion is repeatedly identified to interact with membranes, proteins, DNA and generate ROS and thus the mechanism of action of most silver complexes likely falls under all or some of these categories. The effectiveness of these species is often linked to the ability of the  $\text{Ag}^+$  ion to be released from the ligand framework in a controlled manner so to provide a therapeutic amount over an extended period of time. Although resistance to silver has been identified, the proper use of antibacterials could help prevent widespread resistance.<sup>21</sup> Regardless, the effectiveness of silver complexes and nanoparticles is well documented and is a convenient method for the treatment of bacterial infections.

## **2.2 Trackable Antibacterial Silver Complexes With Aryl Benzothiazoles**

The antibacterial activity of silver complexes has been exploited in the medical world for their use in burn and ulcer treatments, preventative coatings in medical devices and in dressings for wounds as discussed in the previous section.<sup>22</sup> The release of the  $\text{Ag}^+$  ion from the ligand framework and interaction with biological molecules within bacteria is linked to the antibacterial activity. Many silver complexes have been identified, but fewer have shown trackable silver delivery. This property is especially important concerning the topical treatment of infection on the skin or in burn victims

and the changing of wound dressings. For this reason, the use of the highly fluorescent ligands 2-pyridylbenzothiazole (pbt) and 2-quinolylbenzothiazole (qbt) (**Figure 2.3**) was of particular interest. The two ligands contain a benzothiazole which themselves are known to be a class of antibiotics and could offer an additional moiety to aid in the overall activity.<sup>23,24</sup> The synthesis, characterization, tracking properties and antimicrobial activity of two silver(I) complexes with these ligands  $[\text{Ag}(\text{pbt})_2]\text{BF}_4$  (Agpbt) and  $[\text{Ag}(\text{qbt})_2]\text{BF}_4$  (Agqbt) (**Figure 2.3**) are described in the following sections.

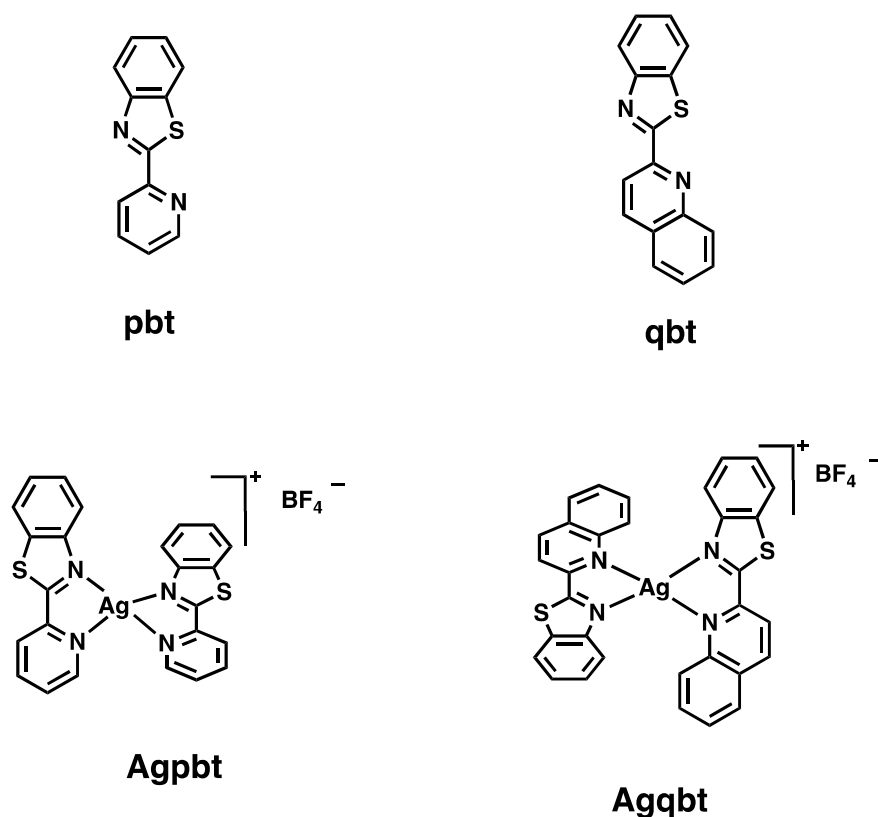


**Figure 2.3.** The two benzothiazole moieties (top) and their complexes with silver (bottom).

### 2.2.1 Synthesis and Spectroscopy

The two aryl benzothiazole silver complexes Agpbt and Agqbt were obtained in good yield by the reactions of  $\text{AgBF}_4$  with pbt and qbt in 1:2 (metal:ligand) molar ratio in  $\text{CHCl}_3/\text{MeOH}$  under stirring conditions. Both reaction flasks were covered with aluminum foil to avoid exposure of any ambient light during the course of reactions. FT-IR spectra of the complexes exhibit all the stretches pertinent to the coordinated aryl benzothiazole ligands employed (**Figure 2.4**). In addition, IR spectra of two the complexes display a strong band at  $1060\text{ cm}^{-1}$  due to of the presence of  $\text{BF}_4^-$  as counter anion. Both complexes exhibit well resolved  $^1\text{H}$  NMR in  $\text{CDCl}_3$  solution (**Figure 2.5**).

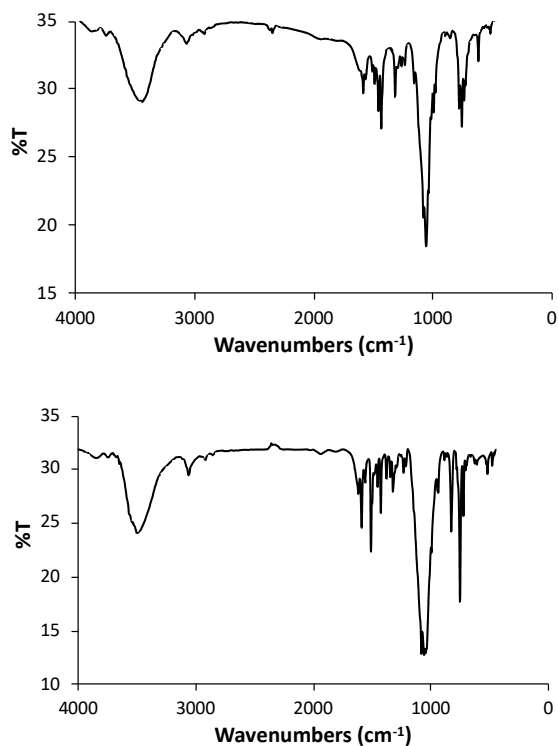


**Figure 2.4.** The FT-IR spectrum of Agpbt(top) and Agqbt(bottom) in KBr.



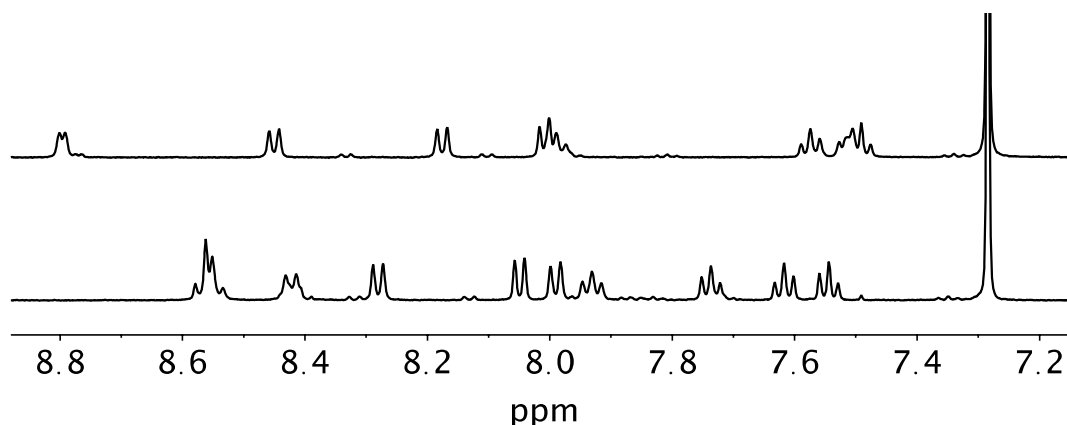


**Figure 2.5.** The  $^1\text{H}$  NMR of Agpbt (top trace) and Agqbt (bottom trace) in  $\text{CDCl}_3$  at 298K.

The electronic absorption spectra in dichloromethane (DCM) solutions exhibit broad absorption bands centered around 320 nm for Agpbt and 350 nm for Agqbt (**Figure 2.6**). These bands have contributions from both MLCT (metal-to-ligand) and ligand-based charge transfer transitions (discussed further in section 2.2.2). Both complexes are fairly stable in DCM and  $\text{CHCl}_3$  solutions and time-dependent UV-Vis spectral studies revealed no significant change in the electronic absorption spectra for at least 24 h.

The aryl benzothiazoles (pbt and qbt) utilized are not only are a class of antibacterials but are also highly fluorescent. The emission spectra of the silver complexes Agpbt and Agqbt compared to the free ligands pbt and qbt are shown in **Figure 2.7** and reveal that upon complexation to the metal center, the emission intensity significantly quenches. This property can provide a means to track the silver release from the respective complexes (through a change in emission property).

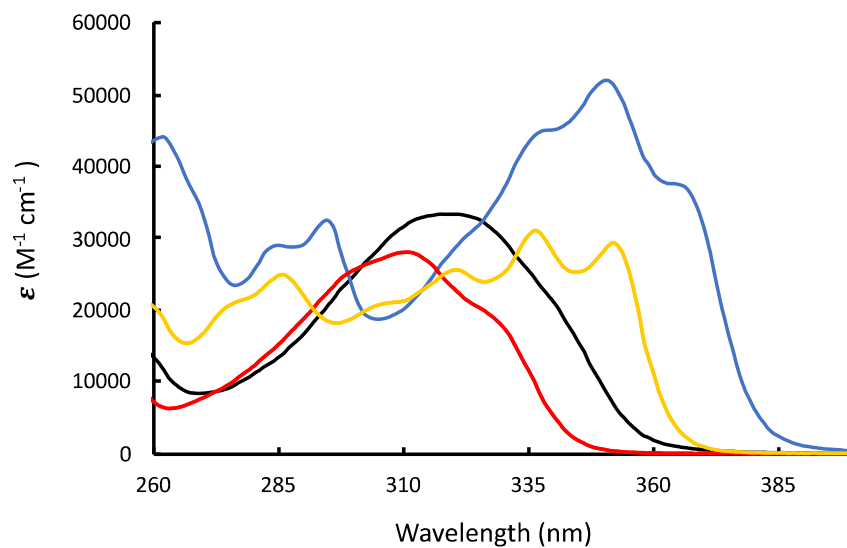


**Figure 2.6.** Absorption spectra of Agpbt (black), Agqbt (blue), pbt (red) and qbt (yellow) in DCM.

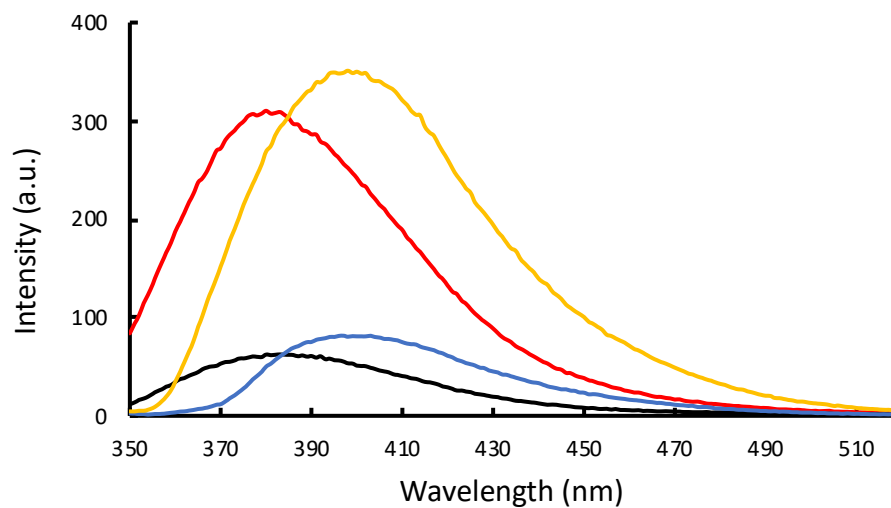


**Figure 2.7.** Emission spectra of Agpbt (black), Agqbt (blue), pbt (red) and qbt (yellow) in DCM ( $\lambda_{\text{ex}}$  at 330, 350, 310 and 335 nm respectively).

Fluorescence spectral studies revealed that both complexes could act as a “turn-on” type sensors through which the delivery of the bioactive  $\text{Ag}^+$  ion can be tracked indirectly within the site of interest. This would then indicate that all silver has depleted from a bandage and replacement is necessary. Both complexes exhibit very low emission intensity in DCM solutions. However, systematic addition of  $\text{Bu}_4\text{NCl}$  resulted in a gradual emergence of the fluorescence, associated with slow release of silver ( $\text{Ag}^+$ ) with simultaneous deligation of the highly fluorescent ligands pbt or qbt (**Figure 2.8 and 2.9**). The interaction of chloride and silver ions in the complexes causes the precipitation of the stable ion pair  $\text{AgCl}$  and releases pbt or qbt from the coordination environment of the silver. The complete deligation of the benzothiazoles from both complexes occurs upon administration of 1.2 equivalent of  $\text{Bu}_4\text{NCl}$ . This process can be potentially beneficial not only as a “turn-on” sensor to track the release of silver, but also the deligation of the aryl benzothiazoles could potentially provide an additional antimicrobial agent to the infected sites. The tracking of slow release of  $\text{Ag}^+$  has also been previously demonstrated in our lab, from a using BODIPY-based  $\text{Ag(I)}$  a-diimine complex through a “turn-on” fluorescence, a property associated with the free ligand.<sup>25</sup>

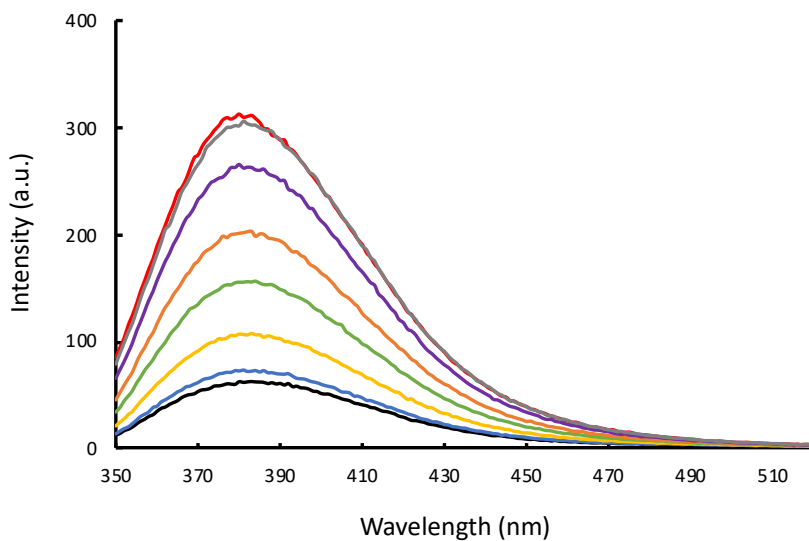


**Figure 2.8.** The turn on fluorescence signaling  $\text{Ag}^+$  deligation from pbt (red trace) upon additions of 0.2eq of  $\text{Bu}_4\text{NCl}$  to Agpbt (black trace,  $40\mu\text{M}$ ) in DCM.

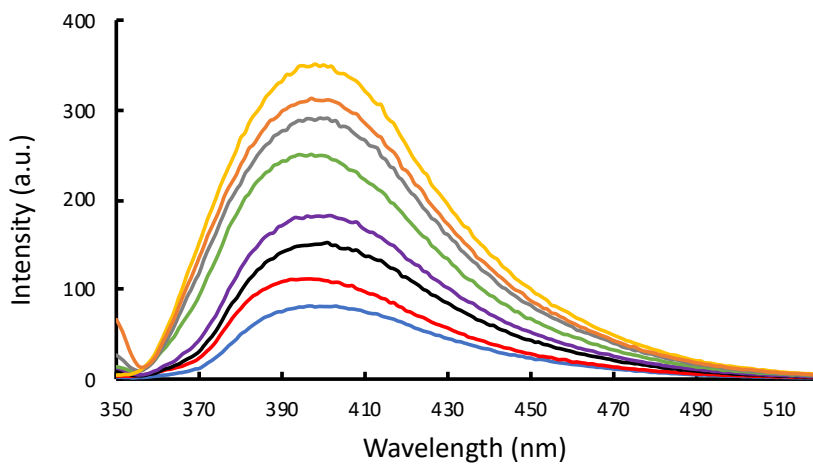


**Figure 2.9.** The turn on fluorescence signaling  $\text{Ag}^+$  deligation from qbt (yellow trace) upon additions of 0.2eq of  $\text{Bu}_4\text{NCl}$  to Agpbt (blue trace,  $40\mu\text{M}$ ) in DCM.

### 2.2.2 Crystal Structure, Binding Mode Discussion and Density Function Theory

The molecular structures for both Agpbt (**Figure 2.10**) and Agqbt (**Figure 2.11**) have been authenticated by single crystal X-ray crystallography. The crystal structures reveal that in both cases the ligand (pbt and qbt) binds the Ag(I) center in bidentate-N<sup>N</sup> fashion. Interestingly, the pyridine and quinolyl rings of pbt and qbt rotate to present their N atoms to the Ag(I) center. This is evidenced in the crystal structures of both the free ligands pbt and qbt revealing the two N atoms are in anti disposition with respect to each other (**Figure 2.12**). The possibility of N,S-bidentate coordination of the ligands has not been achieved in the present complexes despite the considerable propensity of the Ag to bind S atom.

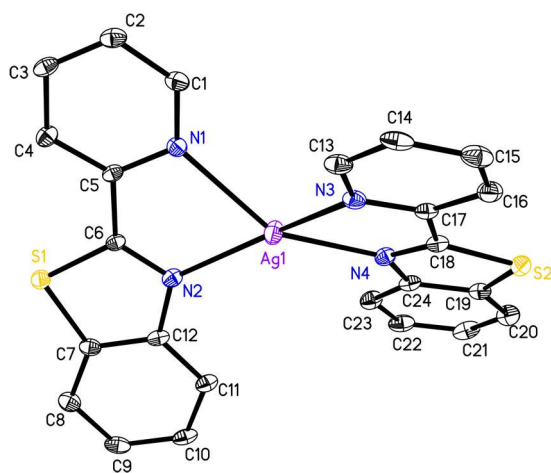


**Figure 2.10.** The perspective view of Agpbt with thermal ellipsoids are shown at 50% probability level with H atoms and BF<sub>4</sub><sup>-</sup> counterion omitted for clarity.

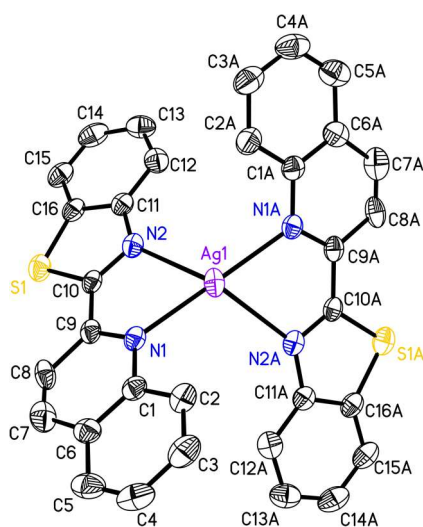


**Figure 2.11.** The perspective view of Agqbt with thermal ellipsoids are shown at 50% probability level with H atoms and  $\text{BF}_4^-$  counterion omitted for clarity.

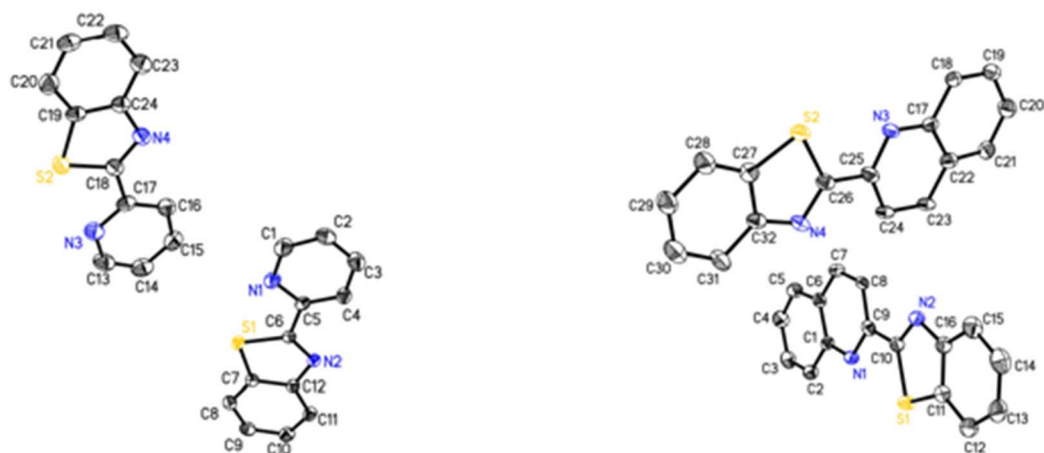


**Figure 2.12.** The perspective view of the ligands pbt (right panel) and qbt (left panel) with thermal ellipsoids are shown at 50% probability level with H atoms omitted for clarity.

In the crystal structure of Agpbt and Agqbt, the Ag(I) center resides in a distorted tetrahedral coordination environment as seen with other bis bidentate N<sup>N</sup> complexes.<sup>26</sup> In Agpbt, the pbt chelate rings (comprised of Ag1, N1, C5, C6, N2 and Ag1, N3, C17, C18, N4 atoms) is relatively planar with mean deviations of 0.019 (3) and 0.011 (4) Å respectively. Both benzothiazole fragments (composed of C6, C7, C8, C9, C10, C11, C12, N2, S1 and C18, C19, C20, C21, C22, C23, C24, N4, S2 atoms) are highly planar with mean deviations of 0.010 (3) and 0.005 (3) Å respectively. The dihedral angles between these fragments and the adjoining pyridyl rings are found to be 2.3 (4)° and 3.0 (3)° respectively. The bond distances and angles of Agpbt are comparable to the similar complexes [Ag(tmpb)<sub>2</sub>]BF<sub>4</sub> (where tmpb = 4,4',6,6'-tetramethyl-2,2'-bipyridine) with average Ag-N distances as 2.355 (6) and 2.321 Å respectively.<sup>26</sup> The average N-Ag-N bite angle in Agpbt is 71.8° also comparable to [Ag(tmpb)<sub>2</sub>]BF<sub>4</sub> with average bite angle of 72.1°.

In the crystal structure of Agqbt, only one of the two qbt ligands appears in the asymmetric unit, with the second qbt ligand consisting of symmetry equivalent atoms. The qbt ligands chelate rings (composed of Ag1, N1, C9, C10, N2 and Ag1, N1A, C9A, C10A, N2A atoms), considerably deviates from planarity (mean deviation, 0.072 (4) Å). The two qbt fragments (composed of N2, C10, C11, C12, C13, C14, C15, C6, S1 atoms and the symmetry equivalent atoms) show excellent planarity with mean deviation of 0.009 (3) Å.

We were interested to see if the rotation of the quinolyl or pyridyl fragment of pbt and qbt created an electronic environment that might be responsible for the

quenching of fluorescence observed by Agpbt and Agqbt. We employed density functional theory (DFT) calculations on qbt and Agqbt to provide information about the confirmation energy, the energy of the HOMO-LUMO gap and the type of transitions observed with these emissive molecules. First, the difference in confirmation energy was calculated between the two qbt ligand states L1 and L1' (**Figure 2.13**). The isomer L1' (the orientation of the qbt ligand in Agqbt) is 3.9 kcal/mol higher in energy than L1. The rotation of the quinolyl ring starting in L1 to L1' has a free energy barrier of 8.4 kcal/mol whereas the rotation starting from L1' to L1 is 5.5 kcal/mol. This, along with the crystal structure of qbt showing L1 confirmation, led us to conclude that the L1 orientation is favorable in solution.

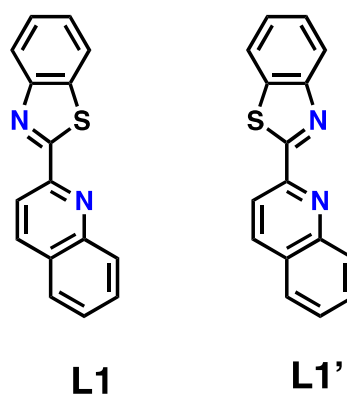


**Figure 2.13.** The isomer confirmations of the qbt ligand.

The HOMO-LUMO gap of L1 was calculated to be 0.23 AU and the Kohn-Sham orbitals in the frontier region are shown in **Figure 2.14**. The HOMO was identified to be a p orbital and the LUMO is a  $\pi^*$  orbital. Further TDDFT



calculations identified the first vertical excitation at 309 nm is the dominant transition and the experimental value of 335 nm was in relatively good agreement. Natural transition orbitals (NTO's) confirmed the  $\pi - \pi^*$  transition is responsible for the excitation. Similar results were obtained for L1' with  $\pi - \pi^*$  excitation occurring at 310 nm. The lowest singlet excited states of both L1 and L1' were optimized and show energetically similar excited states. The emission from the  $S_1$  state for L1 was 394 nm while for L1' was 395 nm, both in agreement with the experimental emission at 400 nm.

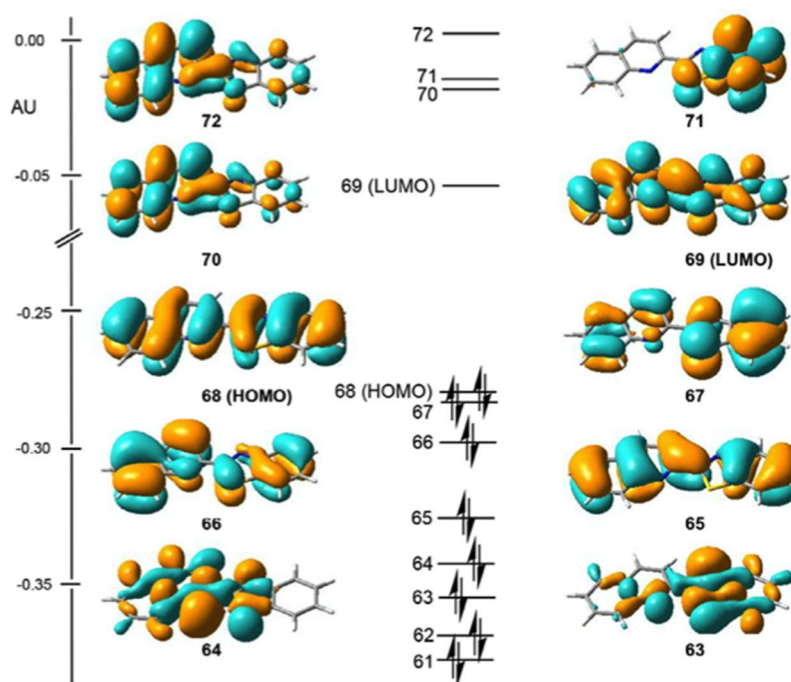


**Figure 2.14.** The Kohn-Sham orbitals in the frontier region of L1 (qbt).

For Agqbt, the optimized ground state structure parameters were similar to the X-ray structure parameters with some Ag-N bonds slightly shorter or longer than in the

X-ray structure. The HOMO - LUMO gap of Agqbt was calculated to be 0.21 AU, slightly smaller than the 0.23 AU gap calculated for qbt. The Kohn-Sham orbitals in the frontier region of Agqbt are shown in **Figure 2.15** and reveal the HOMO to be a  $\pi$  orbital that is delocalized over both the qbt ligands in Agqbt and the LUMO to be the  $\pi^*$  orbital. Two important absorption bands were identified from NTOs and TDDFT calculation as  $^1\text{MLTC}$  (326 nm) and  $^1\text{LC}$  (317 nm) transitions. The optimized the lowest singlet state ( $S_1$ ) of Agqbt was calculated to have  $^1\text{MLCT}$  character and which is 3.07 eV higher than the ground state. The lowest triplet excited state ( $T_1$ ) was also found to lie 1.97 eV above the ground state. Starting from the  $T_1$  geometry, triplet DFT single point energy calculations were performed to plot the total spin density (**Figure 2.16**). Interestingly, two unpaired electrons are located in a qbt ligand, and spin density on Ag is zero, implying that the  $T_1$  state has  $^3\text{LC}$  character. The calculated emission from  $^3\text{LC}$  is 629 nm and substantially longer than the calculated emission for qbt ligand itself (394 nm). Experimentally there is no emission found near to 629 nm for Agqbt, rather a very weakly fluorescent band at 400 nm (similar to the ligand). This observation suggests that the  $^3\text{LC}$  is a non emissive state where the excited state of the molecules likely follows nonradiative decay channels resulting in lack of emission in this 629 nm range. We concluded that the luminescent behavior, or lack of, arises from the facile  $S_1$  to  $T_1$  intersystem crossing commonly observed with heavy metal complexes and then subsequent non radiative decay from the  $T_1$  state.

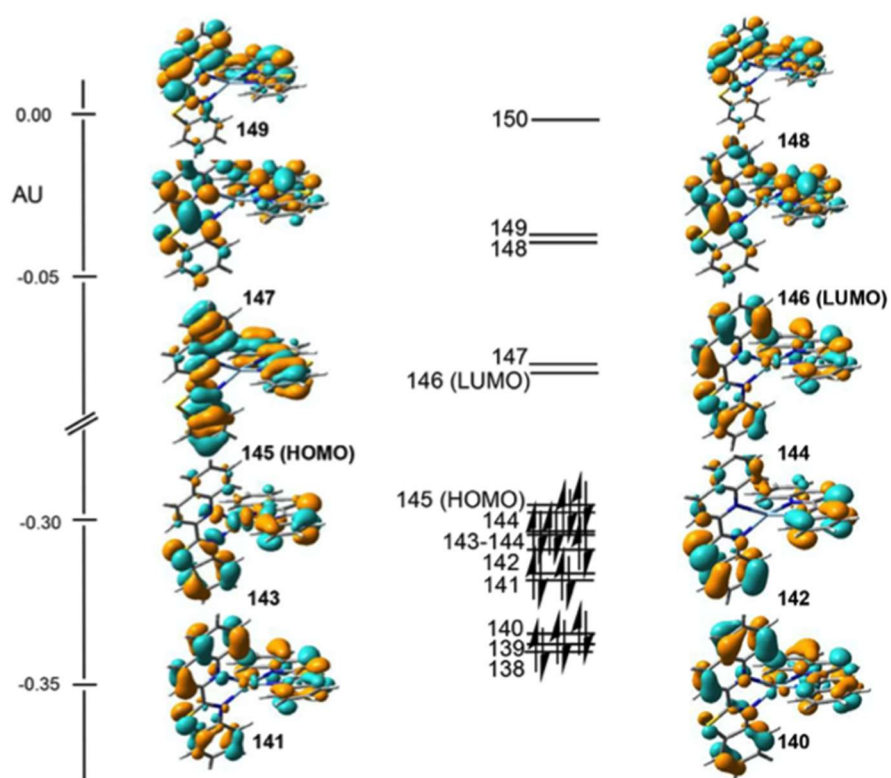


**Figure 2.15.** The Kohn-Sham orbitals in the frontier region of Agqbt.

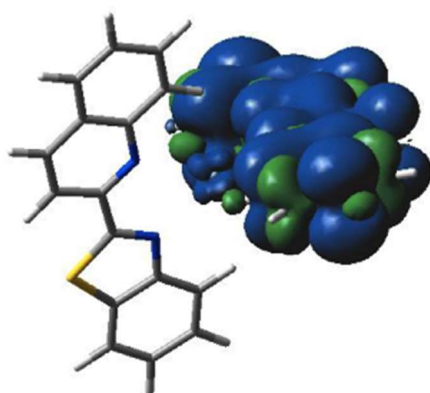


**Figure 2.16.** The total spin density for the T1 state of Agqbt.

### 2.2.3 Antibacterial Action

The antibacterial activity of silver has recently been exploited to tackle chronic infections of wounds by MDR bacteria in hospitals around the world.<sup>27,28</sup> Silver sulfadiazine has been widely used in the treatment and prevention of infections of burn wounds and diabetic wounds of immunocompromised patients. The bioactive  $\text{Ag}^+$  ion is known to interact with thiol and amino groups of proteins, nucleic acids and with cell membranes as reviewed in section 2.1.1. The multiple pathways of exerting pathological damage by the  $\text{Ag}^+$  ion makes it difficult for the microorganisms to develop resistance to this metal. For this reason, a renewed interest in silver treatments has been a trend in drug development efforts. We have been interested in examining the antibacterial effects of new silver complexes of ligands that themselves show antimicrobial effects on two bacteria, *P. aeruginosa* (Gram-negative) and *S. aureus* (Gram-positive). The bacterial cell wall of these species differs and thus treatment efficacy varies, but both often pose threat to burn wounds in hospitals.<sup>29</sup> We chose to examine the antibacterial efficacy of  $\text{Agqbt}$  on these two bacterial species grown on a SSTI model developed in our laboratory.<sup>30</sup> The model is a bilayer of agar with a nutrient rich bottom layer and the top soft layer of which consists of a uniform bacterial “lawn”. The design allows gradual penetration of the bacteria from the top layer to the nutrient-rich bottom layer upon incubation much like the way bacteria penetrate from epidermis to dermis layers of the skin during chronic infection. KBr pellets containing 2% (w/w) of  $\text{qbt}$  and  $\text{Agqbt}$  were placed on the top bacterial lawns and the SSTI models were incubated at 37 °C. Visible circular zones of bacterial clearing around the pellet

containing Agqbt were observed in both cases after incubation for 18 h as shown in **Figure 2.17**. Similar results were obtained with Agpbt. These initial results confirm the antibacterial properties of these Ag(I) complexes.

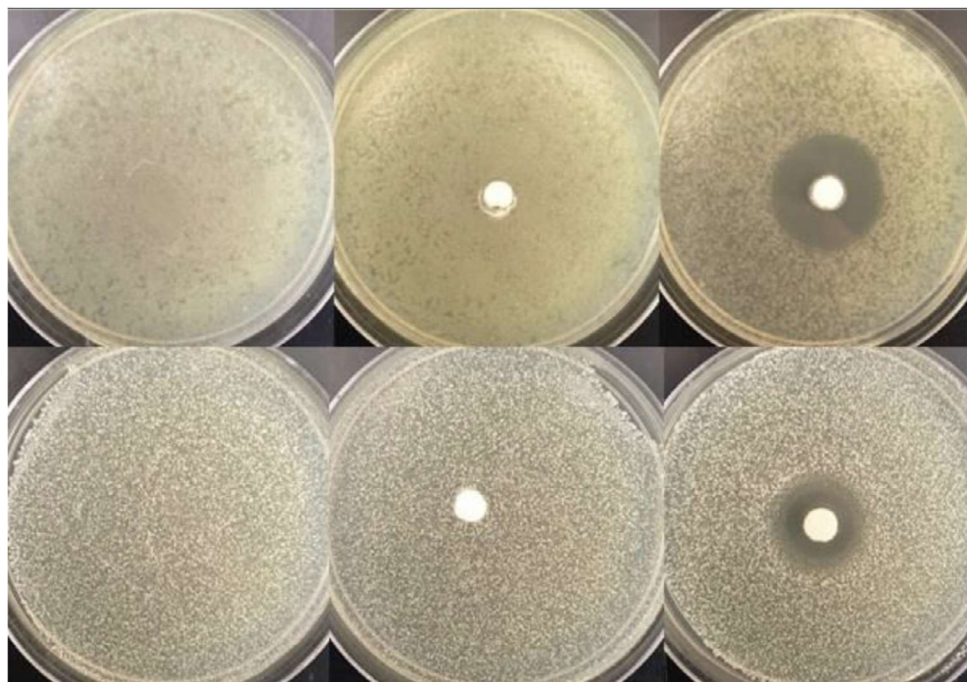


**Figure 2.17.** *P. aeruginosa* lawns (top row) with KBr (left), 2% qbt (center), and 2% Agqbt and *S. aureus* lawns (bottom row) with KBr (left), 2% qbt (center), and 2% Agqbt.

Attempts to increase the diameter of the ring of bacterial clearing by increasing the concentration of the Ag<sup>+</sup> species in the KBr pellet were made, but no significant changes were observed. This, along with the unexpected observation that the qbt ligand did not show antimicrobial action lead us to believe that in this particular experimental

setup, the solubility of the complexes in water may lead to their antimicrobial activity. The free ligands pbt and qbt along with the Agpbt and Agqbt are very sparingly soluble in water and this might prevent the diffusion of the molecules further into the aqueous agar layer. The  $\text{Ag}^+$  complexes may have an advantage being that they are charged species and might be better able to disperse into the bacterial lawn as well as interact with the bacterial cell walls. Nevertheless, these complexes show strong antibacterial activity using the SSTI model and their fluorescence tracking capabilities could provide an effective method for tracking of the release of  $\text{Ag}^+$ .

The antibacterial effectiveness of the Agpbt and Agqbt complexes prompted further investigation into other similar complexes in our lab. The ligand 2,6-bis(benzothiazole)-pyridine (bztpy) shown in **Figure 2.18**, similar in structure to pbt but containing two benzothiazole moieties was synthesized. The complexes of bztpy and  $\text{Ag}^+$  and  $\text{Cu}^{2+}$  were synthesized and structurally characterized revealing the dinuclear complex  $[\text{Ag}_2(\text{bztpy})_2](\text{CF}_3\text{SO}_3)$  (Agbztpy) and mononuclear complex  $[\text{Cu}(\text{bztpy})\text{Cl}_2]$  (Cubztpy).<sup>31</sup> Like silver, copper complexes have also shown potent antibacterial activity.<sup>32</sup> The two complexes were evaluated for their antibacterial activity using the SSTI model and KBr pellet method with *Acinetobacter baumannii* and *S. epidermidis* and compared to  $\text{AgNO}_3$  (**Figure 2.19**). Bacterial rings of clearing similar to those seen with Agpbt and Agqbt were observed with Agbztpy and Cubztpy. In all cases, both the KBr and bztpy controls showed no bactericidal ring, while the Agbztpy was similar in size to the  $\text{AgNO}_3$  control and Cubztpy was noticeable smaller than both silver compounds. As observed with the Agpbt, Agqbt, pbt and qbt

antibacterial results (**Figure 2.17**), the insolubility of the complexes in aqueous agar media seems to limit the diffusion of the compounds and thus their antibacterial efficacy. It is likely for this reason that the overall neutral species Cubztpy showed a smaller ring of bacterial clearing compared to Agbztpy and that bztpy, like pbt or qbt showed no ring of bacterial clearing. The cationic species of Agbztpy was therefore more readily able to diffuse into the agar layer and exert drug action comparable to the water soluble  $\text{AgNO}_3$  control. Bacterial cell walls are also moderately electronegative and therefore ease of penetration of cationic species in to bacterial cell walls compared to neutral species is observed.<sup>33</sup> Taken together, the results of the antimicrobial Agpbt, Agqbt and Agbztpy complexes using the SSTI model prove cationic silver complexes with benzothiazoles as ligands to be an interesting and effective route towards enhanced treatment of this type of infection.

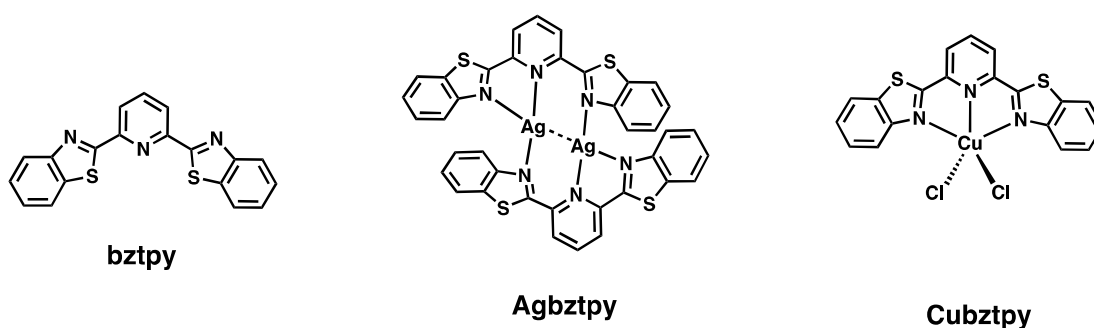


**Figure 2.18.** The bztpy ligand and its structure with  $\text{Ag}^+$  and  $\text{Cu}^{2+}$ .

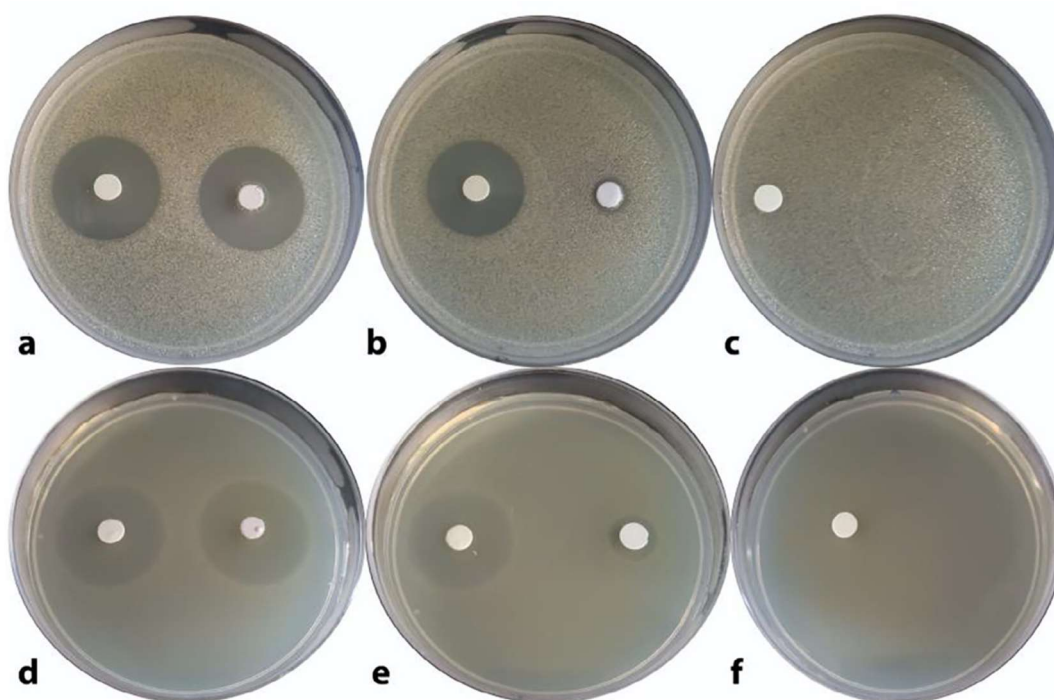


**Figure 2.19.** Clearing of bacterial growth of *A. baumannii* (top row): plate (a) KBr pellet 2% (w/w) with Agbztpy (left side) and AgNO<sub>3</sub> (right side); plate (b) KBr pellet 2% (w/w) with Cubztpy (left side) and Agbztpy (right side); plate (c) KBr pellet 2% (w/w) with bztpy (left side) and blank pellet (right side). *S. epidermidis* (bottom row): plate (a) KBr pellet 2% (w/w) with Agbztpy (left side) and AgNO<sub>3</sub> (right side); plate (b) KBr pellet 2% (w/w) with Agbztpy (left side) and Cubztpy (right side); plate (c) KBr pellet 2% (w/w) with bztpy (left side) and blank pellet (right side).



## 2.2.4 Experimental Section

### 2.2.4.1 General Methods

All reagents and solvents were of commercial grade and used without further purification. The ligands pbt<sup>34</sup> and qbt<sup>35</sup> were synthesized according to the reported procedures. IR and UV-Vis spectra of the ligands and the complexes were obtained using Perkin-Elmer Spectrum-One FT-IR and Varian Cary 50 UV-Vis spectrophotometers respectively. The <sup>1</sup>H NMR spectra of the complexes were recorded at 298 K on a Varian Unity Inova 500 MHz instrument. The emission spectra were recorded with Agilent Cary Eclipse spectrometer. Microanalyses were carried out with a PerkinElmer Series II 2400 Elemental Analyzer.

### 2.2.4.2 Synthesis

[Ag(pbt)<sub>2</sub>](BF<sub>4</sub>) (Agpbt): A solution of silver tetrafluoroborate (84 mg, 0.43 mmol) in 15 mL of methanol was added to a solution of 185 mg (0.87 mmol) of pbt in 30 mL of chloroform. The reaction flask was covered with Al foil to avoid ambient light and stirred for 48 h at room temperature. Next, the solvent was partially removed to obtain a white precipitate. The solid was isolated by vacuum filtration and further recrystallized from hot methanol (yield: 192mg, 72%). Elemental analysis (%) calculated for C<sub>24</sub>H<sub>16</sub>AgN<sub>4</sub>S<sub>2</sub>BF<sub>4</sub>: C 46.55, H 2.60, N 9.05; Found: C 46.60, H 2.58, N 9.02. IR (KBr, cm<sup>-1</sup>): 3486 (w), 1459 (w), 1436 (w), 1084 (s), 1059 (s), 783 (w), 1 760 (w). H NMR (CDCl<sub>3</sub>, ppm): δ 8.77 (d, 1H), 8.42 (d, 1H), 8.15 (d, 1H), 7.97 (m, 2H), 7.55 (t, 1H), 7.48 (m, 2H).

[Ag(qbt)<sub>2</sub>](BF<sub>4</sub>) (Agqbt): This complex was synthesized by the same procedure as above using silver tetrafluoroborate (78 mg, 0.40 mmol) and qbt (213 mg, 0.81 mmol)) to obtain a tan solid which was further recrystallized from hot methanol (yield: 182 mg, 63%). Elemental analysis (%) calculated for C<sub>32</sub>H<sub>20</sub>AgN<sub>4</sub>S<sub>2</sub>BF<sub>4</sub>: C 53.43, H 2.80, N 7.79, Found: C 53.47, H 2.85, N 7.69. IR (KBr, cm<sup>-1</sup>): 3497 (w), 1591 (w), 1512 (w), 1084 (s), 1058 (s), 830 (w), 755 (w). <sup>1</sup>H NMR (CDCl<sub>3</sub>, ppm): δ 8.53 (m, 2H), 8.40 (d, 1H), 8.25 (d, 1H), 8.02 (d, 1H), 7.96 (d, 1H), 7.91 (t, 1H), 7.71 (t, 1H), 7.59 (t, 1H), 7.52 (t, 1H).

#### 2.2.4.3 X-ray Crystallography

Colorless needle-shaped and block-shaped crystals of Agpbt and Agqbt respectively were obtained by recrystallization through diffusion of hexanes into their DCM solutions. In case of Agpbt, a Bruker D8 diffractometer with PHOTON II detector equipped with a low temperature device, operating at T = 100 K was employed. This crystal was kept at T = 100 K during entire tenure of data collection and unit cell determination. Data were measured using  $\phi$  and  $\omega$  shutterless scan technique using synchrotron radiation (Advanced Light Source, Berkeley, station 11.3.1). For Agqbt, a Bruker APEX-II CCD diffractometer with graphite monochromated Mo-K $\alpha$  radiation ( $\lambda$  = 0.71073 Å) was employed. In this case, the crystal was kept at T = 298 K during data collection and unit cell determination. Data were measured using  $\omega$  scan technique. The total number of runs and images for both data collections was based on the strategy calculation from the program APEX2

(Bruker).<sup>36</sup> Cell parameters were retrieved and refined using the SAINT (Bruker) software.<sup>37</sup> Multi-scan absorption corrections were performed with both data sets using SADABS 2014/5.<sup>38</sup> Both structures were solved by intrinsic phasing using the 111 SHELXT (Sheldrick, 2015) structure solution program and refined by full matrix least squares on F<sup>2</sup> using version 2016/6 of ShelXL (Sheldrick, 2015).<sup>39</sup> All non-hydrogen atoms were refined anisotropically in both cases. In Agpbt there is a single molecule in the asymmetric unit, while for Agqbt only half of the formula unit is present in the asymmetric unit, with the other half consisting of symmetry equivalent atoms. Calculations and molecular graphics were performed using SHELXTL 2014 and Olex2 programs.<sup>40</sup> Crystal data and structure refinement parameters are listed in **Table 2.1**. CCDC 1548688 (Agpbt), CCDC 1548689 (Agqbt), CCDC 1556692 (pbt) and CCDC 1556693 (qbt) contain the supplementary crystallographic data for this paper. These data can be obtained free of charge from The Cambridge Crystallographic Data Center via [www.ccdc.cam.ac.uk/data\\_request.cif](http://www.ccdc.cam.ac.uk/data_request.cif).

**Table 2.1.** Crystal data and refinement parameters for Agpbt and Agqbt.

	Agpbt·2H <sub>2</sub> O	Agpbt
Formula	C <sub>24</sub> H <sub>20</sub> AgBF <sub>4</sub> N <sub>4</sub> O <sub>2</sub> S <sub>2</sub>	C <sub>32</sub> H <sub>20</sub> AgBF <sub>5</sub> N <sub>4</sub> S <sub>2</sub>
<i>D</i> <sub>calc.</sub> /g cm <sup>-3</sup>	1.683	1.704
μ/mm <sup>-1</sup>	1.254	0.910
Formula Weight	655.21	738.32
Color	Colorless	Yellow
Shape	Needle	Block
<i>T</i> /K	100 (2)	298 (2)
Crystal System	Orthorhombic	Monoclinic
Space Group	<i>P</i> 2 <sub>1</sub> 2 <sub>1</sub> 2 <sub>1</sub>	<i>C</i> 2/ <i>c</i>
<i>a</i> /Å	7.3901 (5)	14.997 (6)
<i>b</i> /Å	15.5413 (9)	15.288 (6)
<i>c</i> /Å	22.3819 (12)	14.176 (5)
α/°	90	90
β/°	90	117.707(4)
γ/°	90	90
<i>V</i> /Å <sup>3</sup>	2570.6 (3)	2877.5 (19)
<i>Z</i>	4	4
Wavelength/Å	0.7749	0.71073
Radiation type	Synchrotron	Mo-Kα
θ <sub>min</sub> /°	1.739	2.665
θ <sub>max</sub> /°	31.196	25.142
Measured Refl.	29.368	8694
Independent Refl.	6397	2544
Reflections Used	6078	2094
<i>R</i> <sub>int</sub>	0.0478	0.0280
Parameters	343	205
Largest Peak	2.325	0.850
Deepest Hole	-0.814	-0.523
<sup>a</sup> GooF	1.130	1.043
<sup>c</sup> w <i>R</i> <sub>2</sub>	0.1467	0.1409
<sup>b</sup> <i>R</i> <sub>1</sub>	0.0519	0.0494

<sup>a</sup>GOF = [Σ [*w*(*F*<sub>o</sub><sup>2</sup>-*F*<sub>c</sub><sup>2</sup>)<sup>2</sup>]/(*N*<sub>o</sub>-*N*<sub>v</sub>)]<sup>1/2</sup> (*N*<sub>o</sub> = number of observations, *N*<sub>v</sub> = number of variables).

<sup>b</sup>*R*<sub>1</sub> = Σ || *F*<sub>o</sub> | - | *F*<sub>c</sub> | || / Σ | *F*<sub>o</sub> |.

<sup>c</sup>w*R*<sub>2</sub> = [(Σ *w*(*F*<sub>o</sub><sup>2</sup>-*F*<sub>c</sub><sup>2</sup>)<sup>2</sup>/Σ | *F*<sub>o</sub> |<sup>2</sup>)]<sup>1/2</sup>.

#### *2.2.4.4 Computational Methods*

The M06L<sup>41</sup> functional, as implemented in the Gaussian09 program,<sup>42</sup> was used for solvent-phase structure optimizations. The SMD<sup>43</sup> implicit solvation model was used for solvation treatments with dichloromethane as solvent ( $\epsilon = 8.93$ ). The SDD<sup>44,45</sup> basis set and the associated effective core potential was used for Ag, and the Def2-TZVP basis sets were employed for other atoms.<sup>46,47</sup> Nature of the stationary point was confirmed by performing vibrational frequency calculations that were performed to confirm the optimized structures as minima (i.e., no imaginary frequencies for a minima). The time-dependent density functional theory (TDDFT) was used for excited-state calculations with the M062X<sup>48</sup> functional and the above basis sets. The non-equilibrium SMD solvation was employed to calculate vertical excitations, while the equilibrium SMD solvation was used to optimize the lowest excited singlet state and the lowest excited triplet state. The “ultraFine” integration grid was used for TDDFT calculations, where the two-electron integral accuracy parameter was set to 12.

#### *2.2.4.5 Bacterial Studies*

A skin and soft tissue infection (SSTI) model was constructed for antibacterial studies by following a procedure described by us in a previous article.<sup>30</sup> This SSTI model consists of two agar layers, a hard agar bottom layer containing most of the nutrients and a soft agar layer on the top that allows for even dispersion of bacteria. As bacteria grow in the top soft agar (mimicking the lower epidermis of the skin), they migrate towards the bottom nutrient layer modeling a cutaneous infection. Frozen

samples of *Pseudomonas aeruginosa* and *Staphylococcus aureus* were thawed and streaked on two separate agar plates. A single colony from each plate was selected and grown in Luria Broth (LB) for 18 h. The suspensions were diluted with LB until an A600 of 0.5 was reached. The soft agar bacterial suspension was prepared by adding 60 µL of the above solution to 50 mL of 0.8% (w/v) agar with 1% NaCl which had been previously autoclaved and cooled to 45 °C before the addition. The suspension was gently vortexed and 7 mL was spread evenly on the surface of a hard agar layer prepared from 20 mL of a 1.5% (w/v) TSB agar in a 100 x 15 mm<sup>2</sup> plate and allowed to solidify. The plates were then incubated for 2 h at 37 °C in order for the bacteria to reach log phase before KBr pellets (with or without complexes of interest) were placed on the top of the soft agar layer. The bactericidal activity was evaluated after 18 hours incubation with the KBr pellets by observing the circular ring of bacterial clearing.

## 2.3 References

- (1) Alexander, J. W. History of the Medical Use of Silver. *Surg. Infect.* **2009**, *10* (3), 289–292.
- (2) Fox, C. L.; Modak, S. M. Mechanism of Silver Sulfadiazine Action on Burn Wound Infections. *Antimicrob. Agents Chemother.* **1974**, *5* (6), 582–588.
- (3) Sim, W.; Barnard, R. T.; Blaskovich, M. A. T.; Ziora, Z. M. Antimicrobial Silver in Medicinal and Consumer Applications: A Patent Review of the Past Decade (2007–2017). *Antibiotics* **2018**, *7* (4), 1–15.
- (4) Hadrup, N.; Sharma, A. K.; Loeschner, K. Toxicity of Silver Ions, Metallic Silver, and Silver Nanoparticle Materials after in Vivo Dermal and Mucosal Surface Exposure: A Review. *Regul. Toxicol. Pharmacol.* **2018**, *98* (June), 257–267.

- (5) Lansdown, A. B. G. Silver in Health Care: Antimicrobial Effects and Safety in Use. *Curr. Probl. Dermatol.* **2006**, *33*, 17–34.
- (6) Clement, J. L.; Jarrett, P. S. Antibacterial Silver. *Met. Based. Drugs* **1994**, *1* (5–6), 467–482.
- (7) Liang, X.; Luan, S.; Yin, Z.; He, M.; He, C.; Yin, L.; Zou, Y.; Yuan, Z.; Li, L.; Song, X.; Lv, C.; Zhang, W. Recent Advances in the Medical Use of Silver Complex. *Eur. J. Med. Chem.* **2018**, *157*, 62–80.
- (8) Hartinger, C. G.; Dyson, P. J. Bioorganometallic Chemistry—from Teaching Paradigms to Medicinal Applications. *Chem. Soc. Rev.* **2009**, *38* (2), 391–401.
- (9) Gordon, O.; Slenters, T. V.; Brunetto, P. S.; Villaruz, A. E.; Sturdevant, D. E.; Otto, M.; Landmann, R.; Fromm, K. M. Silver Coordination Polymers for Prevention of Implant Infection: Thiol Interaction, Impact on Respiratory Chain Enzymes, and Hydroxyl Radical Induction. *Antimicrob. Agents Chemother.* **2010**, *54* (10), 4208–4218.
- (10) Woo, K. J.; Hye, C. K.; Ki, W. K.; Shin, S.; So, H. K.; Yong, H. P. Antibacterial Activity and Mechanism of Action of the Silver Ion in *Staphylococcus Aureus* and *Escherichia Coli*. *Appl. Environ. Microbiol.* **2008**, *74* (7), 2171–2178.
- (11) Xiu, Z. M.; Ma, J.; Alvarez, P. J. J. Differential Effect of Common Ligands and Molecular Oxygen on Antimicrobial Activity of Silver Nanoparticles versus Silver Ions. *Environ. Sci. Technol.* **2011**, *45* (20), 9003–9008.
- (12) Kędziora, A.; Speruda, M.; Krzyżewska, E.; Rybka, J.; Łukowiak, A.; Bugla-Płoskońska, G. Similarities and Differences between Silver Ions and Silver in Nanoforms as Antibacterial Agents. *Int. J. Mol. Sci.* **2018**, *19* (2).
- (13) Mijndonckx, K.; Leys, N.; Mahillon, J.; Silver, S.; Van Houdt, R. Antimicrobial Silver: Uses, Toxicity and Potential for Resistance. *BioMetals* **2013**, *26* (4), 609–621.
- (14) Cannon, C. L.; Hogue, L. A.; Vajravelu, R. K.; Capps, G. H.; Ibricevic, A.; Hindi, K. M.; Kascatan-Nebioglu, A.; Walter, M. J.; Brody, S. L.; Youngs, W. J. In Vitro and Murine Efficacy and Toxicity Studies of Nebulized SCC1, a Methylated Caffeine-Silver(I) Complex, for Treatment of Pulmonary Infections. *Antimicrob. Agents Chemother.* **2009**, *53* (8), 3285–3293.

- (15) Browne, N.; Hackenberg, F.; Streciwilk, W.; Tacke, M.; Kavanagh, K. Assessment of in Vivo Antimicrobial Activity of the Carbene Silver(I) Acetate Derivative SBC3 Using *Galleria Mellonella* Larvae. *BioMetals* **2014**, *27* (4), 745–752.
- (16) Haque, R. A.; Asekunowo, P. O.; Razali, M. R.; Mohamad, F. NHC–Silver(I) Complexes as Chemical Nucleases; Synthesis, Crystal Structures, and Antibacterial Studies. *Heteroat. Chem.* **2014**, *25* (3), 194–204.
- (17) Carvalho, M. A.; De Paiva, R. E. F.; Bergamini, F. R. G.; Gomes, A. F.; Gozzo, F. C.; Lustri, W. R.; Formiga, A. L. B.; Shishido, S. M.; Ferreira, C. V.; Corbi, P. P. A Silver Complex with Tryptophan: Synthesis, Structural Characterization, DFT Studies and Antibacterial and Antitumor Assays in Vitro. *J. Mol. Struct.* **2013**, *1031*, 125–131.
- (18) Stathopoulou, M. E. K.; Banti, C. N.; Kourkoulis, N.; Hatzidimitriou, A. G.; Kalampounias, A. G.; Hadjikakou, S. K. Silver Complex of Salicylic Acid and Its Hydrogel-Cream in Wound Healing Chemotherapy. *J. Inorg. Biochem.* **2018**, *181* (January), 41–55.
- (19) Kazachenko, A. S.; Legler, A. V.; Per'yanova, O. V.; Vstavskaya, Y. A. Synthesis and Antimicrobial Activity of Silver Complexes with Histidine and Tryptophan. *Pharm. Chem. J.* **2000**, *34* (5), 257–258.
- (20) Aulakh, J. K.; Lobana, T. S.; Sood, H.; Arora, D. S.; Smolinski, V. A.; Duff, C. E.; Jasinski, J. P. Synthesis, Structures, and ESI-Mass Studies of Silver(I) Derivatives of Imidazolidine-2-Thiones: Antimicrobial Potential and Biosafety Evaluation. *J. Inorg. Biochem.* **2018**, *178*, 18–31.
- (21) Hosny, A. E. D. M. S.; Rasmy, S. A.; Aboul-Magd, D. S.; Kashef, M. T.; El-Bazza, Z. E. The Increasing Threat of Silver-Resistance in Clinical Isolates from Wounds and Burns. *Infect. Drug Resist.* **2019**, *12*, 1985–2001.
- (22) Politano, A. D.; Campbell, K. T.; Rosenberger, L. H.; Sawyer, R. G. Use of Silver in the Prevention and Treatment of Infections: Silver Review. *Surg. Infect.* **2013**, *14* (1), 8–20.
- (23) Yamazaki, K.; Kaneko, Y.; Suwa, K.; Ebara, S.; Nakazawa, K.; Yasuno, K. Synthesis of Potent and Selective Inhibitors of *Candida Albicans* N-Myristoyltransferase Based on the Benzothiazole Structure. *Bioorganic Med. Chem.* **2005**, *13* (7), 2509–2522.



- (24) Rajeeva, B.; Srinivasulu, N.; Shantakumar, S. M. Synthesis and Antimicrobial Activity of Some New 2-Substituted Benzothiazole Derivatives. *E-Journal Chem.* **2009**, 6 (3), 775–779.
- (25) Pinto, M. N.; Chakraborty, I.; Schultz-Simonton, W.; Rojas-Andrade, M.; Braslau, R.; Mascharak, P. K. Tracking Silver Delivery to Bacteria Using Turn-on Fluorescence. *Chem. Commun.* **2017**, 53 (9), 1459–1462.
- (26) Goodwin, K. V.; McMillin, D. R.; Robinson, W. R. Crystal and Molecular Structure of  $[\text{Ag}(\text{Tmbp})_2]\text{BF}_4$ . Origin of Flattening Distortions in  $d^{10}$  Complexes of the Type  $\text{M}(\text{NN})_2^+$ . *Inorg. Chem.* **1986**, 25 (12), 2033–2036.
- (27) Maillard, J.; Hartemann, P. Silver as an Antimicrobial : Facts and Gaps in Knowledge. *Crit. Rev. Microbiol.* **2013**, 39 (4), 373–383.
- (28) Chernousova, S.; Eppe, M. Silver as Antibacterial Agent: Ion, Nanoparticle, and Metal. *Angewandte* **2013**, 52 (6), 1636–1653.
- (29) Mayhall, C. G. The Epidemiology of Burn Wound Infections: Then and Now. *Clin. Infect. Dis.* **2003**, 37 (4), 543–550.
- (30) Heilman, B. J.; St. John, J.; Oliver, S. R. J.; Mascharak, P. K. Light-Triggered Eradication of *Acinetobacter Baumannii* by Means of NO Delivery from a Porous Material with an Entrapped Metal Nitrosyl. *J. Am. Chem. Soc.* **2012**, 134 (28), 11573–11582.
- (31) Chakraborty, I.; Pinto, M.; Stenger-smith, J.; Martinez-Gonzalez, J.; Mascharak, P. K. Synthesis , Structures and Antibacterial Properties of  $\text{Cu}(\text{II})$  and  $\text{Ag}(\text{I})$  Complexes Derived from 2 , 6-Bis ( Benzothiazole ) -Pyridine. *Polyhedron* **2019**, 172, 1–7.
- (32) Vincent, M.; Hartemann, P.; Engels-Deutsch, M. Antimicrobial Applications of Copper. *Int. J. Hyg. Environ. Health* **2016**, 219 (7), 585–591.
- (33) van Rijt, S. H.; Sadler, P. J. Current Applications and Future Potential for Bioinorganic Chemistry in the Development of Anticancer Drugs. *Drug Discov. Today* **2009**, 14 (23–24), 1089–1097.
- (34) Chen, X.; Femia, F. J.; Babich, J. W.; Zubieta, J. Spectroscopic and Structural Studies of Complexes of the  $\text{Fac-}[\text{Re}(\text{N}\cap\text{N})(\text{CO})_3\text{L}]^{\text{N}+}$  Type ( $\text{N}\cap\text{N}$  = 2-(2-Pyridyl)Benzothiazole;  $\text{L}$  = Cl, Br,  $\text{CF}_3\text{SO}_3^-$ ,  $\text{CH}_3\text{CN}$ ). *Inorganica Chim. Acta* **2001**, 314 (1–2), 91–96.

- (35) Stenger-Smith, J.; Chakraborty, I.; Carrington, S.; Mascharak, P. Synthesis and Structures of Photoactive Manganese-Carbonyl Complexes Derived from 2-(Pyridin-2-Yl)-1,3-Benzothiazole and 2-(Quinolin-2-Yl)-1,3-Benzothiazole. *Acta Crystallogr. Sect. C Struct. Chem.* **2017**, 73 (4).
- (36) Bruker APEX II. Bruker AXS Inc.: Madison, WI 2012.
- (37) Bruker SAINT. Bruker AXS Inc.: Madison, WI 2012.
- (38) Bruker SADABS. Bruker AXS Inc.: Madison, WI.
- (39) Sheldrick, G. M. SHELXT - Integrated Space-Group and Crystal-Structure Determination. *Acta Crystallogr. Sect. A Found. Crystallogr.* **2015**, 71 (1), 3–8.
- (40) Dolomanov, O. V.; Bourhis, L. J.; Gildea, R. J.; Howard, J. A. K.; Puschmann, H. OLEX2: A Complete Structure Solution, Refinement and Analysis Program. *J. Appl. Crystallogr.* **2009**, 42 (2), 339–341.
- (41) Zhao, Y.; Truhlar, D. G. A New Local Density Functional for Main-Group Thermochemistry, Transition Metal Bonding, Thermochemical Kinetics, and Noncovalent Interactions. *J. Chem. Phys.* **2006**, 125, 194101.
- (42) Frisch, M. J.; Trucks, G. W.; Schlegel, H. B.; Scuseria, G. E.; Robb, M. A.; Cheeseman, J. R.; Scalmani, G.; Barone, V.; Mennucci, B.; Petersson, G. A.; Nakatsuji, H.; et al. Gaussian09 Rev B.01. *Gaussian 09, Rev. B.01*. 2009.
- (43) Marenich, A. V.; Cramer, C. J.; Truhlar, D. G. Universal Solvation Model Based on Solute Electron Density and on a Continuum Model of the Solvent Defined by the Bulk Dielectric Constant and Atomic Surface Tensions. *J. Phys. Chem. B* **2009**, 113 (18), 6378–6396.
- (44) Fuentealba, P.; Preuss, H.; Stoll, H.; Von Szentpály, L. A Proper Account of Core-Polarization with Pseudopotentials: Single Valence-Electron Alkali Compounds. *Chem. Phys. Lett.* **1982**, 89 (5), 418–422.
- (45) Dunning Jr, T. H.; Hay, P. J. *Modern Theoretical Chemistry*, 3rd ed.; Shaefer III, H. F., Ed.; Plenum, New York, 1977.
- (46) Weigend, F.; Ahlrichs, R. Balanced Basis Sets of Split Valence, Triple Zeta Valence and Quadruple Zeta Valence Quality for H to Rn: Design and Assessment of Accuracy. *Phys. Chem. Chem. Phys.* **2005**, 7 (18), 3297–3305.

- (47) Weigend, F. Accurate Coulomb-Fitting Basis Sets for H to Rn. *Phys. Chem. Chem. Phys.* **2006**, 8 (9), 1057–1065.
- (48) Zhao, Y.; Schultz, N. E.; Truhlar, D. G. Design of Density Functionals by Combining the Method of Constraint Satisfaction with Parametrization for Thermochemistry, Thermochemical Kinetics, and Noncovalent Interactions. *J. Chem. Theory Comput.* **2006**, 2 (2), 364–382.

## 2.4 Reprint of Publication and Permissions

Reprinted with permissions from Stenger-Smith, J.; Chakraborty, I.; Sameera, W.M.C.; Mascharak, P. Antimicrobial silver (I) complexes derived from aryl-benzothiazoles as turn-on sensors: Syntheses, properties and density functional studies.” *Inorganica Chimica Acta*. **2018**, 471, 326-335.

Figures reprinted with permissions from Chakraborty, I.; Pinto, M.; Stenger-Smith, J. Martinez-Gonzalez, J.; Mascharak, P. Synthesis, structures and antibacterial properties of Cu(II) and Ag(I) complexes derived from 2,6-bis(benzothiazole)-pyridine. *Polyhedron*, **2019**, 172, 1-7.

**Antimicrobial silver (I) complexes derived from aryl-benzothiazoles as turn-on sensors: Syntheses, properties and density functional studies**

Author: Jenny Stenger-Smith, Indranil Chakraborty, W.M.C. Sameera, Pradip K. Mascharak

Publication: Inorganica Chimica Acta

Publisher: Elsevier

Date: 24 February 2018

Published by Elsevier B.V.

Please note that, as the author of this Elsevier article, you retain the right to include it in a thesis or dissertation, provided it is not published commercially. Permission is not required, but please ensure that you reference the journal as the original source. For more information on this and on your other retained rights, please visit: <https://www.elsevier.com/about/our-business/policies/copyright#Author-rights>

BACK

CLOSE WINDOW

© 2020 Copyright - All Rights Reserved | Copyright Clearance Center, Inc. | [Privacy statement](#) | [Terms and Conditions](#)  
Comments? We would like to hear from you. E-mail us at [customercare@copyright.com](mailto:customercare@copyright.com)

**Synthesis, structures and antibacterial properties of Cu(II) and Ag(I) complexes derived from 2,6-bis(benzothiazole)-pyridine**

Author: Indranil Chakraborty, Miguel Pinto, Jenny Stenger-Smith, Jorge Martinez-Gonzalez, Pradip K. Mascharak

Publication: Polyhedron

Publisher: Elsevier

Date: 1 November 2019

Published by Elsevier Ltd.

Please note that, as the author of this Elsevier article, you retain the right to include it in a thesis or dissertation, provided it is not published commercially. Permission is not required, but please ensure that you reference the journal as the original source. For more information on this and on your other retained rights, please visit: <https://www.elsevier.com/about/our-business/policies/copyright#Author-rights>

BACK

CLOSE WINDOW

© 2020 Copyright - All Rights Reserved | Copyright Clearance Center, Inc. | [Privacy statement](#) | [Terms and Conditions](#)  
Comments? We would like to hear from you. E-mail us at [customercare@copyright.com](mailto:customercare@copyright.com)



Contents lists available at ScienceDirect

Inorganica Chimica Acta

journal homepage: [www.elsevier.com/locate/ica](http://www.elsevier.com/locate/ica)

Research paper

## Antimicrobial silver (I) complexes derived from aryl-benzothiazoles as turn-on sensors: Syntheses, properties and density functional studies

Jenny Stenger-Smith<sup>a</sup>, Indranil Chakraborty<sup>a</sup>, W.M.C. Sameera<sup>b</sup>, Pradip K. Mascharak<sup>a,\*</sup><sup>a</sup> Department of Chemistry and Biochemistry, University of California, Santa Cruz, CA 95064, USA<sup>b</sup> Department of Chemistry, Faculty of Science, Hokkaido University, Sapporo 060-0810, Japan

## ARTICLE INFO

## Article history:

Received 17 October 2017

Accepted 13 November 2017

Available online 14 November 2017

## Keywords:

Benzothiazoles

Silver complexes

Fluorescence turn-ON

Theoretical studies

Antibacterial

## ABSTRACT

Two Ag(I) complexes derived from 2-(pyridyl)benzothiazole (pbt) and 2-(quinolyl)benzothiazole (qbt) namely, [Ag(pbt)<sub>2</sub>]BF<sub>4</sub> (**1**) and [Ag(qbt)<sub>2</sub>]BF<sub>4</sub> (**2**) have been synthesized and structurally characterized. The Ag(I) center in both complexes are distorted tetrahedral and both ligands bind silver in the N,N-bidentate mode. Upon complexation, the fluorescence of both ligands is quenched significantly and it is restored gradually upon release of silver under biological conditions. Results from theoretical studies indicate that a facile <sup>3</sup>MLCT → <sup>3</sup>LC (a <sup>1</sup>S → <sup>1</sup>T intersystem crossing) transition is responsible for the diminution of the luminescence in these complexes of silver (a heavy metal with high spin-orbit coupling). Both complexes exhibit antibacterial properties toward Gram-positive and Gram-negative bacteria. The bactericidal effect of the complexes is accompanied by an enhancement in fluorescence due to silver delivery to the target bacteria.

Published by Elsevier B.V.

## 1. Introduction

The emergence of multiple antibacterial and antifungal resistance has raised alarm in hospitals of many countries around the globe since most commonly used therapeutics have been shown to be ineffective in treating infections [1]. The extensive application of antibiotics is believed to be one of the main reasons for the bacterial and fungal pathogens evolving into their multidrug-resistant (MDR) form. In addition, a recent study has identified certain soil abundant genes that can provide resistance to classes of antibiotics employed to combat a range of bacterial infections [2]. Some of such genes confer resistance to the macrolide antibiotics very important in human and animal medicines such as erythromycin, clarithromycin, and azithromycin. These findings have led to the resurgence of the use of silver-based compounds or composites as antibacterial and antifungal agents [3]. To date, most of the microorganisms have failed to develop a defense mechanism against silver. Although the exact mechanism(s) of antimicrobial effects of silver ions is still unclear, there are certain pathways through which bioactive silver (Ag<sup>+</sup> ion) has been proposed to exert its antimicrobial activities. These possibilities include, generation of reactive oxygen species (ROS), silver binding to DNA,

interactions with microbial cell membranes and with the thiol groups of certain enzymes [3].

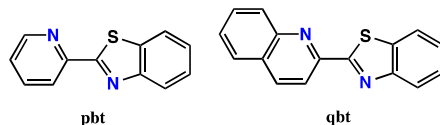
Benzothiazoles are one of the most effective classes of compounds against bacteria and fungi and thus remain as a crucial substructure type towards development of new antibacterial and antifungal agents [4–6]. The broad-spectrum biological activities of benzothiazoles include antibacterial [7], antifungal [4], antitumor [8], anticonvulsant [9], and anti-inflammatory [10] effects among others. Certain arylbenzothiazoles have recently been used in diagnosis of Alzheimer's disease [8]. In the past few decades severe infections, especially with immunocompromised patients, caused by pathogenic fungi have also raised significant concern [4]. It is important to note that all clinically used antifungal agents contain azole moiety, namely, fluconazole, ketoconazole, and clotrimazole [4]. These facts along with our goal of tracking silver release in infected tissues prompted our research group to isolate silver (I) complexes derived from two fluorescent arylbenzothiazoles, namely, 2-(pyridyl)benzothiazole (pbt) and 2-(quinolyl)benzothiazole (qbt) (Scheme 1).

In previous work we have demonstrated the efficacy of designed biocompatible silver (I) complexes towards eradication of several Gram-positive and Gram-negative bacterial strains through slow and sustainable delivery of bioactive silver [11,12]. These studies did not include any benzothiazole moiety. The pbt and qbt ligands have however been employed in syntheses of photoactive Mn and Re carbonyl complexes for a very different

\* Corresponding author.

E-mail address: [pradip@ucsc.edu](mailto:pradip@ucsc.edu) (P.K. Mascharak).<https://doi.org/10.1016/j.ica.2017.11.022>

0020-1693/Published by Elsevier B.V.



Scheme 1. The arylbenzothiazoles reported in the present work.

purpose namely CO delivery under the control of light [13–16]. In such work we noted that the pyridyl and the quinolyl N atom is disposed in *anti* orientation with respect to the benzothiazole-N atom in both free ligands. However, uniformly in all their metal carbonyl complexes the pyridyl (and/or quinolyl) N and the benzothiazole-N atoms assume *syn* orientation and these allow the ligands to bind the metal centers in a bidentate-N,N fashion [13–16]. The affinity of silver to bind S atom is well known. We therefore proceeded to explore the possibility of these arylbenzothiazoles to bind silver in a bidentate-N,S fashion. A thorough literature survey revealed examples of very few Ag(I) complexes incorporating pyridyl-benzothiazoles that have been structurally characterized [17]. In such examples, 3-(pyridyl)benzothiazole and 4-(pyridyl)benzothiazole have been employed as ligands that led to dimeric structures, in which each Ag(I) centers reside uniformly in a quasi linear coordination environment [17]. Herein we report two four-coordinated Ag(I) complexes derived from pbt and qbt, namely, [Ag(pbt)<sub>2</sub>]BF<sub>4</sub> (**1**) and [Ag(qbt)<sub>2</sub>]BF<sub>4</sub> (**2**) respectively. In both complexes the arylbenzothiazole ligands (pbt and qbt) bind the Ag center in a bidentate-N,N mode and despite the expected affinity of silver, the S atom of the benzothiazole moiety remains non-coordinated. We also report that the strong fluorescence of both ligands is significantly quenched upon coordination to Ag(I) center. Quite in contrary, such dowsing of fluorescence has not been noted in the dimeric Ag(I) complexes derived from 3-(pyridyl)benzothiazole and 4-(pyridyl)benzothiazole [17]. This contrast in behavior encouraged us to perform triplet state density functional theory (DFT) calculations to probe into the fluorescence properties of (**1**) and (**2**) the results of which are also discussed in this account. The gradual emergence of the blue fluorescence (turn-on) in presence of chloride from both complexes could provide a convenient means to track the release of bioactive Ag<sup>+</sup> within biological environments.

## 2. Experimental

### 2.1. General

All reagents and solvents were of commercial grade and used without further purification. The ligands pbt [18] and qbt [16] were synthesized according to the reported procedures. IR and UV-Vis spectra of the ligands and the complexes were obtained using Perkin-Elmer Spectrum-One FT-IR and Varian Cary 50 UV-Vis spectrophotometers respectively. The <sup>1</sup>H NMR spectra of the complexes were recorded at 298 K on a Varian Unity Inova 500 MHz instrument. The emission spectra were recorded with Agilent Cary Eclipse spectrometer. Microanalyses were carried out with a PerkinElmer Series II 2400 Elemental Analyzer.

### 2.2. Synthesis of [Ag(pbt)<sub>2</sub>]BF<sub>4</sub> (**1**)

A solution of silver tetrafluoroborate (84 mg, 0.43 mmol) in 15 mL of methanol was added to a solution of 185 mg (0.87 mmol) of pbt in 30 mL of chloroform (CHCl<sub>3</sub>). The reaction flask was covered with Al foil to avoid ambient light and stirred for 48 h at room

temperature. Next, the solvent was partially removed to obtain a white precipitate. The solid was isolated by vacuum filtration and further recrystallized from hot methanol (yield: 192 mg, 72%). Elemental analysis (%) calculated for C<sub>24</sub>H<sub>16</sub>AgN<sub>4</sub>S<sub>2</sub>BF<sub>4</sub>: C 46.55, H 2.60, N 9.05; Found: C 46.60, H 2.58, N 9.02. IR (KBr, cm<sup>-1</sup>): 3486 (w), 1459 (w), 1436 (w), 1084 (s), 1059 (s), 783 (w), 760 (w). <sup>1</sup>H NMR (CDCl<sub>3</sub>, δ ppm): 8.77 (d, 1H), 8.42 (d, 1H), 8.15 (d, 1H), 7.97 (m, 2H), 7.55 (t, 1H), 7.48 (m, 2H).

### 2.3. Synthesis of [Ag(qbt)<sub>2</sub>]BF<sub>4</sub> (**2**)

This complex was synthesized by the same procedure as above using silver tetrafluoroborate (78 mg, 0.40 mmol) and qbt (213 mg, 0.81 mmol) to obtain a tan solid which was further recrystallized from hot methanol (yield: 182 mg, 63%). Elemental analysis (%) calculated for C<sub>22</sub>H<sub>20</sub>AgN<sub>4</sub>S<sub>2</sub>BF<sub>4</sub>: C 53.43, H 2.80, N 7.79; Found: C 53.47, H 2.85, N 7.69. IR (KBr, cm<sup>-1</sup>): 3497 (w), 1591 (w), 1512 (w), 1084 (s), 1058 (s), 830 (w), 755 (w). <sup>1</sup>H NMR (CDCl<sub>3</sub>, δ ppm): 8.53 (m, 2H), 8.40 (d, 1H), 8.25 (d, 1H), 8.02 (d, 1H), 7.96 (d, 1H), 7.91 (t, 1H), 7.71 (t, 1H), 7.59 (t, 1H), 7.52 (t, 1H).

### 2.4. X-ray crystallography

Colorless needle-shaped and block-shaped crystals of complexes **1** and **2** respectively were obtained by recrystallization through diffusion of hexanes into their dichloromethane (CH<sub>2</sub>Cl<sub>2</sub>) solutions. In case of **1**, a suitable crystal was selected and mounted on a Bruker D8 diffractometer with PHOTON II detector equipped with a low temperature device, operating at *T* = 100 K. This crystal was kept at *T* = 100 K during entire tenure of data collection and unit cell determination. Data were measured using  $\phi$  and  $\omega$  shutterless scan technique using synchrotron radiation (Advanced Light Source, Berkeley, station 11.3.1). In case of **2**, a suitable single crystal was selected and mounted on a Bruker APEX-II CCD diffractometer with graphite monochromated Mo-K $\alpha$  radiation ( $\lambda$  = 0.71073 Å). In this case, the crystal was kept at *T* = 298 K during data collection and unit cell determination. Data were measured using  $\omega$  scan technique. The total number of runs and images for both data collections was based on the strategy calculation from the program APEX2 (Bruker) [19]. The maximum resolution achieved was  $\theta$  = 31.196 for **1** and  $\theta$  = 25.142 for **2**. Cell parameters were retrieved using the SAINT (Bruker) software [20] and refined using SAINT (Bruker) on 31,484 reflections, (107% of the observed reflections) for **1** and on 3111 reflections (36% of the observed reflections) for **2**. Data reduction was performed using the SAINT (Bruker) software, which corrects for Lorentz polarization. The final completeness is 99.80% out to 31.196 in  $\theta$  for **1** and 98.80% out to 25.142 in  $\theta$  for **2**. Multi-scan absorption corrections were performed with both data sets using SADABS 2014/5 [21]. The absorption coefficient  $\mu$  for **1** is 1.254 mm<sup>-1</sup> and for **2** is 0.910 mm<sup>-1</sup> and the minimum and maximum transmissions for **1** are 0.6322 and 0.7450 and the corresponding values for **2** are 0.6023 and 0.7452. The structure for **1** and **2** were solved in the space group *P2*<sub>1</sub>*c*<sub>2</sub> (No. 19) and *C2/c* (No. 15) by intrinsic phasing using the ShelXT (Sheldrick, 2015) [22] structure solution program and refined by full matrix least squares on *F*<sup>2</sup> using version 2016/6 of ShelXL (Sheldrick, 2015) [22]. All non-hydrogen atoms were refined anisotropically in both cases. Hydrogen atom positions were calculated geometrically and refined using the riding model. In case of **1**, there is a single molecule in the asymmetric unit, while for **2** only half of the formula unit is present in the asymmetric unit, with the other half consisting of symmetry equivalent atoms. In case of **1** the Flack parameter was refined to 0.447(10). A Flack parameter value around 0.5 indicates that the crystal consists of a racemic mixture of two enantiomers. Calculations and molecular graphics were preformed using SHELXTL 2014 and Olex2 [23] programs.

Crystal data and structure refinement parameters are listed in Table 1.

CCDC 1548688 (complex 1), CCDC 1548689 (complex 2), CCDC 1556692 (pbt) and CCDC 1556693 (qbt) contain the supplementary crystallographic data for this paper. These data can be obtained free of charge from The Cambridge Crystallographic Data Center via [www.ccdc.cam.ac.uk/data\\_request.cif](http://www.ccdc.cam.ac.uk/data_request.cif).

## 2.5. Computational methods

The M06L [24] functional, as implemented in the Gaussian09 program [25], was used for solvent-phase structure optimizations. The SMD [26] implicit solvation model was used for solvation treatments with dichloromethane as solvent ( $\epsilon = 8.93$ ). The SDD [27,28] basis set and the associated effective core potential was used for Ag, and the Def2-TZVP basis sets were employed for other atoms [29,30]. Nature of the stationary point was confirmed by performing vibrational frequency calculations that were performed to confirm the optimized structures as minima (i.e., no imaginary frequencies for a minima). The time-dependent density functional theory (TDDFT) was used for excited-state calculations with the M062X [31] functional and the above basis sets. The non-equilibrium SMD solvation was employed to calculate vertical excitations, while the equilibrium SMD solvation was used to optimize the lowest excited singlet state and the lowest excited triplet state. The “ultraFine” integration grid was used for TDDFT calculations, where the two-electron integral accuracy parameter was set to 12.

## 2.6. Antimicrobial studies

A skin and soft tissue infection (SSTI) model was constructed for antibacterial studies by following a procedure described by us in a

**Table 1**  
Crystal data and structure refinement parameters for 1 and 2.

	1.2H <sub>2</sub> O	2
Formula	C <sub>24</sub> H <sub>20</sub> AgBF <sub>4</sub> N <sub>4</sub> O <sub>2</sub> S <sub>2</sub>	C <sub>32</sub> H <sub>20</sub> AgBF <sub>5</sub> N <sub>4</sub> S <sub>2</sub>
<i>D</i> <sub>calc</sub> /g cm <sup>−3</sup>	1.683	1.704
$\mu$ /mm <sup>−1</sup>	1.254	0.910
Formula Weight	655.21	738.32
Color	Colorless	Yellow
Shape	Needle	Block
<i>T</i> /K	100 (2)	298 (2)
Crystal System	Orthorhombic	Monoclinic
Space Group	<i>P</i> 2 <sub>1</sub> 2 <sub>1</sub> 2 <sub>1</sub>	<i>C</i> 2/ <i>c</i>
<i>a</i> /Å	7.3901 (5)	14.997 (6)
<i>b</i> /Å	15.5413 (9)	15.288 (6)
<i>c</i> /Å	22.3819 (12)	14.176 (5)
$\alpha$ /°	90	90
$\beta$ /°	90	117.707(4)
$\gamma$ /°	90	90
<i>V</i> /Å <sup>3</sup>	2570.6 (3)	2877.5 (19)
<i>Z</i>	4	4
Wavelength/Å	0.7749	0.71073
Radiation type	Synchrotron	Mo-K $\alpha$
$\theta$ <sub>min</sub> /°	1.739	2.665
$\theta$ <sub>max</sub> /°	31.196	25.142
Measured Refl.	29,368	8694
Independent Refl.	6397	2544
Reflections Used	6078	2094
<i>R</i> <sub>int</sub>	0.0478	0.0280
Parameters	343	205
Largest Peak	2.325	0.850
Deepest Hole	−0.814	−0.523
<sup>a</sup> Goof	1.130	1.043
<sup>b</sup> <i>wR</i> <sub>2</sub>	0.1467	0.1409
<sup>c</sup> <i>R</i> <sub>1</sub>	0.0519	0.0494

<sup>a</sup>  $\text{GoF} = [\sum(w(F_o^2 - F_c^2)^2)/(\sum(N_o - N_v))]^{1/2}$  ( $N_o$  = number of observations,  $N_v$  = number of variables).

<sup>b</sup>  $R_1 = \sum|F_o| - |F_c|/\sum|F_o|$ .

<sup>c</sup>  $wR_2 = [(\sum w(F_o^2 - F_c^2)^2)/\sum|F_o|^4]^{1/2}$ .

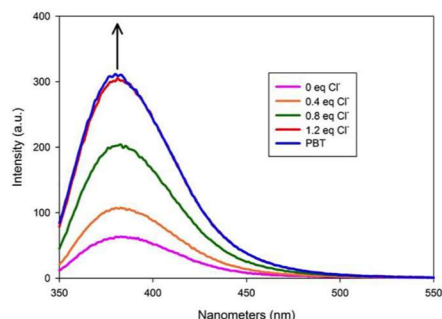


**Fig. 1.** Representative case of “turn-On” fluorescence from complex 1 in CH<sub>2</sub>Cl<sub>2</sub> solution in presence of chloride.

previous article [32]. This SSTI model consists of two agar layers, a hard agar bottom layer containing most of the nutrients and a soft agar layer on the top that allows for even dispersion of bacteria. As bacteria grow in the top soft agar (mimicking the lower epidermis of the skin), they migrate towards the bottom nutrient layer

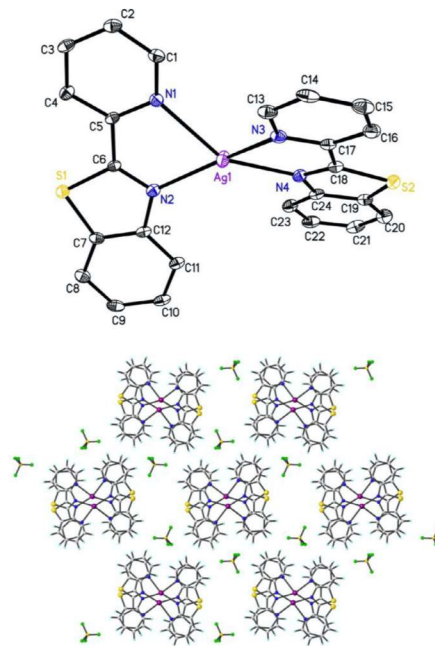


**Fig. 2.** The perspective view of the cation of complex 1 (the thermal ellipsoids are shown at 50% probability level, H atoms of the pbt ligand are omitted for the sake of clarity) (top panel); packing pattern extending along a axis (bottom panel).



modeling a cutaneous infection. Frozen samples of *Pseudomonas aeruginosa* and *Staphylococcus aureus* were thawed and streaked on two separate agar plates. A single colony from each plate was selected and grown in Luria Broth (LB) for 18 h. The suspensions were diluted with LB until an  $A_{600}$  of 0.5 was reached. The soft agar bacterial suspension was prepared by adding 60  $\mu\text{L}$  of the above solution to 50 mL of 0.8% (w/v) agar with 1% NaCl which had been previously autoclaved and cooled to 45 °C before the addition. The

suspension was gently vortexed and 7 mL was spread evenly on the surface of a hard agar layer prepared from 20 mL of a 1.5% (w/v) TSB agar in a 100  $\times$  15 mm<sup>2</sup> plate and allowed to solidify. Plates thus prepared were incubated for 2 h at 37 °C in order for the bacteria to reach log phase before bactericidal experiments were run.

### 3. Results and discussion

#### 3.1. Synthesis and spectroscopic properties

The two arylbenzothiazole ligands have been synthesized by reported procedures. The two complexes (**1** and **2**) were obtained in good yield by the reactions of  $\text{AgBF}_4$  with pbt and qbt in 1:2 (metal:ligand) molar ratio in  $\text{CHCl}_3/\text{MeOH}$  under stirring condition. Both reaction flasks were properly covered with aluminum foil to avoid exposure of any ambient light during the course of reactions. The molecular structures for both complexes have been authenticated by single crystal X-ray crystallography (Figs. 2 and 5, *vide infra*). The crystal structures reveal that in both cases the ligand (pbt and qbt) binds the  $\text{Ag(I)}$  center in bidentate-N,N fashion. In both structures, the pyridine and quinolyl rings rotate to present their N atoms to the  $\text{Ag(I)}$  center because determination of crystal structures of both pbt and qbt ligands revealed that these two N atoms are in *anti* disposition with respect to each other (see [Supporting Information](#)). Therefore, the possibility of N,S-bidentate coordination of the ligands has not been achieved in the present complexes despite the considerable propensity of the Ag to bind S atom. IR spectra of the complexes exhibit all the stretches pertinent to the coordinated arylbenzothiazole ligands employed (see

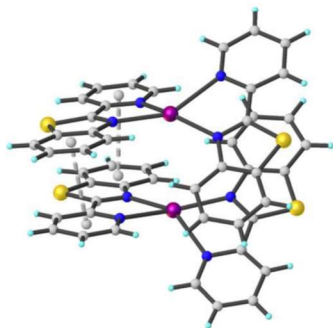


Fig. 3. Representation of intermolecular offset  $\pi$ - $\pi$  stacking interactions in complex **1**.

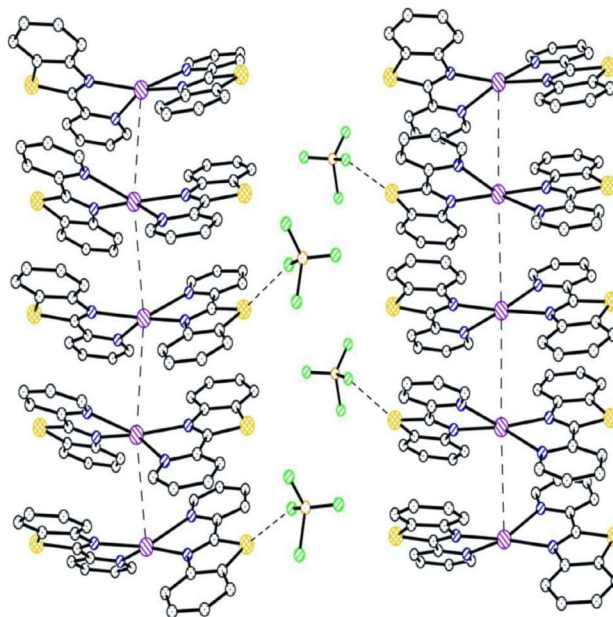


Fig. 4. Representation of intermolecular  $\text{Ag} \cdots \text{Ag}$  and  $\text{S} \cdots \text{F}$  non-bonding interactions within the extended lattice of complex **1**.



experimental section). In addition IR spectra of two the complexes display a strong band at  $\sim 1060\text{ cm}^{-1}$  because of the presence of  $\text{BF}_4^-$  as counter anion. Both complexes exhibit well resolved  $^1\text{H}$  NMR in  $\text{CDCl}_3$  solution (Supporting Information). The electronic absorption spectra in dichloromethane ( $\text{CH}_2\text{Cl}_2$ ) solution exhibit broad absorption band centered around 320 nm for **1** and 350 nm for **2** (Supporting Information). These bands have contributions from both MLCT (metal-to-ligand) and ligand-based charge transfer transitions (*vide infra*). Complexes **1** and **2** are fairly stable in  $\text{CH}_2\text{Cl}_2$  and  $\text{CHCl}_3$  solutions and time-dependent UV-Vis spectral studies revealed no significant change in the electronic absorption spectra in such solutions for at least 24 h.

Apart from the known antimicrobial activities, the arylbenzothiazoles (pbt and qbt) utilized in the present work are also highly fluorescent and the latter property was expected to provide a means to track the silver release from the respective complexes (through a change in emission property). Indeed, fluorescence spectral studies revealed that both complexes could act as a “turn-on” type sensor through which the delivery of bioactive  $\text{Ag}^+$  ion can be tracked

indirectly within the site of interest. Both complexes exhibit very low emission intensity in  $\text{CH}_2\text{Cl}_2$  solutions. However, systematic addition of  $\text{Bu}_4\text{NCl}$  resulted in a gradual emergence of the fluorescence in such solutions, associated with slow release of silver ( $\text{Ag}^+$ ) with concomitant deligation of the highly fluorescent arylbenzothiazole ligands (pbt and qbt). The complete deligation of the benzothiazoles from both complexes has been realized upon administration of 1.2 equivalent of  $\text{Bu}_4\text{NCl}$  (Fig. 1 shows one typical example). This process can be potentially beneficial not only as a “turn-on” sensor to track the release of silver, but also the deligation of the arylbenzothiazoles could potentially provide an additional antimicrobial agent to the infected sites. In a previous account we have demonstrated the tracking of slow release of  $\text{Ag}^+$  from a BODIPY-based  $\text{Ag}(\text{I})$   $\alpha$ -diimine complex through a “turn-on” fluorescence, a property associated with the free ligand [33].

### 3.2. Description of crystal structures

Single crystal analysis reveals that complex **1** crystallizes in orthorhombic  $P2_12_12_1$  space group and the asymmetric unit comprises the complete molecule, along with one  $\text{BF}_4^-$  counter anion and two water molecules of crystallization. The perspective view with atom labeling scheme is shown in Fig. 2. In this structure the  $\text{Ag}(\text{I})$  center resides in a distorted tetrahedral coordination environment where the metal center is coordinated to two N atoms of each of the two pbt ligands. The pbt chelate rings (comprised of  $\text{Ag1}$ , N1, C5, C6, N2 and  $\text{Ag1}$ , N3, C17, C18, N4 atoms) are satisfactorily planar with mean deviations of 0.019 (3) and 0.011 (4) Å respectively. Both benzothiazole fragments (composed of C6, C7, C8, C9, C10, C11, C12, N2, S1 and C18, C19, C20, C21, C22, C23, C24, N4, S2 atoms) are highly planar with mean deviations of 0.010 (3) and 0.005 (3) Å respectively. The dihedral angles between these fragments and the adjoining pyridyl rings are found to be 2.3 (4) and 3.0 (3)° respectively. Silver complexes with [AgN4] chromophore derived from 2,2'-bipyridine and its derivatives have been reported by different research groups. In one of such systems namely,  $[\text{Ag}^+(\text{tmbp})_2]\text{BF}_4^-$  (where tmbp = 4,4',6,6'-tetramethyl-2,2'-

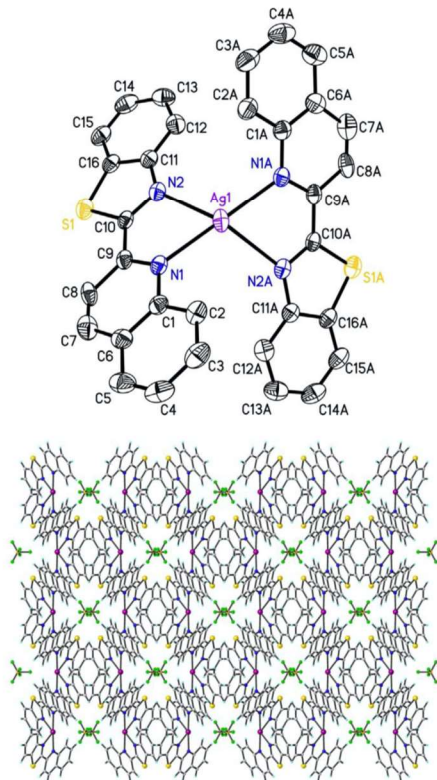


Fig. 5. The perspective view of the cation of complex **2** (the thermal ellipsoids are shown at 50% probability level. H atoms of the qbt ligand are omitted for the sake of clarity) (top panel); packing pattern extending along c axis (bottom panel).

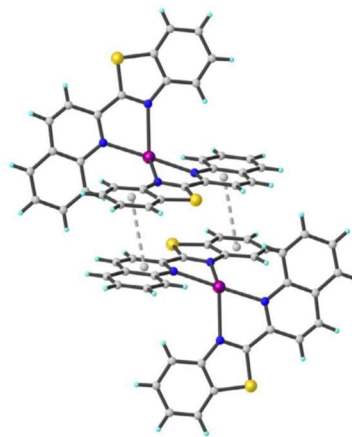


Fig. 6. Representation of intermolecular offset  $\pi$ - $\pi$  stacking interactions in complex **2**.

bipyridine), the average Ag–N distance is 2.321(5) Å [34], somewhat shorter compared to the average Ag–N distance in **1** (2.355(6) Å). In another structurally comparable Ag(I) complex namely, [Ag(L1)<sub>2</sub>]NO<sub>3</sub> (where L1 = 4,4'-dimethyl-2,2'-bipyridine) [35] the average Ag–N distance (2.329(3) Å) is comparable to that in **1**. In [Ag(tmbp)<sub>2</sub>]BF<sub>4</sub> and [Ag(L1)<sub>2</sub>]NO<sub>3</sub> average N–Ag–N bite angles are 72.1 and 71.1° respectively, quite similar to the average N–Ag–N bite angle in **1** (71.8°). The crystal packing of **1** reveals the presence of two types of intermolecular offset  $\pi$ – $\pi$  stacking interactions (Fig. 3, centroid-to-centroid distances 3.666 (3) and 3.674 (4) Å).

Analysis of molecular packing of **1** also reveals significant intermolecular Ag...Ag interactions (3.867 Å). In the extended structure the disposition of the pbt ligands brings two Ag centers close enough to promote such Ag...Ag interaction (Fig. 4). In addition, S(pbt)...F(BF<sub>4</sub>) non bonded contacts (3.114 Å) have been realized from the packing pattern (Fig. 4). The extended lattice is consolidated with few non classical hydrogen bonding interactions [C4–H4...S1, with H...S, 2.68 Å, C4–H4...F4, with H...F, 2.52 Å<sup>i</sup>, C8–H8...F3, with H...F, 2.47 Å<sup>ii</sup>, C14–H14...F1, with H...F, 2.50 Å<sup>iii</sup>, C16–H16...S2, with H...S, 2.72 Å, C20–H20...F1, with H...F, 2.48 Å<sup>iv</sup>, C22–H22...F1, with H...F, 2.51 Å<sup>v</sup>; symmetry codes: (i) x, y + 1, z; (ii) x – 1/2, –y + 1/2, –z – 1; (iii) –x, y + 1/2, –z – 1/2; (iv) x – 1/2, –y – 1/2, –z – 1; (v) –x + 1/2, –y, z – 1/2].

Complex **2** crystallizes in monoclinic C2/c space group and the asymmetric unit contains one Ag coordinated to one pbt ligand and a partial BF<sub>4</sub> anion. The perspective view with atom labeling scheme of the [Ag(qbt)<sub>2</sub>]<sup>+</sup> is shown in Fig. 5. In the structure of **2**, only one of the two qbt ligands appears in the asymmetric unit, with the second qbt ligand consisting of symmetry equivalent atoms. In this structure, each qbt ligand constitutes chelate ring (composed of Ag1, N1, C9, C10, N2 and Ag1, N1A, C9A, C10A, N2A atoms), which considerably deviates from planarity (mean deviation, 0.072 (4) Å). The two benzothiazole fragments composed of N2, C10, C11, C12, C13, C14, C15, C6, S1 atoms and the symmetry equivalent atoms constitute excellent plane with mean deviation of 0.009 (3) Å. The dihedral angles between the benzoth-

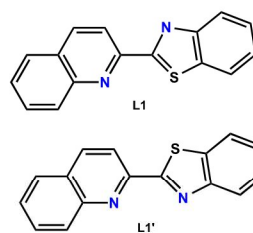
iazole fragments and the conjoining quinoline rings are found to be 3.4 (5)°. Molecular packing of **2** also reveals noticeable intermolecular offset  $\pi$ – $\pi$  stacking interactions (with centroid-to-centroid distance, 3.686 Å) (Fig. 6).

Analysis of the molecular packing for **2** also reveals significant Ag...F(BF<sub>4</sub>) (3.049 Å) and S1(pbt)...F(BF<sub>4</sub>) (3.182 Å) non bonded interactions (Fig. 7). In the extended lattice only one type of non-classical hydrogen bonding contact has been realized [C8–H8...S1, with H...S, 2.80 Å].

### 3.3. Density functional theory calculations

#### 3.3.1. Ground state (*S*<sub>0</sub>) and the lowest singlet state (*S*<sub>1</sub>) of qbt ligand

In the initial calculations of the ground state, optimization led to two conformational energy minima for the qbt ligand (as a representative case) namely, **L1** and **L1'** (Scheme 2). The high-energy isomer **L1'** lies 3.9 kcal/mol higher in energy compared to **L1** with a free energy barrier of 8.4 kcal/mol. The reversed process, **L1'** → **L1**, has a barrier of 5.5 kcal/mol. We therefore conferred that



Scheme 2. Isomers of qbt ligand, **L1** and **L1'**.

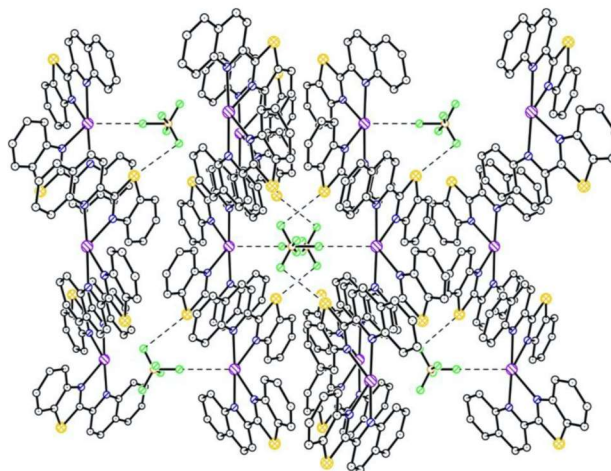


Fig. 7. Representation of intermolecular Ag...F and S...F non-bonding contacts within the extended lattice of complex **2**.

isomer **L1** would be the favorable species in solution under the reaction conditions.

Kohn-Sham orbitals of **L1** in the frontier region are shown in Fig. 8. The HOMO-LUMO gap of **L1** is 0.23 AU, where HOMO is a  $\pi$  orbital and LUMO is a  $\pi^*$  orbital. According to our TDDFT calculations, the first vertical excitation, 309 nm ( $f = 0.94$ ), is the dominant transition, which is in agreement with the experimental values (310 nm). The natural transition orbitals (NTOs) confirmed that this is a  $\pi \rightarrow \pi^*$  excitation (Fig. 9). In case of the high-energy isomer **L1'**, the  $\pi \rightarrow \pi^*$  excitation also occurs at 310 nm ( $f = 0.89$ ) (See Fig. S8, supporting information for the MO diagram). Starting from the Frank Condon geometries of **L1** and **L1'**, we have fully optimized the lowest singlet excited state of both isomers, leading to energetically similar excited states. In the case of **L1**, calculated emission from the  $S_1$  state is 394 nm ( $f = 1.40$ ), and is in agreement with the experimental data (400 nm). Similar picture was observed for **L1'**, where the calculated emission is 395 nm ( $f = 1.37$ ). In **L1**, the N-C-C-N torsion angles of the  $S_0$  and  $S_1$  structures are 2.4 and 0.6° respectively while in case of **L1'**, the values are 9.1 and 0.5° respectively. It is interesting to note that  $S_1$  state geometries are planar.

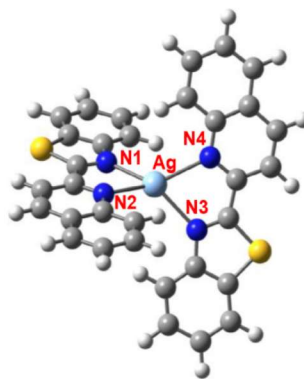


Fig. 10. Optimized structure of the cation of complex 2.

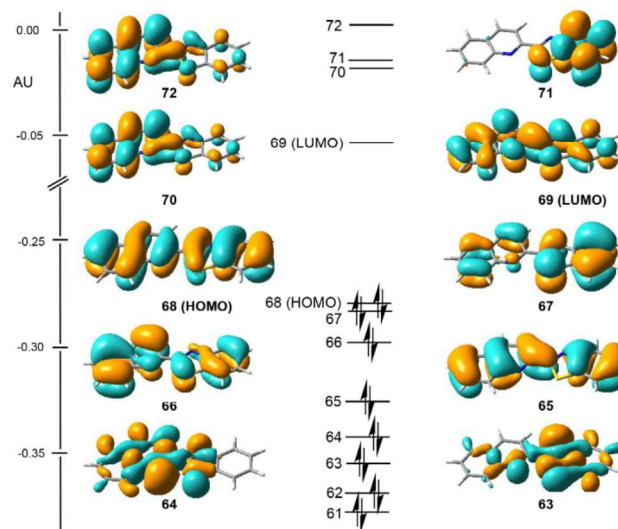


Fig. 8. Kohn-Sham orbitals of qbt (**L1**) in the frontier region.

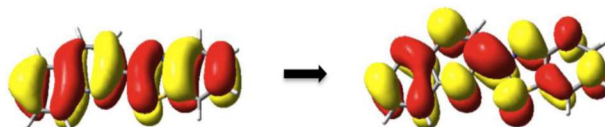


Fig. 9. Natural transition orbitals (NTOs, occupied "hole"/unoccupied "electron") correspond to the first vertical excitation of **L1**.

### 3.3.2. Ground state ( $S_0$ ), the lowest singlet ( $S_1$ ) and triplet ( $T_1$ ) states of complex **2**

The fully optimized ground state structure of complex **2** is shown in Fig. 10, and the key structural parameters are summarized in Table 2. In the X-ray structure (solid phase), the two Ag–N bonds are relatively shorter (2.25 Å) than the other two (2.51 Å). The torsion angle between the two N–Ag–N planes ( $\phi$ , 58.9°) clearly indicates a distorted tetrahedral geometry. In the fully optimized  $S_0$  structure in the solvent phase, the Ag–N bond lengths are rather similar (2.35–2.39 Å), and the torsion angle  $\phi$  is slightly larger (67.6°). In the excited state optimized structures ( $S_1$  and  $T_1$ ), the Ag–N bond becomes slightly larger, while the torsion angle  $\phi$  becomes slightly smaller (see Table 2).

Kohn–Sham orbitals in the frontier region of the  $S_0$  structure are shown in Fig. 11. The HOMO is a  $\pi$  orbital, which is delocalized over the both qbt ligands, and LUMO is the corresponding  $\pi^*$  orbital. The HOMO–LUMO gap of complex **2** (0.21 AU) is marginally

smaller than the HOMO–LUMO gap of the qbt ligand (0.23 AU). Our TDDFT results and NTOs rationalized two important absorption bands as  $^1\text{MLCT}$  (326 nm) and  $^1\text{LC}$  (317 nm) transitions. Starting from the Frank Condon geometry, we have optimized the lowest singlet state ( $S_1$ ) of complex **2**, which is 3.07 eV higher than the ground state, and has  $^1\text{MLCT}$  character. We have also located the lowest triplet excited state ( $T_1$ ), which lies 1.97 eV above the ground state. Starting from the  $T_1$  geometry, we have performed triplet DFT single point energy calculations to plot total spin density (Fig. 12). Interestingly, two unpaired electrons are located in a qbt ligand, and spin density on Ag is zero, implying that the  $T_1$  state has  $^3\text{LC}$  character. The calculated emission from  $^3\text{LC}$  is 629 nm, approaching to the near-IR region. This is substantially longer than the calculated emission for qbt ligand itself (394 nm). However, experimentally, we could not detect an emission band for complex **2** at near-IR region or beyond, suggesting  $^3\text{LC}$  as a non-

**Table 2**  
Key structural parameters in the X-ray structure and calculated structures of complex **2**. Bond lengths are in Å and bond angles and the torsion angle ( $\phi$ ) are in degrees.

	X-ray	$S_0$	$S_1$	$T_1$
Ag–N1	2.254 (4)	2.39	2.41	2.43
Ag–N2	2.514 (4)	2.35	2.39	2.39
Ag–N3	2.514 (4)	2.36	2.45	2.45
Ag–N4	2.254(4)	2.38	2.41	2.40
N1–Ag–N2	71.25 (13)	70.5	70.0	69.7
N1–Ag–N3	126.23 (16)	145.7	145.8	145.6
N1–Ag–N4	177.61 (17)	121.9	123.2	122.0
N2–Ag–N3	177.61 (17)	124.0	122.5	123.9
N2–Ag–N4	126.23 (14)	139.4	141.6	141.9
N3–Ag–N4	71.25 (13)	70.5	69.0	69.1
$\phi$	58.9 (10)	67.7	66.2	66.1

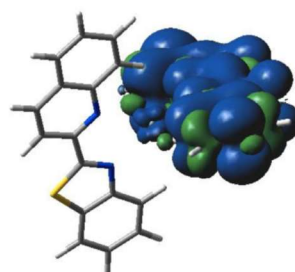


Fig. 12. Total spin density plot for the  $T_1$  state.

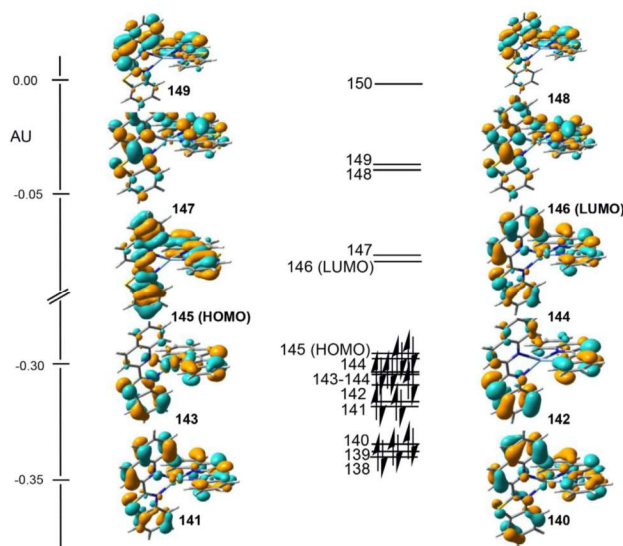
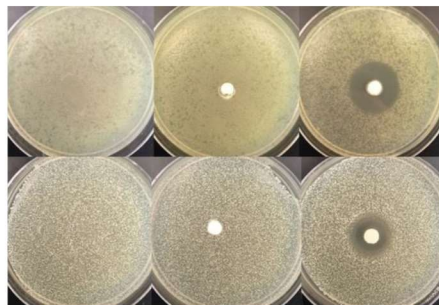


Fig. 11. Kohn–Sham orbitals of complex **2** in the frontier region.





**Fig. 13.** Clearing of bacterial growth of *P. aeruginosa* (top row) and *S. aureus* (bottom row) after 18 h incubation with a blank KBr pellet (left), KBr pellet with 2% (w/w) of qbt (middle), and KBr pellet with 2% (w/w) of **2** (right) placed on the top layer.

emissive state where the excited molecules would follow non-radiative decay channels [36]. Analyzing such non-radiative paths is beyond the scope of the present paper.

Taken together the TDDFT results confirmed that the  $\pi \rightarrow \pi^*$  excitation is dominant for free qbt, leading fluorescence from the lowest singlet excited state ( $S_1$ ). On the other hand, the lowest singlet excited state of complex **2** shows  $^1\text{MLCT}$  character, while the lowest triplet state holds  $^3\text{LC}$  character, which acts as a non-emissive state. It is thus evident that the weak luminescent behavior of complex **2** (and complex **1**) arises from facile  $S_1 \rightarrow T_1$  intersystem crossing commonly observed in complexes with heavy metal (such as Ag) with strong spin-orbit coupling.

#### 3.4. Antimicrobial studies

The antibacterial effects of silver have recently been exploited to tackle chronic infections of wounds by multi drug-resistant bacteria in hospitals around the world [37–39]. Silver salts (such as  $\text{AgNO}_3$  and Ag-sulfadiazine) have found wide use in the treatment and prevention of infections of burn wounds and diabetic wounds of immunocompromised patients. The bioactive  $\text{Ag}^+$  ion is known to interact with thiol and amino groups of proteins, nucleic acids and with cell membranes. Such multiple pathways of exerting pathological damage by the  $\text{Ag}^+$  ion makes it difficult for the microorganisms to develop resistance to this “antibiotic” and thus renewed interest in silver treatments has been a trend in drug development efforts. We have been interested in examining the antibacterial effects of new silver complexes of ligands with inherent antimicrobial effects such as pbt and qbt on two bacteria namely *Pseudomonas aeruginosa* (Gram-negative) and *Staphylococcus aureus* (Gram-positive) that often pose threat to burn wounds in hospitals [40]. In this work we have examined the antibacterial efficacy of complex **2** on these two bacteria grown on a SSTI model developed in our laboratory. The model is a bilayer of agar with a nutrient gradient, the top soft layer of which consists of a uniform bacterial “lawn” (Fig. 13). The design allows gradual “ditching” of the bacteria from the top layer to the nutrient-rich bottom layer upon incubation much like the way bacteria penetrate from epidermis to dermis layers of the skin during chronic infection [32]. KBr pellets of similar weights containing 2% (w/w) of qbt and **2** were carefully placed on the top bacterial lawns (Fig. 13) and the SSTI models were incubated at 37 °C. Visible circular zones of bacterial clearing around the pellet containing **2** were observed in

both cases after incubation for 18 h as shown in Fig. 13. Similar results were obtained with complex **1**. Taken together, these initial results confirm the antibacterial properties of these  $\text{Ag(I)}$  complexes. At this time attempts are being made to make these complexes more soluble in water through alteration of the ligand frames the results of which will be reported in due time.

#### 4. Conclusions

In summary, two silver complexes (**1** and **2**) incorporating 2-(pyridyl)benzothiazole and 2-(quinolyl)benzothiazole have been synthesized and characterized with the aid of different spectroscopic techniques. The molecular structures of both complexes have been determined by X-ray crystallography. The two arylbenzothiazoles employed in this work were selected for two primary reasons. First, they by themselves exhibit antimicrobial activity and hence could provide a “double shot” of antibacterial agents upon the release of silver from their complexes under physiologically relevant conditions. Second, both ligands are photo stable and highly fluorescent. The latter property could be readily exploited to track the complexes within cellular matrices. Interestingly, N,N-bidentate coordination of both ligands to  $\text{Ag(I)}$  results in dramatic diminution of their fluorescence. However, the fluorescence is readily recovered upon release of silver in presence of chloride in a concentration dependent fashion. Thus release of silver can be tracked in solution (and in tissues) by virtue of the “turn-on” fluorescence signal upon deligation of the fluorescent ligands. DFT and TDDFT calculations have been performed to gain insight into the fluorescence quenching behavior of the two silver complexes. The results indicate that a facile  $^1\text{MLCT} \rightarrow ^3\text{LC}$  (a  $1\text{S} \rightarrow T_1$  intersystem crossing) transition is responsible for the diminution of luminescence in these complexes of silver (a heavy metal with high spin-orbit coupling) derived from fluorescent ligands. Both **1** and **2** exhibit strong bactericidal effects towards *P. aeruginosa* and *S. aureus*. The antimicrobial activity is accompanied by an enhancement of luminescence as expected.

#### Acknowledgements

Financial support from National Science Foundation Grant No. DMR-1409335 is gratefully acknowledged. This research used resources of the Advanced Light Source, which is a DOE Office of Science User Facility under contract no. DE-AC0205CH11231. WMCS acknowledges to Hokkaido Univ. for financial support and is grateful to the Institute for Molecular Sciences (Japan) for super-computer facilities and Prof. Masako Kato for useful discussions.

#### Appendix A. Supplementary data

Crystal structures of pbt and qbt ligand (Figs. S1 and S2), crystal data and structure refinement parameters for pbt and qbt (Table S1), FT-IR spectra of complexes **1** and **2** (Figs. S3 and S4), UV-Vis spectra of complexes **1** and **2** in  $\text{CH}_2\text{Cl}_2$  (Figs. S5 and S6), fluorescence “turn-on” study for complex **2** (Fig. S7),  $^1\text{H}$  NMR spectra of **1** and **2** in  $\text{CDCl}_3$  solution at 298 K (Fig. S8), Kohn-Sham orbitals of qbt ( $\text{L1'}$  isomer) in the frontier region (Fig. S9), TDDFT results of qbt (both isomer) and complex **2**, and Cartesian coordinates of the optimized structures of qbt (both isomer) and complex **2**. Supplementary data associated with this article can be found, in the online version, at <https://doi.org/10.1016/j.ica.2017.11.022>.

#### References

- [1] J. Davies, D. Davies, *Mol. Biol. Rev.* 74 (2010) 417–433.
- [2] C.H.-F. Lau, K. van Engelen, S. Gordona, J. Renaud, E. Topp, *Appl. Environ. Microbiol.* (2017), <https://doi.org/10.1128/AEM.00989-17>.

- [3] J.A. Lemire, J.J. Harrison, R.J. Turner, *Nat. Rev. Microbiol.* 11 (2013) 371–384.
- [4] K. Yamazaki, Y. Kaneko, K. Suwa, S. Ebara, K. Nakazawa, K. Yasuno, S. Bioorg. Med. Chem. 13 (2005) 2509–2522.
- [5] B. Rajeeva, N. Srinivasulu, S.M. Shantakumar, *Eur J. Med. Chem.* 6 (2009) 775–779.
- [6] A. Latrofa, M. Franco, A. Lopodota, A. Rosato, D. Carone, C. Vitali, *Il Farmaco* 60 (2005) 291–297.
- [7] P.K. Sahu, S.K. Gupta, D. Thavasvelvam, D.D. Agarwal, *Eur. J. Med. Chem.* 54 (2012) 366–378.
- [8] A.A. Weekes, A.D. Westwell, *Curr. Med. Chem.* 16 (2009) 2430–2440.
- [9] J. Gargia, P.K. Verma, A. Khatkar, *Cent. Nerv. Syst. Agents Med. Chem.* 15 (2015) 11–16.
- [10] V. Kumar, S. Sharma, A. Husain, *Int. Cur. Pharm. J.* 4 (2015) 457–461.
- [11] J. Jimenez, I. Chakraborty, M. Rojas-Andrade, P.K. Mascharak, *J. Inorg. Biochem.* 168 (2017) 13–17.
- [12] J. Jimenez, I. Chakraborty, A.M. Del Cid, P.K. Mascharak, *Inorg. Chem.* 56 (2017) 4784–4787.
- [13] S.J. Carrington, I. Chakraborty, J.M.L. Bernard, P.K. Mascharak, *A.C.S. Med. Chem. Lett.* 5 (2014) 1324–1328.
- [14] S.J. Carrington, I. Chakraborty, J.M.L. Bernard, P.K. Mascharak, *Inorg. Chem.* 55 (2016) 7852–7858.
- [15] I. Chakraborty, S.J. Carrington, G. Roseman, P.K. Mascharak, *Inorg. Chem.* 56 (2017) 1534–1545.
- [16] J. Stenger-Smith, I. Chakraborty, S.J. Carrington, P.K. Mascharak, *Acta Cryst.* (2017) C73.
- [17] N. Kundu, A. Audhya, S.M.T. Abtab, S. Ghosh, E.R.T. Tiekink, M. Chaudhury, *Cryst. Growth Des.* 10 (2010) 1269–1282.
- [18] X. Chen, F.J. Femia, J.W. Babich, J. Zubieta, *Inorg. Chim. Acta.* 314 (2001) 91–96.
- [19] Bruker APEX II, Bruker AXS Inc., Madison, Wisconsin, USA, 2012.
- [20] Bruker SAINT, Bruker AXS Inc., Madison, Wisconsin, USA, 2012.
- [21] Bruker SADABS, Bruker AXS Inc., Madison, Wisconsin, USA, 2014.
- [22] G.M. Sheldrick, *Acta Crystallogr. Sect. A: Found. Adv.* 71 (2015) 3–8.
- [23] O.V. Dolomanov, L.J. Bourhis, R.J. Gildea, J.A.K. Howard, H. Puschmann, *J. Appl. Crystallogr.* 42 (2009) 339–341.
- [24] Y. Zhao, D.G. Truhlar, *J. Chem. Phys.* 125 (2006) 194101, <https://doi.org/10.1063/1.2370993>.
- [25] Gaussian09, Revision D.01, M.J. Frisch, G.W. Trucks, H.B. Schlegel, G.E. Scuseria, M.A. Robb, J.R. Cheeseman, G. Scalmani, V. Barone, B. Mennucci, G.A. Peterson, H. Nakatsuji, M. Caricato, X. Li, H.P. Hratchian, A.F. Izmaylov, J. Bloino, G. Zheng, J.L. Sonnenberg, M. Hada, M. Ehara, K. Toyota, R. Fukuda, J. Hasegawa, M. Ishida, T. Nakajima, Y. Honda, O. Kitao, H. Nakai, T. Vreven, J.A. Montgomery Jr., J.E. Peralta, F. Ogliaro, M. Bearpark, J.J. Heyd, E. Brothers, K.N. Kudin, V.N. Staroverov, R. Kobayashi, J. Normand, K. Raghavachari, A. Rendell, J.C. Burant, S.S. Iyengar, J. Tomasi, M. Cossi, N. Rega, J.M. Millam, M. Klene, J.E. Knox, J.B. Cross, V. Bakken, C. Adamo, J. Jaramillo, R. Gomperts, R.E. Stratmann, O. Yazyev, A.J. Austin, R. Cammi, C. Pomelli, J.W. Ochterski, K.L. Martin, K. Morokuma, V.G. Zakrzewski, G.A. Voth, P. Salvador, J.J. Dannenberg, S. Dapprich, A.D. Daniels, O. Farkas, J.B. Foresman, J.V. Ortiz, J. Cioslowski, D.J. Fox, Gaussian Inc, Wallingford CT, 2009.
- [26] A.V. Marenich, C.J. Cramer, D.G. Truhlar, *J. Phys. Chem. B* 113 (2009) 6378–6396.
- [27] P. Fuentealba, H. Preuss, H. Stoll, L. Vonszentpaly, *Chem. Phys. Lett.* 89 (1982) 418–422.
- [28] T.H. Dunning Jr, P.J. Hay, *Modern Theoretical Chemistry: Plenum: New York*, 3, 1977, pp. 1–28.
- [29] F. Weigend, R. Ahlrichs, *Phys. Chem. Chem. Phys.* 7 (2005) 3297–3305.
- [30] F. Weigend, *Phys. Chem. Chem. Phys.* 8 (2006) 1057–1065.
- [31] Y. Zhao, N.E. Schultz, D.G. Truhlar, *J. Chem. Theory Comput.* 2 (2006) 364–382.
- [32] B.J. Heilman, J.St. John, S.R.J. Oliver, P.K. Mascharak, *J. Am. Chem. Soc.* 134 (2012) 11573–11582.
- [33] M.N. Pinto, I. Chakraborty, W. Schultz-Simonton, M. Rojas-Andrade, R. Braslau, P.K. Mascharak, *Chem. Commun.* 53 (2017) 1459–1462.
- [34] K.V. Goodwin, D.R. McMillin, W.R. Robinson, *Inorg. Chem.* 25 (1986) 2033–2036.
- [35] A. Bellusci, A. Crispini, D. Pucci, E.I. Szerb, M. Ghedini, *Cryst. Growth and Design* 8 (2008) 3114–3122.
- [36] A.J. Howarth, M.B. Majewski, C.M. Brown, F. Leij, M.O. Wolf, B.O. Patrick, *Dalton Trans.* 44 (2015) 16272–16279.
- [37] J.Y. Maillard, P. Hartemann, *Crit. Rev. Microbiol.* 39 (2013) 373–383.
- [38] A.D. Russell, W.B. Hugo, *Prog. Med. Chem.* 31 (1994) 351–370.
- [39] S. Chernousova, M. Epple, *Angew. Chem. Intl. Ed.* 52 (2013) 1636–1653.
- [40] R.A. Weinstein, C.G. Mayhall, *Clin. Infect. Disease* 37 (2003) 543–550.

## Chapter 3. Antimicrobial Gold Complexes With the $\{\text{Au}(\text{PPh}_3)\}^+$ Moiety

### 3.1 Background on Medicinal gold

Gold has been used for medicinal purposes since 2500 B.C. when Chinese physicians and surgeons employed gold foil for treatment of various diseases.<sup>1</sup> Gold therapy had not been of major interest until Robert Koch discovered that  $\text{K}[\text{Au}(\text{CN})_2]$  was effective against *Mycobacterium tuberculosis*, the causative agent of tuberculosis (TB), in the late 1800s.<sup>2</sup> The next major advancement was the development of Au(I) complexes for the treatment of rheumatoid arthritis starting with Au(I) thiolates in the 1930s and later the clinical approval of Auranofin (**Figure 3.1**) in the 1980s.<sup>3</sup>

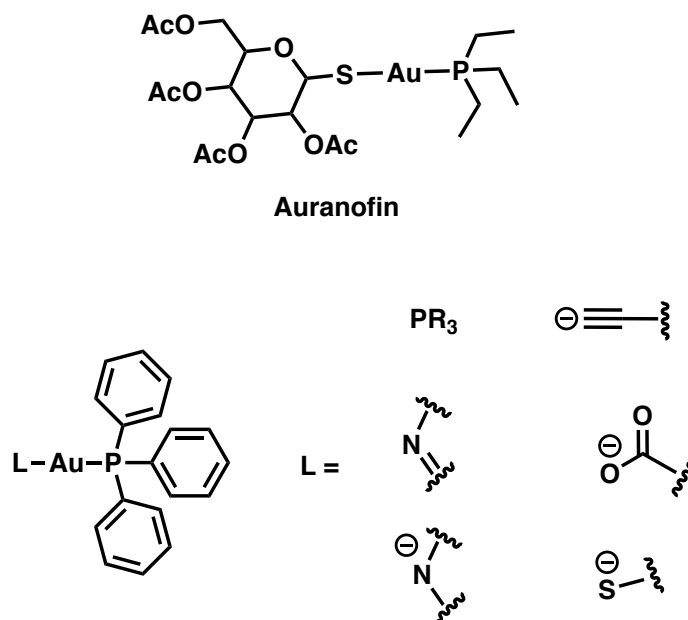


**Figure 3.1.** Auranofin and examples of linear arrangement of  $[\text{L}-\text{Au}(\text{PPh}_3)]$  complexes.

Since then, research into additional therapeutic purposes of gold has expanded into its antimicrobial, anticancer, antiarthritic, antiparasitic, and antiviral effects with much initial success.<sup>4-9</sup> Many of the gold anticancer compounds reported have been claimed to be more effective than cisplatin, one of the most common metal containing chemotherapy drugs. Some gold species show potent activity towards *M. Tuberculosis* and other infectious pathogens.<sup>8</sup> Even Auranofin has been studied for its repurposing as these types of therapeutic agents.<sup>10</sup>

Cationic gold mainly exists in two forms: linear Au(I) and square-planar Au(III), both of which have been evaluated for their biological activity. A special interest has been developed with gold(I) phosphine species not only for their therapeutic activity but also as effective catalysts for numerous reactions with alkynes.<sup>6,11,12</sup> The ligand exchangeability of linear  $\{\text{Au}(\text{PR}_3)\}^+$  species is thought to play a crucial role in both the inhibition of biological molecules and the effectiveness as a catalyst.<sup>12-15</sup> Of these gold(I) phosphine complexes, many gold(I) triphenylphosphine  $[\text{L-Au}(\text{PPh}_3)]$  species (**Figure 3.1**) have been of particular interest due to their stability and wide variety of the L ligand which determines their catalytic reactivity and the kinetic profile of their biological activity.<sup>16,17</sup> Even the “parent” compound  $[\text{Cl-Au}(\text{PPh}_3)]$  has shown effective anticancer activity against human breast (MCF-7) and fetal lung fibroblast cells, and was more selective towards cancerous cells over normal cells than both cisplatin and the  $\{\text{Au}(\text{PEt}_3)\}^+$  containing Auranofin.<sup>18</sup> The antimicrobial, anticancer, antiparasitic, anti-inflammatory and antiviral effects of  $[\text{L-Au}(\text{PPh}_3)]$  complexes have been examined.

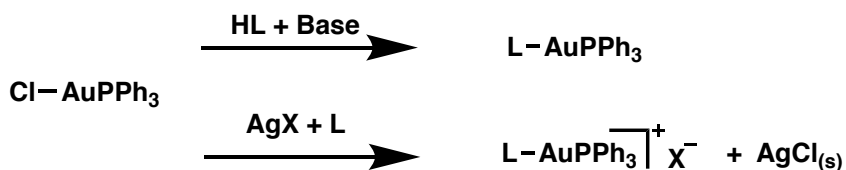


### 3.1.1 Chemistry of Au(I)

Gold(I), an electron rich  $d^{10}$  transition metal, typically forms complexes with linear geometry and this can be partially explained by the relativistic effects of post-lanthanide elements.<sup>19</sup> The aurophilic interactions (gold-gold contacts) observed in gold chemistry give rise to very interesting photophysical, catalytic and clustering properties.<sup>20</sup> Although the gold(I) phosphine complexes of the type  $[L-Au(PR_3)]$  will be discussed hereafter to relate to the findings of this work, there are a variety of other donor ligands that can be present on a gold(I) center such as arsine, isocyanide, carbene, ylide, amine, halide, alkyl, aryl, and chalcogenolide.

Gold(I) phosphine complexes have been extensively studied with particular interest in the influence of the phosphine ligands on the metal–P bond.<sup>17,21,22</sup> For  $PR_3$  ligands, the R substituent plays an important role in their sigma donor strength as well as  $\pi$ -acceptor capabilities; the more electronegative the R group, the more stable the empty P–R  $\sigma^*$  orbital and thus becomes a better acceptor of electron density from the metal center. This property is of special importance in the catalytic activity of  $\{Au(PR_3)\}^+$  species; the R substituents on phosphine determine the electrophilicity of the ionic fragments  $\{Au(PR_3)\}^+$  used as catalytic activators of substrates (usually alkynes and allenes).<sup>17</sup> These slight variations influence the way  $\{Au(PR_3)\}^+$  attacks the substrate and stabilized intermediates and thus the outcome of the reaction. Specifically, this is apparent in cationic gold(I) catalysis of the addition of alcohols to alkynes where  $\{Au(PPh_3)\}^+$  was more active than  $\{Au(PEt_3)\}^+$  in this particular type of reaction.<sup>12</sup> This same concept likely influences the binding of the  $\{Au(PR_3)\}^+$

species to biological molecules and influence their overall activity. Gold(I) interactions with biological proteins and peptides can also be described by hard soft acid base theory: a soft metal center like Au(I) binds tightly to soft ligands like sulfur (present in the common amino acid cysteine).



**Scheme 3.1.** Typical synthetic routes for [L-Au(PPh<sub>3</sub>)] complexes.

Numerous [L-Au(PPh<sub>3</sub>)] species have been identified, the simplest being [Cl-Au(PPh<sub>3</sub>)], which is used extensively for the synthesis of new compounds of this type by replacement of the Cl ligand. The stability of the {Au(PPh<sub>3</sub>)}<sup>+</sup> fragment allows for many L donor ligands, the most common types are alkynyl, nitrogen, phosphorus and sulfur containing (**Figure 3.1**) which result in either a neutral or cationic species.<sup>8,23</sup> One advantage of this type of complexes is their relatively simple synthesis and purification often involving [Cl-Au(PPh<sub>3</sub>)] and either (a) the introduction of the protonated ligand and a base or (b) the addition of Ag<sup>+</sup>X<sup>-</sup> to form AgCl precipitate in the presence of the ligand (**Scheme 3.1**). The structural complexity of potential L ligands provides endless possibilities to rationalize the influence (lipophilicity, hydrophilicity, additional drug targets) it has on the efficacy of [L-Au(PPh<sub>3</sub>)] species.

### 3.1.2. Anticancer Activity of Au(I)PPh<sub>3</sub>

Gold complexes have been widely studied for their activity as anticancer agents.<sup>6,14,24,25</sup> It is generally believed that ligand exchange with linear [L-Au(PPh<sub>3</sub>)] complexes with bioactive molecules results in their antitumor activity.<sup>14,16</sup> The exchange of L = N/S-donor ligands occurs rapidly within the blood (20 min) while exchange of the PPh<sub>3</sub> ligand is much slower.<sup>16,26</sup> The weaker bonded ligands in many cases thus influence the kinetic profile of these compounds. Loss of the L ligand in solution with thiols and relevant biological thiols such as glutathione and cysteine is observed and can be easily detected by ESI-MS and NMR spectroscopy.<sup>16,27</sup> In blood serum, gold species readily binds to albumin and other globulins and maintains a sustained presence of the gold drug in cellular matrices for days.<sup>26</sup> This ligand exchange activity with biological molecules is likely what causes the inhibition cytosolic and mitochondrial Thioredoxin reductase (TrxR) inhibition which has been identified as the major cause of apoptotic death of cancer cells by [L-Au(PPh<sub>3</sub>)] complexes.<sup>28–31</sup> Mammalian TrxR isoenzymes are selenoproteins with a redox active selenocysteine residue at their active sites which likely binds strongly to the {Au(PPh<sub>3</sub>)}<sup>+</sup> moiety and interfere severely with cellular redox homeostasis leading to cell death. The facile ligand exchange property of the [L-Au(PPh<sub>3</sub>)] complexes could also involve other targets in cancer cells and the cellular death could be a result of combination of such bindings. Recent studies also indicate that complexes with {Au(PPh<sub>3</sub>)}<sup>+</sup> moiety suppress cancer-promoting inflammation by inhibiting secretion of pro-inflammatory cytokines such as tumor necrosis factor- $\alpha$  (TNF- $\alpha$ ) and interleukin-1 $\beta$  (IL-1 $\beta$ ).<sup>16,32</sup>

Gold phosphine compounds are known to inhibit the ubiquitin-proteasome system (UPS) in cancer cells.<sup>33</sup> Many different cancers, such as colon, prostate and leukemia, rely on the UPS system more heavily than non-cancer cells. Because UPS is involved in many cellular processes, including cell cycle regulation protein degradation, gene expression and DNA repair, inhibition of these by gold compounds induce apoptosis. These types of complexes have been extensively studied for their anticancer activity, but the same interaction of biomolecules with the  $\{\text{Au}(\text{PPh}_3)\}^+$  unit is likely the same for the observed antimicrobial activity.

### 3.1.3 Antibacterial Activity of Au(I)PPh<sub>3</sub>

To date, a far fewer number of complexes of the type  $[\text{L-Au}(\text{PPh}_3)]$  have been studied for their antibacterial effects compared to complexes evaluated for anticancer effect. Nevertheless, several gold complexes (and gold nanoparticles) have exhibited promising antimicrobial activity.<sup>8</sup> Inhibition of biosynthetic pathways such as cell wall synthesis, DNA and protein synthesis as well as inhibition of enzymes such as ATP synthase have been identified as the mechanism(s) of action of these gold species.<sup>34,35</sup> Such participation in multiple pathways could be advantageous when considering bacterial infections by pathogens that have developed resistance to traditional antibiotics.

Among  $[\text{L-Au}(\text{PPh}_3)]$  complexes with L = N- and S-donor ligands, complexes **1-4 (Figure 3.2)** have been shown to exert antimicrobial activity against Gram-positive *Bacillus subtilis* and *Staphylococcus aureus* (MIC 7.9-125  $\mu\text{g/mL}$ ), but no activity was

noted towards Gram-negative *Escherichia coli* and *Pseudomonas aeruginosa*.<sup>15,36</sup> In order to model the interaction of these complexes with cysteine residues present in biological molecules, the ligand exchangeability of **1-4** and other N/S bound  $\{\text{Au}(\text{PPh}_3)\}^+$  species has been examined. The majority of these reactions led to cleavage of the Au–N/S bond rather than the Au–(PPh<sub>3</sub>) bond and it was concluded that the extent of ligand exchangeability of the complexes is correlated to their antibacterial activity. Like **1-4**, compounds **5** and **6** with O- bound ligands (**Figure 3.2**) also show activity towards only Gram-positive bacteria *B. subtilis* and *S. aureus* (MIC's 31.3-62.5  $\mu\text{g/mL}$ ).<sup>37</sup>

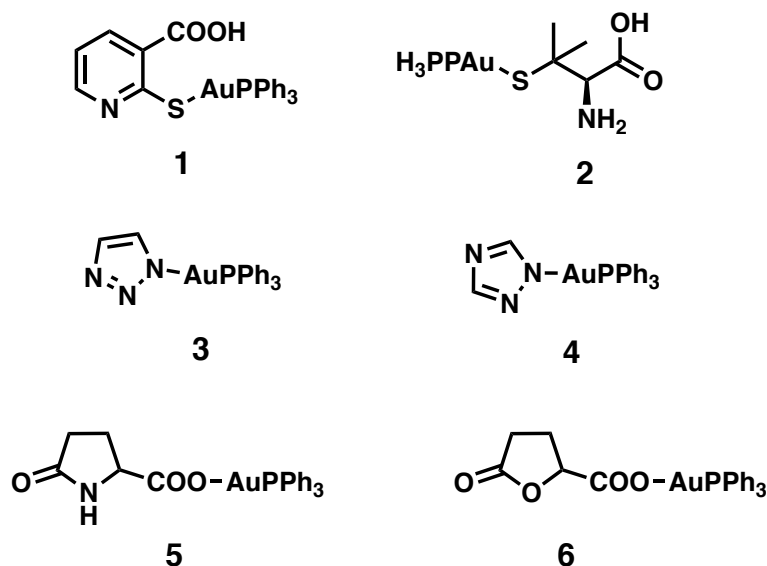


**Figure 3.2.** Complexes of [L-Au(PPh<sub>3</sub>)] that show activity towards Gram-positive bacteria.

Many [L-Au(PPh<sub>3</sub>)] complexes like **7-11** (**Figure 3.3**) show both anticancer and antimicrobial properties. **7** and **8** with alkynyl ligands were evaluated for their activity against methicillin-sensitive and methicillin-resistant *S. aureus* (MRSA) and *E. Coli* showing promising results for Gram-positive MRSA (MIC 2-32 µg/mL) but no activity towards Gram-negative species.<sup>29</sup> As a comparison, the starting material [Cl-Au(PPh<sub>3</sub>)] was also evaluated against these strains and outperformed **7** and **8** with lower MIC's towards MRSA (MIC 1-2 µg/mL) and also showed activity towards Gram-negative *E. coli* (MIC 16-32 µg/mL). This indicated that the replacement of the Cl ligand with the alkynyl species might alter the uptake/activity of these Au complexes, especially considering the permeability of Gram-positive and Gram-negative cell membranes. Complexes **9** and **10**, also showing anticancer activity, were evaluated for their activity towards *S. aureus*, *Staphylococcus epidermitis*, *E. coli* and *P. auriginosa*.<sup>38</sup> All compounds showed potent activity towards Gram-positive species (MIC 1.3-19.1 µM) and increased activity compared to [Cl-Au(PPh<sub>3</sub>)] reference compounds but no activity towards Gram-negative bacteria. Interestingly, the analogous {Au(PEt<sub>3</sub>)}<sup>+</sup> compounds of **9** and **10** performed slightly better. Complex **11** also showed potent antibacterial activity (MIC 8-16 µg/mL) particularly against Gram-positive bacteria *S. aureus*, multidrug-resistant (MDR) *S. aureus*, *Enterococcus faecalis*, *Bacillus cereus*, *S. epidermidis*, and MDR *S. epidermitis*.<sup>39</sup> Bactericidal activity of **11** was also observed towards the Gram-negative *E. coli* and MDR *Kiebsiella oxytoca* (32 and 16 µg/mL respectively).

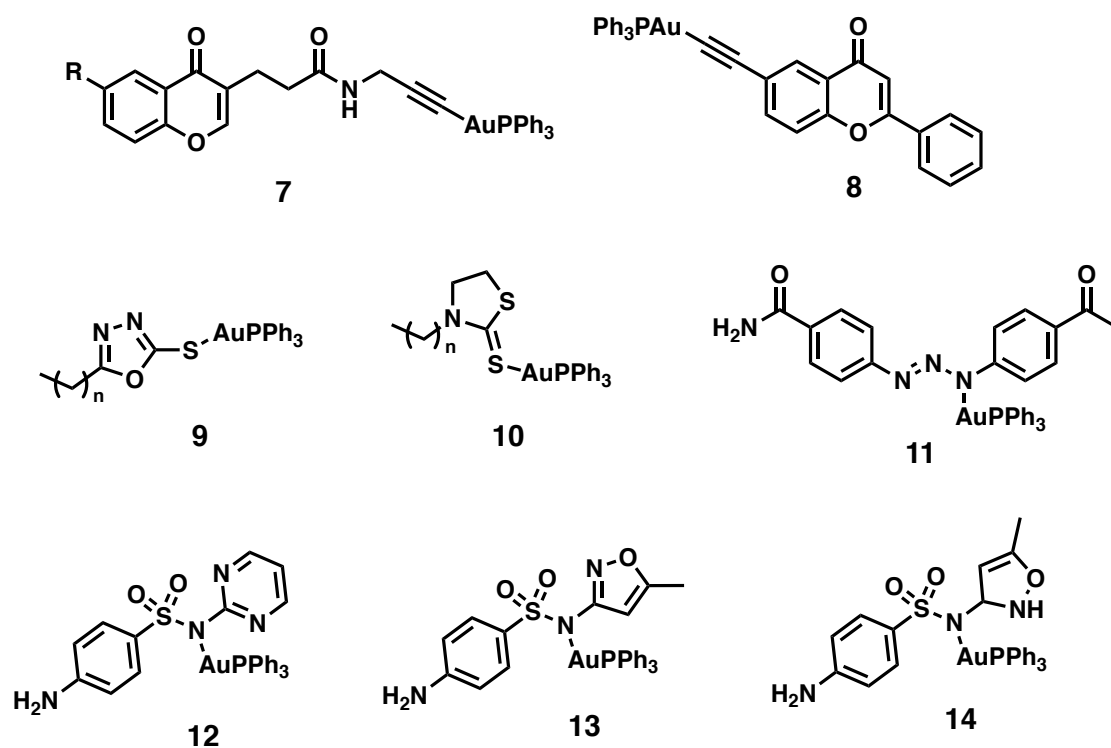


**Figure 3.3.** Antibacterial Au(I) complexes.

Sulfonamide compounds **12-14** (Figure 3.3) are significant antibacterial and antibiofilm agents against *P. aeruginosa* with MIC values ranging from 1-8 µg/mL.<sup>40</sup> *P. aeruginosa* is an opportunistic Gram-negative pathogen and can be difficult to treat due to the rapid formation of a biofilm.<sup>41</sup> To observe the antibiofilm behavior, complexes **12-14** were subjected to swarming motility assay and all showed significant decrease in the biofilm growth compared to the control. This was also confirmed by confocal microscopy of the exopolysaccharides which make up a majority of the mass of biofilms. Interestingly, compounds with bimetallic gold did not perform as well. Molecular docking studies showed that all complexes are able to interact strongly with the LasR protein (related to the quorum sensing and biofilm formation in *P.*

*aeruginosa*) and could be the reason behind the antibiofilm activity. In a different study by the same group, **12-14** showed similar antibacterial and antibiofilm activity towards MRSA, but no toxicity towards *Caenorhabditis elegans* indicating the compounds are well tolerated.<sup>42</sup> All of these results imply that these sulfonamide  $\{\text{Au}(\text{PPh}_3)\}^+$  complexes are promising antibacterial drugs.

While the exact mechanism of action  $[\text{L-Au}(\text{PPh}_3)]$  species still remains widely unknown, research suggests much that like in cancer, there are multiple mechanisms of action that could benefit treatment of MDR pathogens. The majority of the  $[\text{L-Au}(\text{PPh}_3)]$  complexes show activity towards Gram-positive species although a few are also active towards Gram-negative bacteria. This difference in activity could be due to the low permeability of the two-membrane cell wall of the Gram-negative bacteria which is recognized as the major obstacle in the development of antibiotics that are effective towards such species.<sup>43</sup> Close scrutiny of the antibacterial complexes reveals that the activity towards Gram-negative bacteria could be related to the presence of a  $[\text{N-Au}(\text{PPh}_3)]$  core (compounds **11-14**) which could ligand exchange more effectively or rapidly in order to exert drug action. However, further investigation is necessary because complexes **3** and **4**, also containing  $[\text{N-Au}(\text{PPh}_3)]$  cores, were not active towards Gram-negative bacteria.

#### 3.1.4 Antimycobacterial Activity of $\text{Au}(\text{I})\text{PPh}_3$

*M. tuberculosis*, the infectious pathogen responsible for TB is known to be particularly difficult to treat and often the treatment involves three or more drugs in



combination. Unfortunately, resistance to such treatment is emerging in certain populations. Robert Koch discovered that gold(I)cyanide was effective towards *M. tuberculosis* in the 1890s<sup>2</sup> and since then other gold complexes have shown potent activity towards the pathogen. Only a few compounds specifically with an  $\{\text{Au}(\text{PPh}_3)\}^+$  moiety have been evaluated for their antimycobacterial activity. The cationic compound **15** (**Figure 3.4**) with an overall  $2^+$  charge and acridine ligand was evaluated for its effect on *M. tuberculosis* and was proved to be a strong inhibitor.<sup>44</sup> Both **15** and the analogous  $\{\text{Au}(\text{PEt}_3)\}^+$  complex were tested ( $\text{IC}_{90} = 1.204$  and  $1.050 \mu\text{M}$ ) and while the  $\{\text{Au}(\text{PEt}_3)\}^+$  complex was slightly more active, **15** was more selective towards *M. tuberculosis* than Vero cells (selectivity index,  $\text{SI} = 7.310$  and  $4.983$  respectively). Complexes **16** and **17** among others (**Figure 3.4**), with ligands derived from carbohydrates, were also evaluated for their antitubercular activity.<sup>45</sup> Interestingly, **16** was more active than the analogous  $\{\text{Au}(\text{PEt}_3)\}^+$  complex, but the opposite was found for complex **17** and its  $\{\text{Au}(\text{PEt}_3)\}^+$  derivative. **16** was the most active in all of the Au compounds studied in this report ( $\text{MIC}_{90} = 2.50 \mu\text{g/mL}$ ) including the  $[\text{Cl-Au}(\text{PPh}_3)]$  parent compound ( $\text{MIC}_{90} = 25.00 \mu\text{g/mL}$ ).

Studies with **13** and **18** (**Figures 3.3** and **3.4**) also showed activity towards species of mycobacterium.<sup>46</sup> First the compounds were tested against *Mycobacterium smegmatis*, the safer and similar model organism often used prior to working with *M. tuberculosis*, and showed potent activity ( $\text{MICs}$  of  $2.44$  and  $4.88 \mu\text{g/mL}$  for **13** and **18** respectively). Next, the possible synergy between these complexes and trimethoprim,

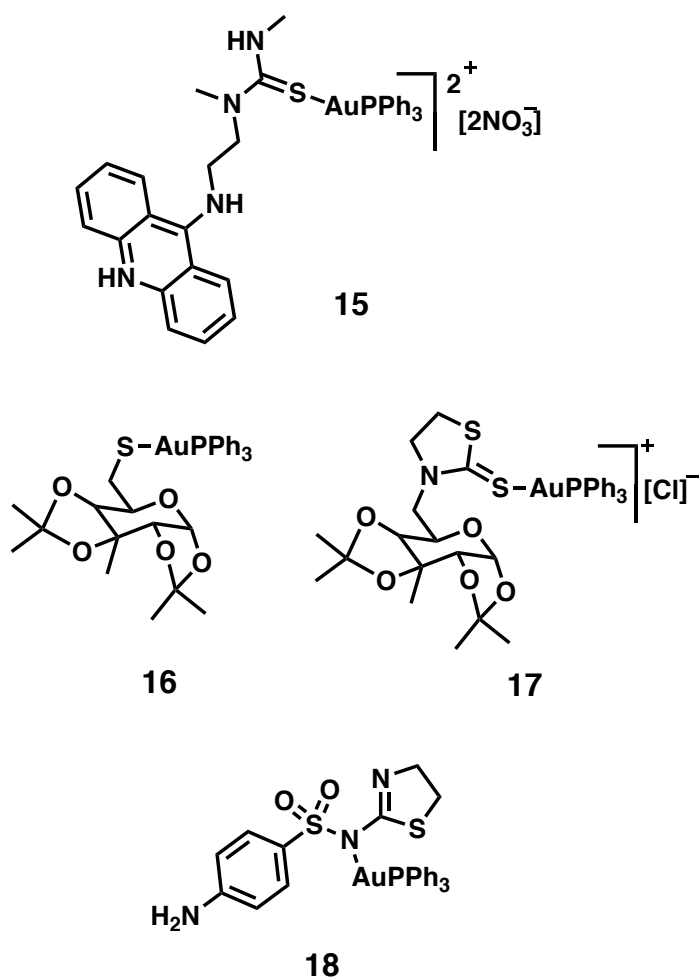


**Figure 3.4.** Complexes with antimycobacterial action.

an antibiotic, was assessed revealing synergy with **18** and only an additive effect with **13**. An added effect was observed with the starting material  $[\text{Cl}-\text{Au}(\text{PPh}_3)]$ , indicating that the synergy in **18** likely was resulting from the ligand although the full mechanism and role of  $\{\text{Au}(\text{PPh}_3)\}^+$  is unknown. The synergy between trimethoprim and **18** was also observed with *M. tuberculosis* providing promising results for future studies.

Compound **12** and **13** (**Figure 3.3**) in a different study were also assessed for their activity and synergistic activity with trimethoprim in different species of *Mycobacterium* (*M. abscessus*, *M. Forticum* and *M. massiliense*) responsible for nosocomial infections that are typically not transmitted human to human but rather from the environment.<sup>47</sup> Significant improvement in activity was observed upon conjugation to a  $\{\text{Au}(\text{PPh}_3)\}^+$  center and synergy between **12** or **13** and trimethoprim was observed in most cases with these *Mycobacterium* species. Multidrug-resistant *M. tuberculosis* and other species are an emerging problem and results these studies indicate that  $\{\text{Au}(\text{PPh}_3)\}^+$  species may be a useful tool in the development of new TB drugs. *Mycobacterium* are particularly robust due to their waxy hydrophobic membrane (unlike Gram-negative and Gram-positive bacterial species) and the  $\{\text{Au}(\text{PPh}_3)\}^+$  unit may provide an increase in lipophilicity to allow more of the unit itself or the drug ligand into the cytosol/membrane to exert increased drug action. At present, few and differing results on this type of complexes and their activity towards *Mycobacteria* in general have been reported; further discoveries in this area could provide valuable insight.

### **3.2 Trackable Antimicrobial Gold Triphenylphosphine Complexes with Aryl**

#### **Benzothiazoles**

Gold triphenylphosphine species have shown their prevalence in many areas of medicinal chemistry and as highlighted previously for their general potent antibacterial

activity. Our group has explored heavy metal benzothiazole complexes for some time and in Chapter 2 the antibacterial activity of silver complexes with these ligands was described and showed promising results. These results and the success shown by gold complexes as antimicrobial agents prompted us to further pursue potential  $\{\text{Au}(\text{PPh}_3)\}^+$  complexes with the same ligands pbt and qbt. Benzothiazoles, a class of antibacterial and antifungal drugs, as ligands could offer an additional antibacterial moiety to aid in the overall action.<sup>48,49</sup> These ligand molecules also offer multiple binding sites for metal centers (typically N<sup>2</sup> seen with Ag, Re and Mn) and we were interested to see if that was the case for gold(I), a soft metal center known to bind sulfur well. The synthesis, characterization and antimicrobial activity of gold(I) complexes with trifluoromethanesulfonate anions (OTf) namely,  $[(\text{pbt})\text{Au}(\text{PPh}_3)](\text{OTf})$  (AuPpbt) and  $[(\text{qbt})\text{Au}(\text{PPh}_3)](\text{OTf})$  (AuPqbt) (**Figure 3.5**) are described hereafter.

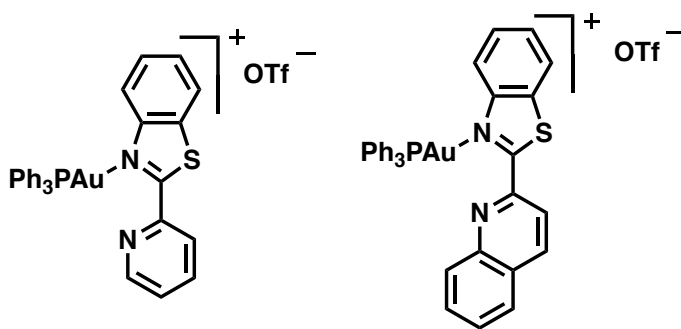
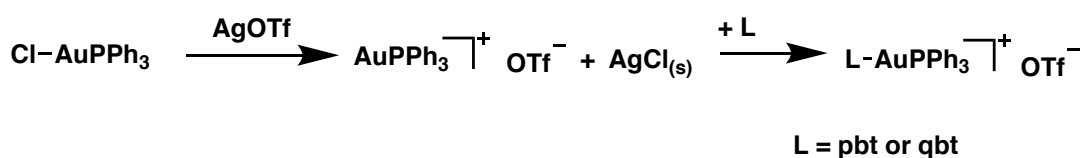


**Figure 3.5.** The complexes AuPpbt (left) and AuPqbt (right) studied in this chapter.

### 3.2.1 Synthesis and Spectroscopy

Complexes AuPpbt and AuPqbt were synthesized by the addition of 1.05 eq of

AgOTf to the widely used starting material [ClAu(PPh<sub>3</sub>)] to afford the highly reactive ion-pair {Au(PPh<sub>3</sub>)}<sup>+</sup> OTf<sup>-</sup>. This species is known to exist on its own, but is relatively unstable when isolated in solid form.<sup>50</sup> Further filtration of the AgCl solid formed and introduction of the pbt or qbt ligand resulted in isolation of AuPpbt and AuPqbt as white solids in good yield (**Scheme 3.2**).



**Scheme 3.2.** Synthetic Route for AuPpbt and AuPqbt.

The IR spectra of AuPpbt and AuPqbt (**Figure 3.6**) in both show an intense band centered around 1265 cm<sup>-1</sup> indicating the presence of the OTf counterion. NMR spectra of the complexes in CDCl<sub>3</sub> at 298K were also recorded (**Figure 3.7** and **3.8**). In both complexes the shifting of the protons of the pbt and qbt ligand are observed as expected upon conjugation to the Au(I) center. The large triphenyl phosphine multiplet is also observed in around 7.6 ppm in both gold species spectra and overlaps with some protons on the benzothiazole ligands. Other cationic {Au(PPh<sub>3</sub>)}<sup>+</sup> species with pyridyl benzimidazole as ligands have shown broad poorly resolved H-MNR signals suggesting a fluxionality between the two iminic nitrogen coordination sites,<sup>51</sup> this seems not to be the case with AuPpbt and AuPqbt. Proton signals, though slightly broadened compared to the free ligand, are still recognizable by their multiplicity and thus in solution are likely bound and remain solely bound to the nitrogen of the

benzothiazole in both complexes.

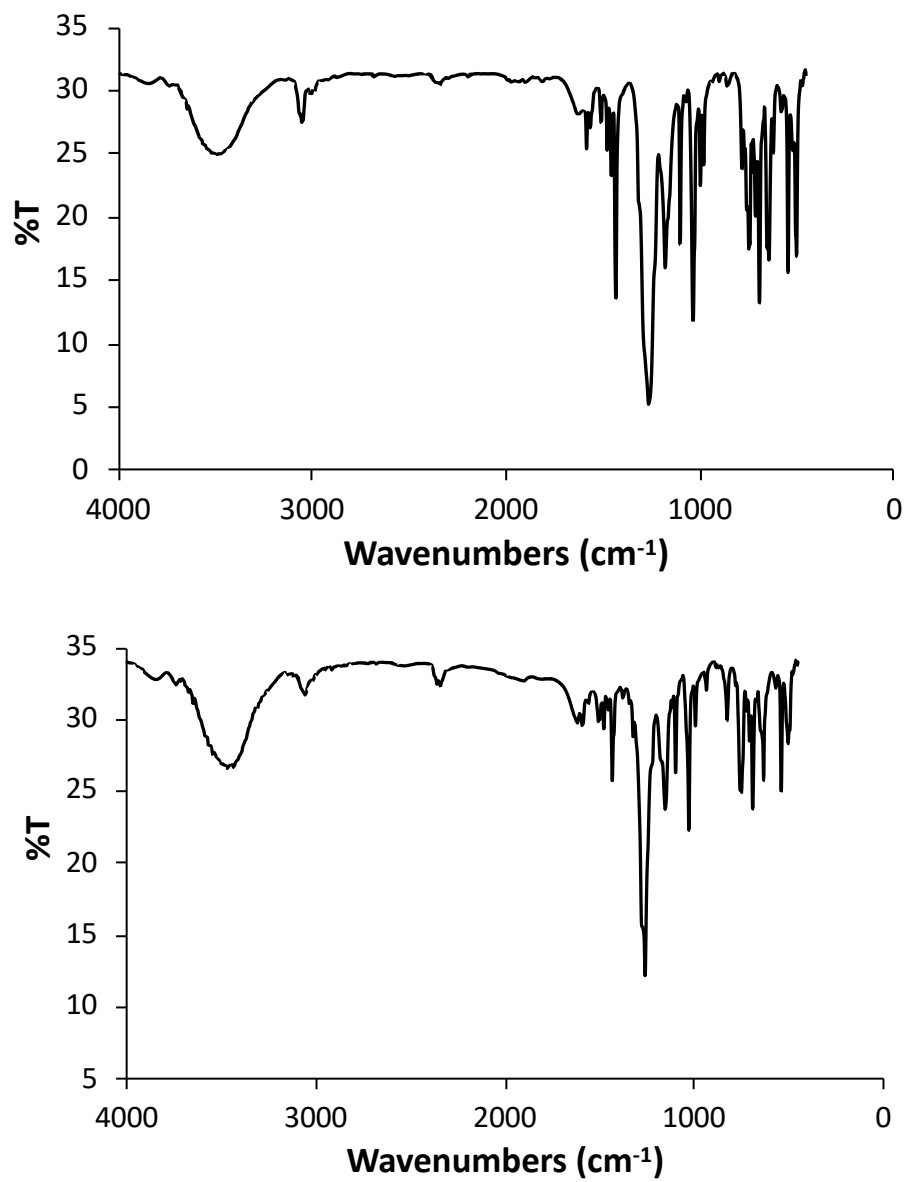


**Figure 3.6.** FT-IR Spectra of AuPpbt (top) and AuPqbt (bottom) in KBr.

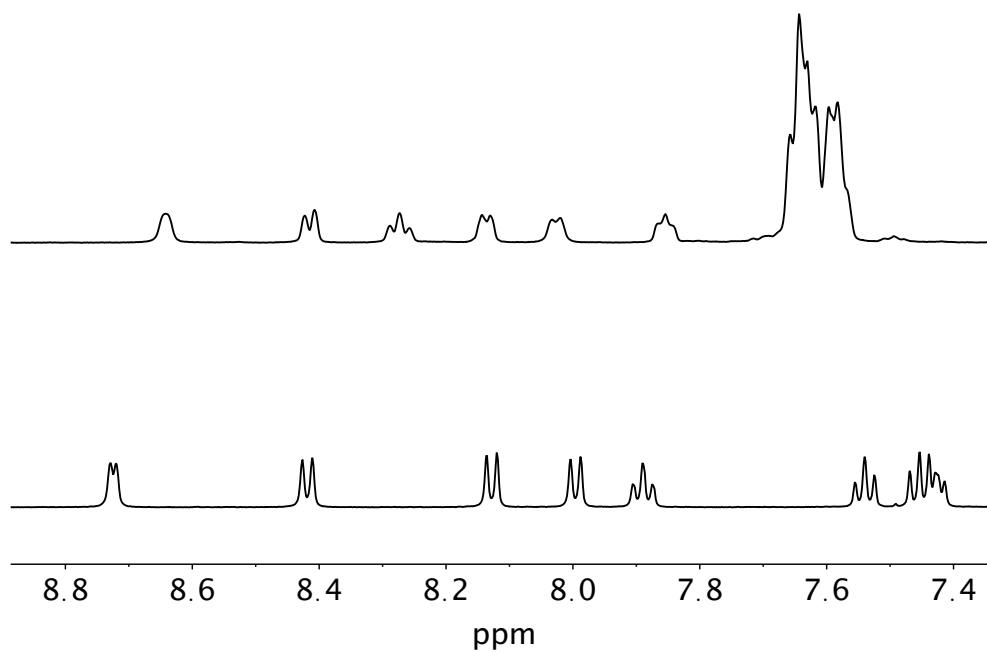


**Figure 3.7.** NMR spectra of AuPpbt (top) and pbt (bottom) in  $\text{CDCl}_3$  at 298K.

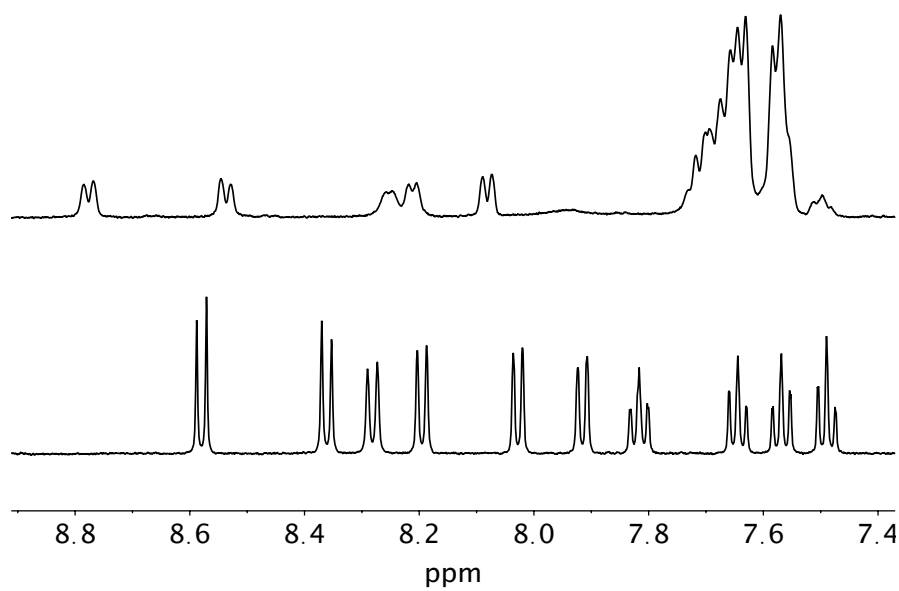


**Figure 3.8.** NMR spectra of AuPqbt (top) and qbt (bottom) in  $\text{CDCl}_3$  at 298K.

The UV-vis absorbance spectra of AuPpbt and AuPqbt and the free ligands pbt and qbt were taken in DCM at the 20  $\mu\text{M}$  of each (**Figure 3.9**). The  $\lambda_{\text{max}}$  of both gold(I) complexes shift approximately 20nm into the red upon compared to the free ligands and molar absorptivity remains roughly comparable indicating the transitions responsible are likely mostly from the ligands and influenced slightly by coordination to the Au(I) metal center.

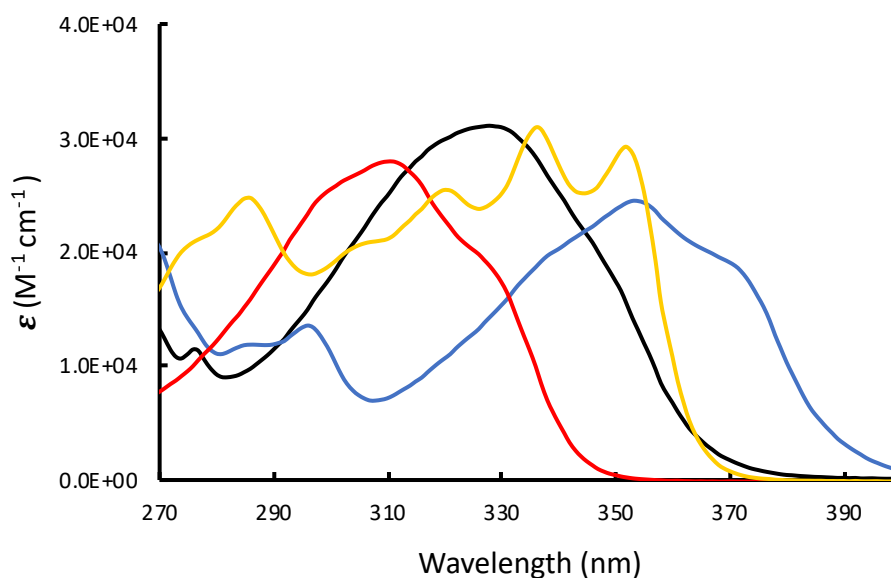


**Figure 3.9.** Absorption spectra of AuPpbt (black), AuPqbt (blue), pbt (red) and qbt (yellow) in DCM.

The emission spectra of AuPpbt, AuPqbt, pbt and qbt were also observed in DCM at the 20  $\mu\text{M}$  of each with  $\lambda_{\text{ex}}$  at 330, 350, 310 and 335 nm respectively. (**Figure 3.10**). The wavelengths of emission for AuPpbt and AuPqbt are 380 nm and 400 nm



respectively which are the wavelength of emission for the corresponding free ligands, however significant luminescence quenching is observed for the gold(I) complexes. A close scrutiny of the literature and previous results from Chapter 2 reveal that both the singlet and triplet excited states of Ag(I) and Au(I) complexes of similar coordination structures essentially possess ligand-centered  $\pi \pi^*$  character with negligible metal-to-ligand charge transfer (MLCT) contribution, and the excited triplet state mostly decay through non-radiative channels.<sup>52,53</sup> These characteristics presumably lead to significant luminescence quenching observed with AuPpbt and AuPqbt compared to their highly fluorescent free ligands.

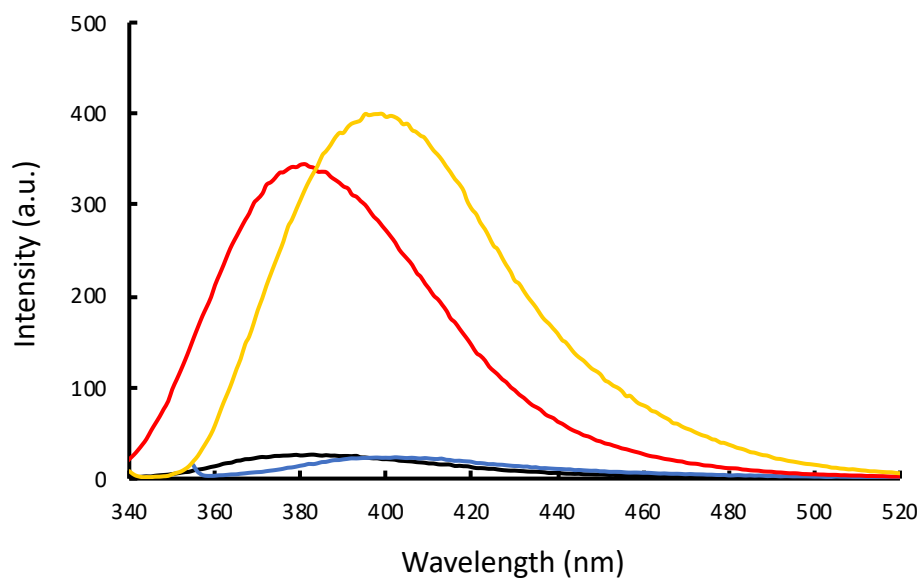


**Figure 3.10.** Emission spectra of AuPpbt (black), AuPqbt (blue), pbt (red) and qbt (yellow) in DCM ( $\lambda_{\text{ex}}$  at 330, 350, 310 and 335 nm respectively).

### 3.2.2 Crystal Structure and Binding Mode Discussion.

Single crystal analysis reveals that complexes AuPpbt and AuPqbt are isostructural with respect to coordination at the Au center; in both cases the Au center resides in a linear N-Au-P coordination environment. For AuPpbt, the asymmetric unit contains two crystallographically independent molecules. The perspective view with atom labeling scheme for the two structures are shown in **Figures 3.11** and bond distances and angles are in **Table 3.1** (note that AuPpbt crystallized with 0.5 eq of CH<sub>2</sub>Cl<sub>2</sub> and is further discussed in the experimental section). The N (benzothiazole)-Au-P angles in complexes AuPpbt and AuPqbt are 164.88(17) and 161.20(15)° respectively. Steric bulk of the qbt ligand leads to lengthening of both the average Au-N(benzothiazole) distance (2.114(5) Å for AuPpbt vs. 2.218(5) Å for AuPqbt) and the average Au-P distance (2.224(14) for AuPpbt vs. 2.303(18) Å for AuPqbt) in complex AuPqbt. Although Cambridge structural database revealed several crystal structures with N-Au-P coordination mode, a representative structurally analogous complex namely, [(py)Au (PPh<sub>3</sub>)]BF<sub>4</sub><sup>54</sup> (where py = pyridine), was chosen to compare its crucial metric parameters with those of the present two complexes. In [(py)Au(PPh<sub>3</sub>)]BF<sub>4</sub>, the N(py)-Au and Au-P bond lengths are 2.073(3) Å and 2.2364(8) Å respectively. These distances are comparable to those noted for AuPpbt and AuPqbt. Interestingly, the N-Au-P angle in [(py)Au (PPh<sub>3</sub>)]BF<sub>4</sub> is 178.09(8)°, closer to a linear geometry, unlike AuPpbt and AuPqbt which reflects the steric bulk of the pbt/qbt ligands compared to the relatively small py. In the two structures, both pbt and qbt exhibit excellent planarity with mean deviations of 0.024(3) and 0.090(4) Å respectively.

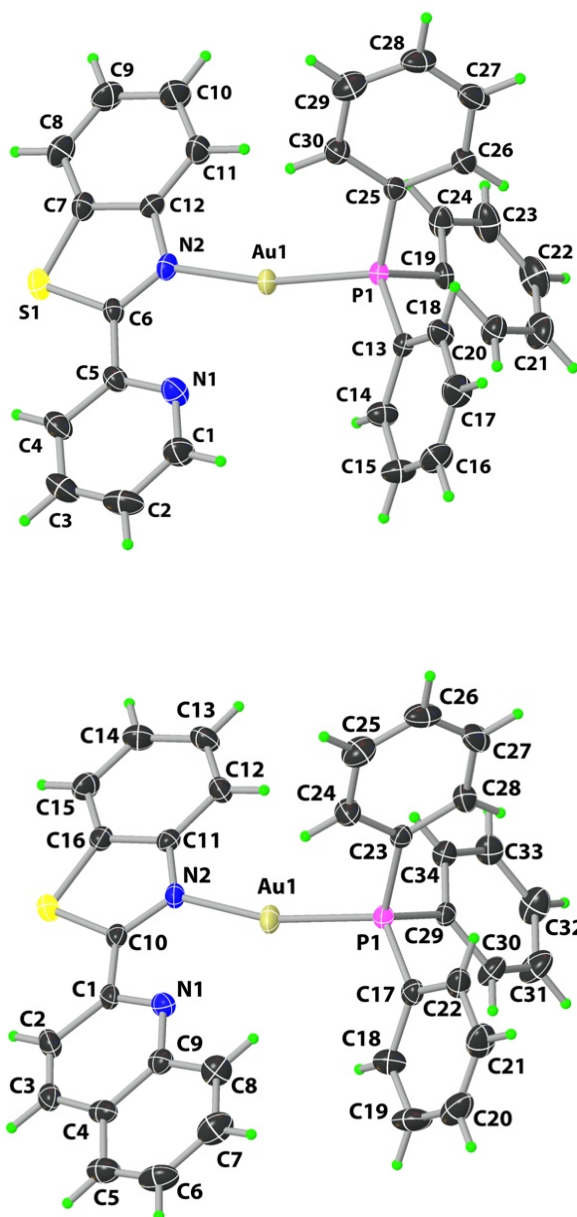


**Figure 3.11.** Perspective view of the cation of complex AuPpbt (top) and AuPqbt (bottom) with the atom-labeling scheme. The thermal ellipsoids are shown at 50% probability level. Only one of the two crystallographically independent molecules in the asymmetric unit is shown for AuPpbt.

**Table 3.1.** Selected bond distances (Å) and angles (°) for complex AuPpbt · CH<sub>2</sub>Cl<sub>2</sub> and AuPqbt.

<b>Complex AuPpbt</b>			
<b>Molecule 1</b>			
Au(1)-P(1)	2.227(13)	Au(1)-N(2)	2.116(4)
P(1)-C(13)	1.810(6)	P(1)-C(19)	1.814(6)
P(1)-C(25)	1.810(6)	N(2)-C(6)	1.292(7)
N(2)-C(12)	1.400(8)	C(6)-S(1)	1.716(6)
P(1)-Au(1)-N(2)	166.50(15)	Au(1)-P(1)-C(13)	113.77(19)
Au(1)-P(1)-C(19)	110.91(18)	Au(1)-P(1)-C(25)	112.66(19)
C(13)-P(1)-C(25)	107.5(3)	Au(1)-N(2)-C(6)	125.8(4)
C(13)-P(1)-C(19)	106.4(3)	C(6)-N(2)-C(12)	111.9(5)
Au(1)-N(2)-C(12)	122.3(4)	C(6)-S(1)-C(7)	90.4 (3)
<b>Molecule 2</b>			
Au(2)-P(2)	2.221(14)	Au(2)-N(4)	2.112(6)
P(2)-C(29)	1.816(6)	P(2)-C(43)	1.812(6)
P(2)-C(55)	1.807(6)	N(4)-C(36)	1.319(9)
N(4)-C(42)	1.378(10)	C(36)-S(2)	1.703(7)
P(2)-Au(2)-N(4)	163.26(19)	Au(2)-P(2)-C(49)	113.5(2)
Au(2)-P(2)-C(42)	110.08(19)	Au(2)-P(2)-C(55)	113.7(2)
C(55)-P(2)-C(49)	107.9(3)	Au(2)-N(4)-C(36)	124.6(6)
C(43)-P(2)-C(49)	106.3(3)	C(36)-N(4)-C(42)	112.1(6)
Au(2)-N(4)-C(42)	123.0(5)	C(37)-S(2)-C(36)	90.9 (4)
<b>Complex AuPqbt</b>			
Au-P	2.303(18)	Au-N(2)	2.218(5)
P-C(17)	1.881(7)	P-C(29)	1.877(7)
P-C(23)	1.873(7)	N(2)-C(10)	1.359(8)
N(2)-C(11)	1.444(8)	C(10)-S	1.789(7)
P-Au-N(2)	161.20(15)	Au-P-C(17)	117.0(2)
Au-P-C(29)	110.2(2)	Au-P-C(23)	111.6(2)
C(17)-P-C(23)	105.5(3)	Au-N(2)-C(10)	121.9(4)
C(17)-P-C(29)	105.7(3)	C(10)-N(2)-C(11)	112.6(5)
Au-N(2)-C(11)	125.5(4)	C(10)-S-C(16)	91.1(3)

The extended structure of AuPpbt (**Figure 3.12**) reveals few non classical hydrogen bonding contacts [C24-H24---O3, with H---O, 2.615 Å<sup>i</sup>; C28-H28---O2, with H---O, 2.595 Å<sup>ii</sup>; C44-H44---O4, with H---O, 2.510 Å<sup>iii</sup>; C45-H45---O5, with H---O, 2.562 Å<sup>iii</sup>; C41-H41---O4, with H---O, 2.551 Å<sup>iii</sup>; symmetry codes: (i) x, y+1, z; (ii)-x+1/2, y+1/2, z; (iii) x, y, z]. Analysis of the molecular packing for AuPqbt (**Figure 3.12**) also reveals few non-classical hydrogen bonding interactions [C3-H3---O1, with H---O, 2.632 Å<sup>i</sup>, C27-H27---O3, with H---O, 2.589 Å<sup>ii</sup>, S1---O2, 3.307 Å<sup>iii</sup>, symmetry codes: (i) x, y, z; (ii) -x+1/2, -y+1, z+1/2; (iii) -x+1/2, y+1/2, z]. Between the two structures only complex AuPpbt divulged weak offset intermolecular  $\pi$  -  $\pi$  stacking interaction as depicted in **Figure 3.13**. This representation also revealed a weak intermolecular C---S non-bonding contacts (3.416(4) Å) between the two adjacent molecules. The centroid-to-centroid distance between the pyridine ring and the benzene ring of benzothiazole motif is found to be 3.816 (4) Å consistent with weak  $\pi$  -stacking interaction.

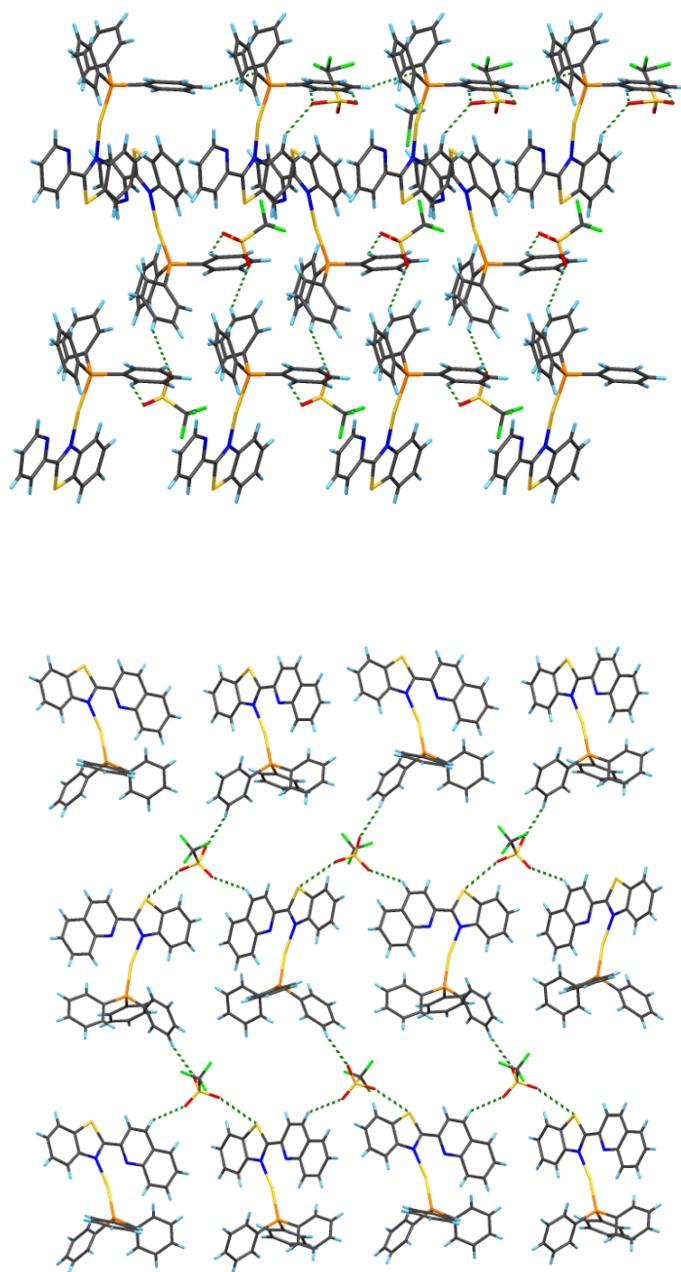


**Figure 3.12.** The packing patterns for complexes AuPpbt (top) and AuPqbt (bottom) along  $a$  axis.

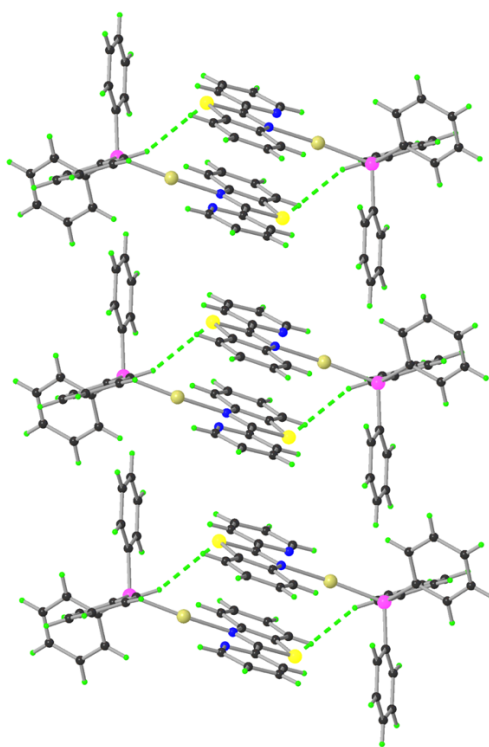


**Figure 3.13.** Representation of intermolecular  $\pi$  -  $\pi$  stacking and C---S non-bonded interactions in complex AuPpbt.

The crystal structures of AuPpbt and AuPqbt reveal different binding modes than typically seen with metal centers. 2-aryl or 2-pyridyl substituted benzothiazole type ligands (like pbt and qbt) typically exhibit bidentate binding modes when coordinated to  $d^{10}$  metal center. This can occur through the N-atom of the benzothiazole moiety and either the N-atom of the 2-pyridyl fragment<sup>52</sup> (Agpbt/Agqbt in Chapter 2) or C-atom of the 2-aryl portion<sup>55</sup> of the ligand (**Figure 3.14a** and **3.14b** respectively). Similar N,N-binding of pbt and qbt has been noted in complexes with low-spin  $d^6$  metal centers such as Mn(I) and Re(I).<sup>56,57</sup> In all cases, the ring S-atom does not coordinate.

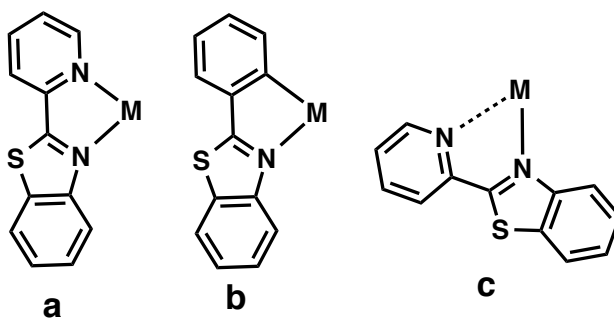


**Figure 3.14.** Different modes of binding of pbt and aryl-benzothiazole.

When this type of ligand was employed for coordination to Au(I) centers in this research, the ligands failed to coordinate as bidentate ligands. Attempts to coordinate pbt and qbt to Au(I) center invariably afforded linear 2-coordinated complexes AuPpbt and AuPqbt, as expected with typical geometries of Au(I) complexes. Despite strong affinity of Au(I) to S-donors, both ligands are coordinated to the metal center through the N-atom of the benzothiazole (N(2)) moiety. This is in agreement with results from similar studies exploring the binding modes of Au(I) to ligands with electronically similar N and S (or N) donor atoms.<sup>58,59</sup> Mono-substituted binding mode of these types of ligands (leading to linear complexes) also arises from steric hindrance arising from the ligand itself.<sup>53</sup> Both the present complexes deviate from linearity; the P-Au-N angle of AuPpbt and AuPqbt are 166.50° and 161.22° respectively (**Figures 3.11** and **Table 3.1**). Also, the P-Au-N angle of AuPqbt with sterically more encumbered qbt ligand deviates more from linearity compared to AuPpbt.

It is important to note that in AuPpbt and AuPqbt, the N atom of the pyridine/quinolyl moiety (N(1)) is facing the metal center, but not bound (**Figure 3.14c**). Results of previous studies on the structures and ground state optimized



geometries of the free ligands<sup>52</sup> (from Chapter 2) have demonstrated that although the structure with the pyridyl-N and benzothiazole-N atom *anti* to each other is lower in energy, in all cases both pbt and qbt bind metal ions as the N-N *syn* structural isomer. The pyridine fragment in these cases rotates to present its N center to be available for coordination in a N-N *syn* fashion (**Figure 3.14a**). In AuPpbt and AuPqbt, this rotation of the aryl ring also occurs, but the pyridyl-N or the quinolyl-N does not bind to the metal center (**Figure 3.14c**). However, in both cases, significant interactions between this N-atom and the Au(I) center is observed in AuPpbt [Au(1)– N(1), 2.713 Å] and AuPqbt [Au(1)– N(10), 2.710 Å] (**Figure 3.14c**, dashed line) which is in agreement with other gold(I) compounds of similar structure.<sup>59</sup>

### 3.2.3 Antibacterial Activity and Interactions

Antibacterial studies were done using the skin and soft tissue infection (SSTI) model previously developed in this laboratory.<sup>60</sup> This model mimics the gradual penetration of bacteria deeper into the skin using a two-layer agar system which has a soft, evenly dispersed bacterial lawn on the top and a nutrient-rich bottom layer. The gradient causes the bacteria to slowly migrate from the thin top layer to the nutrient-rich bottom layer much like the way an infection of the skin would proceed.

Both complexes and the corresponding ligands were tested *in vitro* for their bactericidal activity against the Gram-negative bacterium *A. baumannii*. This bacterium has shown multi-drug resistance in hospitals around the world and at present poses serious threat to human health. In addition to resistance traits carried on mobile

genetic elements, *A. baumannii* also forms biofilms rapidly as defensive barriers. In addition, *A. baumannii* infections are a primary concern to military personnel injured by gun fire and improvised explosive devices (IEDs) in the battlefields of Afghanistan and Iraq.<sup>61</sup> With a limited pipeline of new antibiotics being developed for Gram-negative bacteria, new therapies are in high demand, especially for this pathogen. In the present work, a gold control (the neutral starting material ClAu(PPh<sub>3</sub>)) was also used to show how the ligands and the cationic nature of AuPpbt and AuPqbt affect the ability of the Au(I) complexes to interact with the bacterial colonies. KBr pellets of similar weights containing 0.3 mol % of compounds were placed on the top of the bacterial lawn and incubated at 37 °C for 18 h. Circular zones of clearing were seen around the pellets containing AuPpbt and AuPqbt, but not around the pellets containing KBr, pbt, qbt or ClAu(PPh<sub>3</sub>) (**Figure 3.15**). These results indicate that the two Au(I) complexes are better able to migrate and interfere with a large area of infection while the neutral gold compound exhibits no eradication of the bacteria on the SSTI model.

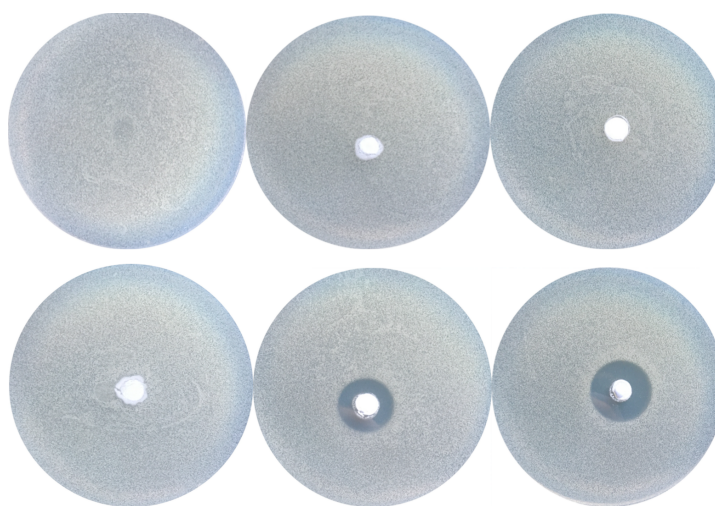


**Figure 3.15.** Bacterial lawns after 18 h incubation with KBr pellets of KBr, pbt and qbt (top panel, left to right) and ClAu(PPh<sub>3</sub>), AuPpbt and AuPqbt (bottom panel, left to right)

The antimicrobial activity of various drugs is highly dependent on their ability to permeate through the cell wall and interfere with cellular pathways.<sup>62</sup> Most bacteria possess a slightly electronegative surface potential which allows cationic complexes to associate more readily with the bacterial membrane. If the drug molecules can easily form bonds with biomolecules either on the membrane or in the cytosol, the efficacy of the drug action is enhanced. For gold compounds this implies that the nature of the ligands bound to the Au(I) center, not just the amount of Au(I) present, plays an important role in their activity.<sup>63</sup> The neutral and very stable compound ClAu(PPh<sub>3</sub>) therefore exhibits no activity against *A. baumannii* using the SSTI model while the more ligand exchangeable and cationic complexes AuPpbt and AuPqbt are very

effective in eradicating bacterial loads throughout the entire “kill zone” of the 4 mm thick SSTI disk.

It is important to note that although AuPpbt and AuPqbt exhibited high level of antibacterial activity (**Figure 3.15**), no reduction of bacterial load was observed with ClAu(PPh<sub>3</sub>). Because pbt and qbt by themselves showed marginal antibacterial effect for *A. baumannii*, it is evident that effective interaction between the cationic gold complexes and bacterial cell membrane is the major cause of their bactericidal activity. The solubility of the tested species could also play a role, the drug must travel through the aqueous agar plate in order for a “kill zone” to be observed. The cationic species AuPpbt and AuPqbt may be able to migrate farther into the agar layer than the neutral ClAu(PPh<sub>3</sub>). Upon deligation of pbt or qbt from the metal center, a step that delivers these antibacterials to the cytosol, the highly reactive Ph<sub>3</sub>PAu<sup>+</sup>.OTf<sup>-</sup> species could also exert strong antibiotic action through binding to membrane and/or cytosolic molecules. In order to check whether AuPpbt and AuPqbt can bind to cellular SH-containing proteins and peptides (such as glutathione) present in the cytosol of the bacteria, AuPpbt was treated with 1.2 equiv of *p*-trifluoromethyl-benzene thiol (F<sub>3</sub>CC<sub>6</sub>H<sub>4</sub>SH) and the reaction was followed by both <sup>19</sup>F and <sup>1</sup>H NMR spectroscopy (in CDCl<sub>3</sub>). Interestingly, addition of the thiol to the Au(I) complex generated a new <sup>19</sup>F-peak at ~0.5 ppm downfield (with respect to F<sub>3</sub>CC<sub>6</sub>H<sub>4</sub>SH) indicating binding of the thiol to the Ph<sub>3</sub>PAu<sup>+</sup> unit (**Figure 3.16**). The <sup>1</sup>H NMR spectrum of the reaction mixture clearly showed loss of pbt from the Au(I) center upon addition of the thiol. In an independent experiment, PPh<sub>3</sub>Au–SC<sub>6</sub>H<sub>4</sub>CF<sub>3</sub> was synthesized by reacting ClAu(PPh<sub>3</sub>) with

$\text{CF}_3\text{C}_6\text{H}_4\text{S}^-$  (prepared from  $\text{CF}_3\text{C}_6\text{H}_4\text{SH}$  and  $\text{Et}_3\text{N}$ ). The  $^{19}\text{F}$  NMR spectrum of  $(\text{PPh}_3)\text{Au}-\text{SC}_6\text{H}_4\text{CF}_3$  clearly confirmed its formation in the reaction between AuPpbt and  $\text{F}_3\text{CC}_6\text{H}_4\text{SH}$  (**Figure 3.16**). In order to confirm that the  $\text{PPh}_3$  ligand is not deligated in such reactions of AuPpbt with SH-containing biomolecules, we allowed AuPpbt to react with N-acetyl-L-cysteine methyl ester ( $\text{HSC}_6\text{H}_{10}\text{NO}_3$ ) in  $\text{CDCl}_3$ . The  $^{31}\text{P}$  NMR spectrum of the reaction mixture clearly showed that the cysteine ester replaced pbt to form  $(\text{PPh}_3)\text{Au}-\text{SC}_6\text{H}_{10}\text{NO}_3$  (**Figure 3.17**). Complete absence of  $^{31}\text{P}$  resonance of free  $\text{PPh}_3$  in such reaction mixture confirms that no  $\text{PPh}_3$  loss occurs upon reaction of AuPpbt with the S-containing amino acid.

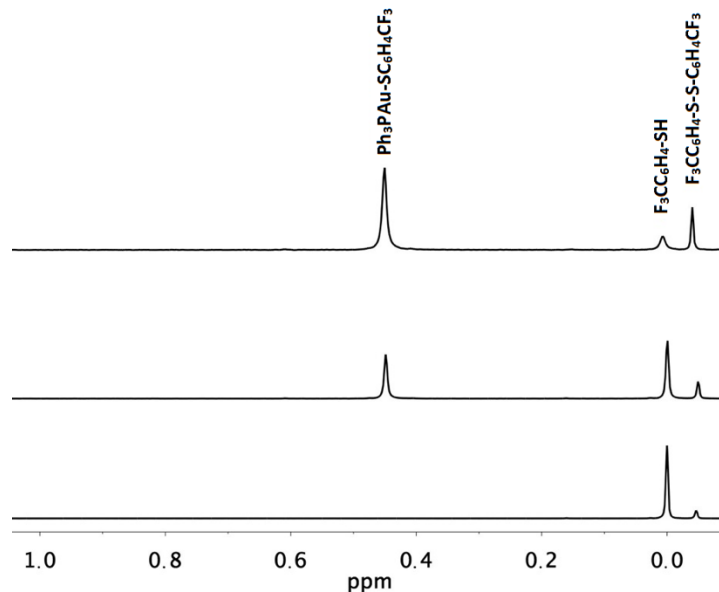


**Figure 3.16.**  $^{19}\text{F}$  NMR spectrum of the mixture of AuPpbt and  $\text{F}_3\text{CC}_6\text{H}_4\text{SH}$  (top trace),  $\text{PPh}_3\text{Au}-\text{SC}_6\text{H}_4\text{CF}_3$  synthesized independently (middle trace) and  $\text{F}_3\text{CC}_6\text{H}_4\text{SH}$  (bottom trace) in  $\text{CDCl}_3$ .  $\text{F}_3\text{CC}_6\text{H}_4\text{S}-\text{SC}_6\text{H}_4\text{CF}_3$  was present in the thiol as an impurity.

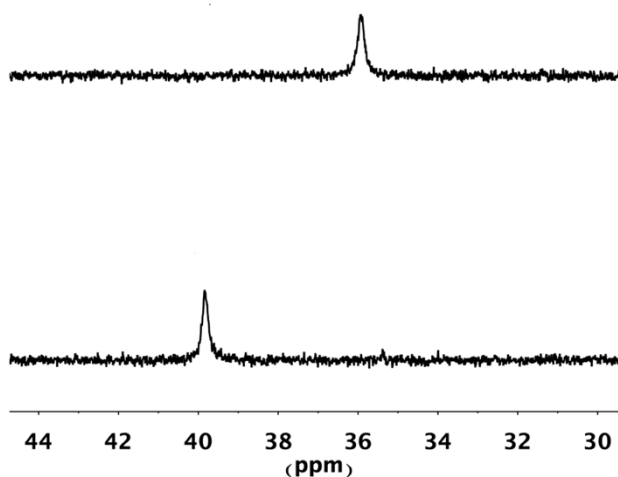


**Figure 3.17.**  $^{31}\text{P}$  NMR spectra of complex AuPpbt (top trace) and  $\text{PPh}_3\text{Au}-\text{SC}_6\text{H}_{10}\text{NO}_3$  (bottom trace, formed upon addition of  $\text{HSC}_6\text{H}_{10}\text{NO}_3$  to AuPpbt) in  $\text{CDCl}_3$  (the ppm values are w.r.t free  $\text{PPh}_3$  in  $\text{CDCl}_3$ )

Deligation of pbt or qbt from both complexes by SH-containing compounds can be readily observed by a dramatic increase in luminescence due to release of the strongly fluorescent ligands in solution. For example, when AuPqbt was allowed to react with  $\text{CF}_3\text{C}_6\text{H}_4\text{SH}$  in chloroform, a sharp increase in luminescence was observed (**Figure 3.18**). Taken together, these observations suggest that complexes like AuPpbt and AuPqbt most likely generate the reactive  $\text{Ph}_3\text{PAu}^+$  species (and free ligand) within the bacterial cell and disrupt the cellular mechanism(s) by binding to various biomolecules. Failure of free pbt and qbt in causing bacterial death could be attributed to their inability to cross cell membrane as well as their insolubility in aqueous media; complexes like AuPpbt and AuPqbt make such entry possible and possibly allow these

ligands to exert their own antibacterial activity. Lack of antibacterial activity of  $\text{ClAu(PPh}_3\text{)}$  most possibly arises from its low solubility, high stability and inability to pass through the cell membrane.

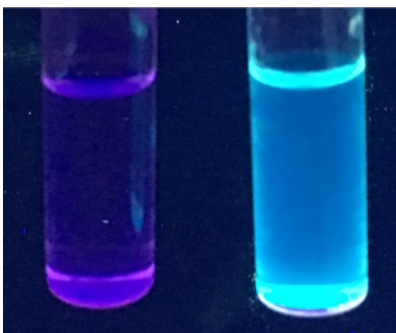


**Figure 3.18.** Dramatic rise in luminescence upon addition of  $\text{CF}_3\text{C}_6\text{H}_4\text{SH}$  to  $\text{AuPqbt}$  in chloroform. Left:  $\text{CHCl}_3$  solution of  $\text{AuPqbt}$ ; right: a mixture of  $\text{AuPqbt}$  and  $\text{CF}_3\text{C}_6\text{H}_4\text{SH}$  in  $\text{CHCl}_3$ .

Finally, in order to test the antimicrobial activity of the present  $\text{Au(I)}$  complexes against a more common and invasive bacterium prevalent in nosocomial skin infections and burn injuries complex  $\text{AuPpbt}$  was tested against *P. aeruginosa*. A KBr pellet containing 0.3 mol% of  $\text{AuPpbt}$  was placed on a *P. aeruginosa* lawn and incubated at  $37^\circ\text{C}$  for 18 h. The large zone of killing (**Figure 3.19**) confirmed that complex  $\text{AuPpbt}$  is highly effective in eradication of *P. aeruginosa*.

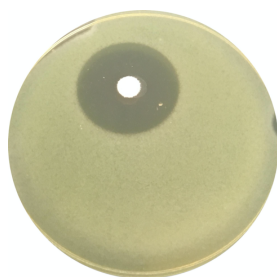


**Figure 3.19.** Circular clearing ring in *P. aeruginosa* lawn upon application of AuPpbt.

### 3.2.4 Experimental Methods

#### 3.2.4.1 General Methods

All reagents and solvents were of commercial grade and used without further purification.  $\text{ClAu(PPh}_3\text{)}$  and  $\text{AgOTf}$  were procured from Sigma. The ligands  $\text{pbt}^{64}$  and  $\text{qbt}^{65}$  were synthesized according to reported procedures. FTIR, UV-Vis, and emission spectra were obtained using Perkin-Elmer Spectrum-One, Varian Cary 50, and Agilent Cary Eclipse spectrophotometers respectively. The  $^1\text{H}$ -,  $^{19}\text{F}$ - and  $^{31}\text{P}$ -NMR spectra of the ligands and the complexes were recorded using a Varian Unity Inova 500 MHz instrument at 298K.

#### 3.2.4.2 Synthesis

$[(\text{pbt})\text{Au(PPh}_3\text{)}](\text{OTf})$  (AuPpbt): To a solution of  $\text{AgOTf}$  (54.8 mg, 0.213 mmol) in 10 mL of methanol was added a solution of  $\text{ClAu(PPh}_3\text{)}$  (100.5 mg, 0.203 mmol) in 15 mL of chloroform. After stirring for 30 min the white  $\text{AgCl}$  precipitate was filtered through a bed of celite. To the filtrate was added a solution of  $\text{pbt}$  (43.1



mg, 0.203 mmol) in 10 mL of chloroform and the mixture was set to reflux for 18 h. The solution was again filtered through celite to remove traces of black particles. The volume of the filtrate was then reduced to approximately 4 mL and 15 mL of hexane was added. The white solid thus formed was collected by filtration and dried in vacuo (131.0 mg, 78.6% yield). Layering of hexanes over a dichloromethane ( $\text{CH}_2\text{Cl}_2$ ) solution of this solid afforded colorless crystals of AuPpbt. Anal. Calcd for  $\text{C}_{31}\text{H}_{23}\text{AuN}_2\text{O}_3\text{PS}_2\text{F}_3$ : C, 45.37; H, 2.83; N, 3.41; found: C, 45.48; H, 2.79; N, 3.37. IR (KBr,  $\text{cm}^{-1}$ ): 3467.97 (w), 3056.49 (w), 1458.58 (w), 1436.08 (m), 1266.69 (s), 1153.59 (m), 1031.63 (m), 762.72 (m), 694.86 (m), 546.06 (m).  $^1\text{H}$  NMR ( $\text{CDCl}_3$ ,  $\delta$  ppm): 8.62 (d, 1H), 8.40 (d, 1H), 8.25 (t, 1H), 8.12 (d, 1H), 8.01 (d, 1H), 7.83 (t, 1H), 7.63-7.55 (m, 17 H).

$[(\text{qbt})\text{Au}(\text{PPh}_3)](\text{OTf})$  (AuPqbt): The same procedure as above using qbt as the ligand. Complex AuPqbt was isolated as a light yellow solid (60.1 mg, 75.0%). Layering of hexanes over a solution of AuPqbt in dichloromethane afforded pale yellow crystals of AuPqbt. Anal. Calcd for  $\text{C}_{35}\text{H}_{25}\text{AuN}_2\text{O}_3\text{PS}_2\text{F}_3$ : C, 48.28; H, 2.89; N, 3.22; found: C, 48.02; H, 2.91; N, 3.12. IR (KBr,  $\text{cm}^{-1}$ ): 3435.99 (w), 3056.53 (w), 1436.13 (w), 1262.84 (s), 1155.75 (m), 1031.38 (m), 762.25 (m), 695.69 (m), 544.91 (m).  $^1\text{H}$  NMR ( $\text{CDCl}_3$ ,  $\delta$  ppm): 8.76 (d, 1H), 8.52 (d, 1H), 8.23 (d, 1H), 8.19 (d, 1H), 8.06 (d, 1H), 7.69-7.53 (m, 19 H), 7.46 (t, 1H).

### 3.2.4.3 X-ray Crystallography

Colorless and light-yellow block-shaped crystals of complexes AuPpbt $\cdot$ 0.5CH<sub>2</sub>Cl<sub>2</sub> and AuPqbt respectively were obtained by recrystallization through diffusion of hexanes into their dichloromethane (CH<sub>2</sub>Cl<sub>2</sub>) solutions. In case of AuPpbt, a suitable crystal was selected and mounted on a Bruker D8 Quest diffractometer equipped with PHOTON II detector operating at T = 298 K. Data were collected with  $\omega$  shutter less scan technique using graphite monochromated Mo-K $\alpha$  radiation ( $\lambda$  = 0.71073 Å). In case of AuPqbt, a suitable single crystal was selected and mounted on a Bruker APEX-II CCD diffractometer with graphite monochromated Mo-K $\alpha$  radiation ( $\lambda$  = 0.71073 Å). In this case the crystal was also kept at T = 298 K during data collection and unit cell determination. Data were measured using  $\omega$  scan technique. The total number of runs and images for both data collections was based on the strategy calculation from the program *APEX3* (Bruker).<sup>66</sup> The maximum resolution achieved was  $\theta$  = 28.4° for AuPpbt and  $\theta$  = 24.2° for AuPqbt. Cell parameters were retrieved using the *SAINT* (Bruker) software<sup>67</sup> and refined using *SAINT* (Bruker) on 9525 reflections for AuPpbt and on 8496 reflections for AuPqbt. Data reduction was performed using the *SAINT* (Bruker) software, which corrects for Lorentz polarization. The final completeness is 99.6% out to 28.4° in  $\theta$  for AuPpbt and 98.8% out to 24.2° in  $\theta$  for AuPqbt. Multi-scan absorption corrections were performed with both data sets using *SADABS* 2016/2 and *SADABS* 2014/5 respectively for AuPpbt and AuPqbt.<sup>68</sup> The absorption coefficient for AuPpbt is 4.88 mm<sup>-1</sup> and for AuPqbt is 4.29 mm<sup>-1</sup>. Minimum and maximum transmissions for AuPpbt are 0.499 and 0.746 and the corresponding

values for AuPqbt are 0.573 and 0.745. The structures of AuPpbt and AuPqbt were solved in the space group C2/c (No. 15) and Pbca (No. 61) respectively by intrinsic phasing using the *ShelXT*<sup>69</sup> structure solution program and refined by full matrix least squares on  $F^2$  using version 2016/6 of *ShelXL*.<sup>70</sup> All non-hydrogen atoms were refined anisotropically in both cases. Hydrogen atom positions were calculated geometrically and refined using the riding model. In case of AuPpbt, there are two crystallographically independent molecules within the asymmetric unit, while for AuPqbt one full molecule is present in the asymmetric unit. Calculations and molecular graphics were performed using *SHELXTL* 2014 and *Olex2*<sup>71</sup> programs. Crystal data and structure refinement parameters are included in Table 1 while the bond distances and angles are listed in **Table 3.2**.

Crystal data for complex AuPpbt (CCDC 1824282) and AuPqbt (CCDC 1824283) can be obtained free of charge from The Cambridge Crystallographic Data Center via [www.ccdc.cam.ac.uk/data\\_request.cif](http://www.ccdc.cam.ac.uk/data_request.cif).

**Table 3.2.** Crystal data and structure refinement parameters for AuPpbt and AuPqbt.

	AuPpbt. 0.5 CH <sub>2</sub> Cl <sub>2</sub>	AuPqbt
Formula	C <sub>31.5</sub> H <sub>24</sub> ClF <sub>3</sub> N <sub>2</sub> O <sub>3</sub> S <sub>2</sub> PAu	C <sub>35</sub> H <sub>25</sub> F <sub>3</sub> N <sub>2</sub> O <sub>3</sub> S <sub>2</sub> PAu
$D_{calc.}/\text{g cm}^{-3}$	1.777	1.601
$\mu/\text{mm}^{-1}$	4.875	4.285
Formula Weight	863.03	870.62
Color	Yellow	Yellow
Shape	Block	Block
$T/\text{K}$	298(2)	298(2)
Crystal System	Monoclinic	Orthorhombic
Space Group	C2/c	Pbca
$a/\text{\AA}$	47.014(2)	9.780(2)
$b/\text{\AA}$	8.7125(4)	22.679(5)
$c/\text{\AA}$	36.5473(18)	32.560(7)
$\alpha/^\circ$	90	90
$\beta/^\circ$	120.4450(10)	90
$\gamma/^\circ$	90	90
$V/\text{\AA}^3$	12905.9(11)	7222(3)
$Z$	8	8
Wavelength/ $\text{\AA}$	0.71073	0.71073
Radiation type	Mo-K $\alpha$	Mo-K $\alpha$
$2\theta_{min}/^\circ$	5.674	4.706
$2\theta_{max}/^\circ$	56.712	48.376
Measured Refl.	123645	40970
Independent Refl.	16063	5736
Reflections Used	12893	4345
$R_{int}$	0.0386	0.0487
Parameters	802	424
<sup>a</sup> GooF	1.125	1.070
<sup>c</sup> $wR_2$	0.1120	0.1008
<sup>b</sup> $R_1$	0.0492	0.0428

<sup>a</sup>GOF =  $[\sum [w(F_o^2 - F_c^2)^2]/(N_o - N_v)]^{1/2}$  ( $N_o$  = number of observations,  $N_v$  = number of variables).

$$^bR_1 = \sum ||F_o| - |F_c|| / \sum |F_o|, \quad ^c wR_2 = [(\sum w(F_o^2 - F_c^2)^2 / \sum |F_o|^2)]^{1/2}$$

#### 3.2.4.4 Bacterial Studies

The SSTI model previously developed in our lab<sup>60</sup> was employed for antimicrobial studies. This uses a soft upper agar layer of evenly-dispersed bacterial “lawn” at the top of a nutrient rich bottom agar layer. Such arrangement allows the bacteria to move slowly into the bottom layer following the nutrient gradient, much like ditching of surface bacteria into the inner layers of skin and soft tissue. Different dilutions of *A. baumannii* and *P. aeruginosa* were employed to grow ideal lawns in these SSTI models. For *A. baumannii*, a frozen stock of bacteria was first streaked on an LB plate and incubated for 18 h. A single colony of bacteria was selected and grown in LB broth for another 18 h. The suspension was diluted with fresh LB until an  $A_{600}$  of 0.8 was reached. A batch of 100 mL of 0.8% (w/v) agar with 1% NaCl was prepared, autoclaved and cooled to 47°C before addition of 80  $\mu$ L of the diluted bacterial suspension. This solution was gently vortexed and aliquots of 8 mL of it were spread evenly over the surface of six 100 x 15 mm<sup>2</sup> plates prepared with 20 mL of 1.5% (w/v) TSB agar (hard nutrient-rich layer). The plates were then incubated at 37°C for 2 h to facilitate adhesion of the bacteria to the nutrient-rich bottom layer and cell-to-cell contact. For *P. aeruginosa*, the same procedure was followed to prepare the SSTI model. Here, the bacterial suspension in LB medium was diluted to an  $A_{600}$  of 0.5 and 120  $\mu$ L of it was added to the 100 mL of soft agar solution. The SSTI models were prepared using 7 mL of the soft agar solution spread evenly over the surface of the hard agar layer. After preparation the plates and initial incubation of 2 h, the KBr pellets

containing the Au(I) complexes were placed on all SSTI models and incubated for 18 h to evaluate the antibacterial activity of the Au(I) compounds.

### 3.3 Antimycobacterial Activity of Gold Complexes with Pyrazinamide

Recent efforts in drug discovery have demonstrated that combination of two antipathogenic moieties in one chemotherapeutic often leads to higher overall efficacy.<sup>16,44,47,51,72</sup> It is evident that such a design provides a dual mechanism of action and potentially increased the effect compared to that of the ligand or the metal center on its own. The promising antibacterial results from the previous section with AuPpbt and AuPqbt as well as reported results on the antitubercular activity of gold complexes prompted us to further study designing new gold(I) complexes comprising the  $\{\text{Au}(\text{PPh}_3)\}^+$  moiety and the known TB drug pyrazinamide (pza). This drug, pza, shortens the treatment duration for TB to a considerable extent although large oral quantities are needed for such effect.<sup>73</sup> We therefore decided to combine pza with the  $\{\text{Au}(\text{PPh}_3)\}^+$  unit and study the synergistic effects on *M. tuberculosis* and the possibility of use of lower doses of pza. We report the syntheses and characterization of one gold(I) complex  $[\text{Au}(\text{PPh}_3)(\text{pza})]\text{OTf}$  (AuPpza) and as a comparison for oxidation state two gold(III) complexes  $[\text{Au}(\text{pza})\text{Cl}_2]$  (Au3pza) and  $[\text{Au}(\text{pzo})\text{Cl}_2]$  (Au3pzo, pzo = pyrazinoic acid, the metabolic product of pza) (**Figure 3.20**). The antimycobacterial properties of these complexes have been evaluated on both *M. tuberculosis* as well as *M. smegmatis*.

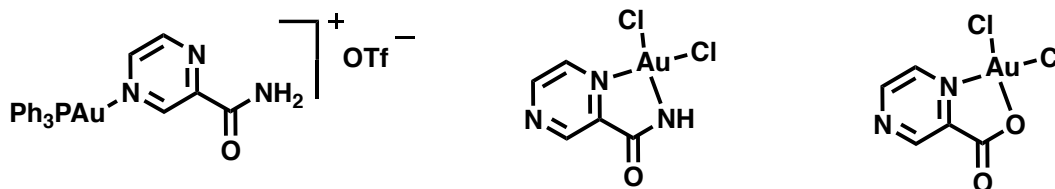


**Figure 3.20.** The gold complexes AuPpza (left), Au3pza (middle) and Au3pzo (right) evaluated for their antimycobacterial activity.

### 3.3.1 Synthesis and Spectroscopy

Complex AuPpza was synthesized by first displacing the chloride ligand from ClAu(PPh<sub>3</sub>) with the aid of Ag(OTf) and introducing pza as the second ligand similarly to that of AuPpbt/qbt. The IR spectrum of AuPpza (**Figure 3.21**) exhibits a strong peak centered around 1261 cm<sup>-1</sup> corresponding to the OTf counterion and carbonyl amide peak of PZA at 1690 cm<sup>-1</sup>. The NMR spectrum of AuPpza in CD<sub>3</sub>OD (**Figure 3.22**) shows three broad proton peaks between 8.8-9.5 ppm representative of the 3 aromatic peaks on the pza ligand and a multiplet around 7.6 ppm indicating the phenyl rings on the PPh<sub>3</sub>.

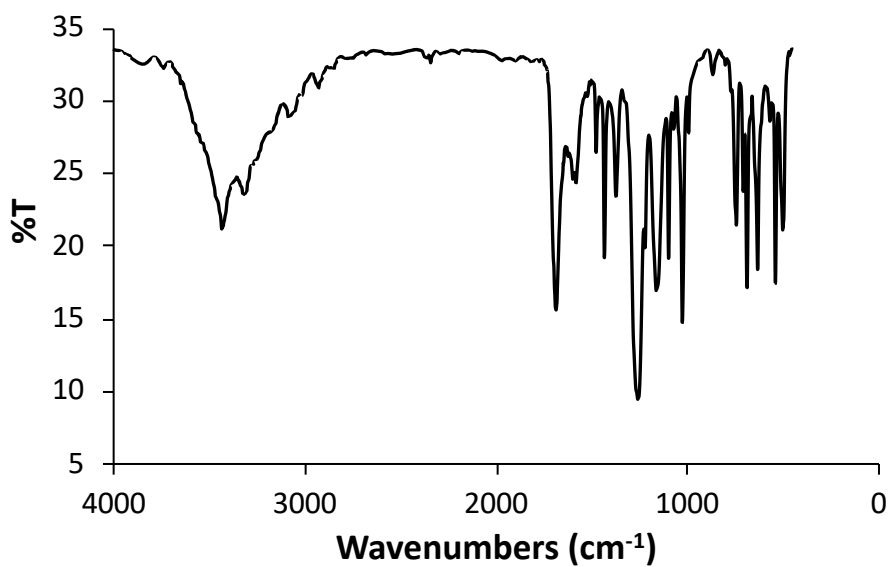


**Figure 3.21** FT-IR spectrum of AuPpza in KBr,  $\text{cm}^{-1}$ .

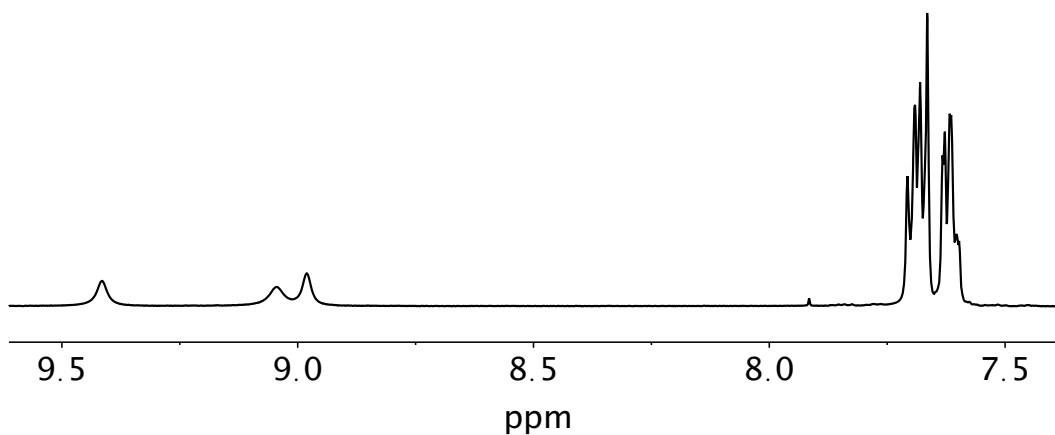


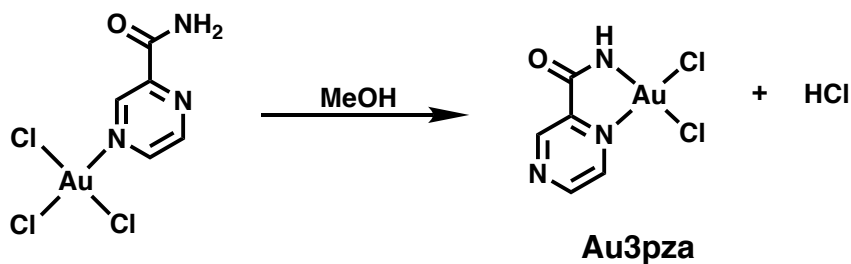
**Figure 3.22.** H-NMR spectrum of AuPpza in  $\text{CD}_3\text{OD}$  at 298K.

$\text{Au}_3\text{pza}$  (**Figure 3.20**) was not obtained from the initial reaction of  $\text{KAuCl}_4$  and pza (synthetic details in the experimental section) but initially afforded the precursor complex as shown in **Scheme 3.3**. The precursor complex is always the first product



that appears as a bright yellow solid and behaves similarly to the analogous  $[\text{AuCl}_3(\text{pyrazine})]$  complex.<sup>74</sup> Slow evaporation of the methanolic solution of this precursor complex eventually affords complex  $\text{Au}_3\text{pza}$ . Comparison of the IR spectra of the precursor complex and  $\text{Au}_3\text{pza}$  reveals different  $\nu_{\text{CO}}$  frequencies (1704 and 1660  $\text{cm}^{-1}$ , respectively) corresponding to the amide CO group of pza (**Figure 3.23**). Because the  $\nu_{\text{CO}}$  of the precursor complex is close to the  $\nu_{\text{CO}}$  value of free pza (1711  $\text{cm}^{-1}$ ), we believe that in this complex the pza ligand is bound to the Au(III) center in a monodentate fashion (as shown in **Scheme 3.3**). In complex  $\text{Au}_3\text{pza}$ , the pza ligand is bonded as a bidentate ligand with the deprotonated amide group (X-ray structure discussed in section 3.3.2). Elimination of HCl from the precursor complex leads to formation of  $\text{Au}_3\text{pza}$  in methanolic solution upon long evaporation (**Scheme 3.3**). Due to the relatively short reaction time (10 min), the precursor material presumably precipitates out as the kinetically favored species while  $\text{Au}_3\text{pza}$  is the thermodynamically favored species obtained after recrystallization from methanol. This assignment is further supported by the fact that while the precursor complex exhibits two amide NH peaks in its NMR spectrum (much like free pza) in  $\text{CD}_3\text{CN}$ , complex  $\text{Au}_3\text{pza}$  displays only one NH peak in its spectrum in the same solvent (**Figure 3.24**). Also the precursor complex, like  $[\text{AuCl}_3(\text{pyrazine})]$ , readily loses the N-donor ligand in dimethyl sulfoxide ( $\text{DMSO}$ )- $\text{d}_6$  (as evidenced by NMR spectra).<sup>74</sup> We hypothesize that the precursor complex, pza is bound to the Au(III) center at the N atom meta to the carboxamide group (as observed in  $\text{AuPpza}$ ) simply because this N center is the most basic site of the pza molecule.<sup>75</sup> Conversion of the precursor  $\text{Au}_3\text{pza}$  is

accelerated by the addition of  $\text{NaHCO}_3$  in a 1:1 MeOH/water reaction mixture, a step that pushes the reaction shown in **Scheme 3.3** to the right.



**Scheme 3.3** Suggested ligand binding mode rearrangement from the precursor complex (left) to Au3pza.

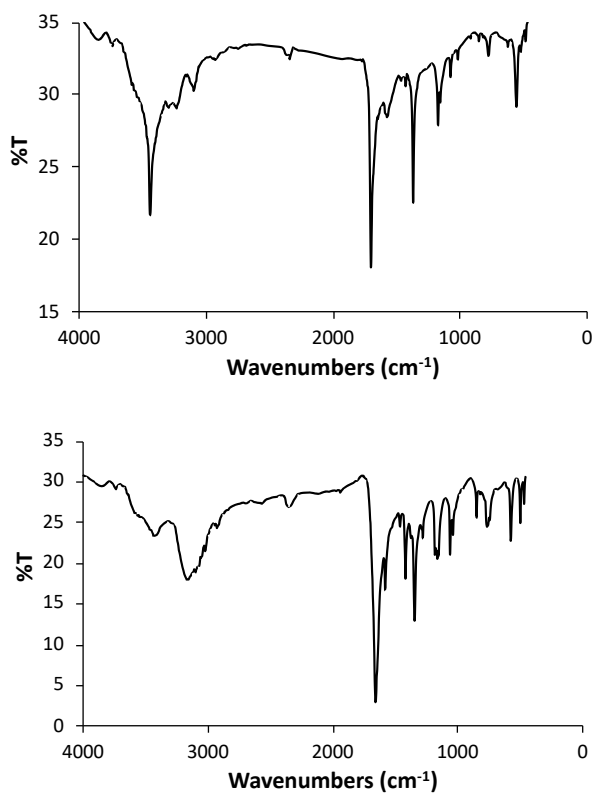


**Figure 3.23.** FT-IR spectra of the precursor complex (top) and Au3pza (bottom).

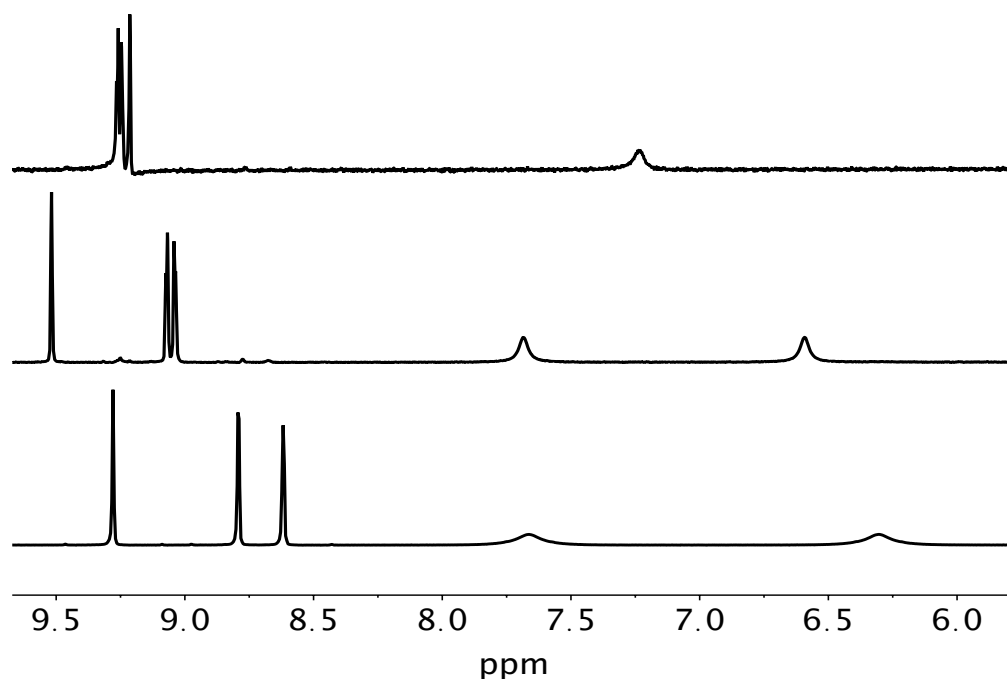


**Figure 3.24.**  $^1\text{H}$  NMR (in  $\text{CD}_3\text{CN}$ ) spectra of  $\text{Au}_3\text{pza}$  (top), the precursor compound (middle) and pza (bottom).

The ligand pzo, the purported metabolic product actually responsible for the drug action of pza, also binds the  $\text{Au(III)}$  center as a bidentate ligand to form the complex  $\text{Au}_3\text{pzo}$  (**Figure 3.20**). Addition of excess deprotonated pzo to  $\text{KAuCl}_4$  in the aqueous medium affords  $\text{Au}_3\text{pzo}$  in high yield. The FT-IR spectrum of  $\text{Au}_3\text{pzo}$  (**Figure 3.25**) shows strong  $\nu_{\text{CO}}$  stretch at  $1705\text{ cm}^{-1}$  and NMR spectrum with three aromatic protons of pza at 9.31 (2H) and 9.12 (1H) (**Figure 3.26**).

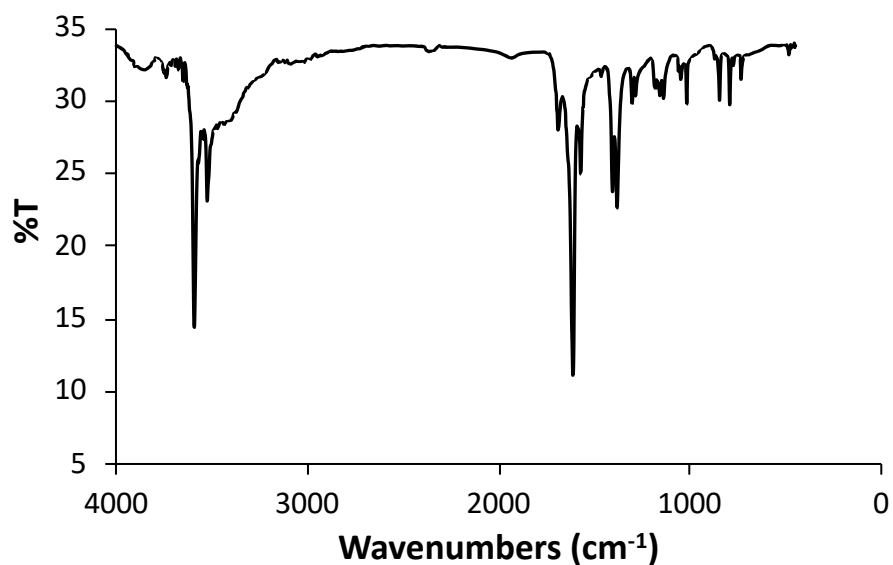


**Figure 3.25.** FT-IR spectrum of Au<sub>3</sub>pzo in KBr.

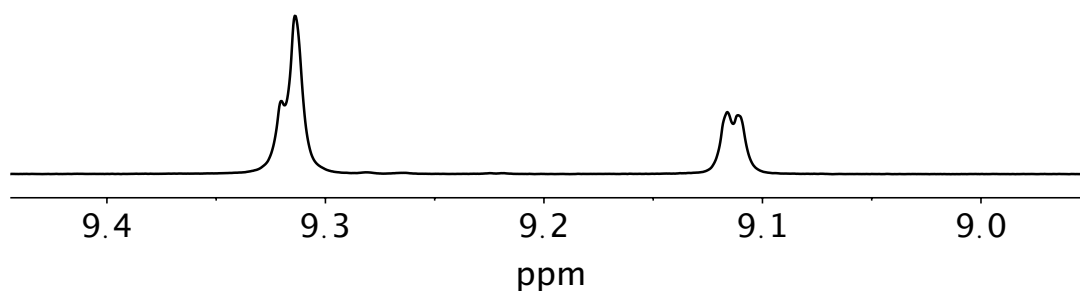


**Figure 3.26.** <sup>1</sup>H NMR spectra of Au<sub>3</sub>pzo in CD<sub>3</sub>CN at 298K.

### 3.3.2 Crystal Structure Descriptions

Structures of AuPpza, Au<sub>3</sub>pza and Au<sub>3</sub>pzo were characterized by X-ray crystallography and the perspective views (with atom labeling schemes) are shown in **Figure 3.27, 3.28 and 3.29** respectively) while the selected bond distances and angles

are listed in **Table 3.3**. As evident from their crystal structures, the Au(I) complex AuPpza exhibits a linear coordination while the two Au(III) complexes Au3pza and Au3pzo are square planar. In the structure of AuPpza, there is one molecule of water in the asymmetric unit while the other two structures contain no solvent of crystallization. The N(1)-Au(1)-P(1) angle in AuPpza deviates slightly from linearity with an angle of 177.8(2)°. The Au-N(pyrazine) (2.081(7) Å) bond is shorter than Au-P (2.244(2) Å) bond as expected. Similar bond lengths and angles are observed in other known structures of Au(I) complexes of [(N-bound ligand)Au(PPh<sub>3</sub>)] type.<sup>16,76</sup> The three nitrogen atoms on pza potentially allow for three different binding modes to the {AuPPh<sub>3</sub>}<sup>+</sup> unit in AuPpza; however, the least sterically hindered and most basic N of pza shows preference to the metal center as shown in **Figure 3.27**.<sup>75</sup>

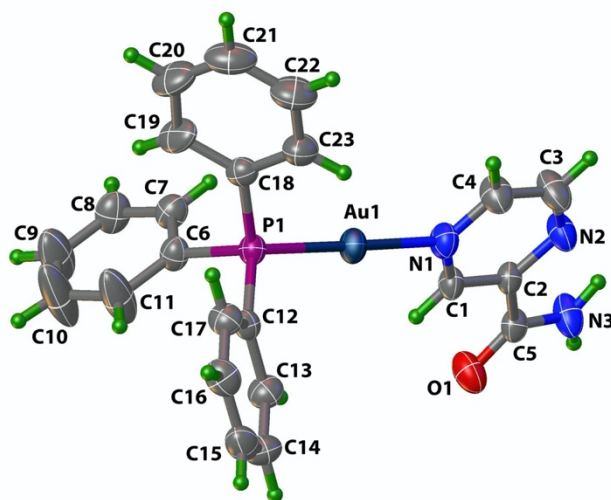


**Figure 3.27.** The structure of AuPpza with water and OTf anion omitted for clarity.

Ellipsoids are shown at the 50% probability level.

**Table 3.3.** Selected bond lengths and angles for AuPpza•H<sub>2</sub>O, Au<sub>3</sub>pza and Au<sub>3</sub>pzo.

	AuPpza•H <sub>2</sub> O	Au <sub>3</sub> pza	Au <sub>3</sub> pzo
Au(I)-P(1))	2.2432 (18)		
Au(I)-N(1)	2.082 (6)		
Au(I)-N(3)		1.985 (4)	
Au(I)-N(2)		2.042 (4)	2.016 (6)
Au(1)-Cl(1)		2.2571 (12)	2.250 (2)
Au(1)-Cl(2)		2.2879 (12)	2.2510 (17)
Au(1)-O(2)			1.998 (4)
N(1)-Au(1)-P(1)	177.8 (2)		
N(3)-Au(1)-Cl(1)		93.22 (12)	
N(2)-Au(1)-N(3)		80.51 (16)	
Cl(1)-Au(1)-Cl(2)		90.75 (5)	90.68 (7)
N(2)-Au(1)-Cl(2)		95.63 (11)	95.57 (14)
N(2)-Au(1)-O(2)			82.7 (2)
O(2)-Au(1)-Cl(1)			91.01 (16)

Au(III) complexes Au<sub>3</sub>pza and Au<sub>3</sub>pzo (**Figure 3.28 and 3.29**) are both distorted square planar and composed of pza/pzo ligand bound as a bidentate ligand. The square planar geometries of Au<sub>3</sub>pza and Au<sub>3</sub>pzo deviate noticeably from planarity with N(2)-Au(1)-N(3) and N(2)-Au(1)-O(2) angles of 80.51(16)° and 82.7(2)° respectively. The Cl(1)-Au(1)-Cl(2) angles of both structures deviate only slightly from the perfect right angle value (90.75(5)° and 90.68(7)° respectively). As expected, the deprotonated Au(1)-N(3) or Au(1)-O(2) of Au<sub>3</sub>pza and Au<sub>3</sub>pzo are significantly shorter than the Au(1)-N(2) bonds shown in **Table 3.3**. Bond lengths and angles are in

agreement with similar known structures of Au(III)-picolinamide and picolinic acid derivatives.<sup>77,78</sup>

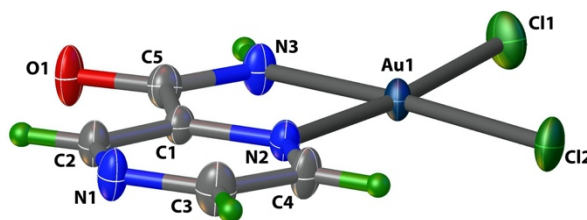


**Figure 3.28.** Crystal structure of Au3pza with thermal ellipsoids at 50% probability.

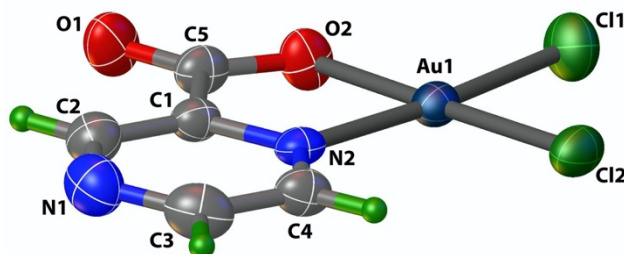


**Figure 3.29.** Crystal structure of Au3pzo with thermal ellipsoids at 50% probability.

In Au3pza the equatorial plane comprised of Au(1), N(2), N(3), Cl(1), Cl(2) atoms is fairly planar with mean deviation of 0.041(3) Å, while the corresponding plane in Au3pzo (comprised of Au(1), O(2), N(2), Cl(1), Cl(2) atoms) is highly planar with mean deviation of 0.011(3) Å. The central metal atom in Au3pza and Au3pzo is deviated from these planes by 0.009(3) and 0.022(3) Å respectively. The two chelate

planes formed by the bidentate pza and pzo ligands along with Au(III) centers in Au<sub>3</sub>pza (Au(1), N(2), N(3), C(1), and C(5)) and Au<sub>3</sub>pzo (Au(1), N(2), O(2), C(1), and C(5)) exhibit minimal deviation from planarity (mean deviations, 0.01(3) Å and 0.019(3) Å for Au<sub>3</sub>pza and Au<sub>3</sub>pzo respectively). The dihedral angles between the pyrazine ring and the five-membered chelate ring in Au<sub>3</sub>pza and Au<sub>3</sub>pzo are 3.18(2)° and 1.83(2)° respectively. In an Au(III) complex with picolinamide as a ligand, which structurally resembles closely to that of complex Au<sub>3</sub>pza, the dihedral angle between the pyridine ring and the five-membered chelate ring is 3.6(2)° which is close to the corresponding value noted for Au<sub>3</sub>pza.<sup>77</sup> Moreover, the mean deviations of the chelate ring are similar to those in Au<sub>3</sub>pza. However, a reported Au(III) complex with a picolinic acid derivative as ligand resemble structurally more to complex Au<sub>3</sub>pzo, and the dihedral angle between the pyridine ring and the five-membered chelate ring is 1.28(2)°.<sup>78</sup>

### 3.3.3 Antimycobacterial Activity and Interactions

Before studying the potential synergistic effects of pza and gold on *M. tuberculosis*, the antimicrobial effects of the Au center alone were studied on *M. smegmatis*. This bacterium is in the same genus as *M. tuberculosis* and has 2000 genes highly conserved with the pathogen. Thus, *M. Smegmatis* is an excellent model organism that is easy to work with, has a fast growth rate, and a relatively safer model.<sup>79,80</sup> *M. Smegmatis* is known to be naturally resistant to pza, and thus provides an opportunity to study the activity of the {Au(I)(PPh<sub>3</sub>)}<sup>+</sup> and {Au(III)Cl<sub>2</sub>}<sup>+</sup>



moieties of AuPpza, Au3pza and Au2pzo. The activities of AuPpza, Au3pza and Au2pzo, [ClAu(PPh<sub>3</sub>)], pza, and a drug control isoniazid (ihn) were tested against *M. smegmatis* in normal growth environment and the results are summarized in **Table 3.4**. Under our conditions, we found the MIC to be 60 μM for AuPpza and [ClAu(PPh<sub>3</sub>)], while Au3pza, Au2pzo and pza showed no activity up to 100 μM. Mycobacteria species are known to have thick, hydrophobic and waxy membranes that prevent foreign substances from permeation more so than traditional Gram-positive and Gram-negative species.<sup>81,82</sup> For this reason, the lipophilic {Au(PPh<sub>3</sub>)}<sup>+</sup> unit in AuPpza might have been able to pass through this membrane and exert drug action. This conclusion is supported by the fact that cell digests from *M. smegmatis* cells exposed to 40 μM (below the MIC) of AuPpza exhibited strong inductively coupled plasma mass spectrometry (ICP-MS) signal(s) for gold. This conclusion is supported by the fact that the gold(III) species Au3pza and Au2pzo with chloro ligands but no {Au(PPh<sub>3</sub>)}<sup>+</sup> moiety were *not* active at these concentrations.

**Table 3.4.** MIC (μM) values for activity against *M. Smegmatis*

Compound	MIC(μM)
AuPpza	60
Au3pza	>100
Au3pzo	>100
[ClAu(PPh <sub>3</sub> )]	60
pza	>100
ihn	80

With results from *M. Smegmatis* study in hand, we proceeded to test the activity of complex AuPpza against *M. tuberculosis in vitro* along with [ClAu(PPh<sub>3</sub>)], pza, and isoniazid (ihn). The OD<sub>600</sub> of *M. tuberculosis* was recorded after 24 h incubation with 80 μM of each compound in 1% acetone (**Figure 3.30**). Interestingly, AuPpza showed significant bactericidal activity (reduction in OD<sub>600</sub>) while pza on its own was only mildly bacteriostatic (OD<sub>600</sub> less than the control but higher than day 0). The mild drug action of pza against *M. tuberculosis* at the 80 μM concentration is expected since higher concentration of pza (up to 400 μM) and *low pH* (5.5) media are usually required to observe any effect on *M. tuberculosis* growth *in vitro*.<sup>83</sup> Results shown in **Figure 3.30** strongly suggest that the {Au(PPh<sub>3</sub>)}<sup>+</sup> moiety of AuPpza augments the efficacy of pza *in vitro*. The standard [ClAuPPh<sub>3</sub>)] was specifically included in this study to determine if AuPpza would show increased activity compared to a compound with the {Au(PPh<sub>3</sub>)}<sup>+</sup> moiety without pza. Inspection of **Figure 3.30** reveals that both AuPpza and [ClAuPPh<sub>3</sub>)] exhibited the greatest reduction in OD at very similar average values of 0.345 and 0.387 respectively. Collectively these results suggest that AuPpza could introduce a dose of pza as well as {Au(PPh<sub>3</sub>)}<sup>+</sup> moiety in one combination and act as a “two-in-one” drug against *M. tuberculosis*. Ultimately, this might reduce the need for much higher doses of pza itself which has severe side effects on humans. The gold-phosphine unit is not so uncommon in metallodrug therapy; Auranofin, a FDA approved drug for rheumatoid arthritis, does contain a {Au(PEt<sub>3</sub>)}<sup>+</sup> unit.<sup>5</sup>

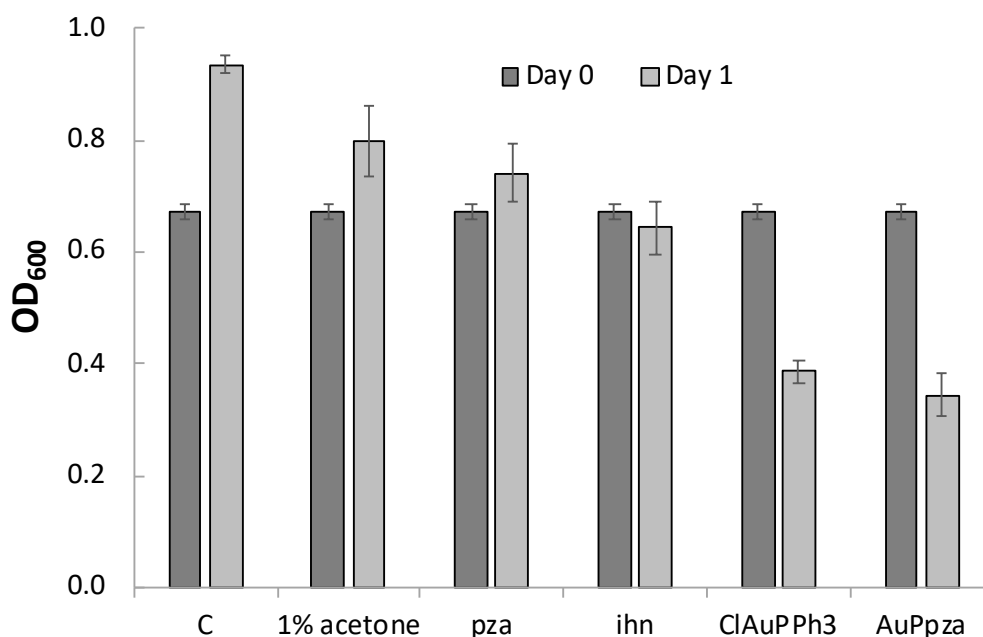


**Figure 3.30.** *M. tuberculosis* OD<sub>600</sub> values of initial (day 0) and after 24h (day 1) incubation with test compounds at 80μM. Column C has no additional compound or acetone.

The clinically used drug pza plays an important role in shortening TB treatment duration from 9-12 months to 6 months. This is likely because pza targets a population of semi-dormant bacilli residing within the macrophages in an environment not accessible to other TB drugs.<sup>83,84</sup> The mechanism of action of the pro-drug pza is not entirely understood, but most agree that the conversion of pza to pzo *within the bacilli* is critical for activity against *M. tuberculosis*. Interestingly pzo itself is not as active as pza against *M. tuberculosis*. It is well established that pza has a broad range of activity highly dependent on pH of the media and because it targets mostly nonreplicating bacilli, pza exhibits slow or no bactericidal activity *in vitro*.<sup>83</sup> This occurrence is likely

the reason why no synergy was observed in our hands. Nevertheless, pza has had a significant clinical impact on TB and therefore research toward modifying pza with additional antimycobacterial moiety might lead to new and improved outcomes.

Results of  $^1\text{H}$ -NMR studies confirm that AuPpza, Au<sub>3</sub>pza and Au<sub>3</sub>pzo are stable in acetone, while Au<sub>3</sub>pza and Au<sub>3</sub>pzo are also stable in acetonitrile. Complexes Au<sub>3</sub>pza and Au<sub>3</sub>pzo are stable in aqueous acetone (90:10) for hours, while AuPpza slowly decomposes in such solutions (used in biological studies). However, inside biologically relevant environments, exposure to sulfur containing biomolecules like glutathione is expected. Gold(I) centers are soft lewis acids and it is well established that they prefer binding to soft lewis bases like thiolate species. The binding of gold(I) species to biologically relevant thiols has been observed and the exchange of N- and S-bound ligands occurs quickly compared to P-bound ligands.<sup>16,85</sup> This exchange has been hypothesized to play an important role in the anticancer effects of [N-AuPPh<sub>3</sub>] complexes<sup>16</sup> as well as in the antimycobacterial effects exhibited by auranofin.<sup>86</sup> Disruption of redox homeostasis within the bacterial cell following binding of the gold unit to glutathione or thioredoxin has been suggested to be responsible for the drug action. Impairment of protein synthesis in bacteria has also been observed with auranofin treatment.<sup>3416</sup> In section 3.2, we have showed that complexes with N bound benzothiazole ligands and the {Au(PPh<sub>3</sub>)}<sup>+</sup> moiety rapidly exchange with thiol species.<sup>76</sup> In the present work, we checked the possibility of exchange between pza and biologically relevant thiols in the case of AuPpza. Both  $^1\text{H}$  and  $^{19}\text{F}$  NMR spectra of the mixture of AuPpza and 4-(trifluoromethyl)thiophenol (FTP) were recorded to observe

if pza does get exchanged with FTP (**Figure 3.31**). As shown in Figure 6 (left panel), addition of FTP to AuPpza showed release of pza as a free ligand (as evident in the  $^1\text{H}$  NMR, not shown) with multiple new  $^{19}\text{F}$  NMR peaks (Figure 6A, bottom) along with a white precipitate. Together, these results indicate the formation of  $\{\text{S-AuPPh}_3\}$ -polymeric species by AuPpza in the presence of a thiol. We hypothesize that such a transformation within macrophages will lead to the presence of both pza and  $\{\text{Au}(\text{PPh}_3)\}^+$  units which will exert their own individual and potentially synergistic actions. In contrast,  $[\text{ClAuPPh}_3]$  does not appear to react with FTP and form any Au-thiol species (**Figure 3.31**, middle panel). In the acidic (pH 6.2-4.5) macrophage compartment, replacement of  $\text{Cl}^-$  by a thiol is highly unlikely. Thus administration of AuPpza (compared to  $[\text{ClAu}(\text{PPh}_3)]$ ) could be more reactive against *M. tuberculosis* residing within the macrophages *in vivo*. We have also employed a more biologically relevant thiol namely, N-acetyl L-cysteine methyl ester, to check this interpretation. Addition of N-acetyl L-cysteine methyl ester to AuPpza resulted in immediate appearance of a white precipitate (**Figure 3.32**) but no such reaction was observed with  $[\text{ClAuPPh}_3]$  (**Figure 3.32**). Taken together our results suggest that formation of  $\{\text{S-AuPPh}_3\}$ -polymeric species with AuPpza within biological targets might promote uptake by host macrophages, similar to the uptake of Au nanoparticles<sup>87,88</sup> and/or breakdown of cellular thiol redox homeostasis.<sup>86</sup> Since *M. tuberculosis* is either contained by macrophages or resides within them, this process could offer a more direct route to TB treatment in a host system. The  $\{\text{S-AuPPh}_3\}$ -polymeric species derived

from AuPpza, along with pza, could cause more damage to the mycobacterium residing within the macrophages thus increasing the efficacy of the treatment.

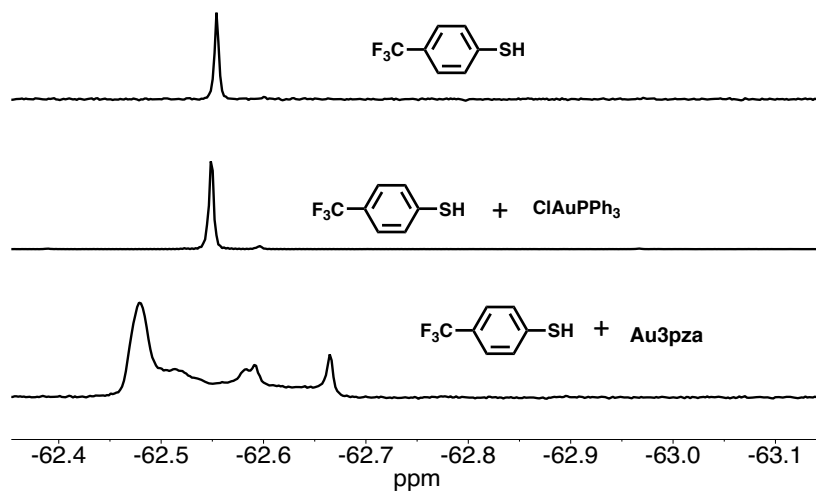


**Figure 3.31.**  $F^{19}$  NMR spectra of  $HSC_6H_4CF_3$  (top),  $ClAuPPh_3 + HSC_6H_4CF_3$  (middle), and  $Au_3pza + HSC_6H_4CF_3$  (bottom).

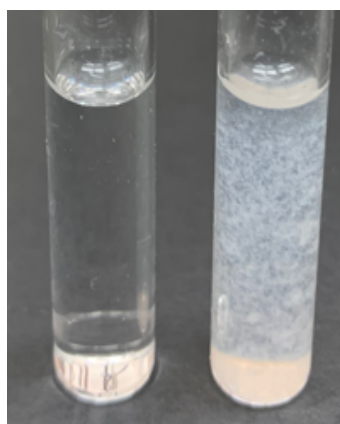


**Figure 3.32.** Reaction of  $ClAuPPh_3$  (left) and  $AuPpza$  (right) after addition of N-acetyl-L-cysteine-methyl-ester.

### 3.3.4 Experimental Section

#### 3.3.4.1 General Methods

All reagents and solvents were of commercial grade and used without further purification. FT-IR spectra were obtained using a Perkin-Elmer Spectrum-One spectrophotometer.  $^1\text{H}$  and  $^{19}\text{F}$  NMR spectra were recorded using a Varian Unity 500MHz instrument at 298 K.

#### 3.3.4.2 Synthesis

[Au(PPh<sub>3</sub>)(pza)]OTf (AuPpza). A solution of 72.0 mg (0.28 mmol) silver trifluoromethanesulfonate (OTf) in 10 mL of methanol was added to a solution of 138.8 mg (0.28 mmol) of chloro(triphenylphosphine)gold(I) dissolved in 15 mL of chloroform. Immediately a suspension of AgCl was formed and the mixture was stirred for 30 min at room temperature and then filtered through a bed of celite. To the filtrate, a solution of 34.4mg (0.28mmol) of pza in 15 mL of methanol/chloroform (1:1) was added and the mixture was stirred for 18 h at room temperature. The flask was covered with Al foil to protect the reaction mixture from ambient light. Next the solvent was removed in vacuo, and the solid was washed with diethyl ether to obtain AuPpza as a white solid (112.1mg, 54%). A solution of the solid in chloroform was layered with hexanes and stored in the fridge. X-ray quality crystals of AuPpza were obtained after one week. Anal. Calc for C<sub>24</sub>H<sub>20</sub>AuN<sub>3</sub>O<sub>4</sub>PSF<sub>3</sub>: C, 39.41; H, 2.76; N 5.74; found: C, 39.35; H, 2.79, N, 5.68. IR (KBr, cm<sup>-1</sup>): 3435(m), 3309(m), 1690(s), 1438(m), 1262(s),

1167(m), 1031(m), 693(m).  $^1\text{H}$  NMR ( $\text{CD}_3\text{OD}$ ,  $\delta$  ppm): 9.40 (b, 1H), 9.03 (b, 1H), 8.96 (b, 1H), 7.69-6.58 (m, 15H).

$[\text{Au}(\text{pza})\text{Cl}_2]$  ( $\text{Au}_3\text{pza}$ ). A batch of 32.5 mg (0.26mmol) of pza was dissolved in 2 mL of water and the solution was added dropwise to a solution of 99.7 mg (0.26mmol) potassium tetrachloroaurate in 1.75 mL of water at room temperature with stirring. A yellow solid appeared quickly and the suspension was allowed to stir for additional 10 min. The precipitate was filtered, washed with 2 mL of cold water and then 10 mL of cold diethyl ether to obtain the precursor complex (*vide infra*) as a bright yellow solid (90 mg). IR (KBr,  $\text{cm}^{-1}$ ): 3442(m), 1705(s), 1373(m), 1177(w), 560(w).  $^1\text{H}$  NMR ( $\text{CD}_3\text{CN}$ ,  $\delta$  ppm): 9.53 (s, 1H), 9.07 (d, 1H), 9.05 (d, 1H), 7.68 (b, 1H), 6.60 (b, 1H). The precursor yellow solid was crystallized from slow evaporation in methanol to form orange blocks of  $\text{Au}_3\text{pza}$  after two weeks. Anal. Calc. for  $\text{C}_5\text{H}_4\text{AuN}_3\text{OCl}_2$ : C, 15.40; H, 1.03; N, 10.77; found: C, 15.38; H, 1.10; N, 10.73. IR (KBr,  $\text{cm}^{-1}$ ): 3167(m), 1660(s), 1584(m), 1421(w), 1348(m), 1166(w), 1065(w), 579(w).  $^1\text{H}$  NMR ( $\text{CD}_3\text{CN}$ ,  $\delta$  ppm): 9.26 (m, 2H), 9.21 (s, 1H), 7.24 (b, 1H).

$[\text{Au}(\text{pzo})\text{Cl}_2]$  ( $\text{Au}_3\text{pzo}$ ). An aqueous solution of sodium hydroxide (0.15M) was used to adjust the pH of a suspension of 100 mg (0.81 mmol) of pzo in 2mL of water until a pH of 7 was reached. At this point, pzo had fully dissolved and the solution was added dropwise to a solution of 101.5mg (0.27mmol) potassium tetrachloroaurate in 1 mL of water at room temperature with stirring. A light yellow precipitate appeared



within minutes. After stirring for an additional 30 min the solid was filtered, washed with 2 mL of cold water then 5 mL of diethyl ether. The light yellow solid was finally recrystallized from MeOH/Ether to yield Au3pza as a yellow microcrystalline solid (60.2mg, 55%). X-ray quality crystals were formed by layering of acetonitrile/ether. Anal. Calc. for  $C_5H_3AuN_2O_2Cl_2$ : C, 15.36; H, 0.77; N, 7.17; found: C, 15.40; H, 0.81; N, 7.13. IR (KBr,  $cm^{-1}$ ): 3586 (s), 3419 (m), 1705(w), 1616(s), 1408(m), 1376(s), 1138(m), 850 (w), 795(w).  $^1H$  NMR ( $CD_3CN$ ,  $\delta$  ppm): 9.31 (m, 2H), 9.12 (d, 1H), 7.58 (s, 1H).

#### 3.3.4.3 X-ray Crystallography

Crystallographic data were collected on a Bruker APEX II single-crystal X-ray diffractometer (PHOTON 100 detector) with graphite monochromated Mo  $K\alpha$  radiation ( $\lambda = 0.71073 \text{ \AA}$ ) by the  $\omega$ -scan technique in the range  $5.8 \leq 2\theta \leq 53$  for AuPpza,  $7 \leq 2\theta \leq 50$  for Au3pza, and  $6.2 \leq 2\theta \leq 50$  for Au3pzo (**Table 3.5**). All data were corrected for Lorentz and polarization effects.<sup>89</sup> All of the structures were solved with the aid of the SHELXT program using intrinsic phasing.<sup>70</sup> The structures were then refined by a full-matrix least-squares procedure on  $F^2$  by SHELXL.<sup>69</sup> All nonhydrogen atoms were refined anisotropically. All hydrogen atoms were included in calculated positions. The absorption corrections are done using SADABS.<sup>70</sup> Calculations were performed using the OLEX2<sup>71</sup> and SHELXTL<sup>90</sup> (V 6.14) program package.

**Table 3.5.** Refinement parameters for AuPpza, Au3pza and Au3pzo.

	AuPpza·H <sub>2</sub> O	Au3pza	Au3pzo
Formula	C <sub>23</sub> H <sub>20</sub> AuN <sub>3</sub> OP·CF <sub>3</sub> O <sub>3</sub> S·H <sub>2</sub> O	C <sub>5</sub> H <sub>4</sub> AuCl <sub>2</sub> N <sub>3</sub> O	C <sub>5</sub> H <sub>3</sub> AuCl <sub>2</sub> N <sub>2</sub> O <sub>2</sub>
$D_{calc.}/\text{g cm}^{-3}$	1.835	3.135	3.013
$\mu/\text{mm}^{-1}$	5.62	18.4	17.65
Formula Weight	749.44	389.98	390.96
Color	Colorless	Yellow	Yellow
Shape	Block	Block	Plate
$T/\text{K}$	298	298	298
Crystal System	Triclinic	Triclinic	Orthorhombic
Space Group	P1	<i>P</i> 1	Pbca
$a/\text{\AA}$	7.0334 (10)	6.6857 (10)	7.2868 (6)
$b/\text{\AA}$	12.6524 (16)	7.2848 (11)	14.4003 (12)
$c/\text{\AA}$	15.688 (2)	8.9057 (13)	16.4259 (13)
$\alpha/^\circ$	79.435 (4)	94.664 (2)	90
$\beta/^\circ$	81.214 (5)	106.878 (2)	90
$\gamma/^\circ$	89.464 (4)	91.649 (2)	90
$V/\text{\AA}^3$	1356.0 (3)	413.06 (11)	1723.6 (2)
$Z$	2	2	8
Wavelength/ $\text{\AA}$	0.71073	0.71076	0.71076
Radiation type	Mo $K\alpha$	Mo $K\alpha$	Mo $K\alpha$
$2\theta_{min}/^\circ$	5.8	7	6.2
$2\theta_{max}/^\circ$	52.8	49.6	49.4
Measured Refl.	24132	4259	15095
Independent Refl.	5469	1395	1462
Reflections Used	5027	1381	1261
$R_{int}$	0.025	0.019	0.044
Parameters	343	113	109
<sup>a</sup> GooF	1.14	1.2	1.08
<sup>c</sup> $wR_2$	0.122	0.043	0.067
<sup>b</sup> $R_I$	0.044	0.017	0.024

<sup>a</sup>GOF =  $[\sum [w(F_o^2 - F_c^2)^2]/(N_o - N_v)]^{1/2}$  ( $N_o$  = number of observations,  $N_v$  = number of variables).

<sup>b</sup> $R_I = \sum ||F_o| - |F_c|| / \sum |F_o|$ .

<sup>c</sup> $wR_2 = [(\sum w(F_o^2 - F_c^2)^2 / \sum |F_o|^2)]^{1/2}$ .

Crystal data for complexes AuPpza (CCDC 1961025), Au<sub>3</sub>pza (CCDC 1961027) and Au<sub>3</sub>pzo (CCDC 1961026) can be obtained free of charge from The Cambridge Crystallographic Data Center via [www.ccdc.cam.ac.uk/data\\_request.cif](http://www.ccdc.cam.ac.uk/data_request.cif).

#### 3.3.4.4 Mycobacterial Studies

*M. smegmatis*. Middlebrook 7H9 liquid medium<sup>79</sup> was inoculated from a frozen stock of *M. smegmatis* and grown overnight to an optical density at 600 nm (OD<sub>600</sub>) of 1. Stock solutions of test compounds in acetone (0.02–0.1 mM) were prepared, and batches of 20 µL of such solutions were added to 250 µL of the bacterial suspensions in 1.73 mL of 7H9 media in 5 mL culture tubes. The tubes were incubated at 37 °C for 18 h. The MIC values were then determined by reading the OD<sub>600</sub> of the suspensions with different concentrations of the test compounds. To ensure that no viable bacteria remained in these tubes was confirmed as follows. Aliquots of 100 µL of the suspensions were added to fresh 7H9 media (1 mL) and incubated at 37 °C for 18 h. In all cases, no bacteria growth was observed. The MIC results are summarized in **Table 3.4** and all concentrations were performed in triplicate.

*M. tuberculosis*. A stock culture of *M. tuberculosis* was prepared by inoculation of a 1 mL frozen stock into 50 mL of Middlebrook 7H9 liquid medium supplemented with 10% (v/v) OADC enrichment (BBL Middlebrook OADC, 212351), 0.5% (v/v) glycerol, and 0.05% (w/v) Tween 80 (P1754, Sigma-Aldrich) in a roller bottle. Cells were grown to an OD<sub>600</sub> of 1.0 to begin the experiments. The culture was then diluted down to a target OD<sub>600</sub> of 0.5 (final OD reading = 0.67). Aliquots of 100 µL of 8 mM

test compound solutions in acetone were added to batches of 10 mL of the culture suspension (final concentration of the test compounds = 80  $\mu$ M in 1% acetone) and the tubes were then incubated at 37°C. After 24 h incubation, the OD<sub>600</sub> values were recorded. Triplicates were run with each test compound, and the results are shown in **Figure 3.30**.

### 3.4 References

- (1) Huaizhi, Z.; Yuantao, N. China's Ancient Gold Drugs. *Gold Bull.* **2001**, *34* (1), 24–29.
- (2) Benedek, T. G. The History of Gold Therapy for Tuberculosis. *J. Hist. Med. Allied Sci.* **2004**, *59* (1), 50–89.
- (3) Sutton, B. M. Gold Compounds for Rheumatoid Arthritis. *Gold Bull.* **1986**, *19* (1), 15–16.
- (4) Sadler, P. J. The Biological Chemistry of Gold. *Gold Bull.* **1976**, *9*, 110–118.
- (5) Faa, G.; Gerosa, C.; Fanni, D.; Lachowicz, J. I.; Nurchi, V. M. Gold - Old Drug with New Potentials. *Curr. Med. Chem.* **2017**, *25*, 75–84.
- (6) Ott, I. On the Medicinal Chemistry of Gold Complexes as Anticancer Drugs. *Coord. Chem. Rev.* **2009**, *253*, 1670–1681.
- (7) Navarro, M. Gold Complexes as Potential Anti-Parasitic Agents. *Coord. Chem. Rev.* **2009**, *253* (11–12), 1619–1626.
- (8) Glišić, B.; Djuran, M. I. Gold Complexes as Antimicrobial Agents: An Overview of Different Biological Activities in Relation to the Oxidation State of the Gold Ion and the Ligand Structure. *J. Chem. Soc. Dalt. Trans.* **2014**, *43* (16), 5950–5969.

- (9) Fricker, S. P. Medical Uses of Gold Compounds: Past, Present and Future. *Gold Bull.* **1996**, 29 (2), 53–60.
- (10) Roder, C.; Thomson, M. J. Auranofin: Repurposing an Old Drug for a Golden New Age. *Drugs R D* **2015**, 15, 13–20.
- (11) Dorel, R.; Echavarren, A. M. Gold(I)-Catalyzed Activation of Alkynes for the Construction of Molecular Complexity. *Chem. Rev.* **2015**, 115 (17), 9028–9072.
- (12) Teles, J. H.; Brode, S.; Chabanas, M. Cationic Gold(i) Complexes: Highly Efficient Catalysts for the Addition of Alcohols to Alkynes. *Angew. Chemie - Int. Ed.* **1998**, 37 (10), 1415–1418.
- (13) Zou, T.; Lum, C. T.; Lok, C. N.; To, W. P.; Low, K. H.; Che, C. M. A Binuclear Gold(I) Complex with Mixed Bridging Diphosphine and Bis(N-Heterocyclic Carbene) Ligands Shows Favorable Thiol Reactivity and Inhibits Tumor Growth and Angiogenesis in Vivo. *Angew. Chemie - Int. Ed.* **2014**, 53 (23), 5810–5814.
- (14) Frank Shaw, C. Gold-Based Therapeutic Agents. *Chem. Rev.* **1999**, 99 (9), 2589–2600.
- (15) Nomiya, K.; Yamamoto, S.; Noguchi, R.; Yokoyama, H.; Kasuga, N. C.; Ohyama, K.; Kato, C. Ligand-Exchangeability of 2-Coordinate Phosphinegold(I) Complexes with AuSP and AuNP Cores Showing Selective Antimicrobial Activities against Gram-Positive Bacteria. Crystal Structures of [Au(2-Hmpa)(PPh<sub>3</sub>)] and [Au(6-Hmna)(PPh<sub>3</sub>)] (2-H2mpa=2-Mercaptopropio. *J. Inorg. Biochem.* **2003**, 95 (2–3), 208–220.
- (16) Křikavová, R.; Hošek, J.; Vančo, J.; Hutýra, J.; Dvořák, Z.; Trávníček, Z. Gold(I)-Triphenylphosphine Complexes with Hypoxanthine-Derived Ligands: In Vitro Evaluations of Anticancer and Anti-Inflammatory Activities. *PLoS One* **2014**, 9 (9), e107373.
- (17) Raubenheimer, H. G.; Schmidbaur, H. The Late Start and Amazing Upswing in Gold Chemistry. *J. Chem. Educ.* **2014**, 91 (12), 2014–2036.
- (18) Chrysouli, M. P.; Banti, C. N.; Kourkoumelis, N.; Panayiotou, N.; Markopoulos, G. S.; Tasiopoulos, A. J.; Hadjikakou, S. K. Chloro(Triphenylphosphine)Gold(I) a Forefront Reagent in Gold Chemistry as Apoptotic Agent for Cancer Cells. *J. Inorg. Biochem.* **2018**, 179, 107–120.

- (19) Gimeno, M. C. Modern Supramolecular Gold Chemistry: Gold-Metal Interactions and Applications. In *Modern Supramolecular Gold Chemistry: Gold-Metal Interactions and Applications*; Laguna, A., Ed.; WILEY-VCH Verlag GmbH & Co. KGaA, Weinheim, 2008; pp 1–63.
- (20) Schmidbaur, H.; Schier, A. Auophilic Interactions as a Subject of Current Research: An up-Date. *Chem. Soc. Rev.* **2012**, *41* (1), 370–412.
- (21) Pacchioni, G.; Bagus, P. S. Metal-Phosphine Bonding Revisited.  $\sigma$ -Basicity,  $\pi$ -Acidity, and the Role of Phosphorus d Orbitals in Zerovalent Metal-Phosphine Complexes. *Inorg. Chem.* **1992**, *31* (21), 4391–4398.
- (22) Häberlen, O. D.; Rösch, N. Effect of Phosphine Substituents in Gold(I) Complexes: A Theoretical Study of MeAuPR<sub>3</sub>, R = H, Me, Ph. *J. Phys. Chem.* **1993**, *97* (19), 4970–4973.
- (23) Carlos Lima, J.; Rodriguez, L. Phosphine-Gold(I) Compounds as Anticancer Agents: General Description and Mechanisms of Action. *Anticancer. Agents Med. Chem.* **2012**, *11* (10), 921–928.
- (24) Berners-Price, S. J.; Filipovska, A. Gold Compounds as Therapeutic Agents for Human Diseases. *Metallomics* **2011**, *3* (9), 863–873.
- (25) Liu, W.; Gust, R. Metal N-Heterocyclic Carbene Complexes as Potential Antitumor Metallodrugs. *Chem. Soc. Rev.* **2013**, *42* (2), 755–773.
- (26) Iqbal, M. S.; Taqi, S. G.; Arif, M.; Wasim, M.; Sher, M. In Vitro Distribution of Gold in Serum Proteins after Incubation of Sodium Aurothiomalate and Auranofin with Human Blood and Its Pharmacological Significance. *Biol. Trace Elem. Res.* **2009**, *130* (3), 204–209.
- (27) Takashi Amagai, T. Preparation and Crystal Structure of New Gold(I) Complexes Linked to Pyrimidines. *Bull. Chem. Soc. Jpn.* **1989**, *62* (4), 1078–1080.
- (28) Andermark, V.; Göke, K.; Kokoschka, M.; Abu El Maaty, M. A.; Lum, C. T.; Zou, T.; Sun, R. W. Y.; Aguiló, E.; Oehninger, L.; Rodríguez, L.; et al. Alkynyl Gold(I) Phosphane Complexes: Evaluation of Structure-Activity-Relationships for the Phosphane Ligands, Effects on Key Signaling Proteins and Preliminary in-Vivo Studies with a Nanoformulated Complex. *J. Inorg. Biochem.* **2016**, *160*, 140–148.

- (29) Hikisz, P.; Szczupak, Ł.; Koceva-Chyla, A.; Gušpiel, A.; Oehninger, L.; Ott, I.; Therrien, B.; Solecka, J.; Kowalski, K. Anticancer and Antibacterial Activity Studies of Gold(I)-Alkynyl Chromones. *Molecules* **2015**, *20* (11), 19699–19718.
- (30) De Nisi, A.; Bergamini, C.; Leonzio, M.; Sartor, G.; Fato, R.; Naldi, M.; Monari, M.; Calonghi, N.; Bandini, M. Synthesis, Cytotoxicity and Anti-Cancer Activity of New Alkynyl-Gold(i) Complexes. *Dalt. Trans.* **2016**, *45* (4), 1546–1553.
- (31) Fernández-Moreira, V.; Herrera, R. P.; Gimeno, M. C. Anticancer Properties of Gold Complexes with Biologically Relevant Ligands. *Pure Appl. Chem.* **2019**, *91* (2), 247–269.
- (32) Yue, S.; Luo, M.; Liu, H.; Wei, S. Recent Advances of Gold Compounds in Anticancer Immunity. *Front. Chem.* **2020**, *8* (543).
- (33) Liu, N.; Li, X.; Huang, H.; Zhao, C.; Liao, S.; Yang, C.; Liu, S.; Song, W.; Lu, X.; Lan, X.; et al. Clinically Used Antirheumatic Agent Auranofin Is a Proteasomal Deubiquitinase Inhibitor and Inhibits Tumor Growth. *Oncotarget* **2014**, *5* (14), 5453–5471.
- (34) Thangamani, S.; Mohammad, H.; Abushahba, M. F. N.; Sobreira, T. J. P.; Hedrick, V. E.; Paul, L. N.; Seleem, M. N. Antibacterial Activity and Mechanism of Action of Auranofin against Multi-Drug Resistant Bacterial Pathogens. *Sci. Rep.* **2016**, *6*, 1–13.
- (35) Cui, Y.; Zhao, Y.; Tian, Y.; Zhang, W.; Lü, X.; Jiang, X. The Molecular Mechanism of Action of Bactericidal Gold Nanoparticles on Escherichia Coli. *Biomaterials* **2012**, *33*, 2327–2333.
- (36) Kenji, N.; Ryusuke, N.; Takaye, S.; Yoshihiro, K.; Tsuda, K.; Ohsawa, K.; Kasuga, N. C.; Oda, M. Synthesis and Structural Characterization of Silver ( I ) and Gold ( I ) Complexes with 2-Mercaptonicotinic Acid ( H<sub>2</sub> Mna ) and Triphenylphosphine Ligands , and Their Antimicrobial Activities . Crystal Structures of Monomeric , 3- and 4-Coordinate Silver. *Bull. Chem. Soc. Jpn.* **2000**, *73* (1143).
- (37) Noguchi, R.; Hara, A.; Sugie, A.; Nomiya, K. Synthesis of Novel Gold ( I ) Complexes Derived by AgCl-Elimination between [ AuCl ( PPh<sub>3</sub> ) ] and Silver ( I ) Heterocyclic Carboxylates , and Their Antimicrobial Activities . Molecular Structure of [ Au ( R , S -Hpyrrld )( PPh<sub>3</sub> ) ] ( H<sub>2</sub> Pyrld = 2-Pyrro. *Inorg. Chem. Commun.* **2006**, *9*, 355–359.

- (38) de Almeida, A. M.; de Oliveira, B. A.; de Castro, P. P.; de Mendonça, C. C.; Furtado, R. A.; Nicoletta, H. D.; da Silva, V. L.; Diniz, C. G.; Tavares, D. C.; Silva, H.; et al. Lipophilic Gold(I) Complexes with 1,3,4-Oxadiazol-2-Thione or 1,3-Thiazolidine-2-Thione Moieties: Synthesis and Their Cytotoxic and Antimicrobial Activities. *BioMetals* **2017**, *30* (6), 841–857.
- (39) Tizotti, M. K.; Hörner, R.; Freitas, A. G. O. De; Kempfer, C. B.; Bottega, A.; Rodrigues, J. N.; Cóser, V. M.; Locatelli, A.; Paraginski, G.; Giacomelli, C.; et al. Inorganica Chimica Acta X-Ray Characterization and in Vitro Biological Evaluation and the Gold ( I ) Triazenide Complex {Au( I ) [ RPhNNNPhR ] [ PPh<sub>3</sub> ] } [ R = ( C=O ) NH<sub>2</sub>, R' = ( C=O ) CH<sub>3</sub> ]. *Inorganica Chim. Acta* **2016**, *441*, 78–85.
- (40) Rigon, C.; Terra, S.; Andrei, P.; Alexandre, F.; Soares, A.; Lourenço, L. De; Matiko, M.; Campos, A. De. Microbial Pathogenesis Molecular Docking , and Anti-Bio Fi Lm Activity of Gold-Complexed Sulfonamides on Pseudomonas Aeruginosa. *Microb. Pthogenes*. **2018**, *125*, 393–400.
- (41) Ciofu, O.; Tolker-nielsen, T. Tolerance and Resistance of Pseudomonas Aeruginosa Biofilms to Antimicrobial Agents — How P . Aeruginosa Can Escape Antibiotics. *Front. Microbiol.* **2019**, *10*, 913.
- (42) Rigon, C.; Terra, S.; Flores, C.; Albertina, V.; Cordenonsi, P.; Guidolin, G.; Cruz, T.; Alexandre, F.; Soares, A.; Lourenço, L. De. Microbial Pathogenesis The Antibacterial and Anti-Bio Film Activity of Gold-Complexed Sulfonamides against Methicillin-Resistant Staphylococcus Aureus. *Microb. Pthogenes*. **2018**, *123*, 440–448.
- (43) Zgurskaya, H. I.; Lopez, C. A.; Gnanakaran, S. Permeability Barrier of Gram-Negative Cell Envelopes and Approaches To Bypass It. *ACS Infect. Dis.* **2015**, *1*, 512–522.
- (44) Eiter, L. C.; Hall, N. W.; Day, C. S.; Saluta, G.; Kucera, G. L.; Bierbach, U. Gold(I) Analogues of a Platinum-Acridine Antitumor Agent Are Only Moderately Cytotoxic but Show Potent Activity against Mycobacterium Tuberculosis. *J. Med. Chem.* **2009**, *52* (21), 6519–6522.
- (45) Chaves, J. D. S.; Damasceno, J. L.; Paula, M. C. F.; De Oliveira, P. F.; Azevedo, G. C.; Matos, R. C.; Lourenço, M. C. S.; Tavares, D. C.; Silva, H.; Fontes, A. P. S.; et al. Synthesis, Characterization, Cytotoxic and Antitubercular Activities of New Gold(I) and Gold(III) Complexes Containing Ligands Derived from Carbohydrates. *BioMetals* **2015**, *28* (5), 845–860.



- (46) Agertt, V. A.; Marques, L. L.; Bonez, P. C.; Dalmolin, T. V.; Manzoni De Oliveira, G. N.; De Campos, M. M. A. Evaluation of Antimycobacterial Activity of a Sulphonamide Derivative. *Tuberculosis* **2013**, *93* (3), 318–321.
- (47) Agertt, V. A.; Bonez, P. C.; Rossi, G. G.; Flores, V. da C.; Siqueira, F. dos S.; Mizdal, C. R.; Marques, L. L.; de Oliveira, G. N. M.; de Campos, M. M. A. Identification of Antimicrobial Activity among New Sulfonamide Metal Complexes for Combating Rapidly Growing Mycobacteria. *BioMetals* **2016**, *29* (5), 807–816.
- (48) Yamazaki, K.; Kaneko, Y.; Suwa, K.; Ebara, S.; Nakazawa, K.; Yasuno, K. Synthesis of Potent and Selective Inhibitors of Candida Albicans N-Myristoyltransferase Based on the Benzothiazole Structure. *Bioorganic Med. Chem.* **2005**, *13* (7), 2509–2522.
- (49) Rajeeva, B.; Srinivasulu, N.; Shantakumar, S. M. Synthesis and Antimicrobial Activity of Some New 2-Substituted Benzothiazole Derivatives. *E-Journal Chem.* **2009**, *6* (3), 775–779.
- (50) Preisenberger, M.; Schier, A.; Schmidbaur, H. (Phosphine)Gold(I) Trifluoromethanesulfonates, Trifluoroacetates and Trichlorothioacetates. *Dalt. Trans.* **1999**, 1645–1650.
- (51) Serratrice, M.; Cinellu, M. A.; Maiore, L.; Pilo, M.; Zucca, A.; Gabbiani, C.; Guerri, A.; Landini, I.; Nobili, S.; Mini, E.; et al. Synthesis, Structural Characterization, Solution Behavior, and in Vitro Antiproliferative Properties of a Series of Gold Complexes with 2-(2'-Pyridyl)Benzimidazole as Ligand: Comparisons of Gold(III) versus Gold(I) and Mononuclear versus Binuclear Derivat. *Inorg. Chem.* **2012**, *51* (5), 3161–3171.
- (52) Stenger-Smith, J.; Chakraborty, I.; Sameera, W. M. C.; Mascharak, P. K. Antimicrobial Silver (I) Complexes Derived from Aryl-Benzothiazoles as Turn-on Sensors: Syntheses, Properties and Density Functional Studies. *Inorganica Chim. Acta* **2018**, *471*, 326–335.
- (53) Hsu, C. W.; Lin, C. C.; Chung, M. W.; Chi, Y.; Lee, G. H.; Chou, P. T.; Chang, C. H.; Chen, P. Y. Systematic Investigation of the Metal-Structure-Photophysics Relationship of Emissive D10-Complexes of Group 11 Elements: The Prospect of Application in Organic Light Emitting Devices. *J. Am. Chem. Soc.* **2011**, *133* (31), 12085–12099.

- (54) Thwaite, S. E.; Schier, A.; Schmidbaur, H. The Auration of 2-Hydroxy-Pyridine (2-Pyridone): Preparative and Structural Studies and a Comparison with Reactions of Related Aliphatic O,N-Donors. *Inorganica Chim. Acta* **2004**, 357 (5), 1549–1557.
- (55) Lalinde, E.; Lara, R.; López, I. P.; Moreno, M. T.; Alfaro-Arnedo, E.; Pichel, J. G.; Piñeiro-Hermida, S. Benzothiazole-Based Cycloplatinated Chromophores: Synthetic, Optical, and Biological Studies. *Chem. - A Eur. J.* **2018**, 24 (10), 2440–2456.
- (56) Carrington, S. J.; Chakraborty, I.; Bernard, J. M. L.; Mascharak, P. K. A Theranostic Two-Tone Luminescent PhotoCORM Derived from Re(I) and (2-Pyridyl)-Benzothiazole: Trackable CO Delivery to Malignant Cells. *Inorg. Chem.* **2016**, 55 (16), 7852–7858.
- (57) Carrington, S. J.; Chakraborty, I.; Bernard, J. M. L.; Mascharak, P. K. Synthesis and Characterization of a “Turn-on” PhotoCORM for Trackable Co Delivery to Biological Targets. *ACS Med. Chem. Lett.* **2014**, 5 (12), 1324–1328.
- (58) Albrecht, M.; Hiibler, K.; Kaim, W. Coordination of the Hetero(N,S)-Bidentate Ligand 1-Methyl-2- (Methylthiomethyl)-1H-Benzimidazole to [(Ph<sub>3</sub>P)Au]<sup>+</sup> Exclusively through the Imine Nitrogen Donor. *Zeitschrift für Naturforsch. B* **1999**, 52 (12), 1606–1608.
- (59) Munakata, M.; Yan, S. G.; Maekawa, M.; Akiyama, M.; Kitagawa, S. Solid and Solution Structures of Ternary Gold(I) Complexes with Triphenylphosphine and Nitrogen-Containing Ligands. *J. Chem. Soc. - Dalt. Trans.* **1997**, No. 22, 4257–4262.
- (60) Heilman, B. J.; St. John, J.; Oliver, S. R. J.; Mascharak, P. K. Light-Triggered Eradication of *Acinetobacter Baumannii* by Means of NO Delivery from a Porous Material with an Entrapped Metal Nitrosyl. *J. Am. Chem. Soc.* **2012**, 134 (28), 11573–11582.
- (61) Scott, P.; Deye, G.; Srinivasan, A.; Murray, C.; Moran, K.; Hulten, E.; Fishbain, J.; Craft, D.; Riddell, S.; Lindler, L.; et al. An Outbreak of Multidrug-Resistant *Acinetobacter Baumannii*-Calcoaceticus Complex Infection in the US Military Health Care System Associated with Military Operations in Iraq. *Clin. Infect. Dis.* **2007**, 44 (12), 1577–1584.
- (62) van Rijt, S. H.; Sadler, P. J. Current Applications and Future Potential for Bioinorganic Chemistry in the Development of Anticancer Drugs. *Drug Discov. Today* **2009**, 14 (23–24), 1089–1097.

- (63) Novelli, F.; Recine, M.; Sparatore, F.; Juliano, C. Gold(I) Complexes as Antimicrobial Agents. *Farmaco* **1999**, *54* (4), 232–236.
- (64) Chen, X.; Femia, F. J.; Babich, J. W.; Zubieta, J. Spectroscopic and Structural Studies of Complexes of the  $\text{Fac-}[\text{Re}(\text{N}\cap\text{N})(\text{CO})_3\text{L}]\text{N}^+$  Type ( $\text{N}\cap\text{N}$  = 2-(2-Pyridyl)Benzothiazole;  $\text{L}$  = Cl, Br,  $\text{CF}_3\text{SO}_3^-$ ,  $\text{CH}_3\text{CN}$ ). *Inorganica Chim. Acta* **2001**, *314* (1–2), 91–96.
- (65) Stenger-Smith, J.; Chakraborty, I.; Carrington, S.; Mascharak, P. Synthesis and Structures of Photoactive Manganese-Carbonyl Complexes Derived from 2-(Pyridin-2-Yl)-1,3-Benzothiazole and 2-(Quinolin-2-Yl)-1,3-Benzothiazole. *Acta Crystallogr. Sect. C Struct. Chem.* **2017**, *73* (4).
- (66) Bruker APEX 3. Bruker AXS Inc.: Madison, WI 2014.
- (67) Bruker SAINT. Bruker AXS Inc.: Madison, WI 2012.
- (68) Bruker SADABS. Bruker AXS Inc.: Madison, WI.
- (69) Sheldrick, G. M. SHELXT - Integrated Space-Group and Crystal-Structure Determination. *Acta Crystallogr. Sect. A Found. Crystallogr.* **2015**, *71* (1), 3–8.
- (70) Sheldrick, G. M. Crystal Structure Refinement with SHELXL. *Acta Crystallogr. Sect. C Struct. Chem.* **2015**, *71* (Md), 3–8.
- (71) Dolomanov, O. V.; Bourhis, L. J.; Gildea, R. J.; Howard, J. A. K.; Puschmann, H. OLEX2: A Complete Structure Solution, Refinement and Analysis Program. *J. Appl. Crystallogr.* **2009**, *42* (2), 339–341.
- (72) Serraticce, M.; Bertrand, B.; Janssen, E. F. J.; Hemelt, E.; Zucca, A.; Cocco, F.; Cinellu, M. A.; Casini, A. Gold(i) Compounds with Lansoprazole-Type Ligands: Synthesis, Characterization and Anticancer Properties in Vitro. *Med. Chem. Commun.* **2014**, *5* (9), 1418–1422.
- (73) Sotgiu, G.; Centis, R.; D'Ambrosio, L.; Battista Migliori, G. Tuberculosis Treatment and Drug Regimens. *Cold Spring Harb. Perspect. Med.* **2015**, *5* (5), 1–12.
- (74) Warzajtis, B.; Glišić, B. D.; Radulović, N. S.; Rychlewska, U.; Djuran, M. I. Gold(III) Complexes with Monodentate Coordinated Diazines: An Evidence for Strong Electron-Withdrawing Effect of Au(III) Ion. *Polyhedron* **2014**, *79*, 221–228.

- (75) Kabanda, M. M.; Tran, V. T.; Tran, Q. T.; Ebenso, E. E. A Computational Study of Pyrazinamide: Tautomerism, Acid-Base Properties, Micro-Solvation Effects and Acid Hydrolysis Mechanism. *Comput. Theor. Chem.* **2014**, *1046*, 30–41.
- (76) Stenger-Smith, J.; Chakraborty, I.; Mascharak, P. K. Cationic Au(I) Complexes with Aryl-Benzothiazoles and Their Antibacterial Activity. *J. Inorg. Biochem.* **2018**, *185*, 80–85.
- (77) Hill, D. T.; Burns, K.; Titus, D. D.; Girard, G. R.; Reiff, W. M.; Mascavage, L. M. Dichloro(Pyridine-2-Carboxamido-N1,N2)Gold(III), a Bis-Nitrogen Aurowcycle: Syntheses, Gold-197 Mossbauer Spectroscopy, and X-Ray Crystal Structure. *Inorganica Chim. Acta* **2003**, *346*, 1–6.
- (78) Dar, A.; Moss, K.; Cottrill, S. M.; Parish, R. V.; McAuliffe, C. A.; Pritchard, R. G.; Beagley, B.; Sandbank, J. Complexes of Gold(III) with Mononegative Bidentate N,O-Ligands. *J. Chem. Soc. Dalt. Trans.* **1992**, No. 12, 1907–1913.
- (79) Singh, A. K.; Reyrat, J.-M. Laboratory Maintenance of Mycobacterium Smegmatis. *Curr. Protoc. Microbiol.* **2009**, *14* (1), 10C.1.1–10C.1.12.
- (80) Catanho, M.; Mascarenhas, D.; Degrave, W.; Miranda, A. B. de. GenoMycDB: A Database for Comparative Analysis of Mycobacterial Genes and Genomes. *Genet. Mol. Res.* **2006**, *5* (1), 115–126.
- (81) Fenton, M. J.; Vermeulen, M. W. Immunopathology of Tuberculosis: Roles of Macrophages and Monocytes. *Infect. Immun.* **1996**, *64* (3), 683–690.
- (82) Bansal-Mutalik, R.; Nikaido, H. Mycobacterial Outer Membrane Is a Lipid Bilayer and the Inner Membrane Is Unusually Rich in Diacyl Phosphatidylinositol Dimannosides. *Proc. Natl. Acad. Sci. U. S. A.* **2014**, *111* (13), 4958–4963.
- (83) Zhang, Y.; Mitchison, D. The Curious Characteristics of Pyrazinamide: A Review. *Int. J. Tuberc. Lung Dis.* **2003**, *7* (1), 6–21.
- (84) Zhang, Y.; Scorpio, A.; Nikaido, H.; Sun, Z. Role of Acid PH and Deficient Efflux of Pyrazinoic Acid in Unique Susceptibility of Mycobacterium Tuberculosis to Pyrazinamide. *J. Bacteriol.* **1999**, *181* (7), 2044–2049.
- (85) Shaw, C. F.; Coffer, M. T.; Klingbeil, J.; Mirabelli, C. K. Application of a <sup>31</sup>P NMR Chemical Shift: Gold Affinity Correlation to Hemoglobin-Gold Binding and the First Inter-Protein Gold Transfer Reaction. *J. Am. Chem. Soc.* **1988**, *110* (3), 729–734.


- (86) Harbut, M. B.; Vilchèze, C.; Luo, X.; Hensler, M. E.; Guo, H.; Yang, B.; Chatterjee, A. K.; Nizet, V.; Jacobs, W. R.; Schultz, P. G.; et al. Auranofin Exerts Broad-Spectrum Bactericidal Activities by Targeting Thiol-Redox Homeostasis. *Proc. Natl. Acad. Sci. U. S. A.* **2015**, *112* (14), 4453–4458.
- (87) França, A.; Aggarwal, P.; Barsov, E. V.; Kozlov, S. V.; Dobrovolskaia, M. A.; González-Fernández, Á. Macrophage Scavenger Receptor A Mediates the Uptake of Gold Colloids by Macrophages in Vitro. *Nanomedicine* **2011**, *6* (7), 1175–1188.
- (88) Singh, R.; Nawale, L.; Arkile, M.; Wadhwani, S.; Shedbalkar, U.; Chopade, S.; Sarkar, D.; Chopade, B. A. Phytogetic Silver, Gold, and Bimetallic Nanoparticles as Novel Antitubercular Agents. *Int. J. Nanomedicine* **2016**, *11*, 1889–1897.
- (89) North, A. C. T.; Phillips, D. C.; Mathews, F. S. A Semi-empirical Method of Absorption Correction. *Acta Crystallogr. Sect. A* **1968**, *24* (3), 351–359.
- (90) Sheldrick, G. M. SHELXTL TM (V 6.14). Bruker Analytical X-ray Systems: Madison, WI 2000.

### 3.5 Reprints of Publications and Permissions


Reprinted with permissions from Stenger-Smith, J.; Mascharak, P. Gold Drugs with  $\{\text{Au}(\text{PPh}_3)\}^+$  moiety: Advantages and Medicinal Applications. *ChemMedChem*, **2020**, *15*, 2136-2145.


Reprinted with permissions from Stenger-Smith, J.; Chakraborty, I.; Mascharak, P. Cationic Au(I) complexes with aryl-benzothiazoles and their antibacterial activity. *Journal of Inorganic Biochemistry*. **2018**, *185*, 80-85.


Reprinted with permissions from Stenger-Smith, J.; Kamariza, M.; Chakraborty, I.; Ouattara, R.; Bertozzi, C. R.; Mascharak, P. K. Enhanced Bactericidal Effects of Pyrazinamide Towards *Mycobacterium smegmatis* and *Mycobacterium tuberculosis* upon conjugation to a [Au(I)-triphenylphosphine]<sup>+</sup> Moiety. *ACS Omega*, **2020**, 5, 6826-6833. <https://pubs.acs.org/doi/10.1021/acsomega.0c00071>.


 **Copyright Clearance Center**


**RightsLink®**


 Home

 Help

 Email Support

 Sign in

 Create Account



**Cationic Au(I) complexes with aryl-benzothiazoles and their antibacterial activity**  
Author: Jenny Stenger-Smith, Indranil Chakraborty, Pradip K. Mascharak  
Publication: Journal of Inorganic Biochemistry  
Publisher: Elsevier  
Date: August 2018  
*Published by Elsevier Inc.*

Please note that, as the author of this Elsevier article, you retain the right to include it in a thesis or dissertation, provided it is not published commercially. Permission is not required, but please ensure that you reference the journal as the original source. For more information on this and on your other retained rights, please visit: <https://www.elsevier.com/about/our-business/policies/copyright#Author-rights>

BACK CLOSE WINDOW

## Special Collection Gold Drugs with $\{\text{Au}(\text{PPh}_3)\}^+$ Moiety: Advantages and Medicinal Applications

Jenny R. Stenger-Smith<sup>[a]</sup> and Pradip K. Mascharak<sup>\*[a]</sup>

Following the success of Auranofin as an anti-arthritis drug, search for novel gold drugs has afforded a large number of  $[\text{L}-\text{Au}(\text{PPh}_3)]$  complexes that exhibit notable salutary effects. Unlike  $\text{Au}(\text{III})$ -containing species, these gold complexes with  $\{\text{Au}(\text{PPh}_3)\}^+$  moiety are stable in biological media and readily exchange L with S- and Se-containing enzymes or proteins. Such exchange leads to rapid reduction of microbial loads or

induction of apoptotic cell death at malignant sites. In many cases the lipophilic  $\{\text{Au}(\text{PPh}_3)\}^+$  moiety delivers a desirable toxic L to the specific cellular target in addition to exhibiting its own beneficial activity. Further research and utilization of this synthon in drug design could lead to novel chemotherapeutics for treatment of drug-resistant pathogens and cancers.

### 1. Introduction

Gold has been used for medicinal purposes since 2500 B.C. when Chinese physicians and surgeons employed gold foil for treatment of various diseases.<sup>[1]</sup> Gold therapy had not been of major interest until Robert Koch discovered that  $\text{K}[\text{Au}(\text{CN})_2]$  was effective against *Mycobacterium tuberculosis*, the causative agent of tuberculosis (TB), in the late 1800's.<sup>[2]</sup> The next major advancement was the development of  $\text{Au}(\text{I})$  complexes for the treatment of rheumatoid arthritis starting with  $\text{Au}(\text{I})$  thiolates in the 1930's and later the clinical approval of Auranofin (Figure 1) in the 1980's.<sup>[3]</sup>

Since then, research into additional therapeutic purposes of gold has expanded into its antimicrobial, anticancer, antiarthritic, antiparasitic, and antiviral effects with much initial success.<sup>[4–9]</sup> Many of the gold anticancer compounds reported have been claimed to be more effective than cisplatin, one of the most common metal containing chemotherapy drugs. Some gold species show potent activity towards *M. tuberculosis* and other infectious pathogens.<sup>[6]</sup> Even Auranofin has been studied for its repurposing as these types of therapeutic agents.<sup>[10]</sup>

Cationic gold mainly exists in two forms; linear  $\text{Au}(\text{I})$  and square-planar  $\text{Au}(\text{III})$ , both of which have been evaluated for their biological activity. A special interest has been developed with gold(I) phosphine species not only for their therapeutic activity but also as effective catalysts for numerous reactions with alkynes.<sup>[6,11,12]</sup> The ligand exchangeability of linear  $\{\text{Au}(\text{PR}_3)\}^+$  species is thought to play a crucial role in both the inhibition of biological molecules and the effectiveness as a catalyst (Figure 1).<sup>[12–15]</sup> Of these gold(I) phosphine complexes,

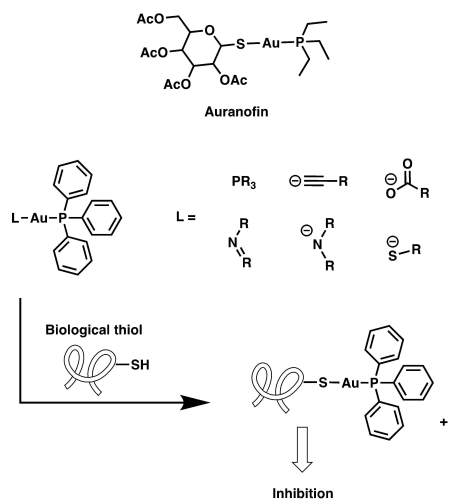


**Figure 1.** Auranofin, examples of linear arrangement of  $[\text{L}-\text{Au}(\text{PPh}_3)]$  complexes and their reaction with biological thiols leading to the biological activity.

many gold(I) triphenylphosphine  $[\text{L}-\text{Au}(\text{PPh}_3)]$  species (Figure 1) have been of particular interest due to their stability and wide variety of the L ligand which determines their catalytic reactivity and the kinetic profile of their biological activity.<sup>[16,17]</sup> Even the "parent" compound  $[\text{Cl}-\text{Au}(\text{PPh}_3)]$  has shown effective anticancer activity against human breast (MCF-7) and fetal lung fibroblast cells, and was more selective towards cancerous cells over normal cells compared to both cisplatin and the  $\{\text{Au}(\text{PET})_3\}^+$  containing Auranofin.<sup>[18]</sup> In this review we aim to highlight the antimicrobial, anticancer, antiparasitic, anti-inflammatory and antiviral effects of  $[\text{L}-\text{Au}(\text{PPh}_3)]$  complexes.

[a] J. R. Stenger-Smith, Prof. P. K. Mascharak  
Department of Chemistry and Biochemistry  
University of California, Santa Cruz  
1156 High Street, Santa Cruz, CA 95064 (USA)  
E-mail: pradip@ucsc.edu

This article belongs to the joint Special Collection with the European Journal of Inorganic Chemistry, "Metals in Medicine".

## 2. Gold-Phosphine Chemistry

Gold(I), an electron rich  $d^{10}$  transition metal, typically forms complexes with linear geometry and can be partially explained by the relativistic effects of post lanthanide elements.<sup>[19]</sup> The aerophilic interactions (gold-gold contacts) observed in gold chemistry give rise to very interesting photophysical, catalytic and clustering properties.<sup>[20]</sup> Although gold(I) phosphine complexes of the type  $[L-Au(PR_3)]$  will be discussed hereafter to keep this review focused, there are variety of other donor ligands that can be present on a gold(I) center such as arsine, isocyanide, carbene, ylide, amine, halide, alkyl, aryl, and chalcogenolide.

Gold(I) phosphine complexes have been extensively studied with particular interest in the influence of the phosphine ligands on the metal-P bond.<sup>[17,21,22]</sup> For  $PR_3$  ligands, the R substituent plays an important role in their sigma donor strength as well as  $\pi$ -acceptor capabilities; the more electro-negative the R group, the more stable the empty  $P-R \sigma^*$  orbital and thus becomes a better acceptor of electron density from the metal center. This property is of special importance in the catalytic activity of  $\{Au(PR_3)\}^+$  species; the R substituents on the phosphine determines the electrophilicity of the ionic fragments  $\{Au(PR_3)\}^+$  used as catalytic activators of substrates (usually alkynes and allenes).<sup>[17]</sup> These slight variations influence the way  $\{Au(PR_3)\}^+$  reacts with the substrate and stabilize intermediates and thus the outcome of the reaction. Specifically, this is apparent in cationic gold(I) catalysis of the addition of alcohols to alkynes where  $\{Au(PPh_3)\}^+$  was more active than  $\{Au(PEt_3)\}^+$  in this particular type of reaction.<sup>[12]</sup> This same concept likely influences the binding of the  $\{Au(PR_3)\}^+$  species to biological molecules and influence their overall activity. Gold (I) interactions with biological proteins and peptides can also be described by hard soft acid base theory; a soft metal center like Au(I) binds tightly to soft ligands like sulfur (present in the common amino acid cysteine).

Numerous  $[L-Au(PPh_3)]$  species have been identified, the simplest being  $[Cl-Au(PPh_3)]$ , which is used extensively for the synthesis of new compounds of this type by replacement of the Cl ligand. The stability of the  $\{Au(PPh_3)\}^+$  fragment allows for

many L donor ligands, the most common types are alkynyl, nitrogen, phosphorus and sulfur containing (Figure 1) which result in either a neutral or cationic species.<sup>[8,23]</sup> One advantage of this type of complexes is their relatively simple synthesis and purification often involving  $[Cl-Au(PPh_3)]$  and either (a) the introduction of the protonated ligand and a base or (b) the addition of  $Ag^+X^-$  to form AgCl precipitate in the presence of the ligand (Scheme 1). The structural complexity of potential L ligands provides endless possibilities to rationalize the influence (lipophilicity, hydrophilicity, additional drug targets) it has on the efficacy of  $[L-Au(PPh_3)]$  species.

## 3. Anticancer Activity

Gold complexes have been widely studied for their activity as anticancer agents.<sup>[6,14,24,25]</sup> It is generally believed that ligand exchange of linear  $[L-Au(PPh_3)]$  complexes with bioactive molecules results in their antitumor activity (Figure 1).<sup>[14,16]</sup> The exchange of  $L=N/S$ -donor ligands occurs rapidly within the blood (20 min) while exchange of the  $PPh_3$  ligand is much slower.<sup>[16,26]</sup> The weaker bonded ligands in many cases thus influence the kinetic profile of these compounds. Loss of the L ligand in solution with relevant biological thiols such as glutathione and cysteine is observed and can be easily detected by ESI-MS and NMR spectroscopy.<sup>[16,27]</sup> In blood serum, gold species readily binds albumin and other globulins and maintains a sustained presence of the gold drug in cellular matrices for days.<sup>[26]</sup> This ligand exchange activity with biological molecules is likely what causes the inhibition of cytosolic and mitochondrial Thioredoxin reductase (TrxR) which has been identified as the major cause of apoptotic death of cancer cells by  $[L-Au(PPh_3)]$  complexes.<sup>[28-31]</sup> Mammalian TrxR isoenzymes are selenoproteins with a redox active selenocysteine residue at their active sites which likely binds strongly to the  $\{Au(PPh_3)\}^+$  moiety and interferes severely with cellular redox homeostasis leading to cell death. The facile ligand exchange property of the  $[L-Au(PPh_3)]$  complexes could also involve other targets in cancer cells and the cellular death could be a result of combination of such bindings. Recent studies also indicate that



Jenny Stenger-Smith received her BS in Chemistry at California Polytechnic University San Luis Obispo in 2015 and is currently finishing her PhD at the University of California Santa Cruz under the supervision of Prof. Pradip Mascharak. Her graduate research has focused on the development of silver and gold complexes as antimicrobial agents.



Pradip Mascharak, Distinguished Professor of Chemistry and Biochemistry at the University of California, Santa Cruz, is a bioinorganic chemist. He received his Ph. D. from the Indian Institute of Technology at Kanpur, India, in 1978 and did his post-doctoral work first at Stanford University and then at Harvard University. He also worked as a research associate at Massachusetts Institute of Technology for two years before he joined the Department of Chemistry and Biochemistry in 1984. His research interests span a wide range of areas including modeling the active sites of metalloenzymes, drug-receptor interactions, delivery of small signaling molecules (such as NO and CO) to biological targets, and design of biomaterials for drug delivery.



Scheme 1. Typical synthetic routes for [L-Au(PPh<sub>3</sub>)] complexes.

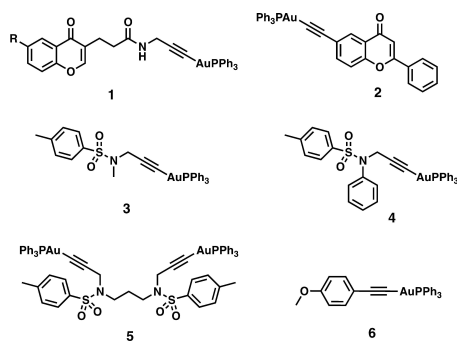
complexes with {Au(PPh<sub>3</sub>)}<sup>+</sup> moiety suppress cancer-promoting inflammation by inhibiting secretion of pro-inflammatory cytokines such as tumor necrosis factor- $\alpha$  (TNF- $\alpha$ ) and interleukin-1b (IL-1b).<sup>[16,32]</sup> Gold phosphine compounds are known to inhibit the ubiquitin-proteasome system (UPS) in cancer cells.<sup>[33]</sup> Many different cancers, such as colon, prostate and leukemia, rely on the UPS system more heavily than non-cancer cells. Because UPS is involved in many cellular processes, including cell cycle regulation, protein degradation, gene expression and DNA repair, inhibition of these by gold compounds induces apoptosis.

A recent study involving the parent complex [Cl-Au(PPh<sub>3</sub>)] has demonstrated anticancer properties against human breast and fetal lung fibroblast cells and the cytotoxic activity is stronger than that of cisplatin and Auranofin.<sup>[18]</sup> Although sparingly soluble in aqueous media, this complex exhibited permeation of mitochondrial membranes due to the presence of the {Au(PPh<sub>3</sub>)}<sup>+</sup> unit and induced robust mitochondrion inhibitory activity in several cancer cell lines. Other [L-Au(PPh<sub>3</sub>)] anticancer complexes reported to date contain a variety of L ligands, most commonly as alkynyl,<sup>[28–30,34]</sup> sulfur,<sup>[35–37]</sup> or nitrogen<sup>[27,38,39]</sup> containing ligands. Alkynyl complexes **1** and **2** (Figure 2) containing chromone derivatives, medicinally important plant metabolites, and {Au(PPh<sub>3</sub>)}<sup>+</sup> showed potent activity against human liver and breast cancer cells with IC<sub>50</sub> (concentration required inhibit 50% growth) values in the low micromolar range.<sup>[29]</sup> These complexes were found to mainly target the mitochondria and promote apoptosis arising from TrxR inhibition, caspase 3 and 9 activation, DNA damage and cell

cycle disturbances. Other alkynyl species **3–5** (Figure 2) were investigated with propargylic amine derivatives to examine the influence of the sidearm towards their biological activity.<sup>[30]</sup> Compound **3**, bearing only one {Au(PPh<sub>3</sub>)}<sup>+</sup> unit was the most active to all three cell lines (human colorectal adenocarcinoma HT29, ovarian carcinoma IGROV1, and human promyelocytic leukaemia HL60 cells) with IC<sub>50</sub> values in the low micromolar range. In contrast complex **4** was only active in this range towards two cancerous lines and interestingly complex **5**, with two {Au(PPh<sub>3</sub>)}<sup>+</sup> moieties, was only active towards the IGROV1 cell line. Contrary to common findings, the most active compound **3**, showed no TrxR inhibition, but toxicity could be attributed to its interactions with DNA. The complex **6** (Figure 2) bearing a 4-ethynylanisole ligand coordinated to the {Au(PPh<sub>3</sub>)}<sup>+</sup> unit along with other alkynyl Au phosphine derivatives have shown promising anticancer activity.<sup>[28,34]</sup> These complexes were identified to be a strong inhibitors of TrxR with activity towards HT-29 and the human breast cancer MDA-MB-231 cell lines in the low  $\mu$ M range. *In vivo* studies with **6** were challenging due to the solubility of this species. Various methods for dissolving the compound were employed, but ultimately peanut oil nanoemulsion showed the greatest loading of **6** (0.098 mg/mL) and was employed as an intertumoral injection into a NCI-H460 xenograft mouse model. Results showed that treatment was not effective as the tumors did not change in size but was well tolerated by the mice. The inactivity might be due to the low dosage caused by the insolubility of the complex.

Triphenylphosphinegold(I) complexes with sulfanyl-propionate ligands such as **7** (Figure 3) exhibit antineoplastic activity in human cervix and ovarian cancer cells comparable to cisplatin.<sup>[35]</sup> [L-Au(PPh<sub>3</sub>)] complexes **8** and **9** (Figure 3), containing 1,3,4-oxadiazol-2-thione or 1,3-thiazolidine-2-thione derivatives, chosen for their analgesic and anti-inflammatory properties, showed activity against various cancer cell lines.<sup>[36]</sup> The variation of the alkyl chain length in both **8** (n=6, 8, 10, 12, 14) and **9** (n=7, 9, 11, 13, 15) proved that the varying biological activity of these types of complexes is not a simple correlation of toxicity to lipophilicity. The bimetallic sulfur bound complex **10** (Figure 3) was tested for its antitumor activity using a mouse model, and showed reduction in tumor growth activity (treatment to control, T/C ratio=128) quite comparable to 5-fluorouracil.<sup>[37]</sup> Interestingly, the similar bimetallic complex with {Au(PEt<sub>3</sub>)}<sup>+</sup> with a bridging dithiolate ligand was extremely toxic, causing the mice to die rapidly (T/C ratio=30) compared to **10**.

Extensive studies on various [L-Au(PPh<sub>3</sub>)] complexes **11–16** with biologically active ligands (amino acids, DNA bases and peptides) reported by Gimeno and coworkers, have provided insight into the structure-activity relationship in this type of complexes.<sup>[31,40–42]</sup> Complexes **11–16** (Figure 3) are just a few of the {Au(PPh<sub>3</sub>)}<sup>+</sup> type species that show potent anticancer activity against various cancer cell lines and show inhibition of TrxR. Two key findings from these studies related to {Au(PPh<sub>3</sub>)}<sup>+</sup> were that compounds containing cysteine dipeptides were the most active towards the cancer cell lines and that structural modifications to include cyclic amino acid (**11–14**) or conjugation

Figure 2. Alkynyl [L-Au(PPh<sub>3</sub>)] complexes showing anticancer activity.

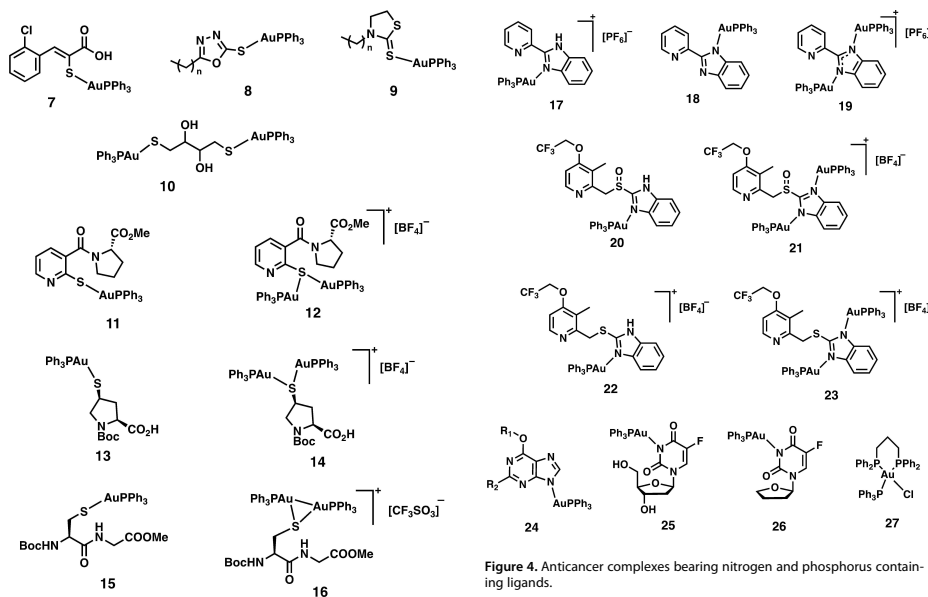


**Figure 4.** Anticancer complexes bearing nitrogen and phosphorus containing ligands.

**Figure 3.** [L–Au(PPh<sub>3</sub>)] compounds with sulfur bound ligands that have been evaluated for their anticancer activity.

tion of a second {Au(PPh<sub>3</sub>)}<sup>+</sup> center seemed to show improved activity (12, 14 and 16).<sup>[31]</sup> The structure relationship comparison was described in great detail in these accounts and the findings could provide insight into future design of anticancer Au-phosphine complexes.

Complexes 17–19 (Figure 4), [L–Au(PPh<sub>3</sub>)] complexes with L = benzimidazole- and pyrimidine-based ligands, have also shown promising antiproliferative results *in vitro*.<sup>[38]</sup> The pyridyl-benzimidazole ligand was chosen for its anti-inflammatory properties and to allow multiple N-donor binding sites for studying structure-function relations. Complexes 17–19 showed impressive antiproliferative activities on the A2780 ovarian cancer cell line and its cisplatin-resistant counterpart line (IC<sub>50</sub> 0.60–3.57 μM). Notably, an improvement in activity was observed in the A2780 line with 17 and 18 (1.50 and 0.60 μM respectively) with {Au(PPh<sub>3</sub>)}<sup>+</sup> compared to the analogous complex with {AuCl} and {Au(TPA)} moieties (6.70 μM and 13.30 μM respectively, TPA = triazaphosphaadamantane). This indicates that the {Au(PPh<sub>3</sub>)}<sup>+</sup> unit plays an important role in the toxicity of gold(I) complexes with this type of ligand. There was no advantage of conjugation of two {Au(PPh<sub>3</sub>)}<sup>+</sup> units in complex 19 compared to 18 on its anticancer activity. Compounds 20–23 (Figure 4) with lansoprazole type ligands also showed potent anticancer results on the same A2780 and cisplatin-resistant cells lines (IC<sub>50</sub> = 0.7–4.2 μM).<sup>[39]</sup> Lansoprazole

(N-donor ligand in 20 and 21) is a proton pump inhibitor and could potentially increase chemosensitivity of tumor cells. The most active compounds against the cisplatin-resistant cells line were 20 and 21 (IC<sub>50</sub> = 0.7 μM and 0.9 μM) bearing lansoprazole derivatives. However, the compounds 22 and 23 (not bearing the sulfinyl group that leads to activation of the ligand responsible for V<sub>H</sub>-ATPase inhibition and thus proton pump inhibition) still showed similar impressive activity in resistant cells lines (IC<sub>50</sub> = 4.2 μM and 1.2 μM). All compounds showed some selectivity towards cancer cells and were less effective towards the non-cancerous HEK-293T cell line.

Complexes of type 24 (R<sub>1</sub> = ethyl, n-butyl, allyl, benzyl, phenylethyl and R<sub>2</sub> = H, Cl, Figure 4) with hypoxanthine derivatives, which have been shown to inhibit several enzymes, were also evaluated for their anticancer activity.<sup>[16]</sup> Most IC<sub>50</sub> values were in the low micromolar range against numerous cell lines including lung adenocarcinoma A549, melanoma G-361, HeLa, and cisplatin-resistant ovarian carcinoma A2780R. Most proved more effective than cisplatin on the cell lines chosen. Results of ESI-MS studies with 24 type of complex indicate that reactions with thiol containing biomolecules like cysteine and reduced glutathione by replacement of the N donor ligand to form [glutathione–Au(PPh<sub>3</sub>)] and [cysteine–Au(PPh<sub>3</sub>)] type intermediates could reflect their ability to inhibit TrxR. Earlier reports of 5-fluorouracil derivatives, 25 and 26 (Figure 4), also react with methanethiol, p-toluene thiol and histidine residues forming the thiolate- or imidazole-bound {Au(PPh<sub>3</sub>)}<sup>+</sup> species, indicating potential reaction with cysteine or histidine residues

*in vitro*.<sup>[27]</sup> Enhanced antitumor activity on a mice model was observed by **25** compared to the ligand itself.

The mixed phosphine complex with  $\{\text{Au}(\text{PPh}_3)\}^+$  moiety **27** exhibits strong anticancer effects on MCF-7 breast cancer cells and human melanoma cells.<sup>[43,44]</sup> In both cases alterations in the nuclear morphology, loss of membrane potential, release of cytochrome c from mitochondria and caspase activation confirm apoptotic cell death. The bridging phosphine ligand is lost when this complex reacts with thiols such as cysteine. Because the complex partially converts to the binuclear complex  $\{[\text{AuCl}(\text{PPh}_3)]_2(\mu_2\text{-dppp})\}$ , the nature of the pharmacologically active species remains unclear.

Several general conclusions could be drawn regarding anticancer  $[\text{L}-\text{Au}(\text{PPh}_3)]$  complexes regardless of the L donor ligand from the results of these studies. Most complexes exhibit notable anticancer activities (low  $\mu\text{M}$  range) *in vitro* and some even show antitumor action *in vivo*. The efficacy of the complexes could be enhanced by choosing L ligands that themselves might have some anticancer activity or might enhance the lipophilicity (thus the overall activity). The results also provide strong support to the conclusion that much of the anticancer activity comes from the  $\{\text{Au}(\text{PPh}_3)\}^+$  moiety and is relatively independent of the L ligand regardless of its function. This is supported by the fact that most complexes afford similar  $\text{IC}_{50}$  values, with moderate variation from the L donor ligand. The superior lipophilicity of the gold complexes bearing  $\text{PPh}_3$  ligand (compared to  $\text{PEt}_3$ ) is evident in many examples although the exact advantage of the phosphine could be more complicated than that elucidated at this time. In fact, multiple studies show contradictory findings in which two  $\{\text{Au}(\text{PPh}_3)\}^+$  units in one complex either did or did not show the expected increase in activity compared to the analogous complex with the same L and one  $\{\text{Au}(\text{PPh}_3)\}^+$  unit. It is now apparent that the rate of uptake of the  $[\text{L}-\text{Au}(\text{PPh}_3)]$  complex into the cell, the extent to which thiol containing proteins and enzymes can be inhibited by this gold species, as well as the solubility of these types of complexes, all influence the overall activity. Although inhibition of TrxR appears to be the most common drug action, it is not the sole reason for the anticancer activity of these complexes. More investigations on the drug mechanism(s) of the  $[\text{L}-\text{Au}(\text{PPh}_3)]$  complexes are required to establish their utility as cancer chemotherapeutics. Because gold phosphine complexes have been shown to induce apoptosis of both cisplatin-sensitive and cisplatin-resistant human ovarian cancer cells,<sup>[45]</sup> co-administration of both the Pt and Au drugs could mitigate the problem related to drug resistance, a common impediment to cancer chemotherapy.

#### 4. Antibacterial Activity

To date, a few number of complexes of the type  $[\text{L}-\text{Au}(\text{PPh}_3)]$  have been studied for their antibacterial effects compared to similar complexes that have been evaluated for anticancer effect. Nevertheless, several gold complexes (and gold nanoparticles) have exhibited promising antimicrobial activity.<sup>[8]</sup> Inhibition of biosynthetic pathways such as cell wall synthesis,

DNA and protein synthesis as well as inhibition of enzymes such as ATP synthase have been identified as the mechanism(s) of action of these gold species.<sup>[46,47]</sup> Such participation in multiple pathways could be advantageous when considering bacterial infections by pathogens that have developed resistance to traditional antibiotics.

Among  $[\text{L}-\text{Au}(\text{PPh}_3)]$  complexes with L = N- and S-donor ligands, complexes **28–31** (Figure 5) have been shown to exert antimicrobial activity against Gram-positive *Bacillus subtilis* and *Staphylococcus aureus* (minimum inhibitory concentration, MIC 7.9–125  $\mu\text{g/mL}$ ), but no activity was noted towards Gram-negative *Escherichia coli* and *Pseudomonas aeruginosa*.<sup>[15,48]</sup> To model the interaction of these complexes with cysteine residues present in biological molecules, the ligand exchangeability of **28–31** and other N/S bound  $\{\text{Au}(\text{PPh}_3)\}^+$  species has been examined. The majority of these reactions led to cleavage of the Au–N/S bond rather than the Au– $\text{PPh}_3$  bond and it was concluded that the extent of ligand exchangeability of the complexes is correlated to their antibacterial activity. Like **28–31**, compounds **32** and **33** with O-bound ligands (Figure 5) also show activity towards only Gram-positive bacteria *B. subtilis* and *S. aureus* (MIC's in the range 31.3–62.5  $\mu\text{g/mL}$ ).<sup>[49]</sup>

Many  $[\text{L}-\text{Au}(\text{PPh}_3)]$  complexes like **1**, **2**, **8**, **9** and **34** (Figures 2, 3, and 6) show both anticancer and antimicrobial properties. **1** and **2** with alkynyl ligands were evaluated for their activity against methicillin-sensitive and methicillin-resistant *S. aureus* (MRSA) and *E. coli* showing promising results for Gram-positive MRSA (MIC 2–32  $\mu\text{g/mL}$ ) but no activity towards Gram-negative species.<sup>[29]</sup> As a comparison, the starting material  $[\text{Cl}-\text{Au}(\text{PPh}_3)]$  was also evaluated against these strains and outperformed **1** and **2** with lower MIC's towards MRSA (MIC 1–2  $\mu\text{g/mL}$ ) and also showing activity towards Gram-negative *E. coli* (MIC 16–32  $\mu\text{g/mL}$ ). This indicated that the replacement of the Cl ligand to the alkynyl species might alter the uptake/activity of these Au complexes especially considering the permeability of Gram-positive and Gram-negative cell membranes. Complexes **8** and **9** also showing anticancer activity were evaluated for their activity towards *S. aureus*, *Staphylococcus epidermidis*, *E. coli* and *P. aeruginosa*.<sup>[36]</sup> All compounds showed potent activity towards Gram-positive species (MIC 1.3–19.1  $\mu\text{M}$ ) and increased activity compared to  $[\text{Cl}-\text{Au}(\text{PPh}_3)]$  reference compounds but no activity towards Gram-negative bacteria. Interestingly, the analogous  $\{\text{Au}(\text{PEt}_3)\}^+$  compounds of **8** and **9** performed slightly better. Complex **34** also showed potent antibacterial activity (MIC 8–16  $\mu\text{g/mL}$ ) particularly

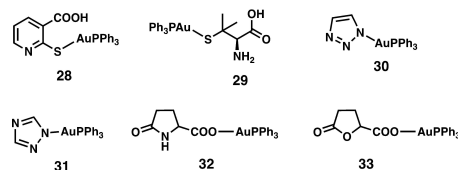


Figure 5. Complexes of  $[\text{L}-\text{Au}(\text{PPh}_3)]$  that show activity towards Gram-positive bacteria.

against Gram-positive bacteria *S. aureus*, multidrug-resistant (MDR) *S. aureus*, *Enterococcus faecalis*, *Bacillus cereus*, *S. epidermidis*, and MDR *S. epidermidis*.<sup>[50]</sup> Bactericidal activity of **34** was also observed towards the Gram-negative *E. coli* and MDR *Klebsiella oxytoca* (32 and 16  $\mu\text{g/mL}$  respectively).

In our own hands, we have observed the antibacterial activity of  $\{\text{Au}(\text{PPh}_3)\}^+$  complexes **35** and **36** with benzothiazoles as ligands (Figure 6).<sup>[51]</sup> A skin and soft tissue infection model was used to evaluate their antibacterial efficacy against *Acinetobacter baumannii* and *P. aeruginosa*, two Gram-negative pathogens. Both complexes showed significant bacterial lawn clearing in case of *A. baumannii* while the control  $[\text{Cl}-\text{Au}(\text{PPh}_3)]$  showed no effect using this method. Compound **36** also showed significant lawn clearing when tested against *P. aeruginosa*. The reactivity of these compounds towards thiols was examined by NMR as a model for the interaction of these gold complexes with SH-containing proteins and peptides present in the bacteria which could play a role in their antibacterial action. Results showed that upon introduction of a thiol, the benzothiazole ligands are replaced and a new  $[\text{S}-\text{Au}(\text{PPh}_3)]$  species is formed indicating interaction with SH-containing proteins and peptides. Because the two benzothiazoles by themselves did not exhibit any significant activity, the results overall indicate that the antibacterial effects **35** and **36** presumably arise from the reactivity of  $\{\text{Au}(\text{PPh}_3)\}^+$  unit.

Sulfonamide compounds **37–39** (Figure 6) are significant antibacterial and antibiofilm agents against *P. aeruginosa* with MIC values ranging from 1–8  $\mu\text{g/mL}$ .<sup>[52]</sup> *P. aeruginosa* is an opportunistic Gram-negative pathogen and can be difficult to treat due to the rapid formation of a biofilm.<sup>[53]</sup> To observe the antibiofilm behavior, complexes **37–39** were subjected to swarming motility assay and all showed significant decrease in the biofilm growth compared to the control. This was also confirmed by confocal microscopy of the exopolysaccharides which make up a majority of the mass of biofilms. Interestingly, compounds with bimetallic gold did not perform as well. Molecular docking studies showed that all complexes are able to interact strongly with the LasR protein (related to the quorum sensing and biofilm formation in *P. aeruginosa*) and could be the reason behind the antibiofilm activity. In a different study by the same group, **37–39** showed similar antibacterial and antibiofilm activity towards MRSA, but no

toxicity towards *Caenorhabditis elegans* indicating the compounds are well tolerated.<sup>[54]</sup> All of these results imply that these sulfonamide  $\{\text{Au}(\text{PPh}_3)\}^+$  complexes could find use in chronic infections by MDR bacteria.

While the exact mechanism of action  $[\text{L}-\text{Au}(\text{PPh}_3)]$  species still remains widely unknown, research suggests much that like in cancer, there are multiple mechanisms of action that could benefit treatment of MDR pathogens. The majority of the  $[\text{L}-\text{Au}(\text{PPh}_3)]$  complexes show activity towards Gram-positive species although a few are also active towards Gram-negative bacteria. This difference in activity could be due to the low permeability of the two-membrane cell wall of the Gram-negative bacteria which is recognized as the major obstacle in the development of antibiotics that are effective towards such species.<sup>[55]</sup> Close scrutiny of the complexes in this section of the review reveals that the activity towards Gram-negative bacteria could be related to the presence of a  $[\text{N}-\text{Au}(\text{PPh}_3)]$  core (compounds **34–39**) which could ligand exchange more effectively or rapidly in order to exert drug action. However, further investigation is necessary because complexes **30** and **31**, also containing  $[\text{N}-\text{Au}(\text{PPh}_3)]$  cores, were not active towards Gram-negative bacteria.

## 5. Antiparasitic Activity

A few  $\{\text{Au}(\text{PPh}_3)\}^+$  containing molecules have been evaluated for their activity against various parasites. For example, the *in vitro* antimalarial activity of the thiosemicarbazonato complexes **40** and **41** (Figure 7) were evaluated on *Plasmodium falciparum*.<sup>[56]</sup> The ligands themselves show antimalarial properties and when combined with an  $\{\text{Au}(\text{PPh}_3)\}^+$  center the complexes show excellent potency and are comparable to chloroquine (CQ), the leading antimalarial drug ( $\text{IC}_{50}$  = 10.7 and 7.06 nM respectively). Analogous complexes of **40** and **41** with selenium, rather than sulfur bound ligands were also evaluated, but only showed moderate activity.

Navarro and coworkers have explored compound **42** (Figure 7) with CQ as a ligand extensively.<sup>[57–59]</sup> Potent activity was observed towards *P. falciparum* with  $\text{IC}_{50}$  in the nano molar range (9.2 and 4.8 times more potent than CQ diphosphate (CQDP) while the control  $[\text{Cl}-\text{Au}(\text{PPh}_3)]$  caused no inhibition of growth.<sup>[57]</sup> This comparison indicates that the inhibition was due to both gold and CQ presence in the medium. Further investigations showed that red blood cells pretreated with **42** showed 0% parasitemia while the value with CQDP as control was 5.60%.<sup>[58]</sup> In 2011, this group found that the increase in activity of **42** towards CQ-resistant *P. falciparum* is likely still due to the inhibition of beta-hematin formation, the main mechanism of action of CQ, and attributed the ability of **42** to overcome CQ resistance and the improved activity to the increased lipophilicity provided by the  $\{\text{Au}(\text{PPh}_3)\}^+$  unit.<sup>[59]</sup> In short the  $\{\text{Au}(\text{PPh}_3)\}^+$  could cause an accumulation at lipid/water interfaces where heme aggregation exists and could prevent recognition of CQ by the protein responsible for resistance. The *in vivo* activity was also tested using the rodent parasite *Plasmodium berghei* mouse model.<sup>[57]</sup> No apparent toxic response or adverse effects were observed in the mice at

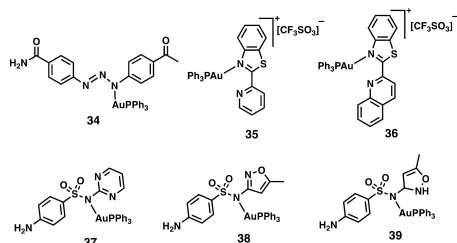


Figure 6. Au(I) complexes showing activity towards Gram-negative bacteria.

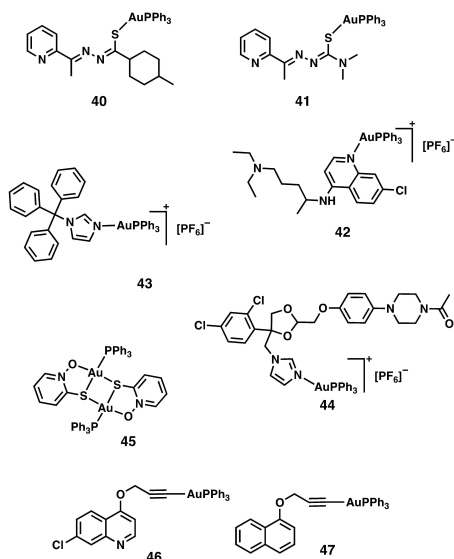


Figure 7. Complexes of  $\{\text{Au}(\text{PPh}_3)\}^+$  investigated for anti-parasitic action.

5.4 mg/kg of **42** and the complex was able to suppress parasitemia by 84% compared to the untreated control while the CQDP standard only suppressed by 44%. These results indicated the addition of the  $\{\text{Au}(\text{PPh}_3)\}^+$  unit to CQ significantly increased the *in vivo* susceptibility in the *P. berghei* mouse model. This same group also reported the activity of **43** and **44** (Figure 7) towards *Trypanosoma cruzi*, the parasite responsible for Chagas disease and found that both dramatically reduced the proliferation of epimastigotes of *T. cruzi* (66 and 71% respectively) compared to the free ligands.<sup>[60]</sup> Similarly, the binuclear complex  $\{\text{Au}(\text{PPh}_3)\}^+$  complex **45** (Figure 7) also showed increased activity towards the parasites *Leishmania mexicana*, *Leishmania braziliensis*, and *T. cruzi* compared to the free ligand and did not show cytotoxicity towards mammalian macrophages at the concentrations used ( $< 1 \mu\text{M}$ ).<sup>[61]</sup> The ligand pyridine-2-thiol N-oxide in **45** was previously shown to inhibit the parasite-specific enzyme NADH-fumarate reductase in *T. cruzi* and a dramatic increase of inhibition of this enzyme was observed upon complexation with  $\{\text{Au}(\text{PPh}_3)\}^+$ . While this finding does not imply the inhibition of NADG-fumarate reductase is the sole mechanism for the observed antiproliferative effect of **45**, it can certainly be attributed to its drug action.

Interestingly, **46** and **47** (Figure 7), with CQ derivatives as ligands showed relatively low activity towards *P. falciparum* compared to CQ and was unexpected due to the improved results seen by Navarro in with **42** (with CQ as a ligand).<sup>[62]</sup> This could be attributed to the difference in bond strength between

the weak Au–N bond in **42** and relatively strong Au–C bond in **46** and **47** where in physiological conditions the latter may be less likely to disassociate and exert drug action. The  $\{\text{Au}(\text{PPh}_3)\}^+$  moiety might help to bring the CQ-type molecule into the site of action in the cell and thus be responsible for the increase in activity. However, in the case of **46** and **47**, because the ligand is less likely to disassociate compared to **42** it could lead to decreased activity. While **46** and **47** were not ideal candidates for their anti-malarial activity, they did show some promising anticancer activity.

With antiparasitic gold complexes, it is unclear exactly how the combination of the  $\{\text{Au}(\text{PPh}_3)\}^+$  unit and a known parasitic drug leads to increase the activity. It could act as a shuttle to the active site and/or exerts its own drug action, but this is not fully understood at this time and is likely different for each  $[\text{drug}-\text{Au}(\text{PPh}_3)]^+$  combination and type of parasite. It seems likely the  $\{\text{Au}(\text{PPh}_3)\}^+$  moiety could have its own activity, due to the fact other gold(I) species have shown inhibition of trypanothione reductase in *Leishmania infantum* by binding of the Au to the two cysteines of the active site.<sup>[63,64]</sup>

## 6. Antimycobacterial Activity

*M. tuberculosis*, the infectious pathogen responsible for TB is known to be particularly difficult to treat and often the treatment involves three or more drugs in combination. Unfortunately, resistance to such treatment is emerging in certain populations. Robert Koch discovered that gold(II)cyanide was effective towards *M. tuberculosis* in the 1890's<sup>[2]</sup> and since then other gold complexes have shown potent activity towards the pathogen. Only a few compounds specifically with an  $\{\text{Au}(\text{PPh}_3)\}^+$  moiety have been evaluated for their antimycobacterial activity. The cationic compound **48** (Figure 8) with an overall 2+ charge and acridine ligand was evaluated for its effect on *M. tuberculosis* and was proved to be a strong inhibitor.<sup>[65]</sup> Both **48**

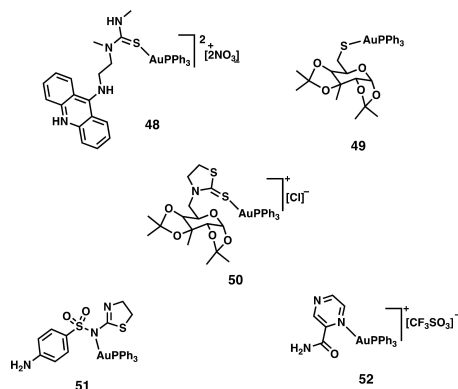


Figure 8. Complexes that exhibit antimycobacterial action.

and the analogous  $\{\text{Au}(\text{PET}_3)\}^+$  complex were tested ( $\text{IC}_{50} = 1.204$  and  $1.050 \mu\text{M}$ ) and while the  $\{\text{Au}(\text{PET}_3)\}^+$  complex was slightly more active, **48** was more selective towards *M. tuberculosis* than Vero cells ( $\text{SI} = 7.310$  and  $4.983$  respectively). Complexes **49** and **50** among others (Figure 8), with ligands derived from carbohydrates, were also evaluated for their antitubercular activity.<sup>[66]</sup> Interestingly, **49** was more active than the analogous  $\{\text{Au}(\text{PET}_3)\}^+$  complex, but the opposite was found for complex **50** and its  $\{\text{Au}(\text{PET}_3)\}^+$  derivative. **49** was the most active in all of the Au compounds studied in this report ( $\text{MIC}_{50} = 2.50 \mu\text{g/mL}$ ) including the  $[\text{Cl}-\text{Au}(\text{PPh}_3)]$  parent compound ( $\text{MIC}_{50} = 25.00 \mu\text{g/mL}$ ).

Studies with **38** and **51** (Figure 6 and 8) also showed activity towards species of mycobacterium.<sup>[67]</sup> First the compounds were tested against *Mycobacterium smegmatis*, the safer and similar model organism often used prior to working with *M. tuberculosis*, and showed potent activity ( $\text{MICs}$  of  $2.44$  and  $4.88 \mu\text{g/mL}$  for **38** and **51** respectively). Next, the possible synergy between these complexes and trimethoprim, an antibiotic, was assessed revealing synergy with **51** and only an additive effect with **38**. An added effect was observed with the starting material  $[\text{Cl}-\text{Au}(\text{PPh}_3)]$ , indicating that the synergy in **51** likely was resulting from the ligand although the full mechanism and role of  $\{\text{Au}(\text{PPh}_3)\}^+$  is unknown. The synergy between trimethoprim and **51** was also observed with *M. tuberculosis* providing promising results for future studies. Compound **37** and **38** (Figure 6) in a different study were also assessed for their activity and synergistic activity with trimethoprim in different species of *Mycobacterium* (*M. abscessus*, *M. forticum* and *M. massiliense*) responsible for nosocomial infections that are typically not transmitted human to human but rather from the environment.<sup>[68]</sup> Significant improvement in activity was observed upon conjugation to a  $\{\text{Au}(\text{PPh}_3)\}^+$  center and synergy between **37** or **38** and trimethoprim was observed in most cases with these *Mycobacterium* species. In our laboratory, complex **52** (Figure 8) with known TB drug pyrazinamide as an N donor ligand was first screened for its activity towards *M. smegmatis* ( $\text{MIC} = 60 \mu\text{M}$ ) and had a higher activity than the control drug isoniazid.<sup>[69]</sup> With these results in hand, **52** was tested for its activity towards *M. tuberculosis* and compared to free pyrazinamide, the starting material  $[\text{Cl}-\text{Au}(\text{PPh}_3)]$  and isoniazid all at the same concentration ( $80 \mu\text{M}$ ). Results indicate that **52** and  $[\text{Cl}-\text{Au}(\text{PPh}_3)]$  showed similarly strong bactericidal activity while the pyrazinamide under these conditions was only mildly bacteriostatic. This observation confirms that most of the antimycobacterial action is coming from the  $\{\text{Au}(\text{PPh}_3)\}^+$  unit itself rather than the ligand (however pyrazinamide is known to be active *in vitro* at much higher concentrations and lower pH of media). MDR *M. tuberculosis* and other species are an emerging problem and results of ours and other studies indicate that  $\{\text{Au}(\text{PPh}_3)\}^+$  species may be a useful tool in the development of new TB drugs. *Mycobacterium* are particularly robust due to their hydrophobic membrane (unlike Gram-negative and Gram-positive bacterial species) and the  $\{\text{Au}(\text{PPh}_3)\}^+$  unit may provide an increase in lipophilicity to allow more of the unit itself or the drug ligand into the cytosol/membrane to exert increased drug action. At present, few and

differing results on this type of complexes and their activity towards *Mycobacteria* in general have been reported; further discoveries in this area could provide valuable insight.

## 7. Anti-inflammatory/Antiviral Activity

The broad activity of gold complexes expands into other areas of medicinal research including anti-inflammatory and antiviral prospects. Gold complexes with peptides as ligands were evaluated for their activity towards HIV infection.<sup>[70]</sup> In complexes of type **53** (Figure 9),  $\{\text{Au}(\text{PPh}_3)\}^+$  is conjugated to the cysteine amino acid residues in the modified E1P8 and E2P45 peptides (represented by the arrow) which themselves showed interference with infectivity of HIV-1. They both performed significantly better than the parent peptides in cell-cell fusion and antiretroviral assays and the  $\text{IC}_{50}$  values were three orders of magnitude lower than the peptides themselves. This increase in activity could be attributed to the increased lipophilicity provided by conjugation of the  $\{\text{Au}(\text{PPh}_3)\}^+$  to the peptides in **53** and/or the introduction of the gold atom which could have its own cytotoxic activity. Another group showed gold species **54** and **55** (Figure 9) as well as others were able to interact and displace zinc in the C-terminal of HIVNCp7 zinc finger, a potential drug target for inhibition of HIV infection.<sup>[71]</sup> Results of ESI-MS experiments with NCp7 peptide indicated that the zinc is replaced rapidly upon introduction of the compounds and the most prominent species formed is the  $[\text{apoNCp7}-\text{Au}(\text{PPh}_3)]^{3+}$  ion and it is stable for at least 78 hour although other Au adducts are also formed. This has important implications in the treatment of viral infections with  $\{\text{Au}(\text{PPh}_3)\}^+$  species. In fact, recent studies showed that the  $\{\text{Au}(\text{PET}_3)\}^+$  containing Auranofin significantly reduced the viral load of SARS-COV-2 in human cells.<sup>[72]</sup>

Auranofin is well known for its treatment of rheumatoid arthritis. Although the specific mechanism of action is not

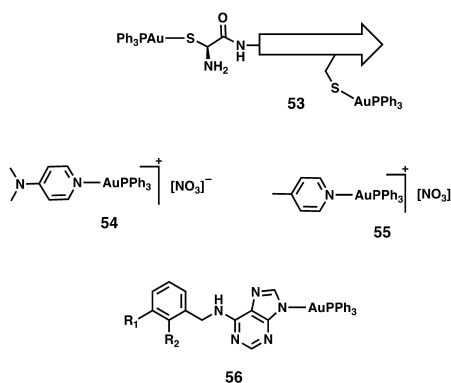


Figure 9. Au(I) complexes with anti-inflammatory or antiviral activity.

entirely elucidated, the drug has been linked to the inhibition of release of  $\beta$ -glucuronidase and lysozyme, the production of superoxide and lymphoblastogenesis.<sup>[73]</sup> Many other inhibitory pathways have been identified for gold(I) species, specifically for the  $\{\text{Au}(\text{PPh}_3)\}^+$ -containing complexes **56** ( $\text{R}_1 = \text{F}$ ,  $\text{Cl}$ ,  $\text{H}$ ;  $\text{R}_2 = \text{H}$ ,  $\text{H}$ ,  $\text{CH}_3$ ) and **24** (Figures 9 and 4) including reduction in production of pro-inflammatory cytokines (TNF- $\alpha$ , IL-1 $\beta$ , HMGB1).<sup>[16,74]</sup> Much like other  $\{\text{Au}(\text{PPh}_3)\}^+$  species, **56** and **24** react with sulfur containing biomolecules by substitution of the N ligand. Both of these showed similar or improved anti-inflammatory effects compared to Auranofin while being less cytotoxic. These results indicate that  $\{\text{Au}(\text{PPh}_3)\}^+$  complexes could be effective in the treatment of inflammatory diseases and potentially offer less side effects than Auranofin.

## 8. Conclusion

Gold is no doubt a useful element for wide spread medicinal applications and is gaining attention in all areas especially as anticancer agents.<sup>[75]</sup> Gold(I) phosphine complexes in general seem to have consistent and broad utility for inhibition of biological processes via interaction with biomolecules. It is known that the phosphine ligand is quite important and influential in relation to the anti-cancer activity and selectivity and often  $\text{PR}_3$  with  $\text{R} = \text{Ph}$  shows higher activity and/or selectivity. Even within a type of  $[\text{L}-\text{Au}(\text{PR}_3)]$  compounds, variations exist. For example,  $[\text{L}-\text{Au}(\text{PR}_3)]$  complexes with  $\text{L} =$  dithiocarbamates and  $\text{R} = \text{Ph}$ ,  $\text{Cy}$ , and  $\text{Et}$  exhibited potent anticancer activity with  $\text{R} = \text{Ph}$  being the most active inducing cell death via apoptosis while  $\text{R} = \text{Cy}$  and  $\text{Et}$  caused necrosis.<sup>[76]</sup> Other examples of this phenomenon exist and despite Auranofin being present on the FDA approved drug list,  $\text{PEt}_3$  complexes in general are more toxic and lead to more side effects *in vivo*. The propensity of alkyl phosphines towards oxidation induces further complication. Although some reports indicate that the solubility of  $[\text{L}-\text{Au}(\text{PPh}_3)]$  may present difficulties in *in vivo* various applications, formulations such as micelles, nanoization, nanoemulsions and others could aid to this problem.<sup>[77]</sup> Further, triphenylphosphine can be functionalized to mono- or trisulphonates to increase water solubility and research shows these types of complexes still remain highly active towards cancer cells.<sup>[78]</sup>

Although there have been multiple mechanisms of action described for their anticancer, antibacterial, and antiparasitic properties, the drug action(s) of the  $[\text{L}-\text{Au}(\text{PPh}_3)]$  complexes could largely be associated with the ability of ligand exchange by replacement of L with biological molecules. The stability of  $\{\text{Au}(\text{PPh}_3)\}^+$  and its tendency to bind tightly to thiols has proved a potent mechanism of inhibition of multiple enzymes and proteins such as TrxR, UPS, and LasR, as well as secretion of cytokines among others. In addition to the direct role in the modulation of the cellular redox state, TrxR directly interacts with other proteins associated with cell death mechanisms leading to apoptosis.<sup>[79]</sup> Another advantage is the increased lipophilicity provided by the  $\{\text{Au}(\text{PPh}_3)\}^+$  unit as more lipophilic drugs (to a certain extent) often are more active.<sup>[80]</sup> For example,

coordination of the  $\{\text{Au}(\text{PPh}_3)\}^+$  to metronidazole leads to increased activity against *Entamoeba histolytica*, by favoring permeation of the complex through the lipid layers of the membrane.<sup>[81]</sup> It is not totally understood if the  $\{\text{Au}(\text{PPh}_3)\}^+$  itself exhibits cytotoxic action or  $\{\text{Au}(\text{PPh}_3)\}^+$  acts more as a shuttle of the drug ligand L at the sites of activity. However, examples listed in this review lead to the reasonable conclusion that it is likely the combination of both and the overall activity varies from organism to organism. Multiple mechanisms/targets of gold drugs do provide an advantage especially when considering drug resistant pathogens and cancers in general. Together, the salutary effects of the  $[\text{L}-\text{Au}(\text{PPh}_3)]$  type of complexes indicate that the  $\{\text{Au}(\text{PPh}_3)\}^+$  moiety is of particular importance in drug design and development for numerous biological applications, and warrant further research into its role and specific activity.

## Acknowledgements

Support from the National Science Foundation grant DMR-1409335, the NIH grant GM058903, and a University of California Cancer Research Coordinating Committee grant UC CTR-19-580346 is gratefully acknowledged.

## Conflict of Interest

The authors declare no conflict of interest.

**Keywords:** gold drugs · the  $\{\text{Au}(\text{PPh}_3)\}^+$  moiety · lipophilic chemotherapeutics · anticancer agents · antimicrobials

- [1] Z. Huaizhi, N. Yuntao, *Gold Bull.* **2001**, *34*, 24–29.
- [2] T. G. Benedek, *J. Hist. Med. Allied Sci.* **2004**, *59*, 50–89.
- [3] B. M. Sutton, *Gold Bull.* **1986**, *19*, 15–16.
- [4] P. J. Sadler, *Gold Bull.* **1976**, *9*, 110–118.
- [5] G. Faa, C. Gerosa, D. Fanni, J. I. Lachowicz, V. M. Nurchi, *Curr. Med. Chem.* **2017**, *25*, 75–84.
- [6] I. Ott, *Coord. Chem. Rev.* **2009**, *253*, 1670–1681.
- [7] M. Navarro, *Coord. Chem. Rev.* **2009**, *253*, 1619–1626.
- [8] B. Glisic, M. I. Djuran, *Dalton Trans.* **2014**, *43*, 5950–5969.
- [9] S. P. Fricker, *Gold Bull.* **1996**, *29*, 53–60.
- [10] C. Roder, M. J. Thomson, *Drugs R&D* **2015**, *15*, 13–20.
- [11] R. Dorel, A. M. Echavarren, *Chem. Rev.* **2015**, *115*, 9028–9072.
- [12] J. H. Teles, S. Brode, M. Chabanas, *Angew. Chem. Int. Ed.* **1998**, *37*, 1415–1418; *Angew. Chem.* **1998**, *110*, 1475–1478.
- [13] T. Zou, C. T. Lum, C. N. Lok, W. P. To, K. H. Low, C. M. Che, *Angew. Chem. Int. Ed.* **2014**, *53*, 5810–5814; *Angew. Chem.* **2014**, *126*, 5920–5924.
- [14] C. F. Shaw, *Chem. Rev.* **1999**, *99*, 2589–2600.
- [15] K. Nomiya, S. Yamamoto, R. Noguchi, H. Yokoyama, N. C. Kasuga, K. Ohyama, C. Kato, *J. Inorg. Biochem.* **2003**, *95*, 208–220.
- [16] R. Křikavová, J. Hošek, J. Vančo, J. Hutýra, Z. Dvořák, Z. Trávníček, *PLoS One* **2014**, *9*, e107373.
- [17] H. G. Raubenheimer, H. Schmidbaur, *J. Chem. Educ.* **2014**, *91*, 2014–2036.
- [18] M. P. Chrysouli, C. N. Banti, N. Kourkoumelis, N. Panayiotou, G. S. Markopoulos, A. J. Tasiopoulos, S. K. Hadjikakou, *J. Inorg. Biochem.* **2018**, *179*, 107–120.
- [19] M. C. Gimeno, in *Mod. Supramol. Gold Chem. Gold-Metal Interact. Appl.* (Ed.: A. Laguna), WILEY-VCH Verlag GmbH & Co. KGaA, Weinheim, **2008**, pp. 1–63.
- [20] H. Schmidbaur, A. Schier, *Chem. Soc. Rev.* **2012**, *41*, 370–412.



- [21] G. Pacchioni, P. S. Bagus, *Inorg. Chem.* **1992**, *31*, 4391–4398.
- [22] O. D. Haberland, N. Rösch, *J. Phys. Chem.* **1993**, *97*, 4970–4973.
- [23] J. Carlos Lima, L. Rodriguez, *Anti-Cancer Agents Med. Chem.* **2012**, *11*, 921–928.
- [24] S. J. Berners-Price, A. Filipovska, *Metallomics* **2011**, *3*, 863–873.
- [25] W. Liu, R. Gust, *Chem. Soc. Rev.* **2013**, *42*, 755–773.
- [26] M. S. Iqbal, S. G. Taqi, M. Arif, M. Wasim, M. Sher, *Biol. Trace Elem. Res.* **2009**, *130*, 204–209.
- [27] A. Takashi, M. T. Ken, I. Hikaru, S. Yukiyoshi, *Bull. Chem. Soc. Jpn.* **1989**, *62*, 1078–1080.
- [28] V. Andermark, K. Göke, M. Kokoschka, M. A. Abu El Maaty, C. T. Lum, T. Zou, R. W. Y. Sun, E. Aguiló, L. Oehninger, L. Rodríguez, H. Bunjes, S. Wölfl, C. M. Che, I. Ott, *J. Inorg. Biochem.* **2016**, *160*, 140–148.
- [29] P. Hkisz, L. Szczupak, A. Koceva-Chyla, A. Gus'piel, L. Oehninger, I. Ott, B. Therrien, J. Solecka, K. Kowalski, *Molecules* **2015**, *20*, 19699–19718.
- [30] A. De Nisi, C. Bergamini, M. Leonzio, G. Sartor, R. Fato, M. Naldi, M. Monari, N. Calonghi, M. Bandini, *Dalton Trans.* **2016**, *45*, 1546–1553.
- [31] V. Fernández-Moreira, R. P. Herrera, M. C. Gimeno, *Pure Appl. Chem.* **2019**, *91*, 247–269.
- [32] S. Yue, M. Luo, H. Liu, S. Wei, *Front. Chem.* **2020**, *8*.
- [33] N. Liu, X. Li, H. Huang, C. Zhao, S. Liao, C. Yang, S. Liu, W. Song, X. Lu, X. Lan, X. Chen, S. Yi, L. Xu, L. Jiang, C. Zhao, X. Dong, P. Zhou, S. Li, S. Wang, X. Shi, P. Q. Dou, X. Wang, J. Liu, *Oncotarget* **2014**, *5*, 5453–5471.
- [34] A. Meyer, C. P. Bagowski, M. Kokoschka, M. Stefanopoulou, H. Alborzinia, S. Can, D. H. Vleck, W. S. Sheldrick, S. Wölfl, I. Ott, *Angew. Chem. Int. Ed.* **2012**, *51*, 8895–8899; *Angew. Chem.* **2012**, *124*, 9025–9030.
- [35] E. Barreiro, J. S. Casas, M. D. Couce, A. Sánchez, Á. Sánchez-González, J. Sordo, J. M. Varela, E. M. Vázquez López, *J. Inorg. Biochem.* **2008**, *102*, 184–192.
- [36] A. M. de Almeida, B. A. de Oliveira, P. P. de Castro, C. C. de Mendonça, R. A. Furtado, H. D. Nicoletta, V. L. da Silva, C. G. Diniz, D. C. Tavares, H. Silva, M. V. de Almeida, *BioMetals* **2017**, *30*, 841–857.
- [37] C. F. Shaw, A. Beery, G. C. Stocco, *Inorg. Chim. Acta* **1986**, *123*, 213–216.
- [38] M. Serratrice, M. A. Cinellu, L. Maggiore, M. Pilo, A. Zucca, C. Gabbiani, A. Guerri, I. Landini, S. Nobili, E. Mini, L. Messori, *Inorg. Chem.* **2012**, *51*, 3161–3171.
- [39] M. Serratrice, B. Bertrand, E. F. J. Janssen, E. Hemelt, A. Zucca, F. Cocco, M. A. Cinellu, A. Casini, *MedChemComm.* **2014**, *5*, 1418–1422.
- [40] A. Gutiérrez, J. Bernal, M. D. Villacampa, C. Cativiela, A. Laguna, M. C. Gimeno, *Inorg. Chem.* **2013**, *52*, 6473–6480.
- [41] A. Gutiérrez, C. Cativiela, A. Laguna, M. C. Gimeno, *Dalton Trans.* **2016**, *45*, 13483–13490.
- [42] A. Gutiérrez, I. Marzo, C. Cativiela, A. Laguna, M. C. Gimeno, *Chem. Eur. J.* **2015**, *21*, 11088–11095.
- [43] F. Caruso, M. Rossi, J. Tanski, C. Pettinari, F. Marchetti, *J. Med. Chem.* **2003**, *46*, 1737–1742.
- [44] F. Caruso, R. Villa, M. Rossi, C. Pettinari, F. Paduano, M. Pennati, M. G. Daidone, N. Zaffaroni, *Biochem. Pharmacol.* **2007**, *73*, 773–781.
- [45] C. Marzano, V. Gandin, A. Folda, G. Scutari, A. Bindoli, M. P. Rigobello, *Free Radical Biol. Med.* **2007**, *42*, 872–881.
- [46] S. Thangamani, H. Mohammad, M. F. N. Abushahba, T. J. P. Sobreira, V. E. Hedrick, L. N. Paul, M. N. Seleem, *Sci. Rep.* **2016**, *6*, 1–13.
- [47] Y. Cui, Y. Zhao, Y. Tian, W. Zhang, X. Lü, X. Jiang, *Biomaterials* **2012**, *33*, 2327–2333.
- [48] N. Kenji, N. Ryusuke, S. Takaye, K. Yoshihiro, K. Tsuda, K. Ohsawa, N. C. Kasuga, M. Oda, *Bull. Chem. Soc. Jpn.* **2000**, *73*.
- [49] R. Noguchi, A. Hara, A. Sugie, K. Nomiya, *Inorg. Chem. Commun.* **2006**, *9*, 355–359.
- [50] M. K. Tizotti, R. Hörner, A. G. O. De Freitas, C. B. Kempfer, A. Bottega, J. N. Rodrigues, V. M. Cósar, A. Locatelli, G. Paraginski, G. Giacomelli, M. Hörner, *Inorg. Chim. Acta* **2016**, *441*, 78–85.
- [51] J. Stenger-Smith, I. Chakraborty, P. K. Mascharak, *J. Inorg. Biochem.* **2018**, *185*, 80–85.
- [52] C. Rigon, S. Terra, P. Andrei, F. Alexandre, A. Soares, L. De Lourenço, M. Matiko, A. De Campos, *Microb. Pathog.* **2018**, *125*, 393–400.
- [53] O. Ciofu, T. Tolker-nielsen, *Front. Microbiol.* **2019**, *10*, 913.
- [54] C. Rigon, S. Terra, C. Flores, V. Albertina, P. Cordenonsi, G. Guidolin, T. Cruz, F. Alexandre, A. Soares, L. De Lourenço, *Microb. Pathog.* **2018**, *123*, 440–448.
- [55] H. I. Zgurskaya, C. A. Lopez, S. Gnanakaran, *ACS Infect. Dis.* **2015**, *1*, 512–522.
- [56] A. Molter, J. Rust, C. W. Lehmann, G. Deepa, P. Chiba, F. Mohr, *Dalton Trans.* **2011**, *40*, 9810–9820.
- [57] M. Navarro, H. Perez, R. A. Sanchez-Delgado, *J. Med. Chem.* **1997**, *40*, 1937–1939.
- [58] M. Navarro, F. Vázquez, R. A. Sánchez-Delgado, H. Pérez, V. Sinou, J. Schrével, *J. Med. Chem.* **2004**, *47*, 5204–5209.
- [59] M. Navarro, W. Castro, A. Martínez, R. A. Sánchez Delgado, *J. Inorg. Biochem.* **2011**, *105*, 276–282.
- [60] M. Navarro, E. J. Cisneros-Fajardo, T. Lehmann, R. A. Sánchez-Delgado, R. Atencio, P. Silva, R. Lira, J. A. Urbina, *Inorg. Chem.* **2001**, *40*, 6879–6884.
- [61] M. Vieites, P. Smirich, L. Guggeri, E. Marchán, A. Gómez-Barrio, M. Navarro, B. Garat, D. Gambino, *J. Inorg. Biochem.* **2009**, *103*, 1300–1306.
- [62] E. Schuh, S. M. Valiahi, M. A. Jakupcic, B. K. Keppler, P. Chiba, F. Mohr, *Dalton Trans.* **2009**, 10841–10845.
- [63] A. Ilari, P. Baiocco, L. Messori, A. Fiorillo, A. Boffi, M. Gramiccia, T. Di Muccio, G. Colotti, *Amino Acids* **2012**, *42*, 803–811.
- [64] G. Colotti, A. Ilari, A. Fiorillo, P. Baiocco, M. A. Cinellu, L. Maggiore, F. Scaletti, C. Gabbiani, L. Messori, *ChemMedChem* **2013**, *8*, 1634–1637.
- [65] L. C. Eiter, N. W. Hall, C. S. Day, G. Saluta, G. L. Kucera, U. Bierbach, *J. Med. Chem.* **2009**, *52*, 6519–6522.
- [66] J. D. S. Chaves, J. L. Damasceno, M. C. F. Paula, P. F. De Oliveira, G. C. Azevedo, R. C. Matos, M. C. S. Lourenço, D. C. Tavares, H. Silva, A. P. S. Fontes, M. V. De Almeida, *BioMetals* **2015**, *28*, 845–860.
- [67] V. A. Agertt, L. L. Marques, P. C. Bonez, T. V. Dalmolin, G. N. Manzonni De Oliveira, M. M. A. De Campos, *Tuberculosis* **2013**, *93*, 318–321.
- [68] V. A. Agertt, P. C. Bonez, G. G. Rossi, V. da C. Flores, F. dos S. Siqueira, C. R. Mizdal, L. L. Marques, G. N. M. de Oliveira, M. M. A. de Campos, *BioMetals* **2016**, *29*, 807–816.
- [69] J. Stenger-Smith, M. Kamariza, I. Chakraborty, R. Ouattara, C. R. Bertozzi, P. K. Mascharak, *ACS Omega* **2020**, *5*, 6826–6833.
- [70] M. Gómara, R. Galatola, A. Gutiérrez, M. Gimeno, J. Gatell, V. Sánchez-Merino, E. Yuste, I. Haro, *Curr. Med. Chem.* **2014**, *21*, 238–250.
- [71] C. Abbehausen, E. J. Peterson, R. E. F. De Paiva, P. P. Corbi, A. L. B. Formiga, Y. Qu, N. P. Farrell, *Inorg. Chem.* **2013**, *52*, 11280–11287.
- [72] H. A. Rothan, S. Stone, J. Natekar, P. Kumari, K. Arora, M. Kumar, *Virology* **2020**, *547*, 7–11.
- [73] W. F. Kean, I. R. L. Kean, *Inflammopharmacology* **2008**, *16*, 112–125.
- [74] Z. Trávníček, P. Štarha, J. Vančo, T. Šilha, J. Hošek, P. Suchý, G. Pražanová, *J. Med. Chem.* **2012**, *55*, 4568–4579.
- [75] C. I. Yeo, K. K. Ooi, E. R. T. Tiekink, *Molecules* **2018**, *23*, 1410.
- [76] N. S. Jamaludin, Z. J. Goh, Y. K. Cheah, K. P. Ang, J. H. Sim, C. H. Khoo, Z. A. Fairuz, S. N. B. A. Halim, S. W. Ng, H. L. Seng, E. R. T. Tiekink, *Eur. J. Med. Chem.* **2013**, *67*, 127–141.
- [77] S. Kalepu, V. Nekkanti, *Acta Pharm. Sin. B* **2015**, *5*, 442–453.
- [78] E. Vergara, E. Cerrada, C. Clavel, A. Casini, M. Laguna, *Dalton Trans.* **2011**, *40*, 10927–10935.
- [79] P. Holenya, S. Can, R. Rubbiani, H. Alborziniz, A. Jünger, X. Cheng, I. Ott, S. Wölfl, *Metallomics* **2014**, *6*, 1591–1601.
- [80] J. A. Arnott, S. L. Planey, *Expert Opin. Drug Discovery* **2012**, *7*, 863–875.
- [81] F. Athar, K. Husain, M. Abid, S. M. Agarwal, S. J. Coles, M. B. Hursthouse, M. R. Maurya, A. Azam, *Chem. Biodiversity* **2005**, *2*, 1320–1330.

Manuscript received: August 11, 2020

Revised manuscript received: September 21, 2020

Accepted manuscript online: October 6, 2020

Version of record online: October 29, 2020





Contents lists available at ScienceDirect

Journal of Inorganic Biochemistry

journal homepage: [www.elsevier.com/locate/jinorgbio](http://www.elsevier.com/locate/jinorgbio)

## Cationic Au(I) complexes with aryl-benzothiazoles and their antibacterial activity

Jenny Stenger-Smith, Indranil Chakraborty, Pradip K. Mascharak\*

Department of Chemistry, University of California, Santa Cruz, CA 95064, United States



## ARTICLE INFO

## Keywords:

Aryl-benzothiazoles  
Gold(I) complexes  
Antibacterial activity  
Gram-negative bacteria  
Skin and soft tissue infection (SSTI)

## ABSTRACT

Two cationic Au(I) complexes derived from aryl-benzothiazoles, namely  $[(PPh_3)Au(pbt)](OTf)$  (1) and  $[(PPh_3)Au(qbt)](OTf)$  (2) (where pbt = 2-(pyridyl)benzothiazole and qbt = (quinolyl)benzothiazole, and  $OTf^-$  = trifluoromethanesulfonate anion), have been synthesized and structurally characterized by X-ray crystallography. Both complexes exhibit strong antibacterial effects against Gram-negative bacteria such as *Acinetobacter baumannii* and *Pseudomonas Aeruginosa*. Results of examination of the reactions of 1 and 2 indicate that these cationic Au(I) complexes rapidly cross the bacterial membrane and exert drug action by disrupting cellular function(s) through binding of cytosolic thiol-containing peptides (such as glutathione) and proteins to the highly reactive  $(PPh_3)Au^+$  intermediate formed upon in situ dissociation of pbt or qbt.

## 1. Introduction

Rapid emergence of antibacterial resistance to common antibiotics has raised alarm in hospitals around the globe. Infections and diseases that were thought to be well controlled by antibiotics are reappearing with resistance to traditional drug therapies [1]. In parallel, other microorganisms such as parasites, fungi, and viruses are also exhibiting similar characteristics [2]. Many resistant strains have appeared in hospitals where antibiotics are being used and administered as routine procedures [3]. The once life-saving drugs like  $\beta$ -lactams that doctors relied upon to keep many bacterial infections at bay are now completely ineffective [4]. Unfortunately, the pace at which new antibiotics are emerging in the market is not nearly fast enough to combat such resistance [5].

Although gold compounds have been used in medicine for centuries, interest in such compounds was noticeably intensified following the discovery by Robert Koch who showed that  $K[Au(CN)_2]$  had activity against *Mycobacterium tuberculosis*, the causative agent of tuberculosis [6,7]. Shortly after this discovery, reports on gold compounds as anticancer, antimicrobial, and antiarthritic agents started appearing in scientific literature and such research led to several gold drugs for commercial use [6–10]. Additional investigation into new gold compounds for clinical use was however greatly diminished following the discovery of antibiotics. Now that resistance is on the rise and the discovery of new antibiotics is comparatively slow [5], reexamination of the bioactivity of new gold compounds could be very relevant.

In recent years a relatively large number of Au(I) compounds have

been synthesized and studied in vitro. The accumulation and in-depth analysis of such data have led scientists to infer that the types of ligands in the gold compounds play a significant role in the effectiveness of the compounds toward eradication of specific bacteria [6]. Interestingly, compounds independently used as drugs, when used as ligands to Au(I), lead to new gold compounds exhibiting improved antibacterial efficacy. Positively-charged species are in general more effective in associating with mostly electronegative bacterial cell walls [11]; close interactions between the cell wall and drug molecules lead to interruptions in various cellular pathways that often result in microbial death.

For some time, we have been exploring the antibacterial properties of heavy metal complexes derived from benzothiazoles, a class of antibacterial and antifungal drugs [12,13]. Our work in such pursuit have shown that Ag(I) complexes of benzothiazole-type ligands act as antimicrobial agents [14]. In these complexes, 2-(pyridyl)benzothiazole (pbt) and 2-(quinolyl)benzothiazole (qbt) are bound to the Ag(I) center as bidentate *N,N*-coordinated fashion to give rise to tetrahedral geometry (Scheme 1). The overall positive charge of these complexes presumably leads to stronger interactions with the bacterial cell walls and give rise to their antibacterial activity. These results prompted us to explore the coordination characteristics of pbt and qbt to Au(I) centers and the antibacterial activity of the Au(I) complexes derived from them.

In this account we report the synthesis, spectroscopy, and structural characterization of two gold(I) compounds derived from pbt and qbt namely,  $[(PPh_3)Au(pbt)](OTf)$  (1) and  $[(PPh_3)Au(qbt)](OTf)$  (2). As shown in Figs. 2 and 3, both ligands bind as monodentate *N*-donors to the Au(I) center. The other ligand in both complexes is

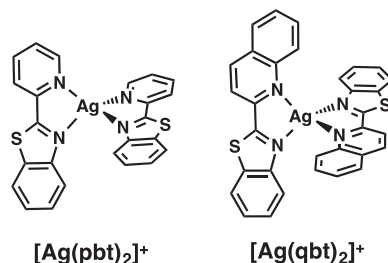
\* Corresponding author.

E-mail address: [pradip@ucsc.edu](mailto:pradip@ucsc.edu) (P.K. Mascharak).<https://doi.org/10.1016/j.jinorgbio.2018.05.003>

Received 24 February 2018; Received in revised form 4 May 2018; Accepted 8 May 2018

Available online 11 May 2018

0162-0134/ Published by Elsevier Inc.



Scheme 1. Structures of the Ag complexes derived from pbt and qbt.

triphenylphosphine. The antibacterial properties of **1** and **2** against two Gram-negative bacteria namely, *Acinetobacter baumannii* and *Pseudomonas aeruginosa* have been evaluated using a skin and soft tissue infection (SSTI) model previously developed in our laboratory.

## 2. Experimental methods

### 2.1. Materials and methods

All reagents and solvents were of commercial grade and used without further purification.  $(\text{PPh}_3)\text{AuCl}$  and  $\text{AgOTf}$  were procured from Sigma. The ligands pbt [15] and qbt [16] were synthesized according to reported procedures. FTIR, UV–Vis, and emission spectra were obtained using Perkin-Elmer Spectrum-One, Varian Cary 50, and Agilent Cary Eclipse spectrophotometers respectively. The  $^1\text{H}$ -,  $^{19}\text{F}$  and  $^{31}\text{P}$  NMR spectra of the ligands and the complexes were recorded using a Varian Unity Inova 500 MHz instrument at 298 K.

### 2.2. Synthesis of complexes

#### 2.2.1. Synthesis of $[(\text{PPh}_3)\text{Au}(\text{pbt})](\text{OTf})$ (**1**)

To a solution of  $\text{AgOTf}$  (54.8 mg, 0.213 mmol) in 10 mL of methanol was added a solution of  $(\text{PPh}_3)\text{AuCl}$  (100.5 mg, 0.203 mmol) in 15 mL of chloroform. After stirring for 30 min the white  $\text{AgCl}$  precipitate was filtered through a bed of celite. To the filtrate was added a solution of pbt (43.1 mg, 0.203 mmol) in 10 mL of chloroform and the mixture was set to reflux for 18 h. The solution was again filtered through celite to remove traces of black particles. The volume of the filtrate was then reduced to approximately 4 mL and 15 mL of hexane was added. The white solid thus formed was collected by filtration and dried in vacuo (131.0 mg, 78.6% yield). Layering hexanes over a dichloromethane ( $\text{CH}_2\text{Cl}_2$ ) solution of this solid afforded colorless crystals of **1**. Anal. Calcd for  $\text{C}_{31}\text{H}_{23}\text{AuN}_2\text{O}_3\text{P}_2\text{F}_3$ : C, 45.37; H, 2.83; N, 3.41; found: C, 45.48; H, 2.79; N, 3.37. IR (KBr,  $\text{cm}^{-1}$ ): 3468 (w), 3056 (w), 1459 (w) 1436 (m), 1267 (s), 1154 (m), 1032 (m), 763 (m), 695 (m), 546 (m).  $^1\text{H}$  NMR ( $\text{CDCl}_3$ , ppm): 8.62 (d, 1H), 8.40 (d, 1H), 8.25 (t, 1H), 8.12 (d, 1H), 8.01 (d, 1H), 7.83 (t, 1H), 7.63–7.55 (m, 17H).  $^{31}\text{P}$  NMR ( $\text{CDCl}_3$ , ppm from  $\text{PPh}_3$ ): 35.90.

#### 2.2.2. Synthesis of $[(\text{PPh}_3)\text{Au}(\text{qbt})](\text{OTf})$ (**2**)

The same procedure as above using qbt as the ligand. Complex **2** was isolated as a light yellow solid (60.1 mg, 75.0%). Layering hexanes over a solution of **2** in dichloromethane afforded pale yellow crystals of  $[(\text{PPh}_3)\text{Au}(\text{qbt})](\text{OTf})$ . Anal. Calcd for  $\text{C}_{35}\text{H}_{25}\text{AuN}_2\text{O}_3\text{P}_2\text{F}_3$ : C, 48.28; H, 2.89; N, 3.22; found: C, 48.02; H, 2.91; N, 3.12. IR (KBr,  $\text{cm}^{-1}$ ): 3436 (w), 3056 (w), 1436 (w), 1263 (s), 1156 (m), 1031 (m), 762 (m), 696 (m), 545 (m).  $^1\text{H}$  NMR ( $\text{CDCl}_3$ , ppm): 8.76 (d, 1H), 8.52 (d, 1H), 8.23 (d, 1H), 8.19 (d, 1H), 8.06 (d, 1H), 7.69–7.53 (m, 19 H), 7.46 (t, 1H).

### 2.3. X-ray crystallography

Colorless and light yellow block-shaped crystals of complexes **1** and **2** respectively were obtained by recrystallization through diffusion of hexanes into their dichloromethane ( $\text{CH}_2\text{Cl}_2$ ) solutions. In case of **1**, a suitable crystal was selected and mounted on a Bruker D8 Quest diffractometer equipped with PHOTON II detector operating at  $T = 298$  K. Data were collected with  $\omega$  shutterless scan technique using graphite monochromated Mo-K $\alpha$  radiation ( $\lambda = 0.71073$  Å). In case of **2**, a suitable single crystal was selected and mounted on a Bruker APEX-II CCD diffractometer with graphite monochromated Mo-K $\alpha$  radiation ( $\lambda = 0.71073$  Å). In this case the crystal was also kept at  $T = 298$  K during data collection and unit cell determination. Data were measured using  $\omega$  scan technique. The total number of runs and images for both data collections was based on the strategy calculation from the program APEX3 (Bruker) [17]. The maximum resolution achieved was  $\theta = 28.4^\circ$  for **1** and  $\theta = 24.2^\circ$  for **2**. Cell parameters were retrieved using the SAINT (Bruker) software [18] and refined using SAINT (Bruker) on 9525 reflections for **1** and on 8496 reflections for **2**. Data reduction was performed using the SAINT (Bruker) software, which corrects for Lorentz polarization. The final completeness is 99.6% out to  $28.4^\circ$  in  $\theta$  for **1** and 98.8% out to  $24.2^\circ$  in  $\theta$  for **2**. Multi-scan absorption corrections were performed with both data sets using SADABS 2016/2 and SADABS 2014/5 respectively for **1** and **2** [19]. The absorption coefficient for **1** is  $4.88 \text{ mm}^{-1}$  and for **2** is  $4.29 \text{ mm}^{-1}$ . Minimum and maximum transmissions for **1** are 0.499 and 0.746 and the corresponding values for **2** are 0.573 and 0.745. The structures of **1** and **2** were solved in the space group C2/c (No. 15) and Pbcn (No. 61) respectively by intrinsic phasing using the ShelXT [20] structure solution program and refined by full matrix least squares on  $F^2$  using version 2016/6 of ShelXL [21]. All non-hydrogen atoms were refined anisotropically in both cases. Hydrogen atom positions were calculated geometrically and refined using the riding model. In case of **1**, there are two crystallographically independent molecules within the asymmetric unit, while for **2** one full molecule is present in the asymmetric unit. Calculations and molecular graphics were performed using SHELXTL 2014 and Olex2 [22] programs. Crystal data and structure refinement parameters are included in Table 1 while the bond distances and angles are listed in Table 2.

Crystal data for complex **1** (CCDC 1824282) and **2** (CCDC 1824283) have been included in the Supplementary data section. These data can be obtained free of charge from The Cambridge Crystallographic Data Center via [www.ccdc.cam.ac.uk/data\\_request.cif](http://www.ccdc.cam.ac.uk/data_request.cif).

### 2.4. Bacterial studies

The SSTI model previously developed in our lab [23] was employed for antimicrobial studies. This uses a soft upper agar layer of evenly-dispersed bacterial “lawn” at the top of a nutrient rich bottom agar layer. Such arrangement allows the bacteria to move slowly into the bottom layer following the nutrient gradient, much like ditching of surface bacteria into the inner layers of skin and soft tissue. Different dilutions of *A. baumannii* and *P. aeruginosa* were employed to grow ideal lawns in these SSTI models. For *A. baumannii*, a frozen stock of bacteria was first streaked on an LB plate and incubated for 18 h. A single colony of bacteria was selected and grown in LB broth for another 18 h. The suspension was diluted with fresh LB until an  $A_{600}$  of 0.8 was reached. A batch of 100 mL of 0.8% (w/v) agar with 1% NaCl was prepared, autoclaved and cooled to  $47^\circ\text{C}$  before addition of 80  $\mu\text{L}$  of the diluted bacterial suspension. This solution was gently vortexed and aliquots of 8 mL of it were spread evenly over the surface of six  $100 \times 15 \text{ mm}^2$  plates prepared with 20 mL of 1.5% (w/v) TSB agar (hard nutrient-rich layer). The plates were then incubated at  $37^\circ\text{C}$  for 2 h to facilitate adhesion of the bacteria to the nutrient-rich bottom layer and cell-to-cell contact. For *P. aeruginosa*, the same procedure was followed to prepare the SSTI model. Here, the bacterial suspension in LB medium was diluted to an  $A_{600}$  of 0.5 and 120  $\mu\text{L}$  of it

**Table 1**  
Crystal data and structure refinement parameters for **1** and **2**.

	1. 0.5 CH <sub>2</sub> Cl <sub>2</sub>	2
Formula	C <sub>31.5</sub> H <sub>24</sub> ClF <sub>3</sub> N <sub>2</sub> O <sub>3</sub> S <sub>2</sub> PAu	C <sub>33</sub> H <sub>25</sub> F <sub>3</sub> N <sub>2</sub> O <sub>3</sub> S <sub>2</sub> PAu
D <sub>calc</sub> /g cm <sup>-3</sup>	1.777	1.601
μ/mm <sup>-1</sup>	4.875	4.285
Formula weight	863.03	870.62
Color	Yellow	Yellow
Shape	Block	Block
T/K	298(2)	298(2)
Crystal system	Monoclinic	Orthorhombic
Space group	C2/c	Pbca
a/Å	47.014(2)	9.780(2)
b/Å	8.7125(4)	22.679(5)
c/Å	36.5473(18)	32.560(7)
α/°	90	90
β/°	120.4450(10)	90
γ/°	90	90
V/Å <sup>3</sup>	12,905.9(11)	7222(3)
Z	8	8
Wavelength/Å	0.71073	0.71073
Radiation type	Mo-Kα	Mo-Kα
2θ <sub>min</sub> /°	5.674	4.706
2θ <sub>max</sub> /°	56.712	48.376
Measured Refl.	123,645	40,970
Independent Refl.	16,063	5736
Reflections used	12,893	4345
R <sub>int</sub>	0.0386	0.0487
Parameters	802	424
Goof	1.125	1.070
wR <sub>2</sub>	0.1120	0.1008
R <sub>1</sub>	0.0492	0.0428

<sup>a</sup> GOF =  $[\sum(w(F_o^2 - F_c^2)^2)/(N_o - N_v)]^{1/2}$  ( $N_o$  = number of observations,  $N_v$  = number of variables).

<sup>b</sup>  $R_1 = \sum||F_o| - |F_c||/\sum|F_o|$ .

<sup>c</sup>  $wR_2 = [(\sum w(F_o^2 - F_c^2)^2)/\sum|F_o|^3]^{1/2}$ .

**Table 2**  
Selected bond distances (Å) and angles (°) for complex **1**.CH<sub>2</sub>Cl<sub>2</sub> and **2**.

Complex 1			
Molecule 1			
Au(1)-P(1)	2.227(13)	Au(1)-N(2)	2.116(4)
P(1)-C(13)	1.810(6)	N(2)-C(6)	1.292(7)
P(1)-Au(1)-N(2)	166.50(15)	Au(1)-P(1)-C(13)	113.77(19)
Au(1)-P(1)-C(19)	110.91(18)	Au(1)-P(1)-C(25)	112.66(19)
C(13)-P(1)-C(25)	107.5(3)	Au(1)-N(2)-C(6)	125.8(4)
Au(1)-N(2)-C(12)	122.3(4)	C(6)-S(1)-C(7)	90.4 (3)
Molecule 2			
Au(2)-P(2)	2.221(14)	Au(2)-N(4)	2.112(6)
P(2)-C(29)	1.816(6)	N(4)-C(36)	1.319(9)
P(2)-Au(2)-N(4)	163.26(19)	Au(2)-P(2)-C(49)	113.5(2)
Au(2)-P(2)-C(42)	110.08(19)	Au(2)-P(2)-C(55)	113.7(2)
C(55)-P(2)-C(49)	107.9(3)	Au(2)-N(4)-C(36)	124.6(6)
Au(2)-N(4)-C(42)	123.0(5)	C(37)-S(2)-C(36)	90.9 (4)
Complex 2			
Au(1)-P(1)	2.303(18)	Au(1)-N(2)	2.218(5)
P(1)-C(17)	1.881(7)	N(2)-C(10)	1.359(8)
P(1)-Au(1)-N(2)	161.20(15)	Au(1)-P(1)-C(17)	117.0(2)
Au(1)-P(1)-C(29)	110.2(2)	Au(1)-P(1)-C(23)	111.6(2)
C(17)-P(1)-C(23)	105.5(3)	Au(1)-N(2)-C(10)	121.9(4)
Au(1)-N(2)-C(11)	125.5(4)	C(10)-S(1)-C(16)	91.1(3)

was added to the 100 mL of soft agar solution. The SSTI models were prepared using 7 mL of the soft agar solution spread evenly over the surface of the hard agar layer. After preparation the plates and initial incubation of 2 h, the KBr pellets containing the Au(I) complexes were placed on all SSTI models and incubated for 18 h to evaluate the antibacterial activity of the Au(I) compounds.

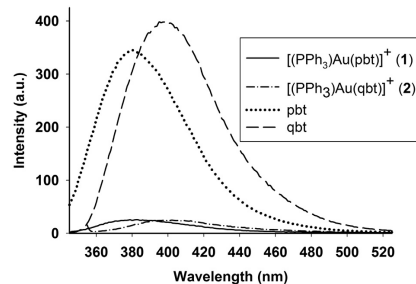
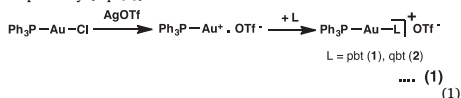


**Fig. 1.** Emission spectra of **1** ( $\lambda_{exc}$  330 nm) and **2** ( $\lambda_{exc}$  350 nm) compared to free ligands in dichloromethane ( $\lambda_{exc}$  310 and 335 nm for pbt and qbt respectively).

### 3. Results and discussion

#### 3.1. Synthesis and spectroscopic properties

The addition of 1.05 eq of AgOTf to (PPh<sub>3</sub>)AuCl afforded the highly reactive ion-pair AuPPh<sub>3</sub><sup>+</sup>.OTf<sup>-</sup> [24] which was then further reacted with 1 eq of pbt or qbt under refluxing condition to obtain **1** and **2** respectively (Eq. (1)).



The IR spectra of both **1** and **2** show a strong band around 1265 cm<sup>-1</sup> corresponding to the presence of the OTf<sup>-</sup> counter ion. Both complexes exhibit significant luminescence quenching in organic solvents when compared to the free ligand at the same concentration (Fig. 1). Similar partial quenching has been observed with [Ag(pbt)<sub>2</sub>]BF<sub>4</sub> and [Ag(qbt)<sub>2</sub>]BF<sub>4</sub> [14]. However, in the Ag(I) complexes, both ligands are bound in a bidentate fashion while in **1** and **2**, the ligands act as monodentate N-donors. The wavelength of emission for **1** and **2** are 380 nm and 400 nm respectively which are the wavelengths of emission for the corresponding free ligands pbt and qbt. A close scrutiny of the literature reveals that both the singlet and triplete excited states of Ag(I) and Au(I) complexes of similar coordination structures essentially possess ligand-centered  $\pi\pi^*$  character with negligible metal-to-ligand charge transfer (MLCT) contribution, and the excited triplet state mostly decay through non-radiative channels [14,25]. These characteristics presumably lead to significant luminescence quenching observed with the pbt and qbt complexes.

#### 3.2. Crystal structure description

Single crystal analysis reveals that complexes **1** and **2** are isostructural with respect to coordination at the Au center; in both cases the Au center resides in a linear N-Au-P coordination environment. For complex **1**, the asymmetric unit contains two crystallographically independent molecules. The perspective view with atom labeling scheme for the two structures are shown in Figs. 2 and 3. The N(benzothiazole)-Au-P angles in complexes **1** and **2** are 164.88(17) and 161.20(15)° respectively. Steric bulk of the qbt ligand leads to lengthening of both the average Au-N(benzothiazole) distance (2.114(5) Å for **1** vs. 2.218(5) Å for **2**) and the average Au-P distance (2.224(14) Å for **1** vs. 2.303(18) Å for **2**) in complex **2**. Although Cambridge structural database revealed several crystal structures with N-Au-P coordination mode, a representative structurally analogous complex namely, ((py)Au

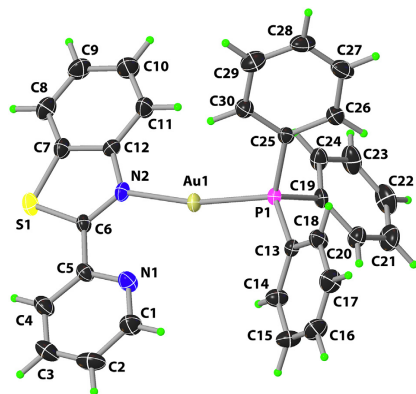


Fig. 2. Perspective view of the cation of complex 1 with the atom-labeling scheme. The thermal ellipsoids are shown at 50% probability level. Only one of the two crystallographically independent molecules in the asymmetric unit is shown.

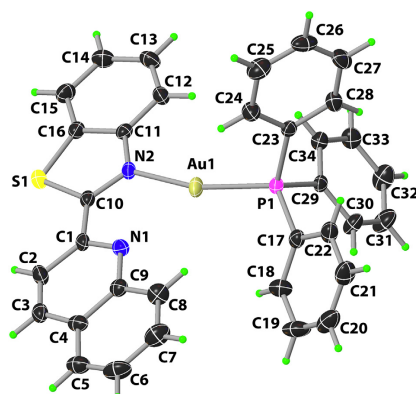


Fig. 3. Perspective view of the cation of complex 2 with the atom-labeling scheme. The thermal ellipsoids are shown at 50% probability level.

(PPh<sub>3</sub>)BF<sub>4</sub> [26] (where py = pyridine), was chosen to compare its crucial metric parameters with those of the present two complexes. In [(py)Au(PPh<sub>3</sub>)]BF<sub>4</sub>, the N(py)–Au and Au–P bond lengths are 2.073(3) Å and 2.2364(8) Å respectively. These distances are quite comparable to those noted for 1 and 2. Interestingly, the N–Au–P angle in [(py)Au(PPh<sub>3</sub>)]BF<sub>4</sub> is 178.09(8)°, more close to a linear geometry, unlike 1 and 2. In the present two structures, both pbt and qbt exhibit excellent planarity with mean deviations of 0.024(3) and 0.090(4) Å respectively. The packing patterns for both structures revealed no classical hydrogen bonding interactions. However, several weak non-bonding contacts consolidated the extended lattice of these two complexes (Supplementary data, Figs. S1–S3).

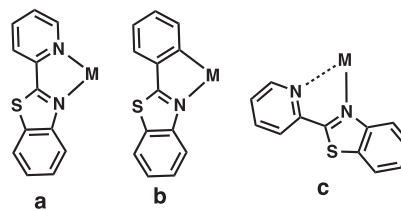


Fig. 4. Different modes of binding of pbt and aryl-benzothiazole.

### 3.3. Binding modes of 2-(aryl)benzothiazoles

2-aryl or 2-pyridyl substituted benzothiazole type ligands (like pbt and qbt) typically exhibit bidentate binding modes when coordinated to d<sup>10</sup> metal center. This can occur through the N-atom of the benzothiazole moiety and either the N-atom of the 2-pyridyl fragment [14] or C-atom of the 2-aryl portion [27] of the ligand (Fig. 4a and b respectively). Similar *N,N*-binding of pbt and qbt has been noted in complexes with low-spin d<sup>6</sup> metal centers such as Mn(I) and Re(I) [16,28–30]. In all cases, the ring S-atom does not coordinate.

When this type of ligands were employed for coordination to Au(I) centers in this research, the ligands failed to coordinate as bidentate ligands. Attempts to coordinate pbt and qbt to Au(I) center invariably afforded linear 2-coordinated complexes 1 and 2. Despite strong affinity of Au(I) to S-donors, both ligands are coordinated to the metal center through the N-atom of the benzothiazole (N(2)) moiety. This is in agreement with results from similar studies exploring the binding modes of Au(I) to ligands with electronically similar N and S (or N) donor atoms [31,32]. Mono-substituted binding mode of these types of ligands (leading to linear complexes) also arises from steric hindrance arising from the ligand itself [25]. Both the present complexes deviate from linearity; the P–Au–N angle of 1 and 2 are 166.50° and 161.22° respectively (Figs. 2 and 3, Table 2). Also, the P–Au–N angle of 2 with sterically more encumbered qbt ligand deviates more from linearity compared to 1.

It is important to note that in 1 and 2, the N atom of the pyridine/quinolyl moiety (N(1)) is facing the metal center, but not bound. Results of previous studies on the structures and ground state optimized geometries of the free ligands [14] have demonstrated that although the structure with the pyridyl–N and benzothiazole–N atom *anti* to each other is lower in energy, in all cases both pbt and qbt bind metal ions as the *N–N syn* structural isomer [14,16,28–30]. The pyridine fragment in these cases rotates to present its N center to be available for coordination in a *N–N syn* fashion (Scheme 1 and Fig. 4a). In 1 and 2, *this rotation of the aryl ring also occurs*, but the pyridyl–N or the quinolyl–N does not bind to the metal center. However, in both cases, significant interactions between this N-atom and the Au(I) center is observed in 1 [Au(1)–N(1), 2.713 Å] and 2 [Au(1)–N(10), 2.710 Å] (Fig. 4c) which is in agreement with other gold(I) compounds of similar structure [33].

### 3.4. Antibacterial studies

Antibacterial studies were done using the skin and soft tissue infection (SSTI) model previously developed in this laboratory [23]. This model mimics the gradual penetration of bacteria deeper into the skin using a two-layer agar system which has a soft, evenly dispersed bacterial lawn on the top and a nutrient-rich bottom layer. The gradient causes the bacteria to slowly migrate from the thin top layer to the nutrient-rich bottom layer much like the way an infection of the skin would proceed.

Both complexes and the corresponding ligands were tested *in vitro* for their bactericidal activity against the Gram-negative bacterium *A.*

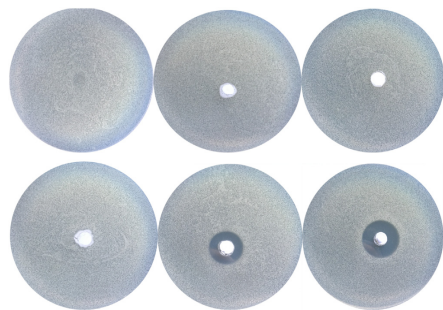


Fig. 5. Bacterial lawns after 18 h incubation with KBr pellets of KBr, pbt and qbt (top panel, left to right) and  $(\text{PPh}_3)\text{AuCl}$ , **1**, and **2** (bottom panel, left to right).

*baumannii*. This bacterium has shown multidrug-resistance in hospitals around the world and at present poses serious threat to human health. In addition to resistance traits carried on mobile genetic elements, *A. baumannii* also forms biofilms rapidly as defensive barriers. In addition, *A. baumannii* infections are a primary concern to military personnel injured by gun fire and improvised explosive devices (IEDs) in the battlefields of Afghanistan and Iraq [34]. With a limited pipeline of new antibiotics being developed for Gram-negative bacteria, new therapies are in high demand, especially for this pathogen. In the present work, a gold control (the neutral starting material  $\text{PPh}_3\text{AuCl}$ ) was also used to show how the ligands and the cationic nature of **1** and **2** affect the ability of the  $\text{Au}(\text{I})$  complexes to interact with the bacterial colonies. KBr pellets of similar weights containing 0.3 mol% of compounds were placed on the top of the bacterial lawn and incubated at 37 °C for 18 h. Circular zones of clearing were seen around the pellets containing **1** and **2**, but not around the pellets containing KBr, pbt, qbt or  $(\text{PPh}_3)\text{AuCl}$  (Fig. 5). These results indicate that the two  $\text{Au}(\text{I})$  complexes are better able to migrate and interfere with a large area of infection while the neutral gold compound exhibit no eradication of the bacteria on the SSTI model.

The antimicrobial activity of various drugs is highly dependent on their ability to permeate through the cell wall and interfere with cellular pathways [9]. Most bacteria possess a slightly electronegative surface potential which allows cationic complexes to associate more readily with the bacterial membrane. If the drug molecules can easily form bonds with biomolecules either on the membrane or in the cytosol, the efficacy of the drug action is enhanced. For gold compounds this implies that the nature of the ligands bound to the  $\text{Au}(\text{I})$  center, not just the amount of  $\text{Au}(\text{I})$  present, plays an important role in their activity [35]. The neutral and very stable compound  $(\text{PPh}_3)\text{AuCl}$  therefore exhibits no activity against *A. baumannii* while the more ligand exchangeable and cationic complexes **1** and **2** are very effective in eradicating bacterial loads throughout the entire “kill zone” of the 4 mm thick SSTI disk.

It is important to note that although **1** and **2** exhibited high level of antibacterial activity (Fig. 5), no reduction of bacterial load was observed with  $(\text{PPh}_3)\text{AuCl}$ . Because pbt and qbt by themselves showed marginal antibacterial effect for *A. baumannii*, it is evident that effective interaction between the cationic gold complexes and bacterial cell membrane is the major cause of their bactericidal activity. Upon deligation of pbt or qbt from the metal center, a step that delivers these antibacterials to the cytosol, the highly reactive  $\text{Ph}_3\text{PAu}^+ \cdot \text{OTf}^-$  species could also exert strong antibiotic action through binding to membrane and/or cytosolic molecules [36]. In order to check whether **1** and **2** can bind to cellular SH-containing proteins and peptides (such as

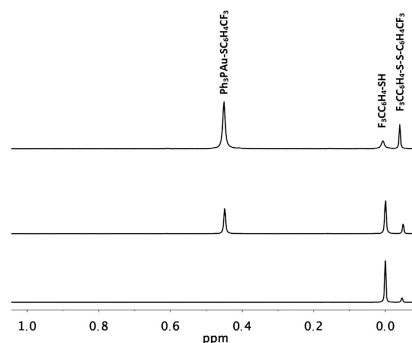


Fig. 6.  $^{19}\text{F}$  NMR spectrum of the mixture of **1** and  $\text{F}_3\text{CC}_6\text{H}_4\text{SH}$  (top trace),  $\text{PPh}_3\text{Au}-\text{SC}_6\text{H}_4\text{CF}_3$  synthesized independently (middle trace) and  $\text{F}_3\text{CC}_6\text{H}_4\text{SH}$  (bottom trace) in  $\text{CDCl}_3$ .  $\text{F}_3\text{CC}_6\text{H}_4\text{S}-\text{SC}_6\text{H}_4\text{CF}_3$  was present in the thiol as an impurity.

glutathione) present in the cytosol of the bacteria, **1** was treated with 1.2 equiv. of *p*-trifluoromethyl-benzene thiol ( $\text{F}_3\text{CC}_6\text{H}_4\text{SH}$ ) and the reaction was followed by both  $^{19}\text{F}$  and  $^1\text{H}$  NMR spectroscopy (in  $\text{CDCl}_3$ ). Interestingly, addition of the thiol to the  $\text{Au}(\text{I})$  complex generated a new  $^{19}\text{F}$ -peak at  $\sim 0.5$  ppm downfield (with respect to  $\text{F}_3\text{CC}_6\text{H}_4\text{SH}$ ) indicating binding of the thiol to the  $\text{Ph}_3\text{PAu}^+$  unit (Fig. 6). The  $^1\text{H}$  NMR spectrum of the reaction mixture clearly showed loss of pbt from the  $\text{Au}(\text{I})$  center upon addition of the thiol. In an independent experiment,  $\text{PPh}_3\text{Au}-\text{SC}_6\text{H}_4\text{CF}_3$  was synthesized by reacting  $(\text{PPh}_3)\text{AuCl}$  with  $\text{CF}_3\text{C}_6\text{H}_4\text{S}^-$  (prepared from  $\text{CF}_3\text{C}_6\text{H}_4\text{SH}$  and  $\text{Et}_3\text{N}$ ). The  $^{19}\text{F}$  NMR spectrum of  $\text{PPh}_3\text{Au}-\text{SC}_6\text{H}_4\text{CF}_3$  clearly confirmed its formation in the reaction between **1** and  $\text{F}_3\text{CC}_6\text{H}_4\text{SH}$  (Fig. 6). In order to confirm that the  $\text{PPh}_3$  ligand is not deligated in such reactions of **1** with SH-containing biomolecules, we allowed **1** to react with *N*-acetyl-L-cysteine methyl ester ( $\text{HSC}_6\text{H}_4\text{NO}_4$ ) in  $\text{CDCl}_3$ . The  $^{31}\text{P}$  NMR spectrum of the reaction mixture clearly showed that the cysteine ester replaced pbt to form  $\text{PPh}_3\text{Au}-\text{SC}_6\text{H}_4\text{NO}_4$  (Fig. 7). Complete absence of  $^{31}\text{P}$  resonance of free  $\text{PPh}_3$  in such reaction mixture confirms that no  $\text{PPh}_3$  loss occurs upon reaction of **1** with the S-containing amino acid.

Deligation of pbt or qbt from both complexes by SH-containing

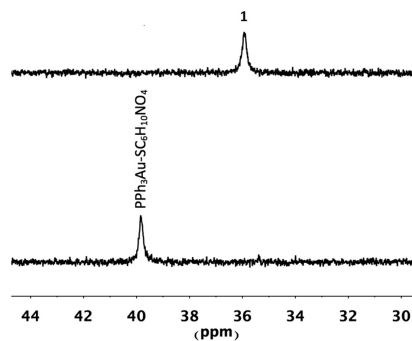


Fig. 7.  $^{31}\text{P}$  NMR spectra of complex **1** and  $\text{PPh}_3\text{Au}-\text{SC}_6\text{H}_4\text{NO}_4$  (formed upon addition of  $\text{HSC}_6\text{H}_4\text{NO}_4$  to **1**) in  $\text{CDCl}_3$  (the ppm values are w.r.t. free  $\text{PPh}_3$  in  $\text{CDCl}_3$ ).

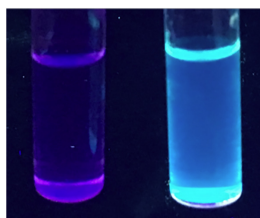


Fig. 8. Dramatic rise in luminescence upon addition of  $\text{CF}_3\text{C}_6\text{H}_4\text{SH}$  to **2** in chloroform. Left:  $\text{CHCl}_3$  solution of **2**; right: a mixture of **2** and  $\text{CF}_3\text{C}_6\text{H}_4\text{SH}$  in  $\text{CHCl}_3$ .



Fig. 9. Circular clearing ring in *P. aeruginosa* lawn upon application of **1**.

compounds can be readily observed by a dramatic increase in luminescence due to release of the strongly fluorescent ligands in solution. For example, when **2** was allowed to react with  $\text{CF}_3\text{C}_6\text{H}_4\text{SH}$  in chloroform, a sharp increase in luminescence was observed (Fig. 8). Taken together, these observations suggest that complexes like **1** and **2** most likely generate the reactive  $\text{Ph}_3\text{PAu}^+$  species (and free ligand) within the bacterial cell and disrupt the cellular mechanism(s) by binding to various biomolecules. Failure of free pbt and qbt in causing bacterial death could be attributed to their inability to cross cell membrane as well as their insolubility in aqueous media; complexes like **1** and **2** make such entry possible and possibly allow these ligands to exert their own antibacterial activity [12,13,37]. Lack of antibacterial activity of  $(\text{PPh}_3)_3\text{AuCl}$  most possibly arises from its high stability and inability to pass through the cell membrane.

Finally, in order to test the antimicrobial activity of the present Au(I) complexes against a more common and invasive bacterium prevalent in nosocomial skin infections and burn injuries complex **1** was tested against *P. aeruginosa*. A KBr pellet containing 0.3 mol% of **1** was placed on a *P. aeruginosa* lawn and incubated at  $37^\circ\text{C}$  for 18 h. The large zone of killing (Fig. 9) confirmed that complex **1** is highly effective in eradication of *P. aeruginosa*. More studies toward application of these two Au(I) complexes to thwart skin and wound infections by several drug-resistant bacteria are in progress in this laboratory. The results will be reported in due time.

#### 4. Conclusions

The strong antibacterial activity of two cationic Au(I) complexes reported here strongly suggest that gold compounds possess potential to combat skin and wound infections through topical applications. These types of Au(I) complexes derived from ligands that themselves exhibit antibacterial properties could be utilized in cases of drug-resistant bacterial infections. Both the ligand and the highly reactive

$\text{Ph}_3\text{PAu}^+\text{OTf}^-$  species could exert synergistic drug effects in such applications leading to better outcome. The present two complexes **1** and **2** provide proof-of-the-concept examples of such drug design approach.

#### Abbreviations

pbt	2-(pyridyl)benzothiazole
qbt	2-(quinolyl)benzothiazole
OTf <sup>−</sup>	trifluoromethanesulfonate anion
LB	luria broth
TSB	tryptone soya broth
SSTI	skin and soft tissue infection
MLCT	metal-to-ligand charge transfer

#### Acknowledgements

Financial support from the NSF grant DMR-1409335 and a UCSC COR-SRG grant is gratefully acknowledged.

#### Appendix A. Supplementary data

Crystal data for complex **1** and complex **2** (in CIF format) and the packing diagrams (Figs. S1–S3). Supplementary data to this article can be found online at doi: <https://doi.org/10.1016/j.jinorgbio.2018.05.003>.

#### References

- [1] S.B. Levy, B. Marshall, Nat. Med. Suppl. 10 (2004) S122–S129.
- [2] C. Ash (Ed.), Trends in Microbiology, vol. 2, Elsevier, Cambridge, UK, 1994, pp. 341–422.
- [3] S.B. Levy, Sci. Am. 278 (1998) 46–53.
- [4] M. Barber, Lancet 2 (1948) 641–644.
- [5] A.R. Coates, G. Halli, Y. Hu, Br. J. Pharmacol. 163 (2011) 184–194.
- [6] D.G. Biljana, M.I. Djuran, Dalton Trans. 43 (2014) 5950–5969.
- [7] E.R. Tieckink, Gold Bull. 36 (2003) 117–124.
- [8] S.J. Berners-Price, A. Filipovska, Metallomics 3 (2011) 863–873.
- [9] S.H. van Rijt, P.J. Sadler, Drug Discov. Today 14 (23–24) (2009) 1089–1097.
- [10] F. Mohr (Ed.), Gold Chemistry: Applications and Future Directions in the Life Sciences, Wiley-VCH Verlag GmbH & Co. Weinheim, Germany, 2009, pp. 283–319 (Ch. 6).
- [11] T.J. Beveridge, L.L. Graham, Microbiol. Rev. 55 (1991) 684–705.
- [12] B. Rajeeva, N. Srinivasulu, S.M. Shantakumar, Eur. J. Med. Chem. 6 (2009) 775–779.
- [13] K. Yamazaki, Y. Kaneko, K. Suwa, S. Ebara, K. Nakazawa, K. Yasuno, Bioorg. Med. Chem. 13 (2005) 2509–2522.
- [14] J. Stenger-Smith, I. Chakraborty, W.M.C. Sameera, P. Mascharak, Inorg. Chim. Acta 471 (2017) 326–335.
- [15] X. Chen, F.J. Femia, J.W. Babich, J. Zubieta, Inorg. Chim. Acta 314 (2001) 91–96.
- [16] J. Stenger-Smith, I. Chakraborty, S. Carrington, P. Mascharak, Acta Cryst. (2017) C73.
- [17] Bruker, APEX 3, Bruker AXS Inc, Madison, Wisconsin, USA, 2014.
- [18] Bruker, SAINT, Bruker AXS Inc, Madison, Wisconsin, USA, 2012.
- [19] Bruker, SADABS, Bruker AXS Inc, Madison, Wisconsin, USA, 2014 and 2016.
- [20] G.M. Sheldrick, Acta Crystallogr., Sect. A: Found. Crystallogr. 71 (2015) 3–8.
- [21] G.M. Sheldrick, Acta Crystallogr., Sect. C 71 (2015) 3–8.
- [22] O.V. Dolomanov, L.J. Bourhis, R.J. Gildea, J.A.K. Howard, H. Puschmann, J. Appl. Crystallogr. 42 (2009) 339–341.
- [23] B.J. Heilman, J.St. John, S.R.J. Oliver, P.K. Mascharak, J. Am. Chem. Soc. 134 (2012) 11573–11582.
- [24] H. Duan, S. Sengupta, J.L. Petersen, N.G. Akhmedov, X. Shi, J. Am. Chem. Soc. 131 (34) (2009) 12100–12102.
- [25] C. Hsu, C. Lin, M. Chung, Y. Chi, G. Lee, P. Chou, C. Chang, P. Chen, J. Am. Chem. Soc. 133 (2011) 12085–12099.
- [26] S.E. Thwaite, A. Schier, H. Schmidbaur, Inorg. Chim. Acta 357 (2004) 1549–1557.
- [27] E. Lalinde, R. Lara, L.P. Lopez, M.T. Moreno, E. Alfaro-Arnedo, J.G. Pichel, S. Pineiro-Hermida, Chem. Eur. J. 24 (2018) 2440–2456.
- [28] I. Chakraborty, S.J. Carrington, G. Roseman, P.K. Mascharak, Inorg. Chem. 56 (2017) 1534–1545.
- [29] S.J. Carrington, I. Chakraborty, J.M.L. Bernard, P.K. Mascharak, Inorg. Chem. 55 (2016) 7852–7858.
- [30] S.J. Carrington, I. Chakraborty, J.M.L. Bernard, P.K. Mascharak, ACS Med. Chem. Lett. 5 (2014) 1324–1328.
- [31] M. Albrecht, K. Hubler, W. Kaim, Z. Naturforsch. 54b (1999) 1606–1608.
- [32] M. Munakata, S.G. Yan, M. Maekawa, M. Akiyama, S. Kitagawa, J. Chem. Soc. Dalton Trans. (1997) 4257–4262.
- [33] A. Ilie, C.I. Rat, S. Scheutrow, C. Kiske, K. Lax, T.M. Klapötke, C. Silvestru, K. Karaghiosoff, Inorg. Chem. 50 (2011) 2675–2684.
- [34] P.S. Gregory, D.A. Srinivasan, C. Murray, K. Moran, E. Hulten, J. Fishbain, D. Craft, S. Riddell, L. Linder, Clin. Infect. Dis. 44 (2007) 1577–1584.
- [35] F. Novelli, M. Recine, F. Sparatore, C. Juliano, Farmaco 54 (1999) 232–236.
- [36] S.J.B. Price, M.J. Dimartino, D.T. Hill, R. Kuroda, M.A. Mazid, P.J. Sadler, Inorg. Chem. 24 (1985) 3425–3434.
- [37] P.S. Jadhav, A. Devprakash, G.P. Senthilkumar, Int. J. Pharm. Sci. Drug Res. 3 (2011) 1–7.





# Enhanced Bactericidal Effects of Pyrazinamide Toward *Mycobacterium smegmatis* and *Mycobacterium tuberculosis* upon Conjugation to a {Au(I)-triphenylphosphine}<sup>+</sup> Moiety

Jenny Stenger-Smith, Mireille Kamariza, Indranil Chakraborty, Ramatoulaye Ouattara, Carolyn R. Bertozzi, and Pradip K. Mascharak\*



Cite This: *ACS Omega* 2020, 5, 6826–6833



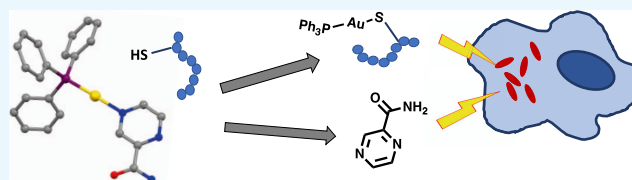
Read Online

ACCESS |

Metrics & More

Article Recommendations

Supporting Information



**ABSTRACT:** As part of the quest for new gold drugs, we have explored the efficacy of three gold complexes derived from the tuberculosis drug pyrazinamide (PZA), namely, the gold(I) complex [Au(PPh<sub>3</sub>)<sub>2</sub>(PZA)]OTf (1, OTf = trifluoromethanesulfonate) and two gold(III) complexes [Au(PZA)Cl<sub>2</sub>] (2) and [Au(PZO)Cl<sub>2</sub>] (3, PZO = pyrazinoic acid, the metabolic product of PZA) against two mycobacteria, *Mycobacterium tuberculosis* and *Mycobacterium smegmatis*. Only complex 1 with the {Au(PPh<sub>3</sub>)<sub>2</sub>}<sup>+</sup> moiety exhibits significant bactericidal activity against both strains. In the presence of thiols, 1 gives rise to free PZA and {Au(PPh<sub>3</sub>)<sub>2</sub>}<sup>+</sup>-thiol polymeric species. A combination of PZA and the {Au(PPh<sub>3</sub>)<sub>2</sub>}<sup>+</sup>-thiol polymeric species appears to lead to enhanced efficacy of 1 against *M. tuberculosis*.

## INTRODUCTION

Gold-based treatment of various diseases has been around for hundreds of years.<sup>1</sup> This area of research was made popular in the late 1800s when Robert Koch discovered gold cyanide to be effective against *Mycobacterium tuberculosis*, the causative agent of tuberculosis (TB).<sup>2</sup> His work inspired numerous others to further research gold as a possible potent antimicrobial agent. Eventually, the toxicity of gold compounds halted their clinical use for the treatment of TB but later became popular for the treatment of rheumatoid arthritis.<sup>3</sup> Auranofin, an antiarthritic drug, was approved for clinical use in the 1980s and continues to be administered today along with various other gold compounds.<sup>4</sup>

The success of auranofin and the rapid increase in drug-resistant pathogens prompted a surge of new research into gold compounds and their broad use as antiarthritic, antimicrobial, anticancer, and antifungal agents.<sup>5–7</sup> Gold(III) complexes, sharing the same geometrical shape as the well-known cancer therapeutic cisplatin, have been evaluated for their anticancer effect and often show increased activity with no cross-resistance to cisplatin.<sup>8,9</sup> Antimicrobial gold(I) and (III) complexes have been investigated for their potency against numerous strains of Gram-positive and Gram-negative bacteria showing promising results.<sup>6</sup> So far, research in this area has

implied that ligand structures of the gold complexes play important roles in both their efficacy and toxicity. In particular, manipulation of ligand structures was shown to affect the passage of the therapeutics across hydrophobic membranes of target cells to a significant extent.<sup>6,10,11</sup> An important class of gold(I) compounds, those with triphenylphosphine as ligands, is emerging as effective therapeutics against bacterial infection<sup>10,11</sup> and cancer (Figure 1).<sup>12–14</sup> The results of our previous work on cationic gold(I) triphenylphosphine complexes have implied that the highly reactive and lipophilic {Au(PPh<sub>3</sub>)<sub>2</sub>}<sup>+</sup> unit plays an important role in their antibacterial activity.<sup>11</sup> Although gold(I) complexes have been studied for their anticancer and antibacterial effectiveness, to our knowledge only two gold(I) complexes with the {Au(PPh<sub>3</sub>)<sub>2</sub>}<sup>+</sup> unit have so far been evaluated for their antimycobacterial behavior.<sup>15,16</sup>

Received: January 13, 2020

Accepted: March 9, 2020

Published: March 18, 2020



ACS Publications

© 2020 American Chemical Society

6826

<https://dx.doi.org/10.1021/acsomega.0c00071>  
*ACS Omega* 2020, 5, 6826–6833

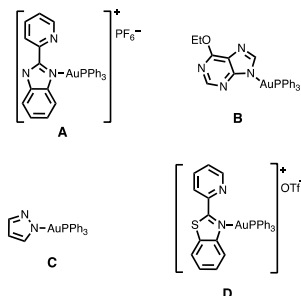


**Figure 1.** Structures of complexes with the  $\{Au(PPh_3)\}^+$  unit that have shown anticancer (A, B)<sup>13,14</sup> and antibacterial (C, D)<sup>10,11</sup> activity.

Recent efforts in drug discovery have demonstrated that combination of two antipathogenic moieties in one chemotherapeutic often leads to higher overall efficacy.<sup>11–16</sup> It is evident that such a design provides a dual mechanism of action and potentially increased the effect compared to that of the ligand or the metal center on its own. Along this line, we have reported Au(I) and Ag(I) complexes of benzothiazoles that exhibit high antibacterial activity against *Acinetobacter*

*baumannii*, *Pseudomonas aeruginosa*, and *Staphylococcus aureus*. Success in these cases prompted us to explore the possibility of designing new gold(I) complexes comprising the  $\{Au(PPh_3)\}^+$  moiety and the known TB drug pyrazinamide (PZA). PZA shortens the treatment duration for TB to a considerable extent although large oral quantities are needed for such effect.<sup>17</sup> We therefore decided to combine PZA with the  $\{Au(PPh_3)\}^+$  unit and study the synergistic effects (if any) on *M. tuberculosis* and the possibility of use of lower doses of PZA.

Herein, we report the syntheses and characterization of one gold(I) complex  $[Au(PPh_3)(PZA)]OTf$  (**1**, OTf = trifluoromethanesulfonate) and two gold(III) complexes  $[Au(PZA)_2Cl_2]$  (**2**) and  $[Au(PZO)_2Cl_2]$  (**3**, PZO = pyrazinoic acid, the metabolic product of PZA). The antimicrobial properties of these complexes have been evaluated on both *M. tuberculosis* and *Mycobacterium smegmatis*.

## EXPERIMENTAL SECTION

**General.** All reagents and solvents were of commercial grade and used without further purification. Fourier-transform infrared (FT-IR) spectra were obtained using a PerkinElmer Spectrum One spectrophotometer. <sup>1</sup>H, <sup>13</sup>C, <sup>31</sup>P, and <sup>19</sup>F nuclear magnetic resonance (NMR) spectra were recorded using a Varian Unity 500 MHz instrument at 298 K.

**Syntheses.**  $[Au(PPh_3)(PZA)]OTf$  (**1**). A solution of 72.0 mg (0.28 mmol) of silver trifluoromethanesulfonate (OTf) in 10 mL of methanol was added to a solution of 138.8 mg (0.28

**Table 1.** Crystal Data and Structure Refinement Parameters for **1**·H<sub>2</sub>O, **2**, and **3**

	1·H <sub>2</sub> O	2	3
formula	C <sub>23</sub> H <sub>30</sub> AuN <sub>3</sub> OP·CF <sub>3</sub> O <sub>3</sub> S·H <sub>2</sub> O	C <sub>3</sub> H <sub>3</sub> AuCl <sub>2</sub> N <sub>3</sub> O	C <sub>3</sub> H <sub>3</sub> AuCl <sub>2</sub> N <sub>2</sub> O <sub>2</sub>
<i>D</i> <sub>calc</sub> (g cm <sup>−3</sup> )	1.835	3.135	3.013
<i>μ</i> (mm <sup>−1</sup> )	5.62	18.4	17.65
formula weight	749.44	389.98	390.96
color	colorless	yellow	yellow
shape	block	block	plate
<i>T</i> (K)	298	298	298
crystal system	triclinic	triclinic	orthorhombic
space group	<i>P</i> 1	<i>P</i> 1	<i>P</i> bca
<i>a</i> (Å)	7.0334 (10)	6.6857 (10)	7.2868 (6)
<i>b</i> (Å)	12.6524 (16)	7.2848 (11)	14.4003 (12)
<i>c</i> (Å)	15.688 (2)	8.9057 (13)	16.4259 (13)
<i>α</i> (°)	79.435 (4)	94.664 (2)	90
<i>β</i> (°)	81.214 (5)	106.878 (2)	90
<i>γ</i> (°)	89.464 (4)	91.649 (2)	90
<i>V</i> (Å <sup>3</sup> )	1356.0 (3)	413.06 (11)	1723.6 (2)
<i>Z</i>	2	2	8
wavelength (Å)	0.71073	0.71076	0.71076
radiation type	Mo <i>Kα</i>	Mo <i>Kα</i>	Mo <i>Kα</i>
2 <i>θ</i> <sub>min</sub> (°)	5.8	7	6.2
2 <i>θ</i> <sub>max</sub> (°)	52.8	49.6	49.4
measured refl.	24 132	4259	15 095
independent refl.	5469	1395	1462
reflections used	5027	1381	1261
<i>R</i> <sub>int</sub>	0.025	0.019	0.044
parameters	343	113	109
GooF <sup>a</sup>	1.14	1.2	1.08
<i>wR</i> <sub>2</sub> <sup>c</sup>	0.122	0.043	0.067
<i>R</i> <sub>1</sub> <sup>c</sup>	0.044	0.017	0.024

<sup>a</sup>GOF =  $[\sum(w(F_o^2 - F_c^2)^2)/(N_o - N_v)]^{1/2}$  (*N*<sub>o</sub> = number of observations, *N*<sub>v</sub> = number of variables). <sup>b</sup>*wR*<sub>2</sub> =  $[(\sum w(F_o^2 - F_c^2)^2)/\sum(F_o^2)]^{1/2}$ . <sup>c</sup>*R*<sub>1</sub> =  $\sum||F_o| - |F_c||/\sum|F_o|$ .



mmol) of chloro(triphenylphosphine)gold(I) dissolved in 15 mL of chloroform. Immediately, a suspension of AgCl was formed and the mixture was stirred for 30 min at room temperature and then filtered through a bed of celite. To the filtrate, a solution of 34.4 mg (0.28 mmol) of PZA in 15 mL of methanol/chloroform (1:1) was added, and the mixture was stirred for 18 h at room temperature. The flask was covered with an Al foil to protect the reaction mixture from ambient light. Next, the solvent was removed in vacuo, and the solid was washed with diethyl ether to obtain **1** as a white solid (112.1 mg, 54%). A solution of the solid in chloroform was layered with hexanes and stored in the fridge. X-ray quality crystals of **1** were obtained after 1 week. Anal. calc. for  $C_{27}H_{20}AuN_3O_4PSF_3$ : C, 39.41; H, 2.76; N, 5.74; found: C, 39.35; H, 2.79; N, 5.68. IR (KBr,  $cm^{-1}$ ): 3435(m), 3309(m), 1690(s), 1438(m), 1262(s), 1167(m), 1031(m), 693(m).  $^1H$  NMR ( $CD_3OD$ ,  $\delta$  ppm): 9.40 (b, 1H), 9.03 (b, 1H), 8.96 (b, 1H), 7.69–6.58 (m, 15H).  $^{13}C$  ( $CDCl_3$ ,  $\delta$  ppm): 148.18, 146.38, 144.29, 134.26, 134.16, 132.54, 132.52, 129.64, 129.55, 127.55, 127.03.  $^{31}P$  (MeOD, referenced to  $PPh_3$ ), 34.88.

**[Au(PZA)Cl<sub>2</sub>] (2).** A batch of 32.5 mg (0.26 mmol) of PZA was dissolved in 2 mL of water and the solution was added dropwise to a solution of 99.7 mg (0.26 mmol) of potassium tetrachloroaurate in 1.75 mL of water at room temperature with stirring. A yellow solid appeared quickly, and the suspension was allowed to stir for an additional 10 min. The precipitate was filtered, washed with 2 mL of cold water and then 10 mL of cold diethyl ether to obtain the precursor complex (vide infra) as a bright yellow solid (90 mg). IR (KBr,  $cm^{-1}$ ): 3442(m), 1704(s), 1373(m), 1177(w), 560(w).  $^1H$  NMR ( $CD_3CN$ , ppm): 9.53 (s, 1H), 9.07 (d, 1H), 9.05 (d, 1H), 7.68 (b, 1H), 6.60 (b, 1H). The precursor yellow solid was crystallized by slow evaporation in methanol to form orange blocks of **2** after 2 weeks. Anal. calc. for  $C_5H_4AuN_3OCl_2$ : C, 15.40; H, 1.03; N, 10.77; found: C, 15.38; H, 1.10; N, 10.73. IR (KBr,  $cm^{-1}$ ): 3167(m), 1660(s), 1584(m), 1421(w), 1348(m), 1166(w), 1065(w), 579(w).  $^1H$  NMR ( $CD_3CN$ ,  $\delta$  ppm): 9.26 (m, 2H), 9.21 (s, 1H), 7.24 (b, 1H).  $^{13}C$  ( $(CD_3)_2SO$ ,  $\delta$  ppm): 171.27, 152.97, 149.89, 141.50, 138.46.

**[Au(PZO)Cl<sub>2</sub>] (3).** An aqueous solution of sodium hydroxide (0.15 M) was used to adjust the pH of a suspension of 100 mg (0.81 mmol) of PZO in 2 mL of water until a pH of 7 was reached. At this point, PZO had fully dissolved and the solution was added dropwise to a solution of 101.5 mg (0.27 mmol) of potassium tetrachloroaurate in 1 mL of water at room temperature with stirring. A light yellow precipitate appeared within minutes. After stirring for an additional 30 min, the solid was filtered, washed with 2 mL of cold water and then 5 mL of diethyl ether. The light yellow solid was finally recrystallized from MeOH/ether to yield **3** as a yellow microcrystalline solid (60.2 mg, 55%). X-ray quality crystals were formed by the layering of acetonitrile/ether. Anal. calc. for  $C_5H_3AuN_3O_2Cl_2$ : C, 15.36; H, 0.77; N, 7.17; found: C, 15.40; H, 0.81; N, 7.13. IR (KBr,  $cm^{-1}$ ): 3586 (m), 3419 (m), 1705(s), 1616(s), 1408(m), 1376(s), 1138(m), 850 (w), 795(w).  $^1H$  NMR ( $CD_3CN$ ,  $\delta$  ppm): 9.31 (m, 2H), 9.12 (d, 1H).  $^{13}C$  ( $CD_3CN$ ,  $\delta$  ppm): 170.00, 154.09, 151.53, 139.90, 137.35.

**X-ray Crystallography.** Crystallographic data were collected on a Bruker APEX II single-crystal X-ray diffractometer (PHOTON 100 detector) with graphite monochromated Mo  $K\alpha$  radiation ( $\lambda = 0.71073$  Å) by the  $\omega$ -scan

technique in the range  $5.8 \leq 2\theta \leq 53$  for (**1**),  $7 \leq 2\theta \leq 50$  for (**2**), and  $6.2 \leq 2\theta \leq 50$  for (**3**) (Table 1). All data were corrected for Lorentz and polarization effects.<sup>18</sup> All of the structures were solved with the aid of the SHELXT program using intrinsic phasing.<sup>19</sup> The structures were then refined by a full-matrix least-squares procedure on  $F^2$  by SHELXL.<sup>20</sup> All nonhydrogen atoms were refined anisotropically. All hydrogen atoms were included in calculated positions. The absorption corrections are done using SADABS.<sup>19</sup> Calculations were performed using the OLEX2<sup>21</sup> and SHELXTL<sup>22</sup> (V 6.14) program package.

**Mycobacterial Studies.** *M. smegmatis*. Middlebrook 7H9 liquid medium<sup>23</sup> was inoculated from a frozen stock of *M. smegmatis* and grown overnight to an optical density at 600 nm ( $OD_{600}$ ) of 1. Stock solutions of test compounds in acetone (0.02–0.1 mM) were prepared, and batches of 20  $\mu L$  of such solutions were added to 250  $\mu L$  of the bacterial suspensions in 1.73 mL of 7H9 media in 5 mL culture tubes. The tubes were incubated at 37 °C for 18 h. The MIC values were then determined by reading the  $OD_{600}$  of the suspensions with different concentrations of the test compounds. To ensure that no viable bacteria remained in such tubes was confirmed as follows. Aliquots of 100  $\mu L$  of the suspensions were added to fresh 7H9 media (1 mL) and incubated at 37 °C for 18 h. In all cases, no bacteria growth was observed. The MIC results are summarized in Table 3, and all concentrations were performed in triplicate.

*M. tuberculosis*. A stock culture of *M. tuberculosis* was prepared by inoculation of a 1 mL frozen stock into 50 mL of Middlebrook 7H9 liquid medium supplemented with 10% (v/v) OADC enrichment (BBL Middlebrook OADC, 212351), 0.5% (v/v) glycerol, and 0.05% (w/v) Tween 80 (P1754, Sigma-Aldrich) in a roller bottle. Cells were grown to an  $OD_{600}$  of 1.0 to begin the experiments. The culture was then diluted down to a target  $OD_{600}$  of 0.5 (final  $OD$  reading = 0.67). Aliquots of 100  $\mu L$  of 8 mM test compound solutions in acetone were added to batches of 10 mL of the culture suspension (final concentration of the test compounds = 80  $\mu M$  in 1% acetone) and the tubes were then incubated at 37 °C. After 24 h incubation, the  $OD_{600}$  values were recorded. Triplicates were run with each test compound, and the results are shown in Figure 5.

## RESULTS AND DISCUSSION

**Synthesis.** Complex **1** was synthesized by first displacing the chloride ligand from  $[ClAu(PPh_3)_2]$  with the aid of Ag(OTf) and introducing PZA as the second ligand. Single-crystal analysis of **1** (Figure 2) revealed PZA as a monodentate N-donor ligand.<sup>24</sup> The IR spectrum of **1** exhibits a strong peak centered around 1261  $cm^{-1}$  corresponding to the OTf counterion and the carbonyl amide peak of PZA at 1690  $cm^{-1}$ .

Complex **2** (Figure 3, top panel) was not obtained from the initial reaction of  $KAuCl_4$  and PZA. That reaction afforded the precursor complex (mentioned above). This precursor complex as shown in Scheme 1 is always the first product that appears as a bright yellow solid and behaves similarly to the analogous  $[AuCl_2(pyrazine)]$  complex.<sup>25</sup> Slow evaporation of the methanolic solution of this precursor complex eventually affords complex **2**. Comparison of the IR spectra of the precursor complex and **2** reveals different  $\nu_{CO}$  frequencies (1704 and 1660  $cm^{-1}$ , respectively) corresponding to the amide CO group of PZA. Because the  $\nu_{CO}$  of the precursor complex is close to the  $\nu_{CO}$  value of free PZA (1711  $cm^{-1}$ ), we

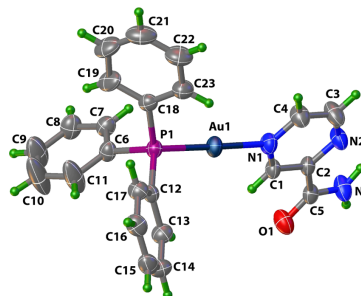


**Figure 2.** Structure of **1** with water and OTf anion omitted for clarity. Ellipsoids are shown at the 50% probability level.

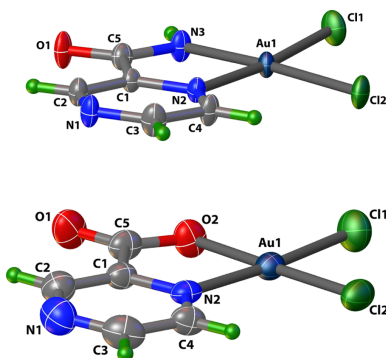
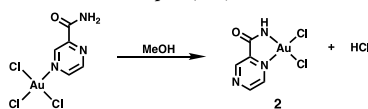


**Figure 3.** Crystal structures of **2** (top) and **3** (bottom) with thermal ellipsoids at 50% probability.

**Scheme 1.** Suggested Ligand Binding Mode Rearrangement from the Precursor Complex (Left) to **2**



believe that in this complex the PZA ligand is bound to the Au(III) center in a monodentate fashion (as shown in Scheme 1). In complex **2**, the PZA ligand is bonded as a bidentate ligand (Figure 3) with the deprotonated amide group. Elimination of HCl from the precursor complex leads to formation of complex **2** in methanolic solution upon long evaporation (Scheme 1). Due to the relatively quick reaction time (10 min), the precursor material presumably precipitates out as the kinetically favored species while **2** is the thermodynamically favored species obtained after recrystallization from methanol. The assignment is further supported by the fact that while the precursor complex exhibits two amide NH peaks in its NMR spectrum (much like free PZA) in

CD<sub>3</sub>CN, complex **2** displays only one NH peak in its NMR spectrum in the same solvent (Figure 4). Also the precursor

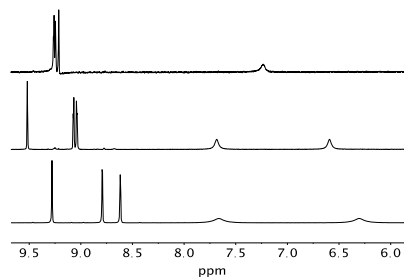


**Figure 4.** <sup>1</sup>H NMR (in CD<sub>3</sub>CN) spectra of **2** (top), the precursor compound (middle), and PZA (bottom).

complex, like [AuCl<sub>3</sub>(pyrazine)], readily loses the N-donor ligand in dimethyl sulfoxide (DMSO)-*d*<sub>6</sub> (as evidenced by NMR spectra).<sup>25</sup> We hypothesize that in the precursor complex, PZA is bound to the Au(III) center at the N atom meta to the carboxamide group (as observed in complex **1**) simply because this N center is the most basic site of the PZA molecule.<sup>26</sup> Conversion of the precursor complex to **2** is accelerated by the addition of NaHCO<sub>3</sub> in a 1:1 MeOH/water reaction mixture, a step that pushes the reaction shown in Scheme 1 to the right.

PZO, the purported metabolic product actually responsible for the drug action of PZA, also binds the Au(III) center as a bidentate ligand (Figure 3, bottom panel). Addition of excess deprotonated PZO to KAuCl<sub>4</sub> in the aqueous medium affords complex **3** in high yield.

**Structures.** Structures of **1–3** were characterized by X-ray crystallography and the perspective views (with atom labeling schemes) are shown in Figures 2 and 3, while the structure refinement parameters and selected bond distances and angles are listed in Tables 1 and 2, respectively. For the sake of comparison of the metric parameters, the two Au(III) complexes (**2** and **3**) are shown in Figure 3. As evident from their crystal structures, the Au(I) complex **1** exhibits a linear

**Table 2.** Selected Bond Lengths and Angles for **1**·H<sub>2</sub>O, **2**, and **3**

	<b>1</b> ·H <sub>2</sub> O	<b>2</b>	<b>3</b>
Au(1)–P(1)	2.2432 (18)		
Au(1)–N(1)	2.082 (6)		
Au(1)–N(3)		1.985 (4)	
Au(1)–N(2)		2.042 (4)	2.016 (6)
Au(1)–Cl(1)		2.2571 (12)	2.250 (2)
Au(1)–Cl(2)		2.2879 (12)	2.2510 (17)
Au(1)–O(2)			1.998 (4)
N(1)–Au(1)–P(1)	177.8 (2)		
N(3)–Au(1)–Cl(1)		93.22 (12)	
N(2)–Au(1)–N(3)		80.51 (16)	
Cl(1)–Au(1)–Cl(2)		90.75 (5)	90.68 (7)
N(2)–Au(1)–Cl(2)		95.63 (11)	95.57 (14)
N(2)–Au(1)–O(2)			82.7 (2)
O(2)–Au(1)–Cl(1)			91.01 (16)

coordination, while the two Au(III) complexes are square planar. In the structure of **1**, there is one molecule of water in the asymmetric unit, while the other two structures contain no solvent of crystallization. The N(1)–Au(1)–P(1) angle in **1** deviates slightly from linearity with an angle of 177.8(2)°. The Au–N(pyridine) (2.081(7) Å) bond is shorter than Au–P (2.244(2) Å) bond as expected. Similar bond lengths and angles are observed in other known structures of Au(I) complexes of [(N-bound ligand)/Au(PPh<sub>3</sub>)]<sup>+</sup>-type.<sup>11,14</sup> The three nitrogen atoms on PZA potentially allow for three different binding modes to the {Au(PPh<sub>3</sub>)}<sup>+</sup> unit in **1**; however, the least sterically hindered and most basic N of PZA shows preference to the metal center, as shown in Figure 1.<sup>26</sup>

Au(III) complexes **2** and **3** are both distorted square planar and composed of the PZA/PZO ligand bound as a bidentate ligand. The square planar geometries of **2** and **3** deviate noticeably from planarity with N(2)–Au(1)–N(3) and N(2)–Au(1)–O(2) angles of 80.51(16) and 82.7(2)°, respectively. The Cl(1)–Au(1)–Cl(2) angles of both structures deviate only slightly from the perfect right angle values 90.75(5) and 90.68(7)°, respectively. As expected, the deprotonated Au(1)–N(3) or Au(1)–O(2) of **2** and **3** are significantly shorter than the Au(1)–N(2) bonds shown in Table 2. Bond lengths and angles are in agreement with similar known structures of Au(III)-picolinamide and picolinic acid derivatives.<sup>27,28</sup>

In **2**, the equatorial plane comprised of Au(1), N(2), N(3), Cl(1), Cl(2) atoms is fairly planar with a mean deviation of 0.041(3) Å, while the corresponding plane in **3** (comprised of Au(1), O(2), N(2), Cl(1), Cl(2) atoms) is highly planar with a mean deviation of 0.011(3) Å. The central metal atom in **2** and **3** is deviated from these planes by 0.009(3) and 0.022(3) Å, respectively. The two chelate planes formed by the bidentate PZA and PZO ligands along with Au(III) centers in **2** (Au(1), N(2), N(3), C(1), and C(5)) and **3** (Au(1), N(2), O(2), C(1), and C(5)) exhibit minimal deviation from planarity (mean deviations, 0.01(3) Å and 0.019(3) Å for **2** and **3**, respectively). The dihedral angles between the pyrazine ring and the five-membered chelate ring in **2** and **3** are 3.18(2) and 1.83(2)°, respectively. In an Au(III) complex with picolinamide as a ligand, which structurally resembles closely to that of complex **2**, the dihedral angle between the pyridine ring and the five-membered chelate ring is 3.6(2)°, which is close to the corresponding value noted for **2**.<sup>27</sup> Moreover, the mean deviations of the chelate ring are similar to those in **2**. However, a reported Au(III) complex with a picolinic acid derivative as the ligand resembles structurally more to complex **3**, and the dihedral angle between the pyridine ring and the five-membered chelate ring is 1.28(2)°.<sup>28</sup>

**Mycobacterial Activity.** Before studying the potential synergistic effects of PZA and gold on *M. tuberculosis*, the antimicrobial effects of the Au center alone were studied on *M. smegmatis*. This bacterium is in the same genus as *M. tuberculosis* and has 2000 genes highly conserved with the pathogen. Thus, *M. Smegmatis* is an excellent model organism that is easy to work with, has a fast growth rate, and a relatively safer model.<sup>23,29</sup> *M. Smegmatis* is known to be naturally resistant to PZA and thus provides an opportunity to study the activity of the {Au(I)(PPh<sub>3</sub>)}<sup>+</sup> and {Au(III)Cl<sub>2</sub>}<sup>+</sup> moieties of **1**–**3**. In the present work, the activities of **1**–**3**, [ClAu(PPh<sub>3</sub>)], PZA, and a drug control isoniazid (INH) were tested against *M. smegmatis* in a normal growth environment and the results

are summarized in Table 3. Under our conditions, we found the MIC to be 60 μM for **1** and [ClAu(PPh<sub>3</sub>)], while **2**, **3**, and

Table 3. MIC (μM) Values for Activity Against *M. smegmatis*

compound	MIC (μM)
<b>1</b>	60
<b>2</b>	>100
<b>3</b>	>100
[ClAu(PPh <sub>3</sub> )]	60
PZA	>100
INH	80

PZA showed no activity up to 100 μM. Mycobacteria species are known to have thick, hydrophobic, and waxy membranes that prevent foreign substances from permeation more so than traditional Gram-positive and Gram-negative species.<sup>30,31</sup> For this reason, the lipophilic {Au(PPh<sub>3</sub>)}<sup>+</sup> unit in **1** might have been able to pass through this membrane and exert drug action. This conclusion is supported by the fact that cell digests from *M. smegmatis* cells exposed to 40 μM (below the MIC) of **1** exhibited strong inductively coupled plasma mass spectrometry (ICP-MS) signal(s) for gold. Also, the gold(III) species **2** and **3** with chloro ligands but no {Au(PPh<sub>3</sub>)}<sup>+</sup> moiety were not active at similar concentrations.

With results from *M. Smegmatis* study in hand, we proceeded to test the activity of complex **1** against *M. tuberculosis* in vitro along with [ClAu(PPh<sub>3</sub>)], PZA, and isoniazid (INH). The OD of *M. tuberculosis* was recorded after 24 h incubation with 80 μM of each compound in 1% acetone (Figure 5). Interestingly,

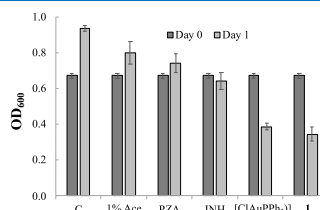
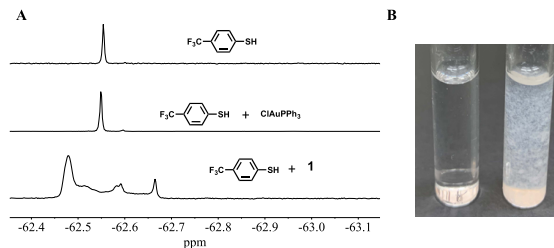


Figure 5. *M. tuberculosis* OD<sub>600</sub> values of the initial (day 0) and after 24 h (day 1) incubation with test compounds at 80 μM. Column C has no additional compound and acetone (Ace).

**1** showed significant bactericidal activity (reduction in OD), while PZA on its own was only mildly bacteriostatic (OD less than the control but higher than day 0). The mild drug action of PZA against *M. tuberculosis* at the 80 μM concentration is expected since the higher concentration of PZA (up to 400 μM) and low pH (5.5) media are usually required to observe any effect on *M. tuberculosis* growth in vitro.<sup>32</sup> The results shown in Figure 5 strongly suggest that the {Au(PPh<sub>3</sub>)}<sup>+</sup> moiety of **1** augments the efficacy of PZA in vitro. The standard [ClAu(PPh<sub>3</sub>)] was specifically included in this study to determine if **1** would show increased activity compared to a compound with the {Au(PPh<sub>3</sub>)}<sup>+</sup> moiety without PZA. Inspection of Figure 5 reveals that both **1** and [ClAu(PPh<sub>3</sub>)] exhibited the greatest reduction in OD at very similar average values of 0.345 and 0.387, respectively. Collectively, these results suggest that complex **1** could introduce a dose of PZA as well as the {Au(PPh<sub>3</sub>)}<sup>+</sup> moiety in one combination and act



**Figure 6.** (A)  $^{19}\text{F}$  NMR spectra of  $\text{HSC}_6\text{H}_4\text{CF}_3$  (top),  $[\text{ClAu}(\text{PPh}_3)] + \text{HSC}_6\text{H}_4\text{CF}_3$  (middle), and  $\mathbf{1} + \text{HSC}_6\text{H}_4\text{CF}_3$  (bottom). (B) Reaction of  $[\text{ClAu}(\text{PPh}_3)]$  (left) and  $\mathbf{1}$  (right) after addition of *N*-acetyl-L-cysteine-methyl-ester.

as a “two-in-one” drug against *M. tuberculosis*. Ultimately, this might reduce the need for much higher doses of PZA itself, which has severe side effects on humans. The gold–phosphine unit is not so uncommon in metaldrug therapy; Auranofin, an FDA-approved drug for rheumatoid arthritis, does contain a  $\{\text{Au}(\text{PET}_3)\}^+$  unit.<sup>4</sup>

PZA plays an important role in shortening TB treatment duration from 9–12 months to 6 months. This is likely because PZA targets a population of semidormant bacilli residing within the macrophages in an environment not accessible to other TB drugs.<sup>32,33</sup> The mechanism of action of the pro-drug PZA is not entirely understood, but most agree that the conversion of PZA to PZO within the bacilli is critical for activity against *M. tuberculosis*. Interestingly, PZO itself is not as active as PZA against *M. tuberculosis*. PZA has a broad range of activity highly dependent on the pH of the media and because it targets mostly nonreplicating bacilli, PZA exhibits slow or no bactericidal activity in vitro.<sup>32</sup> This occurrence is likely the reason why no synergy was observed in our hands. Nevertheless, PZA has had a significant clinical impact on TB and therefore research toward modifying PZA with the additional antimycobacterial moiety might lead to new and improved outcomes.

**Solution studies.** The results of  $^1\text{H}$  NMR studies confirm that  $\mathbf{1}$ – $\mathbf{3}$  are stable in acetone, while  $\mathbf{2}$  and  $\mathbf{3}$  are also stable in acetonitrile. Complexes  $\mathbf{2}$  and  $\mathbf{3}$  are stable in aqueous acetone (90:10) for hours, while  $\mathbf{1}$  slowly decomposes in such solutions (used in biological studies). However, inside biologically relevant environments, exposure to sulfur-containing biomolecules like glutathione is expected. Gold(I) centers are soft Lewis acids, and it is well established that they prefer binding to soft Lewis bases like thiolate species. The binding of gold(I) species to biologically relevant thiols (such as glutathione) and enzymes with thiol-containing active sites (such as thioredoxin) has been observed and the exchange of N- and S-bound ligands occurs quickly compared to P-bound ligands.<sup>14,34</sup> This exchange has been hypothesized to play an important role in the anticancer effects of  $[\text{N}-\text{Au}(\text{PPh}_3)]$  complexes<sup>14</sup> as well as the antimycobacterial effects exhibited by auranofin.<sup>35</sup> Disruption of redox homeostasis within the bacterial cell following binding of the gold unit to glutathione or thioredoxin has been suggested to be responsible for the drug action. Impairment of protein synthesis in bacteria has also been observed with auranofin treatment.<sup>36</sup> In our previous work, we have showed that complexes with N-bound benzothiazole ligands and the  $\{\text{Au}(\text{PPh}_3)\}^+$  moiety rapidly exchange with thiol species.<sup>11</sup> In the present work, we checked the possibility

of exchange between PZA and biologically relevant thiols in the case of  $\mathbf{1}$ . Both  $^1\text{H}$  and  $^{19}\text{F}$  NMR spectra of the mixture of  $\mathbf{1}$  and 4-(trifluoromethyl)thiophenol (FTP) were recorded to observe if PZA does get exchanged with FTP (Figure 6). As shown in Figure 6 (left panel), addition of FTP to  $\mathbf{1}$  showed release of PZA as a free ligand (as evident in the  $^1\text{H}$  NMR, not shown) with multiple new  $^{19}\text{F}$  NMR peaks (Figure 6A, bottom) along with a white precipitate. Together, these results indicate the formation of  $\{\text{S}-\text{Au}(\text{PPh}_3)\}$ -polymeric species by  $\mathbf{1}$  in the presence of a thiol. We hypothesize that such a transformation will lead to the presence of both PZA and  $\{\text{Au}(\text{PPh}_3)\}^+$  units, which will exert their own individual and potentially synergistic actions. In contrast,  $[\text{ClAu}(\text{PPh}_3)]$  does not appear to react with FTP and form any Au–thiol species (Figure 6A, middle panel). In the acidic (pH 6.2–4.5) macrophage compartment,<sup>37</sup> replacement of  $\text{Cl}^-$  by a thiol is highly unlikely. Thus, administration of  $\mathbf{1}$  (compared to  $[\text{ClAu}(\text{PPh}_3)]$ ) could be more reactive against *M. tuberculosis* residing within the macrophages in vivo. We have also employed a more biologically relevant thiol, namely, *N*-acetyl L-cysteine methyl ester, to check this interpretation. Addition of *N*-acetyl L-cysteine methyl ester to  $\mathbf{1}$  resulted in the immediate appearance of a white precipitate (Figure 6B, right), but no such reaction was observed with  $[\text{ClAu}(\text{PPh}_3)]$  (Figure 6B, left). Collectively, these results suggest that formation of  $\{\text{S}-\text{Au}(\text{PPh}_3)\}$ -polymeric species with  $\mathbf{1}$  within biological targets might promote uptake by host macrophages, similar to the uptake of Au nanoparticles<sup>38,39</sup> and/or breakdown of cellular thiol-redox homeostasis.<sup>35</sup> Since *M. tuberculosis* is either contained by macrophages or reside within them, this process could offer a more direct route to TB treatment in a host system. The  $\{\text{S}-\text{Au}(\text{PPh}_3)\}$ -polymeric species derived from  $\mathbf{1}$ , along with PZA, could cause more damage to the mycobacterium residing within the macrophages and thus increasing the efficacy of the treatment.

## CONCLUSIONS

While Au complexes have been evaluated for their antimycobacterial effects previously,<sup>40–43</sup> extensive literature search reveals only two other complexes containing the  $\{\text{Au}(\text{PPh}_3)\}^+$  unit (Figure 7) in such testing.<sup>15,16</sup> Also, in a previous study, the auranofin containing  $\text{PEt}_3$  moiety has been shown to exert potent activity against *M. tuberculosis*.<sup>35</sup> Between the two complexes with the  $\{\text{Au}(\text{PPh}_3)\}^+$  unit, the one with the acridine moiety as a ligand (Figure 7, left) was screened against *M. tuberculosis*, while the other with sulfadiazine as a ligand (Figure 7, right) was tested against

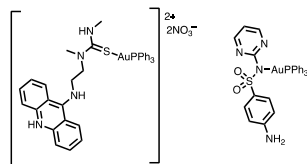


Figure 7. Au Complexes with the  $\{Au(PPh_3)\}^+$  moiety that have been evaluated for their antimycobacterial activity.<sup>15,16</sup>

other members of the mycobacterium genus. The sulfadiazine–Au(PPh<sub>3</sub>) complex showed synergy of the sulfadiazine antibiotic with the  $\{Au(PPh_3)\}^+$  unit. We expect that similar synergy between PZA and the  $\{Au(PPh_3)\}^+$  moiety (arising from 1) could increase the efficacy of the treatment compared to PZA alone under in vitro conditions.

Current TB treatment regimens require four orally taken drugs (PZA, ethambutol, rifampicin, isoniazid) at high dosages for 6 months with the daily dose of PZA recommended at 30 mg/kg for at least 2 of those months.<sup>17</sup> Much of the difficulty of treatment for this disease arises from both the inherent thick, waxy mycomembrane (preventing foreign substances from permeation) of *M. tuberculosis* and the success to survive within host macrophages.<sup>40,31</sup> Complexes like 1, as evidenced by our results, may react immediately with biologically relevant thiols to produce free PZA and  $\{Au(PPh_3)\}$ -thiol polymeric species. The  $\{Au(PPh_3)\}^+$  moiety of 1 may provide the lipophilicity required to pass through the mycomembrane to exert its action, while a dose of PZA is also provided simultaneously. So far, the success of PZA in the TB treatment has been an extremely valuable finding; further investigation into the possible synergistic effects between PZA (or other TB drugs) and the  $\{Au(PPh_3)\}^+$  moiety in vivo could be valuable toward identifying new drugs, especially for future treatment of emerging drug-resistant strains. Such studies are in progress in this laboratory.

## ■ ASSOCIATED CONTENT

### Supporting Information

The Supporting Information is available free of charge at <https://pubs.acs.org/doi/10.1021/acsomega.0c00071>.

Crystallographic Data (CIF)

## ■ AUTHOR INFORMATION

### Corresponding Author

Pradip K. Mascharak – Department of Chemistry and Biochemistry, University of California, Santa Cruz, California 95064, United States; [orcid.org/0000-0002-7044-944X](https://orcid.org/0000-0002-7044-944X); Email: [pradip@ucsc.edu](mailto:pradip@ucsc.edu)

### Authors

Jenny Stenger-Smith – Department of Chemistry and Biochemistry, University of California, Santa Cruz, California 95064, United States

Mireille Kamariza – Department of Chemistry, Stanford University, Stanford, California 94305, United States

Indranil Chakraborty – Department of Chemistry and Biochemistry, University of California, Santa Cruz, California 95064, United States

Ramatoulaye Ouattara – Department of Chemistry and Biochemistry, University of California, Santa Cruz, California 95064, United States

Carolyn R. Bertozzi – Department of Chemistry, Stanford University, Stanford, California 94305, United States; [orcid.org/0000-0003-4482-2754](https://orcid.org/0000-0003-4482-2754)

Complete contact information is available at: <https://pubs.acs.org/doi/10.1021/acsomega.0c00071>

## Notes

The authors declare no competing financial interest.

## ■ ACKNOWLEDGMENTS

Financial support from a UCSC COR Grant and the DMR Grant 1409335 from NSF is gratefully acknowledged. R.O. received support from the NIH IMSD Grant 2R25GM058903.

## ■ REFERENCES

- (1) Pricker, S. P. Medical Uses of Gold Compounds: Past, Present and Future. *Gold Bull.* **1996**, 29, 53–60.
- (2) Benedek, T. G. The History of Gold Therapy for Tuberculosis. *J. Hist. Med. Allied Sci.* **2004**, 59, 50–89.
- (3) Parish, R. V.; Cottrill, S. M. Medicinal Gold Compounds. *Gold Bull.* **1987**, 20, 3–12.
- (4) Faa, G.; Gerosa, C.; Fanni, D.; Lachowicz, J. I.; Nurchi, V. M. Gold - Old Drug with New Potentials. *Curr. Med. Chem.* **2018**, 25, 75–84.
- (5) Ortego, L.; Gonzalo-Asensio, J.; Laguna, A.; Villacampa, M. D.; Gimeno, M. C. Aminophosphane Gold(I) and Silver(I) Complexes as Antibacterial Agents. *J. Inorg. Biochem.* **2015**, 146, 19–27.
- (6) Glišić, B. D.; Djuran, M. I. Gold Complexes as Antimicrobial Agents: An Overview of Different Biological Activities in Relation to the Oxidation State of the Gold Ion and the Ligand Structure. *Dalton Trans.* **2014**, 43, S950–S969.
- (7) Ott, I. On the Medicinal Chemistry of Gold Complexes as Anticancer Drugs. *Coord. Chem. Rev.* **2009**, 253, 1670–1681.
- (8) Nardon, C.; Boscutti, G.; Fregona, D. Beyond Platins: Gold Complexes as Anticancer Agents. *Anticancer Res.* **2014**, 34, 487–492.
- (9) Messori, L.; Abbate, F.; Marcon, G.; Orioli, P.; Fontani, M.; Mini, E.; Mazzei, T.; Carotti, S.; O'Connell, T.; Zanello, P. Gold(III) Complexes as Potential Antitumor Agents: Solution Chemistry and Cytotoxic Properties of Some Selected Gold(III) Compounds. *J. Med. Chem.* **2000**, 43, 3541–3548.
- (10) Nomiya, K.; Noguchi, R.; Ohsawa, K.; Tsuda, K.; Oda, M. Synthesis, Crystal Structure and Antimicrobial Activities of Two Isomeric Gold(I) Complexes with Nitrogen-Containing Heterocycle and Triphenylphosphine Ligands,  $[Au(L)(PPh_3)]$  (HL = pyrazole and Imidazole). *J. Inorg. Biochem.* **2000**, 78, 363–370.
- (11) Stenger-Smith, J.; Chakraborty, I.; Mascharak, P. K. Cationic Au(I) Complexes with Aryl-Benzothiazoles and Their Antibacterial Activity. *J. Inorg. Biochem.* **2018**, 185, 80–85.
- (12) Serrate, M.; Bertrand, B.; Janssen, E. F. J.; Hemelt, E.; Zucca, A.; Cocco, F.; Cinellu, M. A.; Casini, A. Gold (I) Compounds with Lansoprazole-type Ligands: Synthesis, Characterization and Anticancer Properties in vitro. *Med. Chem. Commun.* **2014**, 5, 1418–1422.
- (13) Serrate, M.; Cinellu, M. A.; Maiore, L.; Pilo, M.; Zucca, A.; Gabbiani, C.; Guerri, A.; Landini, I.; Nobili, S.; Mini, E.; Messori, L. Synthesis, Structural Characterization, Solution Behavior, and in Vitro Antiproliferative Properties of a Series of Gold Complexes with 2-(2'-Pyridyl)Benzimidazole as Ligand: Comparisons of Gold(III) versus Gold(I) and Mononuclear versus Binuclear Derivat. *Inorg. Chem.* **2012**, 51, 3161–3171.
- (14) Křikavová, R.; Hošek, J.; Vančo, J.; Hutýra, J.; Dvořák, Z.; Trávníček, Z. Gold(I)-Triphenylphosphine Complexes with Hypoxanthine-Derived Ligands: In Vitro Evaluations of Anticancer and Anti-Inflammatory Activities. *PLoS One* **2014**, 9, No. e107373.



- (15) Eiter, L. C.; Hall, N. W.; Day, C. S.; Saluta, G.; Kucera, G. L.; Bierbach, U. Gold(I) Analogues of a Platinum–Acridine Antitumor Agent Are Only Moderately Cytotoxic but Show Potent Activity against *Mycobacterium tuberculosis*. *J. Med. Chem.* **2009**, *52*, 6519–6522.
- (16) Agertt, V. A.; Bonez, P. C.; Rossi, G. G.; da Costa Flores, V.; dos Santos Siqueira, F.; Mizdal, C. R.; Marques, L. L.; de Oliveira, G. N. M.; de Campos, M. M. A. Identification of Antimicrobial Activity among New Sulfonamide Metal Complexes for Combating Rapidly Growing Mycobacteria. *BioMetals* **2016**, *29*, 807–816.
- (17) Sotgiu, G.; Centis, R.; D'Ambrosio, L.; Migliori, G. B. Tuberculosis Treatment and Drug Regimens. *Cold Spring Harbor Perspect. Med.* **2015**, *5*, No. a017822.
- (18) North, A. C. T.; Phillips, D. C.; Mathews, F. S. A Semiempirical Method of Absorption Correction. *Acta Crystallogr., Sect. A* **1968**, *24*, 351–359.
- (19) Sheldrick, G. M. Crystal Structure Refinement with SHELXL. *Acta Crystallogr., Sect. C: Struct. Chem.* **2015**, *71*, 3–8.
- (20) Sheldrick, G. M. SHELXT - Integrated Space-Group and Crystal-Structure Determination. *Acta Crystallogr., Sect. A: Found. Crystallogr.* **2015**, *71*, 3–8.
- (21) Dolomanov, O. V.; Bourhis, L. J.; Gildea, R. J.; Howard, J. A. K.; Puschmann, H. OLEX2: A Complete Structure Solution, Refinement and Analysis Program. *J. Appl. Crystallogr.* **2009**, *42*, 339–341.
- (22) Sheldrick, G. M. *SHELXTL TM* (V 6.14); Bruker Analytical X-ray Systems: Madison, WI, 2000.
- (23) Singh, A. K.; Reyrat, J.-M. Laboratory Maintenance of *Mycobacterium smegmatis*. *Curr. Protoc. Microbiol.* **2009**, *14*, 10C.1.1–10C.1.12.
- (24) Duan, H.; Sengupta, S.; Petersen, J. L.; Akhmedov, N. G.; Shi, X. Triazole–Au(I) Complexes: A New Class of Catalysts with Improved Thermal Stability and Reactivity for Intermolecular Alkyne Hydroamination. *J. Am. Chem. Soc.* **2009**, *131*, 12100–12102.
- (25) Warzajtis, B.; Glišić, B. D.; Radulović, N. S.; Rychlewski, U.; Djuran, M. I. Gold(III) Complexes with Monodentate Coordinated Diazines: An Evidence for Strong Electron-Withdrawing Effect of Au(III) Ion. *Polyhedron* **2014**, *79*, 221–228.
- (26) Kabanda, M. M.; Tran, V. T.; Tran, Q. T.; Ebenso, E. E. A Computational Study of Pyrazinamide: Tautomerism, Acid-Base Properties, Micro-Solvation Effects and Acid Hydrolysis Mechanism. *Comput. Theor. Chem.* **2014**, *1046*, 30–41.
- (27) Hill, D. T.; Burns, K.; Titus, D. D.; Girard, G. R.; Reiff, W. M.; Mascavage, L. M. Dichloro(Pyridine-2-Carboxamido-N1,N2)Gold(III), a Bis-Nitrogen Aurocycle: Syntheses, Gold-197 Mossbauer Spectroscopy, and X-Ray Crystal Structure. *Inorg. Chim. Acta* **2003**, *346*, 1–6.
- (28) Dar, A.; Moss, K.; Cottrill, S. M.; Parish, R. V.; McAuliffe, C. A.; Pritchard, R. G.; Beagley, B.; Sandbank, J. Complexes of Gold(III) with Mononegative Bidentate N,O-Ligands. *J. Chem. Soc., Dalton Trans.* **1992**, 1907–1913.
- (29) Catanho, M.; Mascarenhas, D.; Degrave, W.; de Miranda, A. B. GenoMycDB: A Database for Comparative Analysis of Mycobacterial Genes and Genomes. *Genet. Mol. Res.* **2006**, *5*, 115–126.
- (30) Fenton, M. J.; Vermeulen, M. W. Immunopathology of Tuberculosis: Roles of Macrophages and Monocytes. *Infect. Immun.* **1996**, *64*, 683–690.
- (31) Machado, D.; Girardini, M.; Viveiros, M.; Pieroni, M. Challenging the Drug-likeness Dogma for New Drug Discovery in Tuberculosis. *Front. Microbiol.* **2018**, *9*, No. 1367.
- (32) Zhang, Y.; Mitchison, D. The Curious Characteristics of Pyrazinamide: A Review. *Int. J. Tuberc. Lung Dis.* **2003**, *7*, 6–21.
- (33) Zhang, Y.; Scropio, A.; Nikaído, H.; Sun, Z. Role of Acid PH and Deficient Efflux of Pyrazinoic Acid in Unique Susceptibility of *Mycobacterium tuberculosis* to Pyrazinamide. *J. Bacteriol.* **1999**, *181*, 2044–2049.
- (34) Shaw, C. F.; Coffey, M. T.; Klingbeil, J.; Mirabelli, C. K. Application of a 31P NMR Chemical Shift: Gold Affinity Correlation to Hemoglobin-Gold Binding and the First Inter-Protein Gold Transfer Reaction. *J. Am. Chem. Soc.* **1988**, *110*, 729–734.
- (35) Harbut, M. B.; Vilchèze, C.; Luo, X.; Hensler, M. E.; Guo, H.; Yang, B.; Chatterjee, A. K.; Nizet, V.; Jacobs, W. R.; Schultz, P. G.; Wang, F. Auranofoin Exerts Broad-Spectrum Bactericidal Activities by Targeting Thiol-Redox Homeostasis. *Proc. Natl. Acad. Sci. U.S.A.* **2015**, *112*, 4453–4458.
- (36) Thangamani, S.; Mohammad, H.; Abushahba, M. F. N.; Sobreira, T. J. P.; Hedrick, V. E.; Paul, L. N.; Seleem, M. N. Antibacterial Activity and Mechanism of Action of Auranofoin against Multi-Drug Resistant bacterial pathogens. *Sci. Rep.* **2016**, *6*, No. 22571.
- (37) Vandal, O. H.; Nathan, C. F.; Ehrt, S. Acid Resistance in *Mycobacterium tuberculosis*. *J. Bacteriol.* **2009**, *191*, 4714–4721.
- (38) França, A.; Aggarwal, P.; Barsov, E. V.; Kozlov, S. V.; Dobrovolskaia, M. A.; González-Fernández, A. Macrophage Scavenger Receptor A Mediates the Uptake of Gold Colloids by Macrophages in Vitro. *Nanomedicine* **2011**, *6*, 1175–1188.
- (39) Singh, R.; Nawale, L.; Arkile, M.; Wadhvani, S.; Shedbalkar, U.; Chopade, S.; Sarkar, D.; Chopade, B. A. Phytochemical Silver, Gold, and Bimetallic Nanoparticles as Novel Antitubercular Agents. *Int. J. Nanomed.* **2016**, *11*, 1889–1897.
- (40) Khanye, S. D.; Wan, B.; Franzblau, S. G.; Gut, J.; Rosenthal, P. J.; Smith, G. S.; Chibale, K. Synthesis and in Vitro Antimalarial and Antitubercular Activity of Gold(III) Complexes Containing Thiosemicarbazone Ligands. *J. Organomet. Chem.* **2011**, *696*, 3392–3396.
- (41) Cuin, A.; Massabni, A. C.; Pereira, G. A.; Leite, C. Q. F.; Pavan, F. R.; Sesti-Costa, R.; Heinrich, T. A.; Costa-Neto, C. M. 6-Mercaptopurine Complexes with Silver and Gold Ions: Anti-Tuberculosis and Anti-Cancer Activities. *Biomed. Pharmacother.* **2011**, *65*, 334–338.
- (42) Pereira, G. A.; Massabni, A. C.; Castellano, E. E.; Costa, L. A. S.; Leite, C. Q. F.; Pavan, F. R.; Cuin, A. A Broad Study of Two New Promising Antimycobacterial Drugs: Ag(I) and Au(I) Complexes with 2-(2-Thienyl)Benzothiazole. *Polyhedron* **2012**, *38*, 291–296.
- (43) Gupta, R.; Felix, C. R.; Akerman, M. P.; Akerman, K. J.; Slabber, C. A.; Wang, W.; Adams, J.; Shaw, L. N.; Tse-Dinh, Y. C.; Munro, O. Q.; et al. Evidence for Inhibition of Topoisomerase 1a by Gold(III) Macrocycles and Chelates Targeting *Mycobacterium tuberculosis* and *Mycobacterium abscessus*. *Antimicrob. Agents Chemother.* **2018**, *62*, No. e01696.

## Chapter 4. Manganese Carbonyl Complexes

### 4.1 Background on CO and photoCORMs

Carbon monoxide (CO), the toxic small molecule causing thousands of hospital visits by Americans every year, has gained increasing attention in the scientific community for its therapeutic effects.<sup>1</sup> Anti-inflammatory, anti-proliferative and many other therapeutic properties of low doses of CO have been identified and studied.<sup>2</sup> One of the most popular areas of applications of CO has been in the development of CO releasing molecules (CORMs) for the treatment of cancer. Prospects of CORMs for the treatment of colon, breast, prostate, cervical, pancreatic, skin, lung and other have been explored with much initial success.<sup>3</sup>

The anti-proliferative and pro-apoptotic effects of CO in cancerous cell lines have been attributed to the increase of cellular reactive oxygen species (ROS) and mitochondrial collapse.<sup>4</sup> Exogenous CO has shown to inhibit cytochrome c oxidase which ultimately leads to the production of mitochondrial ROS.<sup>5</sup> Further, CO has been shown to inhibit cystathionine  $\beta$ - synthase which leads to reduction of antioxidant capacity and the cells ability to handle to increased ROS.<sup>6</sup> It is important to note that there may be other targets or pathways (hemoproteins) of CO that could aid in the overall anticancer activity. Nonetheless, the disruption of the redox homeostasis brought about from ROS production and other pathways is linked to the chemotherapeutic mechanism of action for CO.

There are many different CORM systems and which can release CO upon exposure to external stimuli like heat,<sup>7</sup> H<sub>2</sub>O<sub>2</sub><sup>8</sup> or light.<sup>9,10</sup> CORMs that release CO upon irradiation of light have been termed photoCORMs and have shown increasing potential as therapeutic agents due to the convenience of the control of location, dosage and timing.<sup>11</sup> Of these photoCORMs, metal carbonyl systems containing iron, manganese, rhenium, ruthenium and molybdenum (**Figure 4.1**) are commonly employed, however organic based photoCORMs have also been identified.<sup>12,13</sup> For use as a biological therapeutic, it is important that the photoCORMs and the photoproduct be nontoxic, stable and soluble under biological conditions. Additionally, the wavelengths of light that cause release of CO are important and must not cause additional damage to tissue. Sensitivity to red light, specifically within the phototherapeutic window (650 – 1000 nm),<sup>14,15</sup> which penetrates further into tissue and causes less damage than UV exposure, would be ideal for the development of potential photoCORMs.

Among the reported photoCORMs that could be activated by light in the visible light region (**Figure 4.1**), very few within the phototherapeutic region (650 – 1000 nm). Design strategies to move activation from the UV to visible region in Mn carbonyl complexes involve increase in the  $\pi$  conjugation of the ligand framework and the ancillary ligands which determine the extent of MLCT (metal to ligand charge transfer) that is responsible for the labialization of the metal-CO bond.<sup>11</sup> In attempts to further utilize near infrared (near IR) light within the phototherapeutic region to release CO,



various methods such as upconverting nanoparticles<sup>16,17</sup> and two photon excitation (TPE)<sup>18,19</sup> have been employed.

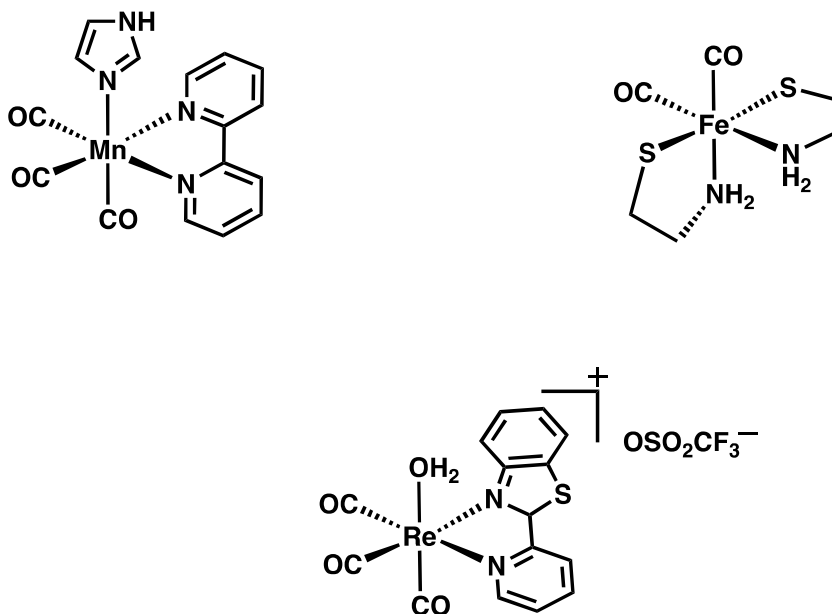


**Figure 4.1.** Examples of photoCORMs that exhibit release of CO upon illumination of UV or visible light.

TPE is triggered by the simultaneous absorption of two low-energy photons by one chromophore causing excitation and photochemistry events to occur in higher energy range. This technique has been highly useful in the areas of 3D microscopy, fluorescence microscopy and photodynamic therapy due to the ability of low energy near IR light to initiate this excitation and make imaging possible deeper into tissues compared to visible or UV light excitation events.<sup>20,21</sup> Employing a ligand with TPE

capability on a metal carbonyl center release of CO is possible upon exposure to light around 800 nm (**Figure 4.2**). Because TPE requires the simultaneous absorption of photons, a laser with very high power and pulse frequency (enough to allow for two photons to essentially be in the same location at the same time) is always required.<sup>22</sup> However the high intensity laser can cause tissue damage from prolonged radiation limiting its applications in photoCORM-based treatment of cancerous tissues.<sup>23,24</sup> For this reason, systems requiring single photon excitation (SPE) in the phototherapeutic region rather than TPE could be more well-suited for anticancer applications of photoCORMs.

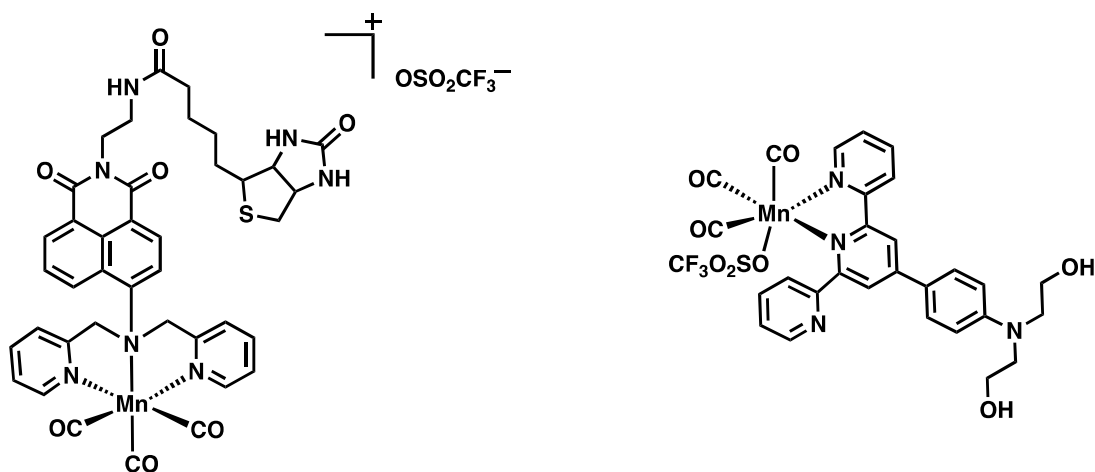


**Figure 4.2** TPE active manganese carbonyl complexes that exhibit loss of CO upon irradiation with an 800 nm laser.

## 4.2 Manganese Based photoCORMs With Aryl Benzothiazoles

Manganese based photoCORMs have been developed and evaluated in our group for the past few years. Much of this research has been focused on shifting the wavelength of light required for the photoCORM to release CO to the visible region.<sup>11,25,26</sup> The role of the ancillary ligands (Br, PPh<sub>3</sub>, CH<sub>3</sub>CN) is important in determining the energy of the MLTC transitions that is linked to wavelength of activation (red or blue shifts) required for CO release. The ligands pbt and qbt have previously shown a useful means of “Turn-On” tracking of CO release for the [MnBr(CO)<sub>3</sub>(pbt)] and [MnBr(CO)<sub>3</sub>(qbt)] complexes which exhibit anticancer activity.<sup>25</sup> Along the same lines, we wanted to observe if similar complexes with pbt and qbt using Cl<sup>-</sup> as the ancillary ligands namely, [MnCl(CO)<sub>3</sub>(pbt)] (Mnpbt) and [MnCl(CO)<sub>3</sub>(qbt)] (Mnqbt) (**Figure 4.3**) showed similar tracking and release properties.

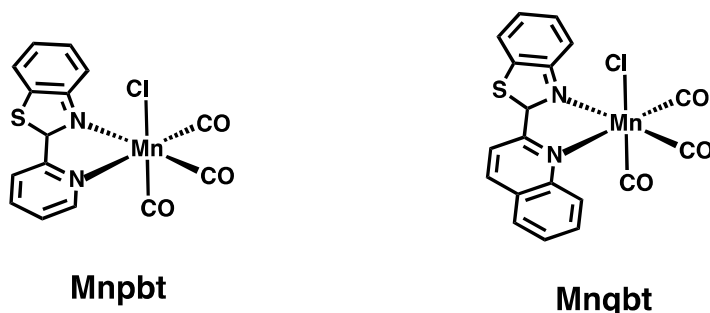


**Figure 4.3.** Mn(I) pbt and qbt based visible light active photoCORMs.

### 4.2.1 Synthesis and Spectroscopy

The complexes Mnpbt and Mnqbt were synthesized by stirring the ligands pbt and qbt in the presence of chloropentacarbonylmanganese(I) in dichloromethane in the absence of light. Both complexes exhibit prominent CO stretching in their FT-IR spectra consistent with a facial disposition of three CO ligands (**Figure 4.4**) at 2023  $\text{cm}^{-1}$  and 1927  $\text{cm}^{-1}$  (overlapping of two CO stretches) for Mnpbt and 2021  $\text{cm}^{-1}$ , 1935  $\text{cm}^{-1}$ , and 1909  $\text{cm}^{-1}$  for Mnqbt. The  $^1\text{H}$  NMR spectra of both complexes are well resolved indicating the presence of Mn(I) centers (**Figure 4.5**).

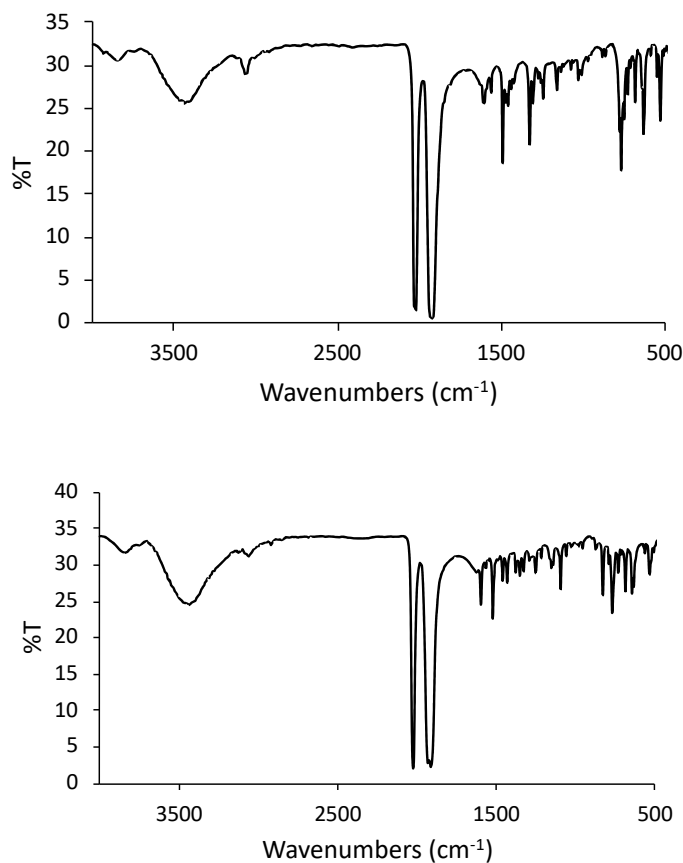


**Figure 4.4.** FT-IR spectra of Mnpbt (top) and Mnqbt (bottom) in KBr matrix.

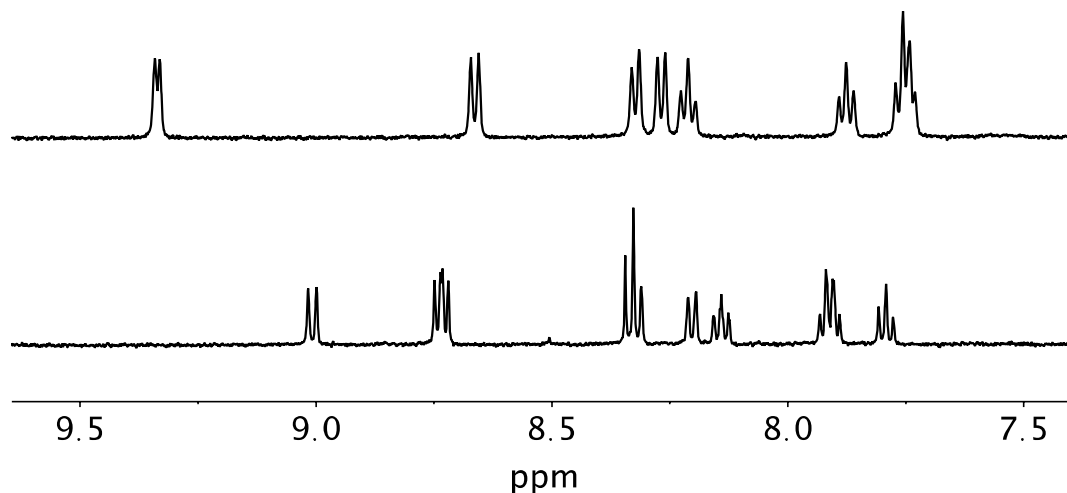


**Figure 4.5.** The  $^1\text{H}$  NMR spectra of Mnpbt (top) and Mnqbt (bottom) in  $\text{CD}_3\text{CN}$  at 298K.

#### 4.2.2 Crystal Structure Descriptions

The molecular structures of Mnpbt and Mnqbt reveal that the coordination geometry of both complexes is distorted octahedral about the Mn(I) center (**Figure 4.6** and **4.7** respectively). Much like Agpbt and Agqbt the two pbt and qbt ligands are bound as bidentate ligand to the Mn(I) center. In Mnpbt, the equatorial plane, comprising atoms C2, C3, N1, and N2, is approximately planar, with a mean deviation of 0.033 (5) Å, while the corresponding plane in Mnqbt is almost planar [mean deviation = 0.015 (3) Å]. In complex Mnpbt, the chelate ring composed of atoms Mn1, N1, C8, C9, and N2 is highly planar, with a mean deviation of 0.017 (3) Å. In contrast, Mnqbt, the chelate ring composed of atoms Mn1, N1, C12, C13, and N2 deviates

significantly from planarity [mean deviation = 0.115 (5) Å]. The dihedral angle between the pyridyl ring and the benzothiazole moiety are 6.0 (6)° and 9.6 (6)° for Mnpbt and Mnqbt respectively. The refinement parameters, selected bond distances and angles, and packing pattern descriptions can be found in section 4.2.4.3.

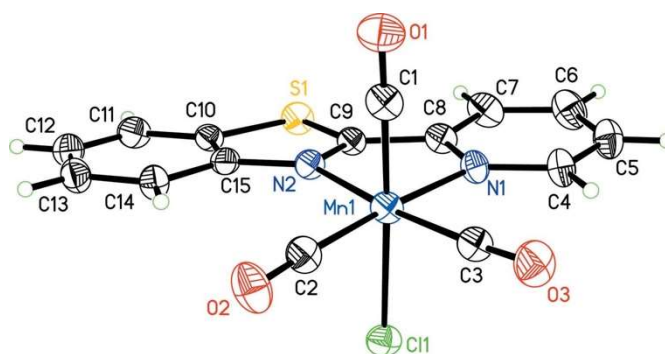


**Figure 4.6.** A perspective view of Mnpbt showing the atom-labeling scheme with ellipsoids at the 50% probability level.

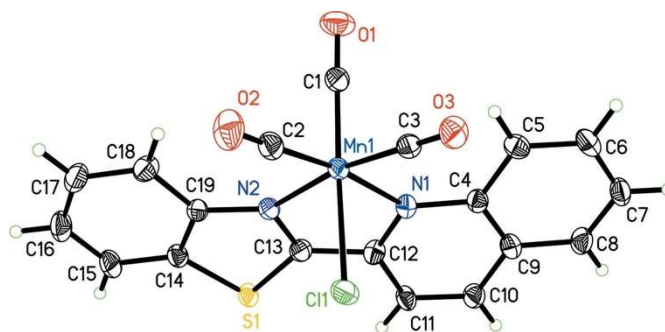


**Figure 4.7.** A perspective view of Mnqbt showing the atom-labeling scheme with ellipsoids at the 50% probability level.

### 4.2.3 CO Release Properties and “Turn On” Fluorescence Tracking

The UV-vis spectra of Mnpbt and Mnqbt reveal absorption bands in the visible region centered around 415 and 440 nm respectively (**Figure 4.8** (black trace) and **4.9** (black trace)). These bands presumably arise from MLCT transitions and similarly observed in  $[\text{MnBr}(\text{CO})_3(\text{pbt})]$  and  $[\text{MnBr}(\text{CO})_3(\text{qbt})]$ .<sup>25</sup> Exposure of solutions of the bromo adduct of Mnpbt and Mnqbt to visible light causes the release of CO and this same process was monitored for Mnpbt and Mnqbt by recording the electronic absorption spectra after intervals of exposure to visible light. Further, the  $\ln[\text{C}]$  vs time plot determines the apparent rates of photorelease ( $k_{\text{CO}}$ ). For Mnpbt and Mnqbt the electronic absorption spectra were recorded in acetonitrile after intervals of illumination with low power visible light ( $10 \text{ mW cm}^{-2}$ ) (**Figure 4.8** and **4.9**). The  $k_{\text{CO}}$  values calculated from the  $\ln[\text{C}]$  vs time were calculated to be  $0.98 \pm 0.02$  (concentration  $7.76 \times 10^{-5} \text{ M}$ ) and  $2.51 \pm 0.02$  (concentration  $6.87 \times 10^{-5} \text{ M}$ ) for Mnpbt and Mnqbt (**Figure 4.10** and **4.11**) respectively. Mnqbt has a much higher rate of CO release under the same experimental conditions as Mnpbt and could be attributed to the relatively superior  $\pi$  acceptor character of qbt compared to pbt (due to the extended conjugations).

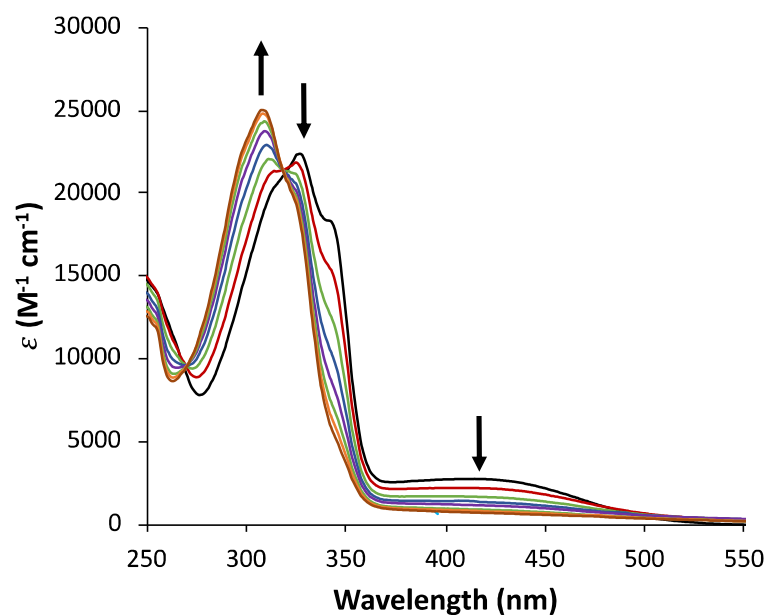


**Figure 4.8.** Changes in the electronic absorption spectrum of Mnpt in acetonitrile upon exposure to intervals of visible light in MeCN.

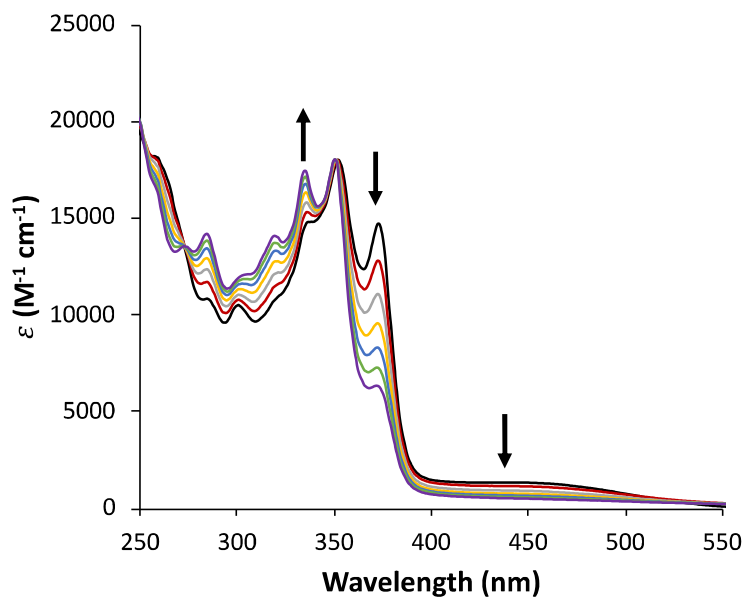


**Figure 4.9.** Changes in the electronic absorption spectrum of Mnqbt in acetonitrile upon exposure to intervals of visible light in MeCN.



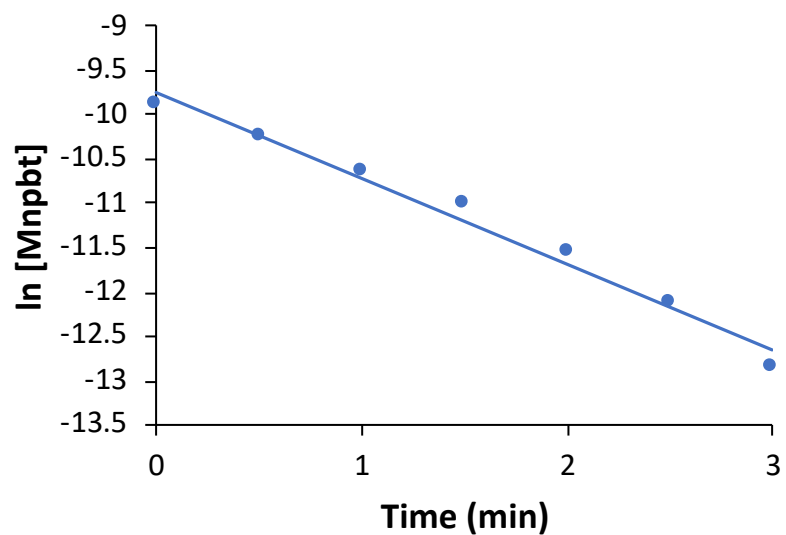


**Figure 4.10.** The  $\ln[C]$  vs time plot for Mnpbt indicating  $k_{CO}$  value of  $0.98 \pm 0.02$   
(concentration  $7.76 \times 10^{-5}$  M).

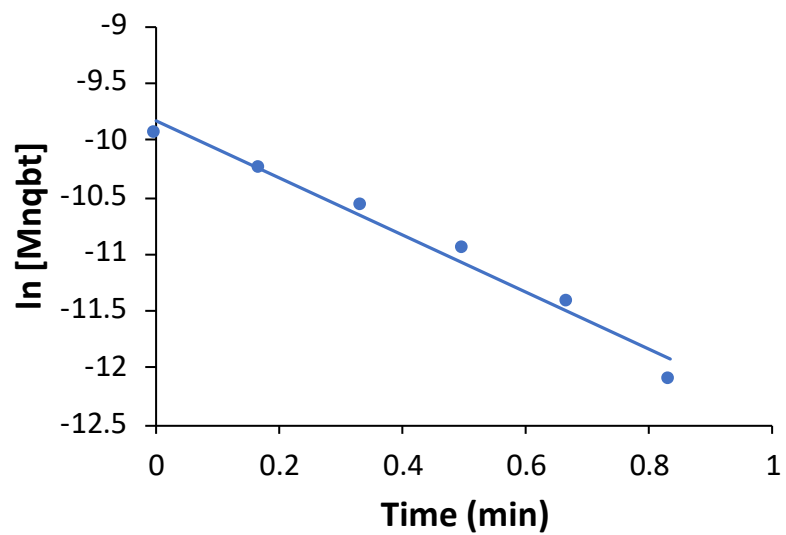


**Figure 4.11.** The  $\ln[C]$  vs time plot for Mnqbt indicating  $k_{CO}$  value of  $2.51 \pm 0.02$   
(concentration  $6.87 \times 10^{-5}$  M).

Accompanying the CO release is the gradual turn-on of fluorescence from the release of the free pbt and qbt ligands (as observed in  $[\text{MnBr}(\text{CO})_3(\text{pbt})]$  and  $[\text{MnBr}(\text{CO})_3(\text{qbt})]$ ). The time dependent enhancement of fluorescence can be observed upon exposure to visible light for Mnpbt and Mnqbt in **Figures 4.12** and **4.13** respectively. The fluorescent signal returns to full saturation (comparable to the free ligands pbt and qbt) after 6 min (Mnpbt) and 1 min (Mnqbt) exposure to light. This “turn on” of fluorescence provides a convenient method of tracking CO release from the present complexes in a similar manner as the previously reported bromo adducts.

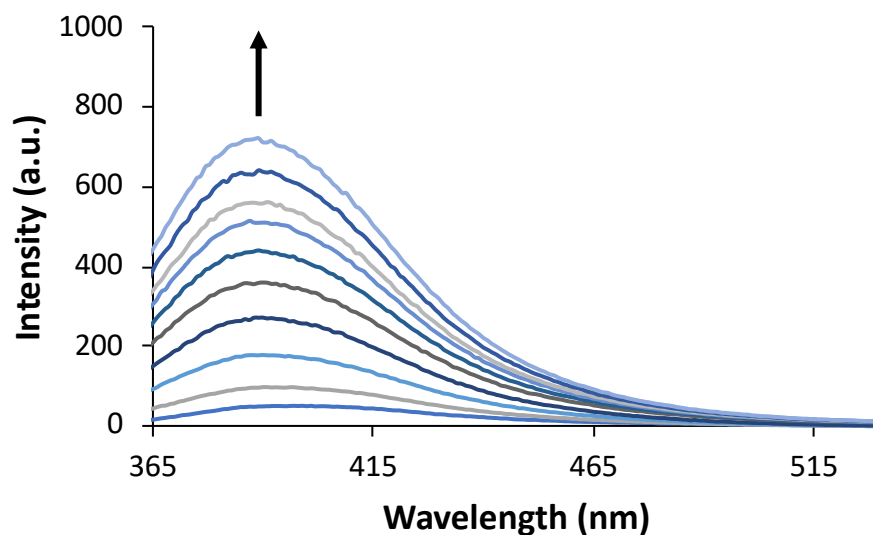


**Figure 4.12.** Enhancement of emission intensity for Mnpbt in acetonitrile upon exposure to visible light ( $\lambda_{\text{ex}} = 345 \text{ nm}$ ,  $\lambda_{\text{ex}} = 390 \text{ nm}$ ).

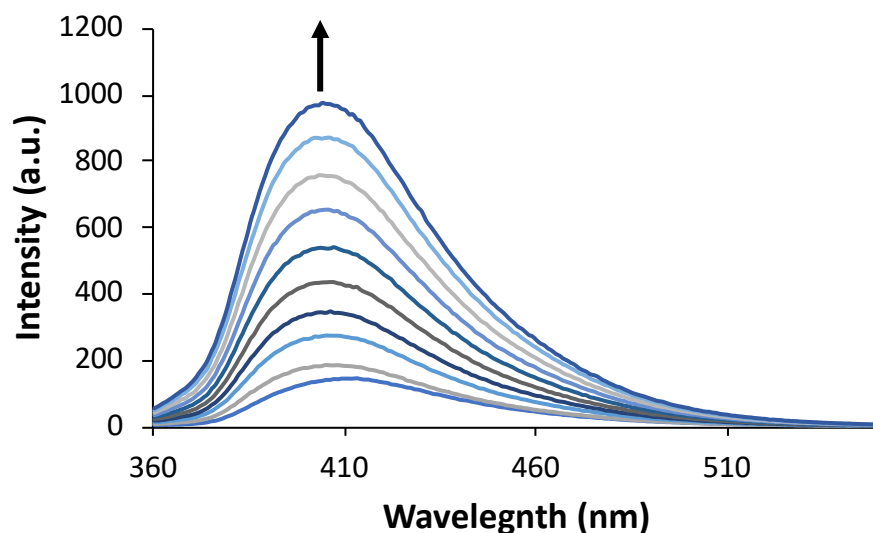


**Figure 4.13.** Enhancement of emission intensity for Mnqbt in acetonitrile upon exposure to visible light ( $\lambda_{\text{ex}} = 345 \text{ nm}$ ,  $\lambda_{\text{ex}} = 405 \text{ nm}$ ).

#### 4.2.4 Experimental Section

##### 4.2.4.1 General Methods

All reagents were of commercial grade and were used without further purification. The solvents were purified according to standard procedures. The ligand pbt<sup>27</sup> and  $[\text{MnCl}(\text{CO})_5]$ <sup>28</sup> were synthesized according to reported procedures. A Perkin-Elmer Spectrum-One FT-IR spectrophotometer was employed to record the IR spectra of the complexes and the ligands. UV-vis spectra were monitored with a Varian Cary 50 UV-Vis spectrophotometer. The <sup>1</sup>H NMR spectra of the compounds were recorded at 298 K on a Varian Unity Inova 500 MHz instrument. Microanalyses were carried out with a PerkinElmer Series II 2400 Elemental Analyzer.

#### 4.2.4.2 Synthesis

2-(quinolin-2-yl)-1,3-benzothiazole (qbt): A yellow solution of quinoline-2-carbaldehyde (409 mg, 2.6 mmol) and 2-aminothiophenol (326 mg, 2.6 mmol) in xylenes (30 ml) was heated under reflux for 24 h. Next, the reaction mixture was cooled to ambient temperature and the solvent was removed under reduced pressure. The solid thus obtained was purified by recrystallization from hot methanol (yield 279mg, 41%). Elemental analysis (%) found: C 73.31, H 3.87, N 10.72; calculated for  $C_{16}H_{10}N_2S$ : C 73.26, H 3.84, N 10.68. IR (KBr,  $cm^{-1}$ ): 3057 (w), 1595 (s), 1560 (w), 1500 (s), 1454 (w), 1428 (w), 1327(s), 1118(w), 997(s), 940(w), 830(s), 754(s), 727(w).  $^1H$  NMR ( $CDCl_3$ ):  $\delta$  8.54 (d, 1H), 8.33 (d, 1H), 8.24 (d, 1H), 8.16 (d, 1H), 8.00 (d, 1H), 7.89 (d, 1H), 7.79 (t, 1H), 7.61 (t, 1H), 7.54 (t, 1H), 7.46 (t, 1H).

$[MnBr(CO)_3(pbt)]$  (Mnpbt): A batch of  $[MnCl(CO)_5]$  (60 mg, 0.26 mmol) and pbt (55 mg, 0.26 mmol) in dichloromethane ( $CH_2Cl_2$ , 20 ml) was stirred at room temperature for 20 h. The reaction mixture was covered carefully with aluminum foil to avoid any light exposure during the entire course of the reaction. Next, the solvent was completely removed under reduced pressure and the solid thus obtained was washed thoroughly with hexanes and finally dried in vacuo (yield 85 mg, 85%). Elemental analysis (%) found: C 46.63, H 2.11, N 7.27; calculated for  $C_{15}H_8ClMnN_2O_3S$ : C 46.59, H 2.09, N 7.24. IR (KBr,  $cm^{-1}$ ): 2023 (s), 1927 (s), 1492 (w), 1327 (w), 1 777 (w), 768 (w), 631 (w), 528 (w).  $^1H$  NMR ( $CD_3CN$ ):  $\delta$  9.32 (d, 1H), 8.66 (d, 1H), 8.32 (d, 1H), 8.26 (d, 1H), 8.20 (t, 1H), 7.87 (t, 1H), 7.75 (m, 2H).

[MnBr(CO)<sub>3</sub>(qbt)] (Mnqbt): This complex was prepared by the same procedure as used for Mnpbt, employing [MnCl(CO)<sub>5</sub>] (51 mg, 0.22 mmol) and qbt (58 mg, 0.22 mmol) (yield 89 mg, 91%). Elemental analysis (%) found: C 52.29, H 2.36, N 6.45; calculated for C<sub>19</sub>H<sub>10</sub>ClMnN<sub>2</sub>O<sub>3</sub>S: C 52.25, H 2.31, N 6.41. IR (KBr, cm<sup>-1</sup>): 2021 (s), 1926 (s), 1909 (s), 1594 (w), 1519 (w), 1090 (w), 825 (w), 765 (w), 641 (w). <sup>1</sup>H NMR (CD<sub>3</sub>CN): δ 8.98 (d, 1H), 8.71 (m, 2H), 8.30 (t, 2H), 8.18 (d, 1H), 8.11 (t, 1H), 7.89 (m, 2H), 7.76 (t, 1H).

#### 4.2.4.3 X-ray Crystallography

Crystal data, data collection details and structure refinement are summarized in **Table 4.1**. The non-H atoms were located through intrinsic phasing using SHELXT<sup>29</sup> integrated in the OLEX2 graphical user interface.<sup>30</sup> H atoms were included in calculated positions riding on the C atoms to which they bonded, with C - H = 0.93 Å and U<sub>iso</sub>(H) = 1.2U<sub>eq</sub>(C). In Mnpbt, the highest residual electron-density peak is located near atom S1. No satisfactory disorder of the twinning model could be found. In Mnqbt, an orientational disorder [0.843 (6):0.157 (6)] within the qbt ligand was observed, in which the quinoline and benzothiazole frames partially switch positions. This disorder is similar to that observed for a copper complex with the same ligand.<sup>31</sup> The disorder was modeled by assigning partly occupied positions of the S atom (S1 and S1B) of the benzothiazole fragment and the C10 and C11 atoms of the quinoline fragment (C10, C11, C10B, and C11B), and the anisotropic displacement parameters of the C10B and

C11B atoms were constrained to be equal.<sup>32</sup> All other atoms of qbt ligand in Mnqbt were refined as fully occupied sites. The selected bond angles and distances for Mnpbt and Mnqbt can be found in **Tables 4.2** and **4.3** respectively.

**Table 4.1** Crystal data and structure refinement experimental details of Mnpbt and Mnqbt.

	Mnpbt	Mnqbt
Crystal data		
Chemical formula	[MnCl(C <sub>12</sub> H <sub>8</sub> N <sub>2</sub> S)(CO) <sub>3</sub> ]	[MnCl(C <sub>16</sub> H <sub>10</sub> N <sub>2</sub> S)(CO) <sub>3</sub> ]
<i>M<sub>r</sub></i>	386.68	436.74
Crystal system, space group	Monoclinic, <i>P</i> 2 <sub>1</sub> / <i>c</i>	Monoclinic, <i>P</i> 2 <sub>1</sub> / <i>n</i>
Temperature (K)	296	296
<i>a</i> , <i>b</i> , <i>c</i> (Å)	15.008 (3), 11.798 (3), 9.0384 (19)	9.1239 (5), 16.4292 (9), 12.2101 (6)
$\beta$ (°)	106.756 (2)	96.737 (1)
<i>V</i> (Å <sup>3</sup> )	1532.4 (6)	1817.64 (17)
<i>Z</i>	4	4
Radiation type	Mo <i>K</i> α	Mo <i>K</i> α
$\mu$ (mm <sup>-1</sup> )	1.19	1.01
Crystal size (mm)	0.20 × 0.18 × 0.15	0.15 × 0.12 × 0.10
Data collection		
Diffractionmeter	Bruker APEXII CCD	Bruker APEXII CCD
Absorption correction	Multi-scan ( <i>SADABS</i> ; Bruker, 2015)	Multi-scan ( <i>SADABS</i> ; Bruker, 2015)
<i>T<sub>min</sub></i> , <i>T<sub>max</sub></i>	0.637, 0.746	0.648, 0.746
No. of measured, independent and observed [ <i>I</i> > 2σ( <i>I</i> )] reflections	12045, 3769, 2011	20380, 4479, 3291
<i>R<sub>int</sub></i>	0.063	0.046
(sin $\theta/\lambda$ ) <sub>max</sub> (Å <sup>-1</sup> )	0.668	0.667
Refinement		
<i>R</i> [ <i>F</i> <sup>2</sup> > 2σ( <i>F</i> <sup>2</sup> )], <i>wR</i> ( <i>F</i> <sup>2</sup> ), <i>S</i>	0.065, 0.196, 1.04	0.038, 0.093, 1.04
No. of reflections	3769	4479
No. of parameters	208	266
H-atom treatment	H-atom parameters constrained	H-atom parameters constrained
$\Delta\rho_{\text{max}}$ , $\Delta\rho_{\text{min}}$ (e Å <sup>-3</sup> )	1.42, -0.73	0.32, -0.31

**Table 4.2.** Selected bond lengths and angles for Mnpbt.

Mn1—Cl1	2.3916 (15)	Mn1—C1	1.773 (6)
Mn1—N2	2.054 (4)	Mn1—C3	1.793 (6)
Mn1—N1	2.078 (4)	Mn1—C2	1.805 (6)
N2—Mn1—Cl1	85.68 (12)	C3—Mn1—Cl1	94.19 (16)
N2—Mn1—N1	78.15 (16)	C3—Mn1—N2	171.6 (2)
N1—Mn1—Cl1	87.39 (12)	C3—Mn1—N1	93.5 (2)
C1—Mn1—Cl1	177.79 (19)	C3—Mn1—C2	86.2 (2)
C1—Mn1—N2	93.2 (2)	C2—Mn1—Cl1	88.60 (18)
C1—Mn1—N1	94.2 (2)	C2—Mn1—N2	102.1 (2)
C1—Mn1—C3	87.2 (2)	C2—Mn1—N1	175.9 (2)
C1—Mn1—C2	89.8 (2)		

**Table 4.3.** Selected bond lengths and angles for Mnqbt.

Mn1—Cl1	2.3837 (7)	Mn1—C3	1.798 (2)
Mn1—N2	2.0668 (18)	Mn1—C1	1.796 (3)
Mn1—N1	2.0962 (18)	Mn1—C2	1.795 (3)
N2—Mn1—Cl1	86.32 (5)	C1—Mn1—N1	94.57 (10)
N2—Mn1—N1	78.36 (7)	C1—Mn1—C3	92.99 (10)
N1—Mn1—Cl1	84.96 (5)	C2—Mn1—Cl1	88.28 (9)
C3—Mn1—Cl1	84.97 (8)	C2—Mn1—N2	98.04 (10)
C3—Mn1—N2	170.75 (9)	C2—Mn1—N1	172.52 (10)
C3—Mn1—N1	97.75 (9)	C2—Mn1—C3	84.82 (11)
C1—Mn1—Cl1	177.82 (8)	C2—Mn1—C1	92.31 (11)
C1—Mn1—N2	95.68 (9)		

### 4.3 Single Photon Near IR active photoCORMs

The application of photoCORMs as chemotherapeutics has been widely explored in the past few years. Manganese carbonyl complexes in particular have been explored due to their CO release upon exposure to visible light and relatively nontoxic photoproducts. After much initial success, there has been a shift to explore photoCORMs that are active with light in the phototherapeutic region (650-1000 nm) which penetrates deeper in to tissue and with less damage than visible or UV light.<sup>14,15</sup> This has been observed with manganese carbonyl systems employing TPE (**Figure 4.2**), but SPE has not yet been observed to cause release of CO with light in the near IR region for these complexes. To avoid potential damage to tissues caused by the use of high intensity lasers<sup>23,24</sup> that are required for TPE, we chose to investigate the effects of using extended  $\pi$  conjugated ligands that show absorption around 625nm on their own.<sup>33-36</sup> These ligands, 5-(4'-dimethylaminophenylimino)-7-chloroquinolin-8-one (NIR1) and 3-(4'-dimethylaminophenylimino)pyrido[2,3-*a*]phenothiazine (NIR2) were used to synthesize manganese carbonyl complexes [MnBr(CO)<sub>3</sub>(NIR1)] (MnNIR1) and [MnBr(CO)<sub>3</sub>(NIR2)] (MnNIR2) (**Figure 4.14**) which show SPE and simultaneous release of CO with low power near IR light. To the best of our knowledge, these are the first manganese based photoCORMs active in the near IR region of light caused by SPE.



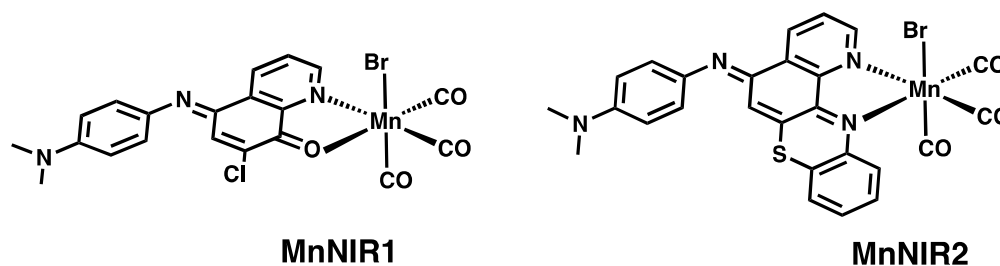


**Figure 4.14.** Near IR active photoCORMs.

### 4.3.1 Synthesis

The red absorbing ligands NIR1 and NIR2 were synthesized according to literature procedures<sup>33–36</sup> and specific details can be found in section 4.3.6.2. After careful isolation of NIR1 and NIR2, the complexes MnNIR1 and MnNIR2 were prepared by stirring bromopentacarbonylmanganese(I) and an equimolar amount of the corresponding ligands in dichloromethane for 72 h protected from ambient light. The initial dark blue/black solutions turned slightly green indicating complex formation. The suspension of MnNIR1 was filtered directly to isolate a dark green/black solid while the MnNIR2 solution was reduced in volume, precipitated with hexanes and filtered to collect the dark green/black solid.

### 4.3.2 Crystal Structures Descriptions

The molecular structure of MnNIR1 (**Figure 4.15**) revealed distorted octahedral geometry around the Mn(I) with three facially disposed CO ligands. NIR1 binds the metal center in a bidentate fashion and the sixth coordination site is occupied by a bromide ligand. The equatorial plane comprised of C2, C3, N1, and O4 is fairly

planar with mean deviation of 0.046(3) Å. The five membered chelate ring comprised of Mn1 N1, O4, C11 and C12 forms a plane with mean deviation of 0.025(3) Å. The dihedral angle between the dimethylaminophenylimino moiety and the quinoline is 13.1°. The axial Mn-CO distance is noticeably longer (1.873(2) Å.) compared to the two equatorial Mn-CO distances (1.800(9) and 1.783(10) Å.). This can be attributed to the *trans* effect of the bromide ligand across the axial Mn-CO bond. It is also interesting to note that all the Mn-C distances in MnNIR1 are noticeably longer compared to the structurally similar Mn(I)carbonyl complex [MnBr(CO)<sub>3</sub>(MIAN)]<sup>37</sup> (**Figure 4.16**). The axial Mn-C1 distance in MnNIR1 is 1.873(2) while the corresponding bond distance in [MnBr(CO)<sub>3</sub>(MIAN)] is 1.819(11) Å. In a similar trend (albeit to a lesser extent) the average equatorial Mn-C distance in MnNIR1 is 1.792(9) Å slightly longer compared to corresponding average Mn-C bond lengths in [MnBr(CO)<sub>3</sub>(MIAN)] (1.787(12) Å). In general, the relatively weaker Mn-CO bonds in complex MnNIR1 could be due to superior  $\pi$ -accepting capacity of NIR1 that competes strongly with CO in terms of back-bonding from the metal d-orbitals. As a consequence of this competition, Mn-CO back-bonding in complex MnNIR1 is moderate which presumably caused the relative weakening of the bonds.

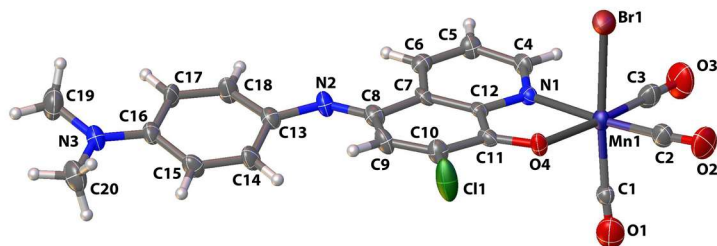


**Figure 4.15.** Molecular structure of MnNIR1 with atom labeling scheme. The thermal ellipsoids are shown at 50% probability level.

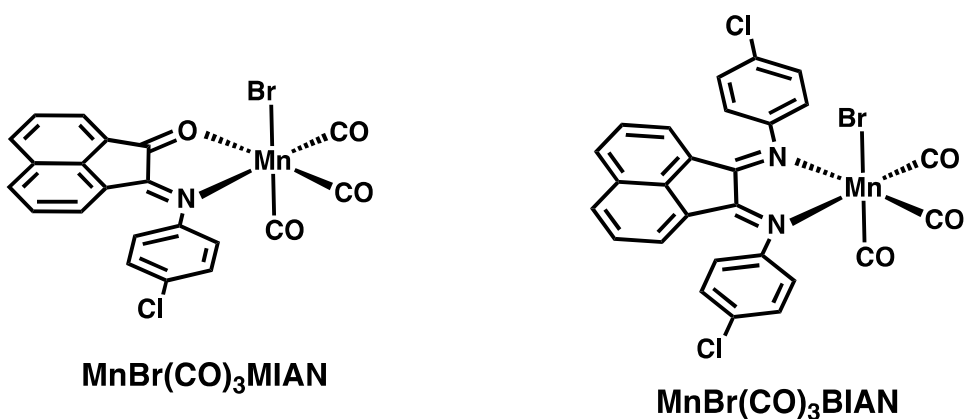


**Figure 4.16.** Structures of previously reported photoCORMs.

The molecular structure of complex MnNIR2 (**Figure 4.17**) is similar to that of complex MnNIR1. Although the molecular structure reveals the identity of MnNIR2 beyond doubt, we refrain from a detailed comparative analysis involving this structure due to a crystallographic complication. In the asymmetric unit, the site of the axial CO group is also partially occupied by a bromide ligand (in a normal situation should reside exclusively trans to the axial CO). During the refinement process, this has been handled through PART refinement but allowed the partially occupied CO group and the

bromide ligand to refine freely. However, due to this constraint on the overall refinement, we choose not to expand any discussion based on metric parameters derived from this crystal structure. Nonetheless, apart from the above-mentioned disorder, the overall structure divulges no other crystallographic complications. Repeated attempts to grow better crystals to evade the disorder remain unsuccessful.

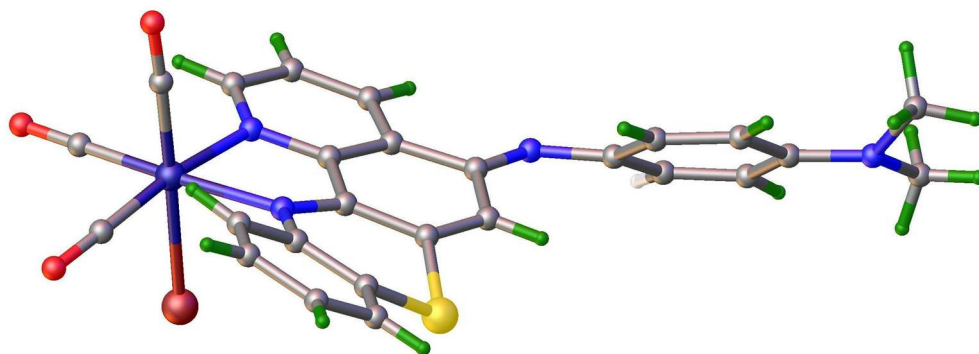


**Figure 4.17.** Molecular structure of MnNIR2. The thermal ellipsoids are shown at 50% probability level.

### 4.3.3 Spectroscopy

The complexes were validated by spectroscopic studies. The FT-IR spectrum of MnNIR1 and MnNIR2 reveal three facial disposed CO ligands at 2016  $\text{cm}^{-1}$ , 1932  $\text{cm}^{-1}$  and 1912  $\text{cm}^{-1}$  and 2022  $\text{cm}^{-1}$ , 1937  $\text{cm}^{-1}$  and 1920  $\text{cm}^{-1}$  respectively (**Figure 4.18**).

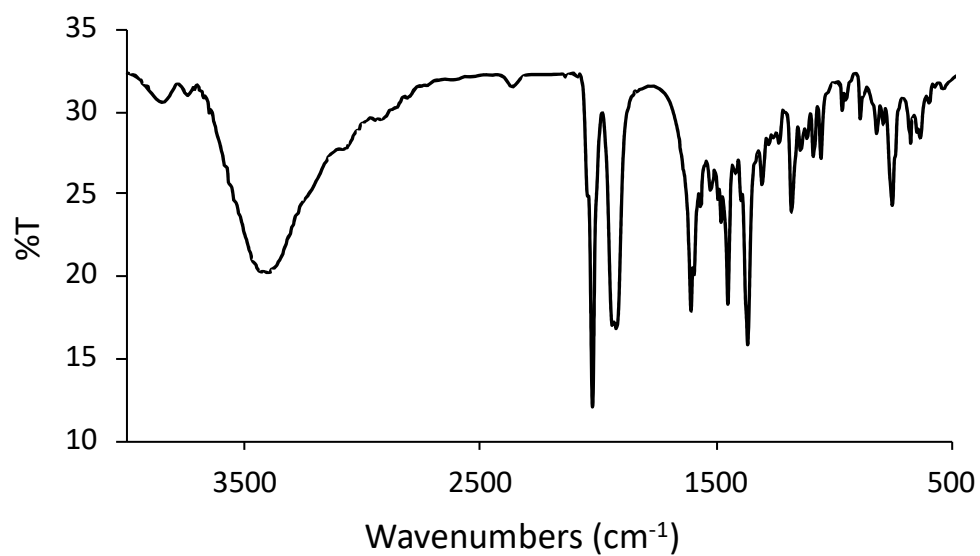
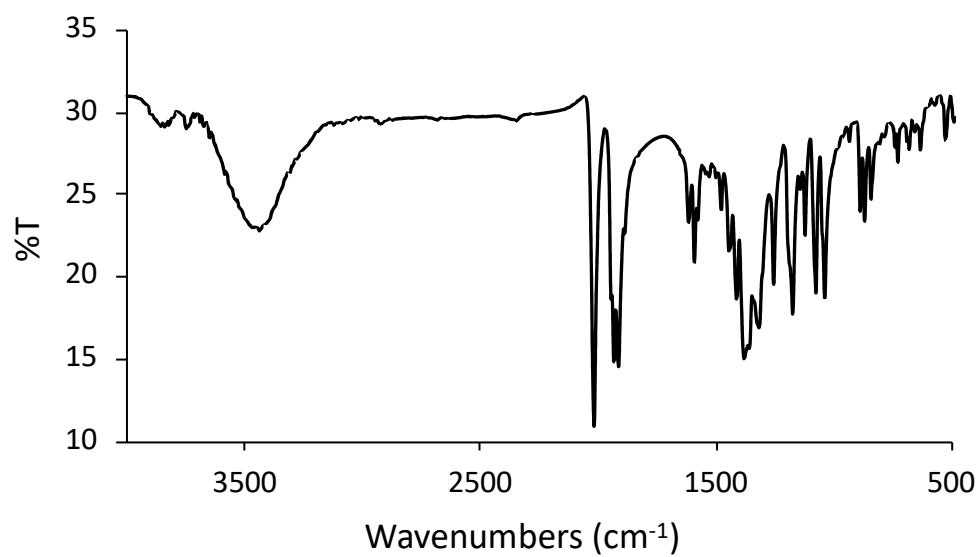


**Figure 4.18.** FT-IR spectrum of MnNIR1 (top) and MnNIR2(bottom) in KBr matrix.

The  $^1\text{H}$  NMR spectrum of MnNIR1 and MnNIR2 reveal well defined peaks in the expected region and shifted from their respective NIR1 and NIR2 free ligands. A comparison of the complex to the ligand's  $^1\text{H}$  NMR spectra is shown in **Figure 4.19** for MnNIR1 and **Figure 4.20** for MnNIR2.

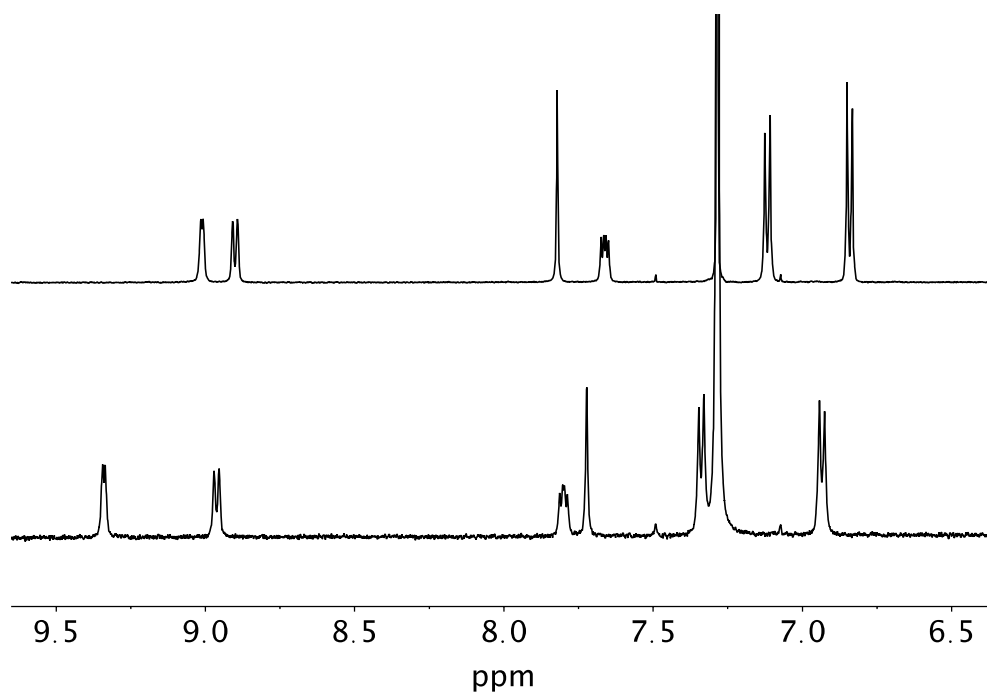


**Figure 4.19.**  $^1\text{H}$  NMR spectrum of NIR1 (top trace) and MnNIR1 (bottom trace) in  $\text{CDCl}_3$  at 298K (not shown; 3.07 ppm, s, 6H for NIR1 and 3.25 ppm, s, 6H for MnNIR1).

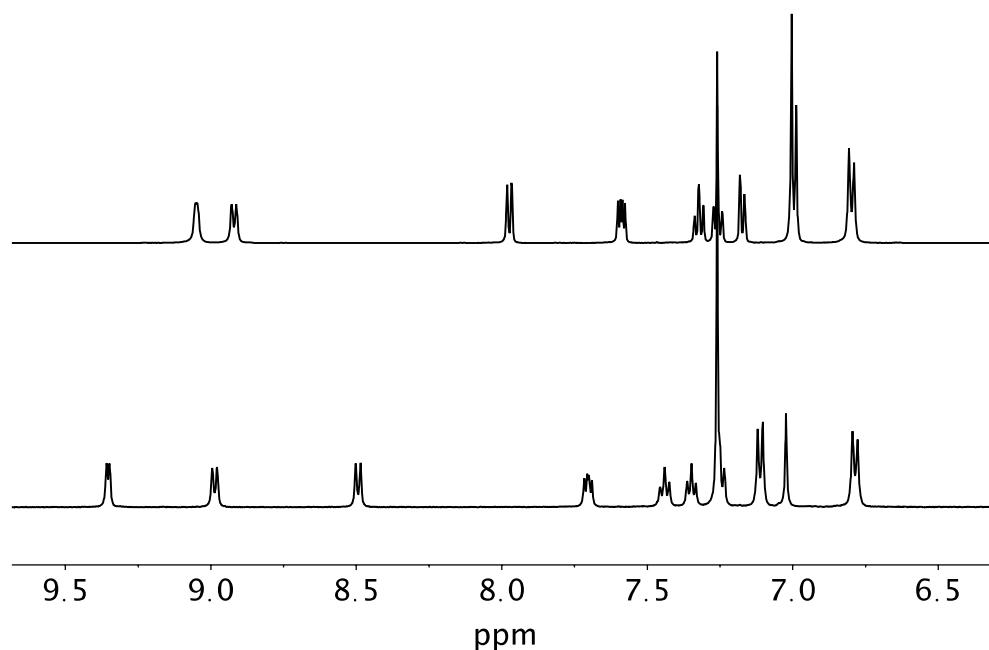


**Figure 4.20.**  $^1\text{H}$  NMR spectrum of NIR2 (top trace) and MnNIR2 (bottom trace) in  $\text{CDCl}_3$  at 298K (not shown; 3.02 ppm, s, 6H for NIR2 and 3.08 ppm, s, 6H for MnNIR2).

Complexes MnNIR1 and MnNIR2 are indefinitely stable in the absence of light and are highly soluble in dichloromethane and  $\text{CHCl}_3$ . When dissolved in MeCN and DMSO, both complexes undergo slow degradation over time. Similarly, aqueous solutions of MnNIR1 and MnNIR2 (prepared with 1% DMSO) vitiate upon prolonged storage even when kept in the dark. It is presumed that these donor solvents will ligand exchange with the complexes causing the structures to degrade. The electronic spectrum of MnNIR1 and MnNIR2 compared to their respective free ligands (**Figure 4.21** and **4.22**) reveal a large bathochromic shift upon complexation to the Mn center.

MnNIR1 showed an intense absorption in  $\text{CHCl}_3$  at 785 nm, shifted 160nm from the ligands  $\lambda_{\text{max}}$  at 625nm. A similar phenomenon is observed with MnNIR2,  $\lambda_{\text{max}}$  shifting roughly 145nm from 614 (NIR1) to 760nm (MnNIR2) in  $\text{CHCl}_3$ . The molar absorptivity at  $\lambda_{\text{max}}$  of MnNIR1 compared to NIR1 (38000 and 18000  $\text{M}^{-1} \text{cm}^{-1}$  respectively) more than doubles and a similar change is observed with MnNIR2 and NIR2 (25000 and 12000  $\text{M}^{-1} \text{cm}^{-1}$  respectively). Both the large red shift and increase in molar extinction coefficient are consistent with Ni(II) and Cu(II) complexes of the same ligands NIR1 and NIR2 and are believed to arise from intermolecular charge transfer involving the metal centers.<sup>35</sup> In 1% DMSO/PBS solution MnNIR1 also shows strong near IR absorption at 735nm (41000  $\text{M}^{-1} \text{cm}^{-1}$ ) (**Figure 4.23**).

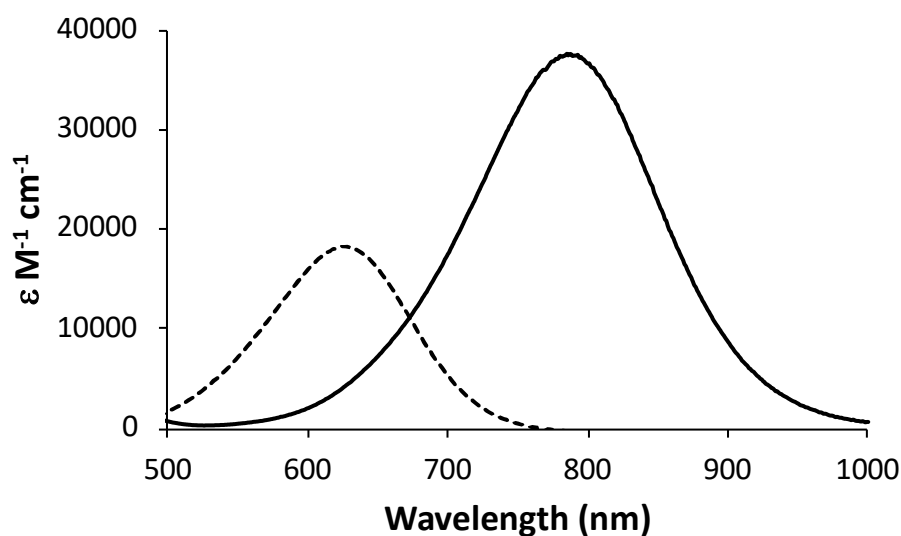


**Figure 4.21.** Electronic absorption spectrum of MnNIR1 (black trace) and NIR1 (black dashed trace) in  $\text{CHCl}_3$ .



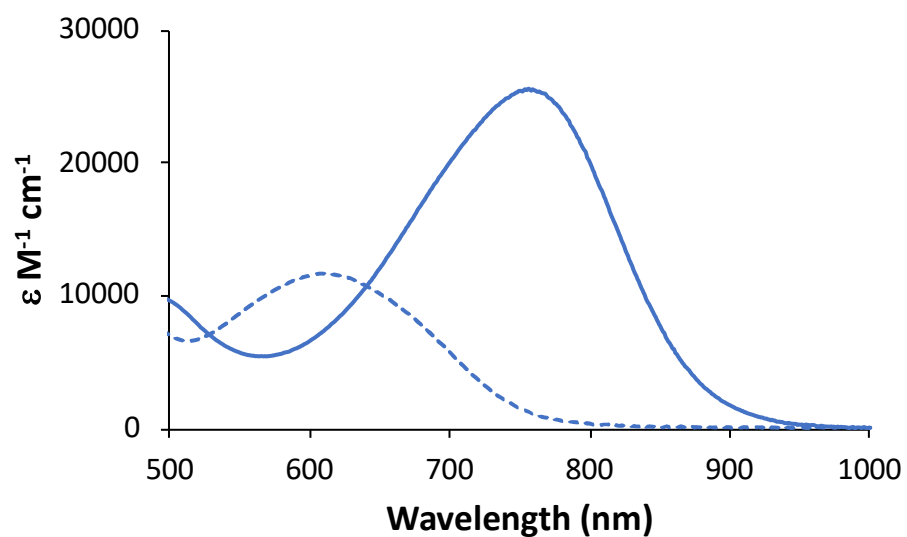


**Figure 4.22.** Electronic absorption spectrum of MnNIR2 (black trace) and NIR2 (black dashed trace) in  $\text{CHCl}_3$ .

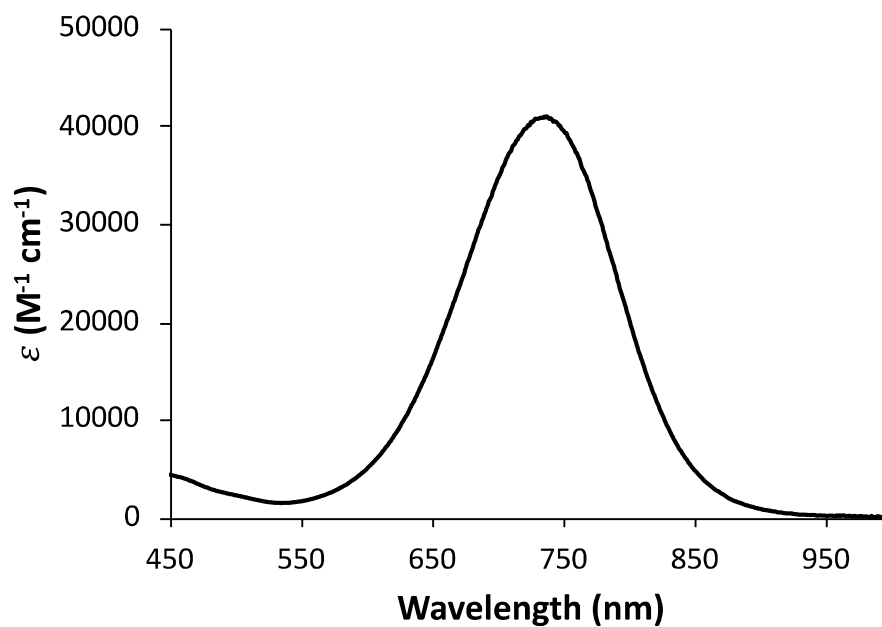


**Figure 4.23.** Electronic absorption spectrum of MnNIR1 in 1% DMSO/PBS.

#### 4.3.4 CO Release Kinetics and Evaluation

Manganese carbonyl complexes are well known to release CO upon radiation with UV and visible light.<sup>11,26,37,38</sup> Other Mn(I) photoCORMs have used near IR light (approximately 800nm) to release CO, but always employ TPE which requires an expensive and high powered laser that could potentially lead to damage of tissues.<sup>16,18,23,24</sup> Due to the presence of the low energy absorption bands (785 and 760nm) in MnNIR1 and MnNIR2, we hypothesized that these complexes would release CO by excitation with the wavelengths of absorption (near IR region) without the use of TPE. In order to determine if MnNIR1 was able to release CO upon activation with single-photon excitation (SPE) in the NIR region, the changes in its electronic absorption spectra (**Figure 4.24**) were recorded upon exposure to a low-power 730 nm LED light source (spectral distribution: 690 - 780 nm, 147mW/cm<sup>2</sup>, purchased from Asahi Spectral). It is important to note that this light source has a peak wavelength of 730 nm but works like a flashlight rather than a high power laser required for TPE. The systematic reduction of 785 nm band indicated that MnNIR1 is in fact active in the NIR region and release of CO from this photoCORM was confirmed by Myoglobin assay (**Figure 4.25**). Similarly, reduction in the 760nm band of MnNIR2 was observed upon SPE using the same light source (**Figure 4.26**). To our knowledge, MnNIR1 and MnNIR2 are the only Mn(I)-based photoCORMs utilizing SPE that show activity in the phototherapeutic region. In a recent report, a NIR-active flavonol-cyanine dye conjugate has been shown to release CO upon exposure to light in the 770-820 nm range.<sup>39</sup> The severe mitochondrial toxicity of cyanine dyes however diminishes the

potential of such CO-donors in therapeutic applications. In contrast, the present manganese carbonyl complexes are derived from organic dyes with more favorable properties. Among the Mn(I)-based photoCORMs with *fac*-[Mn(CO)<sub>3</sub>] moiety, the two previously reported metal-carbonyl complexes [MnBr(CO)<sub>3</sub>MIAN] and [MnBr(CO)<sub>3</sub>BIAN] (**Figure 4.16**,  $\lambda_{\text{max}}$  = 630 nm and 580 nm respectively) demonstrated CO photorelease with long-wavelength light in the visible region.<sup>37</sup>

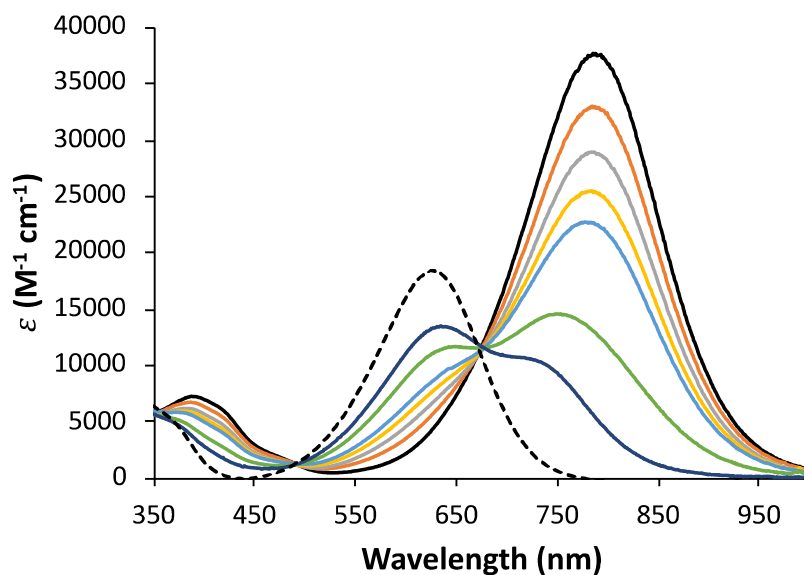


**Figure 4.24.** Changes in the electronic spectrum of MnNIR1 (solid traces) upon illumination of 730 nm light in CHCl<sub>3</sub> at 298K. The absorption spectrum of NIR1 is also shown (dashed trace).

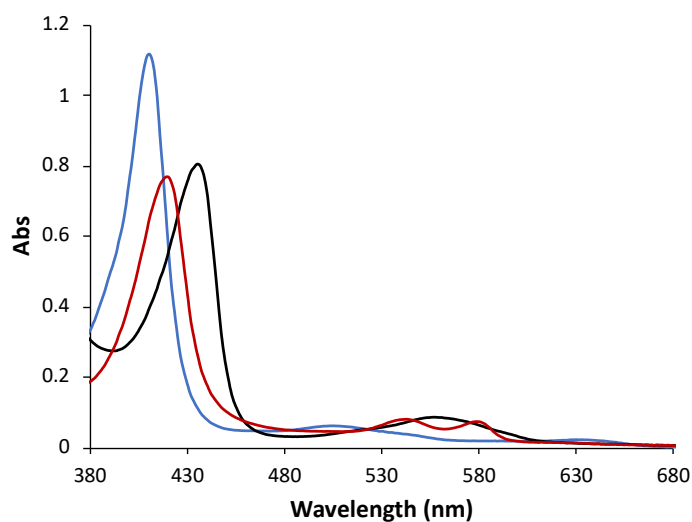


**Figure 4.25.** UV-vis traces from the Myoglobin assay with a  $\text{CHCl}_3$  solution of MnNIR1 at 298K: blue trace, oxidized Mb; black trace, reduced Mb; red trace, COMb.

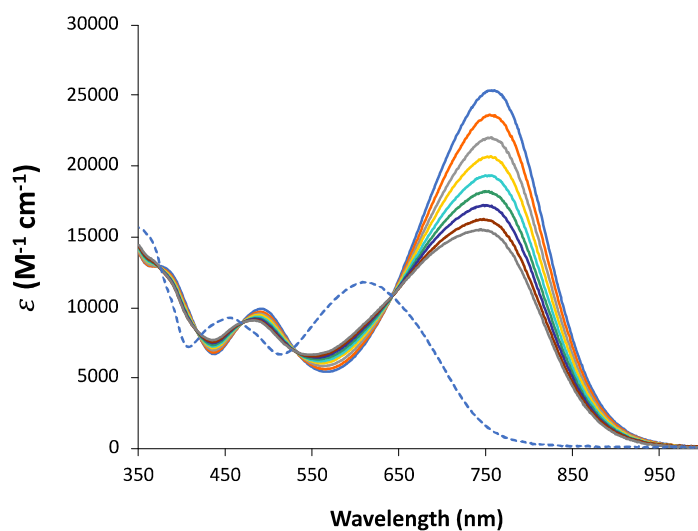


**Figure 4.26.** Spectral Changes of MnNIR2 (solid traces) upon exposure to 730 nm light in 2 min intervals and MIR2 (blue dashed trace) in  $\text{CHCl}_3$ .

The apparent rate of CO photo release ( $k_{\text{CO}}$ ) of MnNIR1 and MnNIR2 (25  $\mu\text{M}$ ) were determined by recording the changes in their electronic absorption spectra at 2 min interval exposures to the 730 nm LED light source. From the  $\ln[C]$  vs time plot, the  $k_{\text{CO}}$  values of MnNIR1 and MnNIR2 in  $\text{CHCl}_3$  were determined to be  $0.0661 \pm 0.0007 \text{ min}^{-1}$  (**Figure 4.27**, black trace) and  $0.0566 \pm 0.0008 \text{ min}^{-1}$  (**Figure 4.28**) respectively. In order to determine how the  $k_{\text{CO}}$  was affected by the power of the incident light, the changes in the absorption spectrum of MnNIR1 were recorded upon exposure to the LED light source at various powers. The  $k_{\text{CO}}$  values dropped to  $0.0431 \pm 0.0007 \text{ min}^{-1}$ ,  $0.0274 \pm 0.0003 \text{ min}^{-1}$  and  $0.0139 \pm 0.0003 \text{ min}^{-1}$  respectively when exposed to 75%, 50% and 25% power of the light source (**Figure 4.27 and Table 4.4**). These rates follow an almost linear pattern with respect to the %power of light vs %CO-release rate with proportionality constant =  $1.04 \pm 0.09$  (**Figure 4.29**). The  $k_{\text{CO}}$  of MnNIR1 in 1% DMSO/PBS was also determined to be  $0.0088 \pm 0.0006 \text{ min}^{-1}$  (**Figure 4.30**).

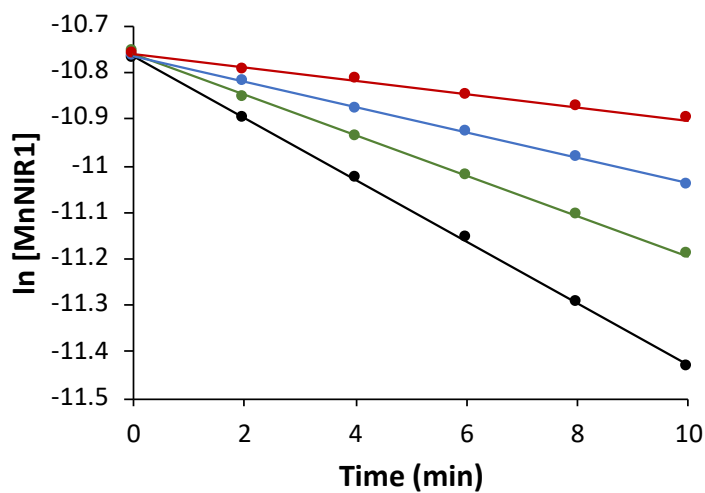


**Figure 4.27.** The  $\ln[\text{MnNIR1}]$  vs Time plot used to determine  $k_{\text{CO}}$  at 100% (black trace), 75% (green trace), 50% (blue trace) and 25% (red trace) power of 730nm light.

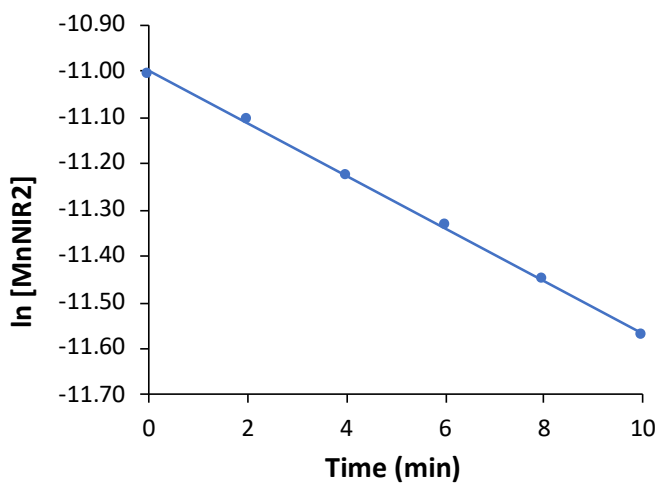


**Figure 4.28.** The  $\ln[\text{MnNIR2}]$  vs time plot used to find the  $k_{\text{CO}}$  of MnNIR2  
( $0.0566 \pm 0.0008$ ) in  $\text{CHCl}_3$ .

**Table 4.4.** Rates of CO release from MnNIR1 calculated from various power of NIR light.

Power	Rate
25%	$0.0139 \pm 0.0003$
50%	$0.0274 \pm 0.0003$
75%	$0.0431 \pm 0.0007$
100%	$0.0661 \pm 0.0007$

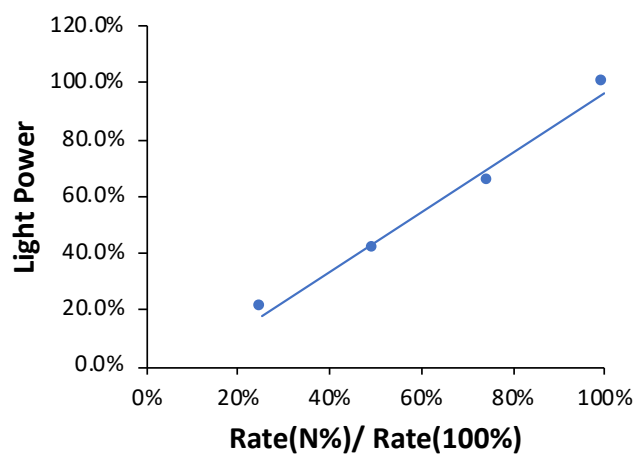


**Figure 4.29.** Comparison of  $k_{CO}$  release rates for MnNIR1 compared to power of light source output. Proportionality constant =  $1.04 \pm 0.09$ .

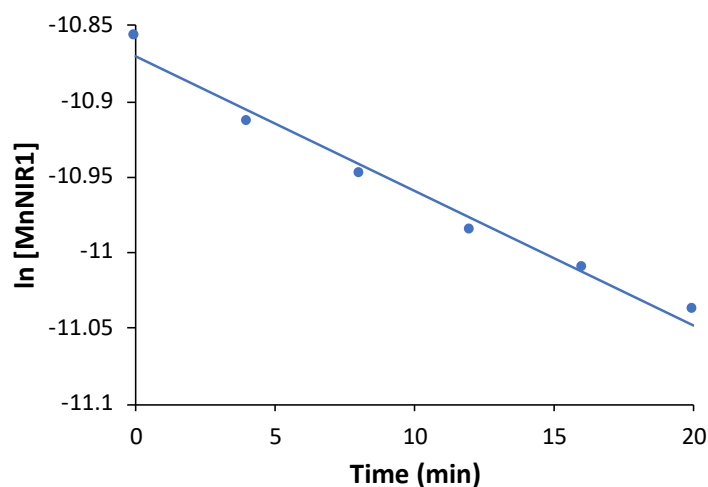


**Figure 4.30.** The  $\ln[\text{MnNIR1}]$  vs time plot used to find the  $k_{\text{CO}}$  of MnNIR1 ( $0.0088 \pm 0.0006$ ) in 1%DMSO/PBS.

Extensive photolysis of the green solution of MnNIR1 yields a blue solution (**Figure 4.31**) indicative loss of the free NIR1 as evidenced by TLC along with the appearance of the NIR1 absorption band at 625 nm (**Figure 4.24**, dark blue trace). Further evidence of loss of CO upon irradiation with 730 nm light is indicated in the FT-IR spectrum of MnNIR1 after irradiation showing significant reduction in the M-CO stretching band intensity (**Figure 4.32**). It should be noted that as the irradiation of 730 nm light causes NIR1 to be released, the extent of light absorption by MnNIR1 diminishes due to absorption of light by NIR1 itself thus slowing down the CO release rate. The extensively photolyzed solution of MnNIR1 in MeCN displays a six-line X-band EPR spectrum (**Figure 4.33**) indicating the formation of a Mn(II) species. It is therefore evident that the photolysis of MnNIR1 likely affords free NIR1 ligand and an Mn(II) species. The NIR-active complexes MnNIR1 and MnNIR2 provide further



evidence of our hypothesis that the choice of ligand readily affects the absorption and CO-releasing properties of transition metal photoCORMs.



**Figure 4.31.** CHCl<sub>3</sub> solutions of MnNIR1 (green) and after irradiation with 730nm light (blue).

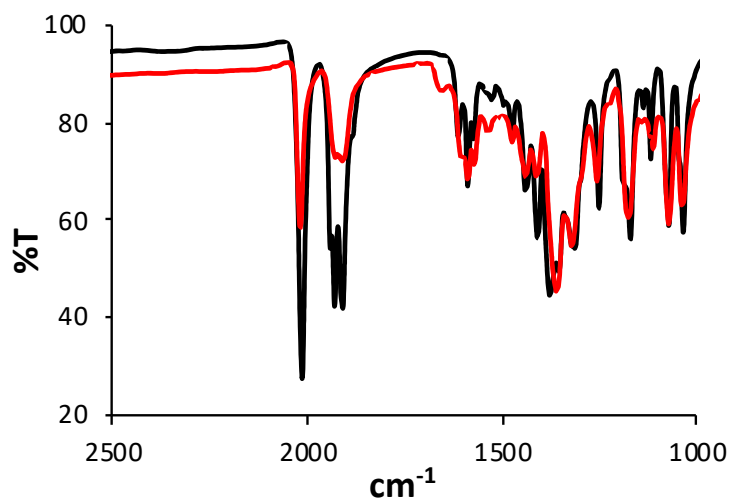


**Figure 4.32.** The FT-IR spectrum of MnNIR1 (black trace) and MnNIR1 after irradiation with 730 nm light (red trace) in KBr. A solution of MnNIR1 in CHCl<sub>3</sub> was irradiated and further removal of the solvent afforded the photolyzed solid (red trace).

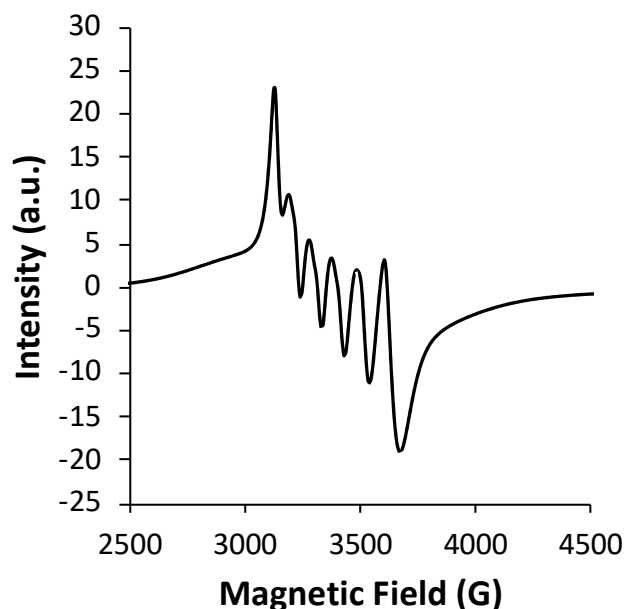


**Figure 4.33.** The EPR spectrum of photolyzed MnNIR1 in MeCN.

#### 4.3.5 Density Functional Studies

Coordination of a ligand which inherently has low energy absorption like NIR1 and NIR2 to a metal center like Mn(I) could allow for charge transfer from HOMO with some M-CO bonding character to LUMO with predominantly ligand  $p^*$  character and result in CO photorelease upon NIR illumination. We performed density function theory (DFT) computations to shed light on this phenomenon within our system. Results of the DFT studies on NIR1 and MnNIR1 indicate that the HOMO-LUMO gap for NIR1 is 1.11eV while in MnNIR1 the gap is reduced to 0.97 eV as depicted in **Figure 4.34**. As a consequence, the absorption maximum of MnNIR1 moves to longer

wavelength compared to the free ligand as seen experimentally in **Figure 4.21**. As shown in **Figure 4.34** the HOMO (132) of MnNIR1 has contribution from Mn  $d_{z^2}$  (9.1%) and C  $p_z$  (5.1%, 4.4%, 3.6%) indicating some Mn-CO bonding character. In contrast, the LUMO (133) has no contribution from the Mn center. Thus, the HOMO to LUMO excitation, the dominant absorption band of MnNIR1, lowers the M-CO bond order and causes CO release.

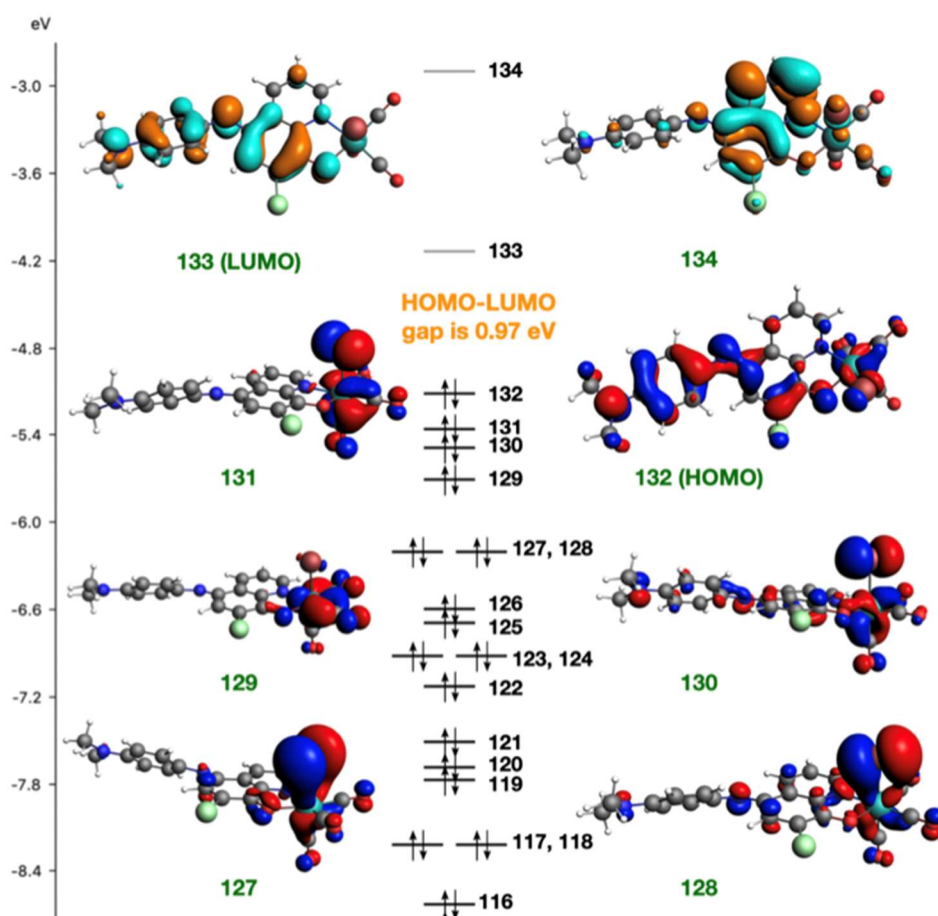


**Figure 4.34.** Calculated energy diagram of MnNIR1 with the MOs involved in the HOMO to LUMO transition.

### 4.3.6 Experimental Section

#### 4.3.6.1 General Methods

All reagents and solvents were of commercial grade and used without further purification. NIR1 and NIR2 were synthesized similarly to reported procedures.<sup>33–36</sup> The IR spectra were recorded using a Perkin-Elmer Spectrum-One FT-IR and <sup>1</sup>H-NMR spectra obtained at 298 K on Varian Unity Inova 500 MHz instrument. A Varian Cary 50 UV-Vis spectrophotometer was employed for UV-Vis spectra at room temperature.

#### 4.3.6.2 Synthesis

5-(4'-dimethylaminophenylimino)-7-chloroquinolin-8-one (NIR1): (40.400 g (1.87 mmol)) of 5,7-Dichloro-8-quinolinol and 0.470 g (11.8 mmol, 6.3 eq) of NaOH were added to water (150 mL) stirred at 50 °C until the suspension completely dissolved. To this yellow solution, 0.382 g (2.80 mmol, 1.5 eq) of N,N-Dimethyl-p-phenylenediamine was added. Then, a solution of 0.854 g (3.74, 2 eq) of ammonium peroxydisulfate in water (12 mL) was added dropwise with stirring at 50 C. After 10 min, the black suspension was filtered, and solid allowed to fully dry in the air overnight. The crude material was carefully purified in batches by column chromatography using acetone/chloroform (1:10) and NIR1 isolated as a blue solid (0.233 g, 40% yield). <sup>1</sup>H-NMR (CDCl<sub>3</sub>): δ 8.96 (dd, 1H), 8.84 (dd, 1H), 7.76 (s, 1H), 7.60 (dt, 1H), 7.06 (d, 2H), 6.79 (d, 2H), 3.07 (s, 6H).

3-(4'-dimethylaminophenylimino)pyrido[2,3-*a*]phenothiazine (NIR2): A solution of 209  $\mu$ L (1.30 mmol, 2 eq) of 2-aminothiophenol and 0.0725 g of KOH were mixed in 5 mL of ethanol and added dropwise to a refluxing solution of 0.2013 g (0.65 mmol) of L1 in 30 mL of ethanol. The solution turned darker blue and was stirred and refluxed for 20 min and then poured in to 150 mL of ice/water. The dark purple precipitate was filtered and allowed to air dry overnight. The crude product was separated in batches using column chromatography with 1:1 benzene/ethyl acetate. NIR2 was isolated as a dark blue/black solid (0.121, 49% yield).  $^1\text{H-NMR}$  ( $\text{CDCl}_3$ ):  $\delta$  9.05 (dd, 1H), 8.92 (dd, 1H), 7.97 (d, 1H), 7.58 (dd, 1H), 7.33 (t, 1H), 7.28 (overlap with  $\text{CDCl}_3$ , 1H), 7.17 (d, 1H), 6.99 (m, 3H), 6.80 (d, 2H), 3.02 (s, 6H).

$[\text{MnBr}(\text{CO})_3(\text{NIR1})]$  (MnNIR1): 0.174 g (0.63 mmol) of Bromopentacarbonylmanganese(I) was dissolved in dichloromethane (4 mL) and a solution of 0.197 g (0.63 mmol, 1 eq) of L1 in dichloromethane (30 mL) was added in the dark at room temperature. The flask was covered in foil to protect from light and allowed to stir in the dark for 3 days after which a dark green precipitate appeared. The solvent was reduced to 15 mL, precipitate filtered and washed with 2 mL of cold dichloromethane and complex isolated as a dark green solid (0.280 g, 84% yield). IR ( $\text{KBr}$ ,  $\text{cm}^{-1}$ ): 2016 (s), 1932 (s), 1912 (s), 1614 (w), 1590 (m), 1410 (m), 1377 (s), 1314 (s), 1172 (m), 1073 (m), 1036 (m), 867 (w).  $^1\text{H-NMR}$  ( $\text{CDCl}_3$ ):  $\delta$  9.32 (d, 1H), 8.95 (d, 1H), 7.78 (m, 1H), 7.70 (s, 1H), 7.32 (d, 2H), 6.92 (d, 2H), 3.25 (s, 6H).

[MnBr(CO)<sub>3</sub>(NIR2)] (MnNIR2): A similar procedure to MnNIR1 was employed using 0.0726 g (0.26 mmol) of Bromopentacarbonylmanganese(I) and 0.1008 g (0.26, 1eq) of L2 in dichloromethane. After 3 days of stirring in the dark the solvent was reduced to 10mL and 50mL of hexanes was added. The precipitate was filtered and washed with cold hexanes and complex isolated as a dark green solid (0.115 g, 76% yield). IR (KBr, cm<sup>-1</sup>): 2022 (s), 1937(s), 1920 (s), 1604 (m), 1591 (m), 1448 (m), 1364 (s), 1177 (w), 749 (w) <sup>1</sup>H-NMR (CDCl<sub>3</sub>): δ 9.36 (d, 1H), 9.00 (d, 1H), 8.50 (d, 1H), 7.71 (m, 1H), 7.44 (t, 1H), 7.35 (t, 1H), 7.24 (m, 1H, overlaps with CDCl<sub>3</sub>), 7.12 (d, 2H), 7.02 (s, 1H), 6.79 (d, 2H), 3.08 (s, 6H).

#### 4.3.6.3 X-ray Crystallography

Data were collected on a Bruker D8 Quest single crystal X-ray diffractometer (PHOTON 100 CMOS detector) with graphite monochromated Mo K $\alpha$  radiation ( $\lambda$  = 0.71073 Å) by the  $\omega$ -scan technique in the range  $5.4 \leq 2\theta \leq 50$  for (for both MnNIR1 and MnNIR1). All data were corrected for Lorentz and polarization effects.<sup>40</sup> All the structures were solved with the aid of *SHELXT* program using intrinsic phasing.<sup>32</sup> The structures were then refined by a full-matrix least squares procedure on F<sup>2</sup> by *SHELXL*.<sup>29</sup> All non-hydrogen atoms were refined anisotropically. Hydrogen atom positions were calculated geometrically and refined using the riding model. Multi-scan absorption corrections are applied using SADABS<sup>2</sup>. Calculations were performed using the *OLEX2*<sup>30</sup> and *SHELXTL*<sup>TM</sup> (V 6.14)<sup>41</sup> program packages. The experimental details are listed in **Table 4.5**.

**Table 4.5.** Crystal data and structure refinement parameters for **MnNIR1** and **MnNIR1**.

	<b>MnNIR1</b>	<b>MnNIR2</b>
Empirical formula	C <sub>20</sub> H <sub>14</sub> MnN <sub>3</sub> O <sub>4</sub> BrCl	C <sub>26</sub> H <sub>18</sub> MnN <sub>4</sub> O <sub>3</sub> SBr
FW	530.64	601.36
Temp(K)	298	150
Wavelength (Å)	0.71073	0.71073
Crystal system	Orthorhombic	Monoclinic
Space group	<i>Pcab</i>	<i>P2<sub>1</sub>/c</i>
a (Å)	7.6931 (7)	13.6697 (17)
b (Å)	17.5230 (15)	22.226 (3)
c (Å)	30.345 (3)	8.017 (1)
a (°)	90	90
b (°)	90	99.760 (3)
g (°)	90	90
Z	8	4
V (Å <sup>3</sup> )	4090.7 (6)	2400.5 (5)
Density (calcd) (Mg m <sup>-3</sup> )	1.723	1.724
Abs coeff (mm <sup>-1</sup> )	2.76	2.78
No. of unique reflns.	3640	4252
R <sub>1</sub> <sup>b</sup>	0.080	0.100
wR <sub>2c</sub>	0.163	0.193
GOF <sup>a</sup> on F <sup>2</sup>	1.12	1.04

<sup>a</sup> GOF =  $[\sum[w(\text{Fo}^2 - \text{Fc}^2)^2]/(\text{No} - \text{Nv})]^{1/2}$  (No = number of observations, Nv = number of variables).

<sup>b</sup> R<sub>1</sub> =  $\sum||\text{Fo}| - |\text{Fc}||/\sum|\text{Fo}|$ .

<sup>c</sup> wR<sub>2</sub> =  $[(\sum w(\text{Fo}^2 - \text{Fc}^2)^2/\sum|\text{Fo}|^2)]^{1/2}$ .

#### 4.3.6.4 Computational Methods

Density functional theory (DFT), as implemented in the ADF program (version 2019.103),<sup>42</sup> was used for the ground state structure optimizations without any constraints. The revPBE functional,<sup>43</sup> including the Grimme D3 corrections and the Becke-Johnson damping,<sup>44</sup> was used. The TZP<sup>45,46</sup> basis sets were used for all atoms,

and the relativistic Scalar ZORA<sup>47</sup> approach was applied for the Mn. The COSMO<sup>48–50</sup> approach was used as the implicit solvent model, where dichloromethane was used as the solvent. For all calculations, the numerical quality was set to “normal”. Vibrational frequency calculations were performed at 298.15K and 1 atm to confirm the local minima (*i.e.* no imaginary frequency). Time dependent DFT (TDDFT) method was used for calculating the vertical excited states using the ground state optimized structures. The range separated LYC-PBE<sup>51</sup> functional with the Gamma value of 0.22 was employed. The TZ2P basis sets were used for all atoms, the Scalar ZORA approach was used for Mn, and the COSMO implicit solvent model was employed.

In the case of NIR1, two energetically equivalent conformers, consisting the C1-C2-N-C3 torsion angle 18.7° and 340.5°, were found (**Figure 4.35**, a). The former and latter conformers represent 46% and 41% of the molecules in the ground state ensemble, respectively. In the case of MnNIR1, the most stable conformer has the C1-C2-N-C3 torsion angle of 18.8°, representing 87% of complexes in the ground state ensemble (**Figure 4.35**, b). Further results of TD-DFT studies can be found in **Table 4.6**.



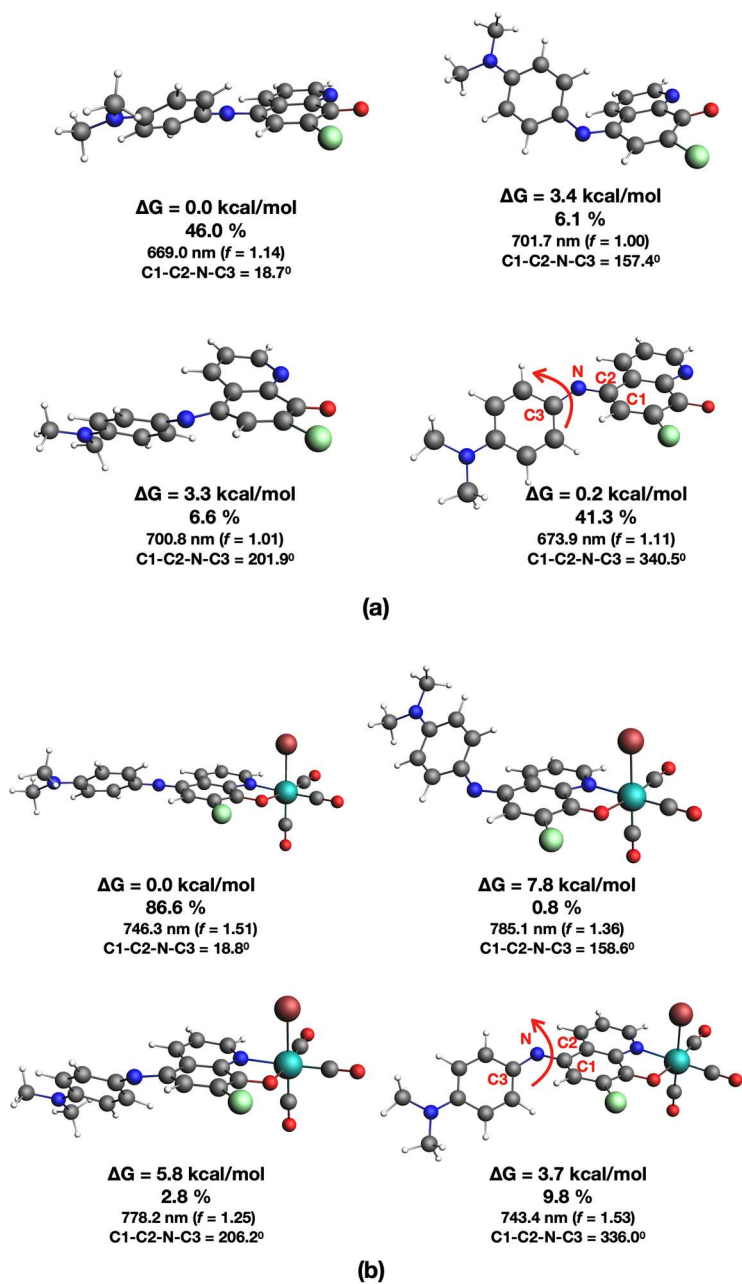


**Figure 4.35.** Relative Gibbs free energy (in kcal/mol), fraction of molecules in the ground state ensemble for the conformation (%), excitation wavelength (oscillator strength), C1-C2-N-C3 torsion angle (in °) of the conformers of (a) NIR1 and (b) MnNIR1.

**Table 4.5.** TD-DFT results of MnNIR1 and NIR1

NIR1:		
<u>C1-C2-N-C3 = 18.7<sup>0</sup></u>		
orbitals		weight
81a -> 82a		0.9402
<u>C1-C2-N-C3 = 157.4<sup>0</sup></u>		
orbitals		weight
81a -> 82a		0.9325
<u>C1-C2-N-C3 = 201.9<sup>0</sup></u>		
orbitals		weight
81a -> 82a		0.9318
<u>C1-C2-N-C3 = 340.5<sup>0</sup></u>		
orbitals		weight
81a -> 82a		0.9401
MnNIR1:		
<u>C1-C2-N-C3 = 18.8<sup>0</sup></u>		
orbitals		weight
132a -> 133a		0.9298
<u>C1-C2-N-C3 = 158.6<sup>0</sup></u>		
orbitals		weight
132a -> 133a		0.9272
<u>C1-C2-N-C3 = 206.2<sup>0</sup></u>		
orbitals		weight
132a -> 133a		0.9311
<u>C1-C2-N-C3 = 336.0<sup>0</sup></u>		
orbitals		weight
132a -> 133a		0.9331

#### 4.4 References

- (1) Rose, J. J.; Wang, L.; Xu, Q.; McTiernan, C. F.; Shiva, S.; Tejero, J.; Gladwin, M. T. Carbon Monoxide Poisoning: Pathogenesis, Management, and Future Directions of Therapy. *Am. J. Respir. Crit. Care Med.* **2017**, *195* (5), 596–606.
- (2) Motterlini, R.; Otterbein, L. E. The Therapeutic Potential of Carbon Monoxide. *Nat. Rev. Drug Discov.* **2010**, *9*, 728–743.
- (3) Kourti, M.; Jiang, W. G.; Cai, J. Aspects of Carbon Monoxide in Form of CO-Releasing Molecules Used in Cancer Treatment: More Light on the Way. *Oxid. Med. Cell. Longev.* **2017**, *2017*.
- (4) Wegiel, B.; Gallo, D.; Csizmadia, E.; Harris, C.; Belcher, J.; Vercellotti, G. M.; Penacho, N.; Seth, P.; Sukhatme, V.; Ahmed, A.; et al. Carbon Monoxide Expedites Metabolic Exhaustion to Inhibit Tumor Growth. *Cancer Res.* **2013**, *73* (23), 7009–7021.
- (5) Zuckerbraun, B. S.; Chin, B. Y.; Bilban, M.; d'Avila, J. de C.; Rao, J.; Billiar, T. R.; Otterbein, L. E. Carbon Monoxide Signals via Inhibition of Cytochrome c Oxidase and Generation of Mitochondrial Reactive Oxygen Species. *FASEB J.* **2007**, *21* (4), 1099–1106.
- (6) Kawahara, B.; Moller, T.; Hu-Moore, K.; Carrington, S.; Faull, K. F.; Sen, S.; Mascharak, P. K. Attenuation of Antioxidant Capacity in Human Breast Cancer Cells by Carbon Monoxide through Inhibition of Cystathionine  $\beta$ -Synthase Activity: Implications in Chemotherapeutic Drug Sensitivity. *J. Med. Chem.* **2017**, *60* (19), 8000–8010.
- (7) Kunz, P. C.; Meyer, H.; Sollazzo, S.; Schmidt, A. M.; Janiak, C. Metal Carbonyls Supported on Iron Oxide Nanoparticles to Trigger the CO-Gasotransmitter Release by Magnetic Heating. *Chem. Commun.* **2013**, *49* (43), 4896–4898.
- (8) Upendar Reddy, G.; Axthelm, J.; Hoffmann, P.; Taye, N.; Gläser, S.; Görls, H.; Hopkins, S. L.; Plass, W.; Neugebauer, U.; Bonnet, S.; et al. Co-Registered Molecular Logic Gate with a CO-Releasing Molecule Triggered by Light and Peroxide. *J. Am. Chem. Soc.* **2017**, *139* (14), 4991–4994.
- (9) Gonzales, M. A.; Mascharak, P. K. Photoactive Metal Carbonyl Complexes as Potential Agents for Targeted CO Delivery. *J. Inorg. Biochem.* **2014**, *133*, 127–135.

- (10) Stenger-Smith, J.; Kamariza, M.; Chakraborty, I.; Ouattara, R.; Bertozzi, C. R.; Mascharak, P. K. Enhanced Bactericidal Effects of Pyrazinamide Toward *Mycobacterium Smegmatis* and *Mycobacterium Tuberculosis* upon Conjugation to a {Au(I)-Triphenylphosphine}<sup>+</sup> Moiety. *ACS Omega* **2020**, *5*, 6826–6833.
- (11) Chakraborty, I.; Carrington, S. J.; Mascharak, P. K. Design Strategies to Improve the Sensitivity of Photoactive Metal Carbonyl Complexes (PhotoCORMs) to Visible Light and Their Potential as CO-Donors to Biological Targets. *Acc. Chem. Res.* **2014**, *47* (8), 2603–2611.
- (12) Marhenke, J.; Trevino, K.; Works, C. The Chemistry, Biology and Design of Photochemical CO Releasing Molecules and the Efforts to Detect CO for Biological Applications. *Coord. Chem. Rev.* **2016**, *306*, 533–543.
- (13) Romão, C. C.; Blättler, W. A.; Seixas, J. D.; Bernardes, G. J. L. Developing Drug Molecules for Therapy with Carbon Monoxide. *Chem. Soc. Rev.* **2012**, *41* (9), 3571–3583.
- (14) Smith, A. M.; Mancini, M. C.; Nie, S. Second Window for in Vivo Imaging. *Nat. Nanotechnol.* **2009**, *4* (11), 710–711.
- (15) Plaetzer, K.; Krammer, B.; Berlanda, J.; Berr, F.; Kiesslich, T. Photophysics and Photochemistry of Photodynamic Therapy: Fundamental Aspects. *Lasers Med. Sci.* **2009**, *24* (2), 259–268.
- (16) Pierri, A. E.; Huang, P. J.; Garcia, J. V.; Stanfill, J. G.; Chui, M.; Wu, G.; Zheng, N.; Ford, P. C. A PhotoCORM Nanocarrier for CO Release Using NIR Light. *Chem. Commun.* **2015**, *51* (11), 2072–2075.
- (17) Ou, J.; Zheng, W.; Xiao, Z.; Yan, Y.; Jiang, X.; Dou, Y.; Jiang, R.; Liu, X. Core-Shell Materials Bearing Iron(II) Carbonyl Units and Their CO-Release: Via an Upconversion Process. *J. Mater. Chem. B* **2017**, *5* (41), 8161–8168.
- (18) Jiang, Q.; Xia, Y.; Barrett, J.; Mikhailovsky, A.; Wu, G.; Wang, D.; Shi, P.; Ford, P. C. Near-Infrared and Visible Photoactivation to Uncage Carbon Monoxide from an Aqueous-Soluble PhotoCORM. *Inorg. Chem.* **2019**, *58* (16), 11066–11075.
- (19) Ramu, V.; Upendar Reddy, G.; Liu, J.; Hoffmann, P.; Sollapur, R.; Wyrwa, R.; Kupfer, S.; Spielmann, C.; Bonnet, S.; Neugebauer, U.; et al. Two-Photon-Induced CO-Releasing Molecules as Molecular Logic Systems in Solution, Polymers, and Cells. *Chem. - A Eur. J.* **2019**, *25* (36), 8453–8458.

- (20) Denk, W.; Strickler, J. H.; Webb, W. W. Two-Photon Laser Scanning Fluorescence Microscopy. *Science* **1990**, *248* (4951), 73—76.
- (21) Zipfel, W. R.; Williams, R. M.; Webb, W. W. Nonlinear Magic: Multiphoton Microscopy in the Biosciences. *Nat. Biotechnol.* **2003**, *21* (11), 1369–1377.
- (22) Terenziani, F.; Katan, C.; Badaeva, E.; Tretiak, S.; Blanchara-Desce, M. Enhanced Two-Photon Absorption of Organic Chromophores: Theoretical and Experimental Assessments. *Adv. Mater.* **2008**, *20* (24), 4641–4678.
- (23) Masters, B. R.; So, P. T. C.; Buehler, C.; Barry, N.; Sutin, J. D.; Mantulin, W. W.; Gratton, E. Mitigating Thermal Mechanical Damage Potential during Two-Photon Dermal Imaging. *J. Biomed. Opt.* **2004**, *9* (6), 1265–1270.
- (24) Watanabe, W.; Arakawa, N.; Matsunaga, S.; Higashi, T.; Fukui, K.; Isobe, K.; Itoh, K. Femtosecond Laser Disruption of Subcellular Organelles in Living Cells. *Opt. Express* **2004**, *12* (18), 4203–4213.
- (25) Carrington, S. J.; Chakraborty, I.; Bernard, J. M. L.; Mascharak, P. K. Synthesis and Characterization of a “Turn-on”PhotoCORM for Trackable Co Delivery to Biological Targets. *ACS Med. Chem. Lett.* **2014**, *5* (12), 1324–1328.
- (26) Pinto, M. N.; Chakraborty, I.; Jimenez, J.; Murphy, K.; Wenger, J.; Mascharak, P. K. Therapeutic Potential of Two Visible Light Responsive Luminescent PhotoCORMs: Enhanced Cellular Internalization Driven by Lipophilicity. *Inorg. Chem.* **2019**, *58* (21), 14522–14531.
- (27) Chen, X.; Femia, F. J.; Babich, J. W.; Zubietta, J. Spectroscopic and Structural Studies of Complexes of the Fac-[Re(N $\cap$ N)(CO)<sub>3</sub>L]N<sup>+</sup> Type (N $\cap$ N = 2-(2-Pyridyl)Benzothiazole; L = Cl, Br, CF<sub>3</sub>SO<sub>3</sub><sup>-</sup>, CH<sub>3</sub>CN). *Inorganica Chim. Acta* **2001**, *314* (1–2), 91–96.
- (28) Davis, R.; Durrant, J. L. A.; Rowland, C. C. The Halogenation of Toluene with Sulphuryl Chloride and Dichlorine in the Presence of Transition Metal Complexes. *J. Organomet. Chem.* **1986**, *315* (1), 119–133.
- (29) Sheldrick, G. M. SHELXT - Integrated Space-Group and Crystal-Structure Determination. *Acta Crystallogr. Sect. A Found. Crystallogr.* **2015**, *71* (1), 3–8.
- (30) Dolomanov, O. V.; Bourhis, L. J.; Gildea, R. J.; Howard, J. A. K.; Puschmann, H. OLEX2: A Complete Structure Solution, Refinement and Analysis Program. *J. Appl. Crystallogr.* **2009**, *42* (2), 339–341.

- (31) Meghdadi, S.; Amirnasr, M.; Mirhashemi, A.; Amiri, A. Synthesis, Characterization and X-Ray Crystal Structure of Copper(I) Complexes of the 2-(2-Quinoly)Benzothiazole Ligand. Electrochemical and Antibacterial Studies. *Polyhedron* **2015**, *97*, 234–239.
- (32) Sheldrick, G. M. Crystal Structure Refinement with SHELXL. *Acta Crystallogr. Sect. C Struct. Chem.* **2015**, *71* (Md), 3–8.
- (33) Kubo, Y.; Sasaki, K.; Yoshida, K. Syntheses and Characteristics of Near-Infrared Absorbing Metal Complex Dyes with Indoaniline-Type Ligands. *Chem. Lett.* **1987**, 5241–5244.
- (34) Kubo, Y.; Sasaki, K.; Kataoka, H.; Yoshida, K. Synthesis of Novel Near-Infrared Absorbing Metal Complex Dyes with Indoaniline-Type Ligands. *J. Chem. Soc. Perkin Trans. 1* **1989**, 1469–1472.
- (35) Kubo, Y.; Kataoka, H.; Ikezawa, M.; Yoshida, K. New Near-Infrared Absorbing Metal Complex Dyes with Heterocyclic Phenyliminoquinone-Type Ligands. *J. Chem. Soc. Perkin Trans. 1* **1990**, No. 3, 585–589.
- (36) Kubo, Y.; Kataoka, H.; Yoshida, K. New Bis[3-(4'-Dialkylaminophenylimino)Pyrido[2,3-a]Phenothiazine]Nickel(II) Complexes with Near-Infrared Absorptions. *J. Chem. Soc. Perkin Trans. 1* **1988**, 1457–1458.
- (37) Carrington, S. J.; Chakraborty, I.; Mascharak, P. K. Exceptionally Rapid CO Release from a Manganese(i) Tricarbonyl Complex Derived from Bis(4-Chloro-Phenylimino)Acenaphthene upon Exposure to Visible Light. *Dalt. Trans.* **2015**, *44* (31), 13828–13834.
- (38) Stenger-Smith, J.; Chakraborty, I.; Carrington, S.; Mascharak, P. Synthesis and Structures of Photoactive Manganese-Carbonyl Complexes Derived from 2-(Pyridin-2-Yl)-1,3-Benzothiazole and 2-(Quinolin-2-Yl)-1,3-Benzothiazole. *Acta Crystallogr. Sect. C Struct. Chem.* **2017**, *73* (4).
- (39) Šťáková, L.; Russo, M.; Muchová, L.; Orel, V.; Vitek, L.; Šťácko, P.; Klán, P. Cyanine-Flavonol Hybrids for Near-Infrared Light-Activated Delivery of Carbon Monoxide. *Chem. - A Eur. J.* **2020**, 1–8.
- (40) North, A. C. T.; Phillips, D. C.; Mathews, F. S. A Semi-empirical Method of Absorption Correction. *Acta Crystallogr. Sect. A* **1968**, *24* (3), 351–359.
- (41) Sheldrick, G. M. SHELXTL TM (V 6.14). Bruker Analytical X-ray Systems: Madison, WI 2000.

- (42) te Velde, G.; Bickelhaupt, F. M.; Baerends, E. J.; Fonseca Guerra, C.; van Gisbergen, S. J. A.; Snijders, J. G.; Ziegler, T. Chemistry with ADF. *J. Comput. Chem.* **2001**, 22 (9), 931–967.
- (43) Hammer, B.; Hansen, L. B.; Nørskov, J. K. Improved Adsorption Energetics within Density-Functional Theory Using Revised Perdew-Burke-Ernzerhof Functionals. *Phys. Rev. B - Condens. Matter Mater. Phys.* **1999**, 59 (11), 7413–7421.
- (44) Grimme, S.; Ehrlich, S.; Goerigk, L. Effect of the Damping Function in Dispersion Corrected Density Functional Theory. *J. Comput. Chem.* **2011**, 32 (7), 1456–1465.
- (45) Weigend, F.; Ahlrichs, R. Balanced Basis Sets of Split Valence, Triple Zeta Valence and Quadruple Zeta Valence Quality for H to Rn: Design and Assessment of Accuracy. *Phys. Chem. Chem. Phys.* **2005**, 7 (18), 3297–3305.
- (46) Weigend, F. Accurate Coulomb-Fitting Basis Sets for H to Rn. *Phys. Chem. Chem. Phys.* **2006**, 8 (9), 1057–1065.
- (47) Philipsen, P.; van Lenthe, E.; Snijders, J.; Baerends, E. Relativistic Calculations on the Adsorption of CO on the (111) Surfaces of Ni, Pd, and Pt within the Zeroth-Order Regular Approximation. *Phys. Rev. B - Condens. Matter Mater. Phys.* **1997**, 56 (20), 13556–13562.
- (48) Klamt, A.; Schüürmann, G. COSMO: A New Approach to Dielectric Screening in Solvents with Explicit Expressions for the Screening Energy and Its Gradient. *J. Chem. Soc. Perkin Trans. 2* **1993**, No. 5, 799–805.
- (49) Klamt, A. Conductor-like Screening Model for Real Solvents: A New Approach to the Quantitative Calculation of Solvation Phenomena. *J. Phys. Chem.* **1995**, 99 (7), 2224–2235..
- (50) Klamt, A.; Jonas, V. Treatment of the Outlying Charge in Continuum Solvation Models. *J. Chem. Phys.* **1996**, 105 (22), 9972–9981.
- (51) Seth, M.; Ziegler, T. Range-Separated Exchange Functionals with Slater-Type Functions. *J. Chem. Theory Comput.* **2012**, 8 (3), 901–907.

#### 4.5 Reprints of Publication and Permissions

Reprinted with permissions from Stenger-Smith, J.; Chakraborty, I.; Carrington, S.; Mascharak, P. Synthesis and structures of photoactive manganese-carbonyl complexes derived from 2-(pyridine-2-yl)-1,3-benzthiazole and 2-(quinolin-2-yl)-1,3-benzthiazole. *Acta Cryst.* **2017**, C73, 357-361.





STRUCTURAL  
CHEMISTRY

ISSN 2053-2296

## Synthesis and structures of photoactive manganese–carbonyl complexes derived from 2-(pyridin-2-yl)-1,3-benzothiazole and 2-(quinolin-2-yl)-1,3-benzothiazole

Jenny Stenger-Smith, Indranil Chakraborty, Samantha Carrington and Pradip Mascharak\*

Received 27 February 2017  
Accepted 20 March 2017

Edited by A. L. Spek, Utrecht University, The Netherlands

**Keywords:** crystal structure; metal–carbonyl complexes; CO photorelease; photoreactivity; fluorescence; manganese complexes; visible light; trackable photoCORMs.

**CCDC references:** 1539276; 1539275

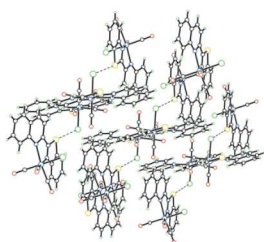
**Supporting information:** this article has supporting information at journals.iucr.org/c

Department of Chemistry, University of California Santa Cruz, CA 95064, USA. \*Correspondence e-mail: pradip@ucsc.edu

PhotoCORMs (photo-active CO-releasing molecules) have emerged as a class of CO donors where the CO release process can be triggered upon illumination with light of appropriate wavelength. We have recently reported an Mn-based photoCORM, namely [MnBr(pbt)(CO)<sub>3</sub>] [pbt is 2-(pyridin-2-yl)-1,3-benzothiazole], where the CO release event can be tracked within cellular milieu by virtue of the emergence of strong blue fluorescence. In pursuit of developing more such trackable photoCORMs, we report herein the syntheses and structural characterization of two Mn<sup>I</sup>–carbonyl complexes, namely *fac*-tricarbonylchlorido[2-(pyridin-2-yl)-1,3-benzothiazole-κ<sup>2</sup>N,N']manganese(I), [MnCl(C<sub>12</sub>H<sub>8</sub>N<sub>2</sub>S)(CO)<sub>3</sub>], (1), and *fac*-tricarbonylchlorido[2-(quinolin-2-yl)-1,3-benzothiazole-κ<sup>2</sup>N,N']manganese(I), [MnCl(C<sub>16</sub>H<sub>10</sub>N<sub>2</sub>S)(CO)<sub>3</sub>], (2). In both complexes, the Mn<sup>I</sup> center resides in a distorted octahedral coordination environment. Weak intermolecular C—H...Cl contacts in complex (1) and Cl...S contacts in complex (2) consolidate their extended structures. These complexes also exhibit CO release upon exposure to low-power broadband visible light. The apparent CO release rates for the two complexes have been measured to compare their CO donating capacity. The fluorogenic 2-(pyridin-2-yl)-1,3-benzothiazole and 2-(quinolin-2-yl)-1,3-benzothiazole ligands provide a convenient way to track the CO release event through the 'turn-ON' fluorescence which results upon deligation of the ligands from their respective metal centers following CO photorelease.

### 1. Introduction

Carbon monoxide (CO) has recently been implicated as a key signalling molecule in mammalian pathophysiology (Motterlini & Otterbien, 2010). This small gaseous molecule forms endogenously in mammals as a by-product of heme catabolism (Tenhunen *et al.*, 1968). In lower concentrations, CO has been shown to impart anti-inflammatory, anti-apoptotic, and vasoregulatory effects. However, at a slightly elevated level of concentration, CO exerts a significant proapoptotic effect towards dysregulated or hyperproliferative cells, such as cancer cells (Motterlini & Otterbien, 2010). Collectively, these observations have prompted researchers to explore the possibility of the administration of CO as a therapeutic. However, delivery of CO in a controlled manner to biological targets presents a technical challenge. CO-releasing molecules (CORMs) have thus been developed as an alternative means for CO delivery in a more controllable fashion (Bernardes & Garcia-Gallego, 2014; Romao *et al.*, 2012). Although CORMs (metal carbonyls and a few organic CO donors) have been



© 2017 International Union of Crystallography

Acta Cryst. (2017), C73

<https://doi.org/10.1107/S2053229617004429> 1 of 5

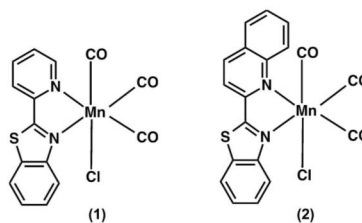
Table 1  
Experimental details.

	(1)	(2)
Crystal data		
Chemical formula	$[\text{MnCl}(\text{C}_{12}\text{H}_8\text{N}_2\text{S})(\text{CO})_3]$	$[\text{MnCl}(\text{C}_{16}\text{H}_{10}\text{N}_2\text{S})(\text{CO})_3]$
$M_r$	386.68	436.74
Crystal system, space group	Monoclinic, $P2_1/c$	Monoclinic, $P2_1/n$
Temperature (K)	296	296
$a, b, c$ (Å)	15.008 (3), 11.798 (3), 9.0384 (19)	9.1239 (5), 16.4292 (9), 12.2101 (6)
$\beta$ (°)	106.756 (2)	96.737 (1)
$V$ (Å <sup>3</sup> )	1532.4 (6)	1817.64 (17)
$Z$	4	4
Radiation type	Mo $K\alpha$	Mo $K\alpha$
$\mu$ (mm <sup>-1</sup> )	1.19	1.01
Crystal size (mm)	0.20 $\times$ 0.18 $\times$ 0.15	0.15 $\times$ 0.12 $\times$ 0.10
Data collection		
Diffraction	Bruker APEXII CCD	Bruker APEXII CCD
Absorption correction	Multi-scan ( <i>SADABS</i> ; Bruker, 2015)	Multi-scan ( <i>SADABS</i> ; Bruker, 2015)
$T_{\text{min}}-T_{\text{max}}$	0.637, 0.746	0.648, 0.746
No. of measured, independent and observed [ $I > 2\sigma(I)$ ] reflections	12045, 3769, 2011	20380, 4479, 3291
$R_{\text{int}}$	0.063	0.046
$(\sin \theta/\lambda)_{\text{max}}$ (Å <sup>-1</sup> )	0.668	0.667
Refinement		
$R[F^2 > 2\sigma(F^2)], wR(F^2), S$	0.065, 0.196, 1.04	0.038, 0.093, 1.04
No. of reflections	3769	4479
No. of parameters	208	266
H-atom treatment	H-atom parameters constrained	H-atom parameters constrained
$\Delta\rho_{\text{max}}, \Delta\rho_{\text{min}}$ (e Å <sup>-3</sup> )	1.42, -0.73	0.32, -0.31

Computer programs: *APEX2* (Bruker, 2015), *SAINT* (Bruker, 2015), *SHELXT* (Sheldrick, 2015a), *SHELXL2014* (Sheldrick, 2015b) and *OLEX2* (Dolomanov *et al.*, 2009).

utilized to demonstrate some beneficial physiological effects of CO, the short half-life and unsustainable CO release barred their full-scale applications under clinical settings (Romao *et al.*, 2012). PhotoCORMs (photoactive CO-releasing molecules) have subsequently emerged as a class of CO donors where the CO release process can be triggered upon illumination with light of appropriate wavelength (Gonzalez & Mascharak, 2014; Chakraborty *et al.*, 2014; Schatzschneider, 2015). This, in turn, offers a way for more sustainable and site-specific delivery of CO to the desired targets. Our laboratory has been engaged in developing photoCORMs with improved light sensitivity based on strategic ligand design (Chakraborty *et al.*, 2014). Along that line, we have recently reported an Mn-based photoCORM, namely  $[\text{MnBr}(\text{pbt})(\text{CO})_3]$  [pbt is 2-(pyridin-2-yl)-1,3-benzothiazole], where the CO release event can be tracked within cellular milieu by virtue of the emergence of a strong blue fluorescence upon deligation of the pbt ligand concomitant to CO delivery (Carrington *et al.*, 2014). In pursuit of developing more such trackable photoCORMs, we report herein the chloride analog  $[\text{MnCl}(\text{pbt})(\text{CO})_3]$ , (1). Furthermore, we have isolated the structurally similar Mn<sup>I</sup>-carbonyl complex  $[\text{MnCl}(\text{qbt})(\text{CO})_3]$ , (2) [qbt is 2-(quinolin-2-yl)-1,3-benzothiazole] (Scheme 1), with additional conjugation within the ligand frame. Both complexes exhibit CO release under low-power visible light and, in both cases, the CO release process can be tracked through the emergence of a blue fluorescence from these complexes upon CO delivery. Complex (2) exhibited a much faster CO release rate compared to complex (1) and hence led

to a rapid 'turn-ON' effect. The two complexes have been characterized by a variety of analytical techniques in addition to single-crystal X-ray diffraction.



## 2. Experimental

All reagents were of commercial grade and were used without further purification. The solvents were purified according to standard procedures (Armarego & Chai, 2003). The ligand pbt and  $[\text{MnCl}(\text{CO})_5]$  were synthesized according to reported procedures (Chen *et al.*, 2001; Davis *et al.*, 1986). A Perkin-Elmer Spectrum-One FT-IR spectrophotometer was employed to record the IR spectra of the complexes and the ligands. UV-vis spectra were monitored with a Varian Cary 50 UV-Vis spectrophotometer. The <sup>1</sup>H NMR spectra of the compounds were recorded at 298 K on a Varian Unity Inova 500 MHz instrument. Microanalyses were carried out with a PerkinElmer Series II 2400 Elemental Analyzer.

## 2.1. Synthesis and crystallization

2.1.1. Synthesis of 2-(quinolin-2-yl)-1,3-benzothiazole (qbt). A yellow solution of quinoline-2-carbaldehyde (409 mg, 2.6 mmol) and 2-aminothiophenol (326 mg, 2.6 mmol) in xylenes (30 ml) was heated under reflux for 24 h. Next, the reaction mixture was cooled to ambient temperature and the solvent was removed under reduced pressure. The solid thus obtained was purified by recrystallization from methanol (yield 279 mg, 41%). Elemental analysis (%) found: C 73.31, H 3.87, N 10.72; calculated for  $C_{16}H_{10}N_2S$ : C 73.26, H 3.84, N 10.68. IR (KBr,  $cm^{-1}$ ): 3057 (w), 1595 (s), 1560 (w), 1500 (s), 1454 (w), 1428 (w), 1327 (s), 1118 (w), 997 (s), 940 (w), 830 (s), 754 (s), 727 (w).  $^1H$  NMR ( $CDCl_3$ ):  $\delta$  8.54 (d, 1H), 8.33 (d, 1H), 8.24 (d, 1H), 8.16 (d, 1H), 8.00 (d, 1H), 7.89 (d, 1H), 7.79 (t, 1H), 7.61 (t, 1H), 7.54 (t, 1H), 7.46 (t, 1H).

2.1.2. Synthesis of complex (1). A batch of  $[MnCl(CO)_5]$  (60 mg, 0.26 mmol) and pbt (55 mg, 0.26 mmol) in dichloromethane ( $CH_2Cl_2$ , 20 ml) was stirred at room temperature for 20 h. The reaction mixture was covered carefully with aluminium foil to avoid any light exposure during the entire course of the reaction. Next, the solvent was completely removed under reduced pressure and the solid thus obtained was washed thoroughly with hexanes and finally dried *in vacuo* (yield 85 mg, 85%). Elemental analysis (%) found: C 46.63, H 2.11, N 7.27; calculated for  $C_{15}H_8ClMnN_2O_3S$ : C 46.59, H 2.09, N 7.24. IR (KBr,  $cm^{-1}$ ): 2023 (s), 1927 (s), 1492 (w), 1327 (w), 777 (w), 768 (w), 631 (w), 528 (w).  $^1H$  NMR ( $CD_3CN$ ):  $\delta$  9.32 (d, 1H), 8.66 (d, 1H), 8.32 (d, 1H), 8.26 (d, 1H), 8.20 (t, 1H), 7.87 (t, 1H), 7.75 (m, 2H).

2.1.3. Synthesis of complex (2). This complex was prepared by the same procedure as used for complex (1), employing  $[MnCl(CO)_5]$  (51 mg, 0.22 mmol) and qbt (58 mg, 0.22 mmol) (yield 89 mg, 91%). Elemental analysis (%) found: C 52.29, H 2.36, N 6.45; calculated for  $C_{19}H_{10}ClMnN_2O_3S$ : C 52.25, H 2.31, N 6.41. IR (KBr,  $cm^{-1}$ ): 2021 (s), 1926 (s), 1909 (s), 1594 (w), 1519 (w), 1090 (w), 825 (w), 765 (w), 641 (w).  $^1H$  NMR ( $CD_3CN$ ):  $\delta$  8.98 (d, 1H), 8.71 (m, 2H), 8.30 (t, 2H), 8.18 (d, 1H), 8.11 (t, 1H), 7.89 (m, 2H), 7.76 (t, 1H).

2.1.4. Isolation of single crystals of (1) and (2). Single crystals of both complexes were obtained by layering hexanes over their dichloromethane solutions. One crystal of each complex was selected and fixed on top of MiTiGen micro-mounts using Paratone Oil and transferred to the diffractometer.

## 2.2. Refinement

Crystal data, data collection and structure refinement details are summarized in Table 1. The non-H atoms were located through intrinsic phasing using *SHELXT* (Sheldrick, 2015b) integrated in the *OLEX2* graphical user interface (Dolomanov *et al.*, 2009). H atoms were included in calculated positions riding on the C atoms to which they bonded, with  $C-H = 0.93$  Å and  $U_{iso}(H) = 1.2U_{eq}(C)$ . In (1), the highest residual electron-density peak is located near atom S1. No satisfactory disorder of the twinning model could be found. In complex (2), an orientational disorder [0.843 (6):0.157 (6)]

Table 2

Selected geometric parameters (Å, °) for (1).

Mn1—C11	2.3916 (15)	Mn1—C1	1.773 (6)
Mn1—N2	2.054 (4)	Mn1—C3	1.793 (6)
Mn1—N1	2.078 (4)	Mn1—C2	1.805 (6)
N2—Mn1—C11	85.68 (12)	C3—Mn1—C11	94.19 (16)
N2—Mn1—N1	78.15 (16)	C3—Mn1—N2	171.6 (2)
N1—Mn1—C11	87.39 (12)	C3—Mn1—N1	93.5 (2)
C1—Mn1—C11	177.79 (19)	C3—Mn1—C2	86.2 (2)
C1—Mn1—N2	93.2 (2)	C2—Mn1—C11	88.60 (18)
C1—Mn1—N1	94.2 (2)	C2—Mn1—N2	102.1 (2)
C1—Mn1—C3	87.2 (2)	C2—Mn1—N1	175.9 (2)
C1—Mn1—C2	89.8 (2)		

Table 3

Selected geometric parameters (Å, °) for (2).

Mn1—C11	2.3837 (7)	Mn1—C3	1.798 (2)
Mn1—N2	2.0668 (18)	Mn1—C1	1.796 (3)
Mn1—N1	2.0962 (18)	Mn1—C2	1.795 (3)
N2—Mn1—C11	86.32 (5)	C1—Mn1—N1	94.57 (10)
N2—Mn1—N1	78.36 (7)	C1—Mn1—C3	92.99 (10)
N1—Mn1—C11	84.96 (5)	C2—Mn1—C11	88.28 (9)
C3—Mn1—C11	84.97 (8)	C2—Mn1—N2	98.04 (10)
C3—Mn1—N2	170.75 (9)	C2—Mn1—N1	172.52 (10)
C3—Mn1—N1	97.75 (9)	C2—Mn1—C3	84.82 (11)
C1—Mn1—C11	177.82 (8)	C2—Mn1—C1	92.31 (11)
C1—Mn1—N2	95.68 (9)		

within the qbt ligand was observed, in which the quinoline and benzothiazole frames partially switch positions. This disorder is similar to that observed for the same ligand by Meghadi *et al.* (2015). The disorder was modeled by assigning partly occupied positions of the S atom (S1 and S1B) of the benzothiazole fragment and the C10 and C11 atoms of the quinoline fragment (C10, C11, C10B, and C11B), and the anisotropic displacement parameters of the C10B and C11B atoms were constrained to be equal (*SHELXL*; Sheldrick, 2015a). All other atoms of qbt ligand in (2) were refined as fully occupied sites.

## 3. Results and discussion

The coordination geometry of the  $Mn^I$  atom in both complexes is distorted octahedral (Tables 2 and 3). In both structures, the equatorial planes are composed of two *cis* CO and two N atoms from the bidentate ligands (pbt and qbt), while the axial positions are occupied by the third CO ligand and a chloride ligand (Figs. 1 and 2). In (1), the equatorial plane, comprising atoms C2, C3, N1, and N2, is approximately planar, with a mean deviation of 0.033 (5) Å, while the corresponding plane in (2) is almost planar [mean deviation = 0.015 (3) Å]. In complex (1), the chelate ring composed of atoms Mn1, N1, C8, C9, and N2 is highly planar, with a mean deviation of 0.017 (3) Å. In contrast, in complex (2), the chelate ring composed of atoms Mn1, N1, C12, C13, and N2 deviates significantly from planarity [mean deviation = 0.115 (5) Å]. The dihedral angles between the planes of the pyridyl ring and the benzothiazole moiety in (1) and (2) are

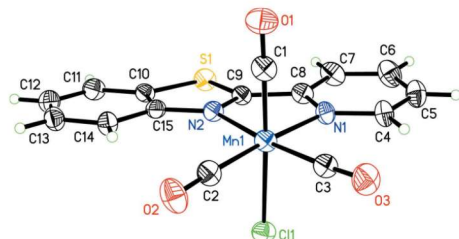


Figure 1  
A perspective view of complex (1), showing the atom-labeling scheme. Displacement ellipsoids are drawn at the 50% probability level.

6.0 (6) and 9.6 (6) $^{\circ}$ , respectively. In both cases, the benzothiazole frame is considerably planar, with mean deviations of 0.005 (5) and 0.012 (4) Å for (1) and (2), respectively. The average Mn—C bond lengths in complexes (1) and (2) are 1.790 (6) and 1.800 (6) Å, respectively. These distances are very similar to that found in the bromide analog (Carrington *et al.*, 2014) of complex (1) and the structurally comparable [MnCl(bpy)(CO) $_3$ ] (bpy is bipyridine) complex [1.780 (9) and 1.801 (5) Å, respectively].

The crystal packing of the two complexes reveals no  $\pi$ – $\pi$  stacking interactions. However, in complex (1), a few nonclassical hydrogen-bonding contacts have been observed [C4—H4 $\cdots$ Cl1 $^i$ , with H4 $\cdots$ Cl1 $^i$  = 2.83 Å, and C6—H6 $\cdots$ Cl1 $^{ii}$ , with H6 $\cdots$ Cl1 $^{ii}$  = 2.78 Å; symmetry codes: (i)  $x, -y + \frac{3}{2}, z - \frac{1}{2}$ ; (ii)  $-x + 1, -y + 1, -z + 1$ ]. In complex (2), analysis of the packing pattern revealed an intermolecular Cl1 $\cdots$ S1( $x + \frac{1}{2}, y + \frac{1}{2}, -z + \frac{1}{2}$ ) [3.542 (6) Å] contact which consolidates the extended structure (Figs. 3 and 4).

Complexes (1) and (2) exhibit prominent CO stretching consistent with a *facial* disposition of the three CO ligands. The complexes also display well-resolved  $^1\text{H}$  NMR spectra, indicating the presence of diamagnetic Mn $^{\text{I}}$  centers.

The UV–Vis spectra of (1) and (2) revealed moderately strong absorption bands around 415 and 440 nm, respectively. The origin of these bands is presumably due to MLCT (metal-to-ligand charge transfer) transitions (Carrington *et al.*, 2014). In acetonitrile, both complexes exhibit systematic changes in

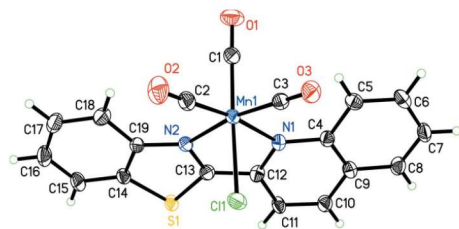


Figure 2  
A perspective view of the major-disorder component of complex (2), showing the atom-labeling scheme. Displacement ellipsoids are drawn at the 50% probability level.

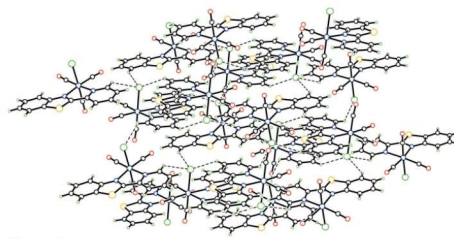


Figure 3  
The crystal packing of complex (1) along the *c* axis.

the UV–Vis spectra upon exposure to low-power visible light (10 mW cm $^{-2}$ ). These changes can be attributed to the CO release, as evidenced by a standard Myoglobin assay (Carrington *et al.*, 2014). The apparent rates of CO photo-release ( $k_{\text{CO}}$ ) from complexes (1) and (2) have been determined by recording the electronic absorption spectra and monitoring the changes of the spectral traces upon exposure to broadband visible light at regular time intervals [30 s for (1) and 10 s for (2)]. The  $k_{\text{CO}}$  values calculated from  $\ln(C)$  versus time (*t*) plots were found to be  $0.98 \pm 0.02$  (concentration  $7.76 \times 10^{-5}$  M) and  $2.51 \pm 0.02$  min $^{-1}$  (concentration  $6.87 \times 10^{-5}$  M) for complexes (1) and (2), respectively. It is worthy of mention that complex (2) exhibits a much faster CO release rate compared to complex (1) under the same experimental conditions. This can be attributed to the relatively superior  $\pi$ -acceptor character of qbt due to the extended conjugation, which in turn could facilitate faster CO release from the corresponding complex, *i.e.* (2). A representative case showing the changes in UV–Vis spectral traces of complex (2) upon illumination is shown in Fig. 5. The two fluorogenic ligands (pbt and qbt) are purposefully employed in the present study

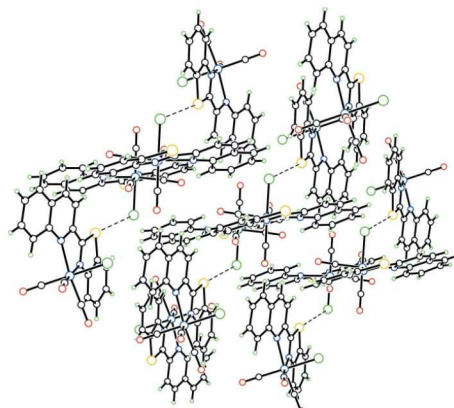


Figure 4  
The crystal packing of complex (2) along the *c* axis.



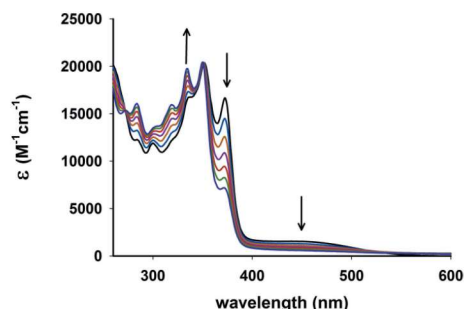


Figure 5  
Spectral changes of complex (2) in acetonitrile solution upon exposure to broadband visible light ( $10 \text{ mW cm}^{-2}$ ).

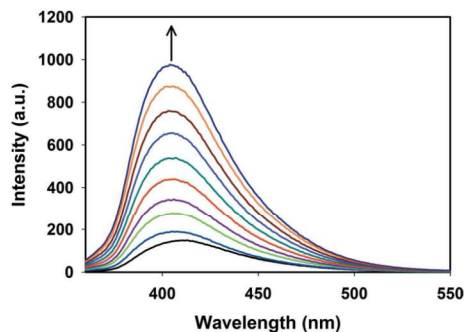


Figure 6  
Time-dependent enhancement of emission intensity ( $\lambda_{\text{em}} = 405 \text{ nm}$ ) for complex (2) in acetonitrile solution upon exposure to visible light ( $\lambda_{\text{ex}} = 345 \text{ nm}$ ).

to evaluate any de-ligation event associated with CO photo-release from their Mn complexes. In fact, time-dependent fluorescence studies revealed the gradual emergence of a

strong blue fluorescence with concomitant CO release for both complexes in acetonitrile solutions under illumination. The fluorescence signals reach saturation points within 6 min for complex (1) and within 1 min for complex (2), and the final intensity is comparable with those of free pbt and qbt. A representative example of time-dependent fluorescence enhancement is shown in Fig. 6. This unique fluorescence 'turn-ON' feature provides a convenient means of tracking CO release from these complexes within biological matrices upon exposure to light.

#### Funding information

Funding for this research was provided by: National Science Foundation (award No. DMR-1409335).

#### References

- Armarego, W. L. F. & Chai, C. L. L. (2003). In *Purification of Laboratory Chemicals*. Oxford: Butterworth Heinemann.
- Bernardes, G. J. L. & Garcia-Gallego, S. (2014). *Angew. Chem. Int. Ed.* **53**, 9712–9721.
- Bruker (2015). *APEX2*, *SAINT*, and *SADABS*. Bruker AXS Inc., Madison, Wisconsin, USA.
- Carrington, S. J., Chakraborty, I., Bernard, J. M. L. & Mascharak, P. K. (2014). *ACS Med. Chem. Lett.* **5**, 1324–1328.
- Chakraborty, I., Carrington, S. J. & Mascharak, P. K. (2014). *Acc. Chem. Res.* **47**, 2603–2611.
- Chen, X., Femia, F. J., Babich, J. W. & Zubieta, J. (2001). *Inorg. Chim. Acta*, **314**, 91–96.
- Davis, R., Durrant, J. L. A. & Rowland, C. C. (1986). *J. Organomet. Chem.* **315**, 119–133.
- Dolomanov, O. V., Bourhis, L. J., Gildea, R. J., Howard, J. A. K. & Puschmann, H. (2009). *J. Appl. Cryst.* **42**, 339–341.
- Gonzalez, M. A. & Mascharak, P. K. (2014). *J. Inorg. Biochem.* **133**, 127–135.
- Meghdadi, S., Amiras, M., Mirhashemi, A. & Amiri, A. (2015). *Polyhedron*, **97**, 234–239.
- Motterlini, R. & Otterbien, L. E. (2010). *Nat. Rev. Drug Discov.* **9**, 728–743.
- Romao, C. C., Blatter, W. A., Seixas, J. D. & Bernardes, G. J. L. (2012). *Chem. Soc. Rev.* **41**, 3571–3583.
- Schatzschneider, U. (2015). *Br. J. Pharmacol.* **172**, 1638–1650.
- Sheldrick, G. M. (2015a). *Acta Cryst.* **A71**, 3–8.
- Sheldrick, G. M. (2015b). *Acta Cryst.* **C71**, 3–8.
- Tenhunen, R., Marver, H. S. & Schmid, R. (1968). *Proc. Natl Acad. Sci. USA*, **61**, 748–755.

## Chapter 5. Conclusions

### 5.1 Evaluation of Silver and Gold Complexes With Benzothiazoles as Antimicrobial Agents

The demand for new and improved antimicrobial therapeutics is evident through the rapid emergence of MDR pathogens that can no longer be treated by traditional antibiotics.<sup>1</sup> Metal complexes have been used for centuries to treat infection and have shown their effectiveness in current research. The mechanism of action of metals offers the advantage of multiple mechanistic pathways compared to traditional antibiotics which usually target only one pathway within a microbe. This could prevent resistance from occurring as rapidly as observed with organic based antibiotics. Both gold and silver complexes with potent antimicrobial activity discussed in this work could be beneficial in the development of new antibiotic therapies.

In Chapter 2 and 3, the antimicrobial activity of gold and silver complexes with benzothiazoles pbt and qbt were evaluated using the SSTI model. Benzothiazoles in general show antibacterial activity themselves and could add to the therapeutic potential of the metal centers. While the Agpbt/Agqbt and AuPpbt/AuPqbt structures differ in coordination environment, the overall charge of the complexes is +1 which likely aids in the overall efficacy of the complexes due to the slight electronegative charge of microbial membranes. It is difficult to directly compare the efficacy of the silver complexes to the gold complexes using the SSTI model, however based on the size of the ring of clearing of *P. aeruginosa* lawns, the activity can at least be considered

comparable for Agqbt and AuPpbt (**Figure 5.1**). It should be noted that the antimicrobial activities observed in **Figure 5.1** were done at different times and under slightly different experimental conditions for the silver and gold species. However, in both cases increasing the concentration of the complex in the KBr pellet did not increase the diameter of the ring and thus led us to the conclusion that the activity was dictated by the solubility and ability to diffuse through the aqueous agar layer. This hypothesis is also validated by the observation of no bacterial ring of clearing for the overall neutral starting material ClAuPPh<sub>3</sub>.

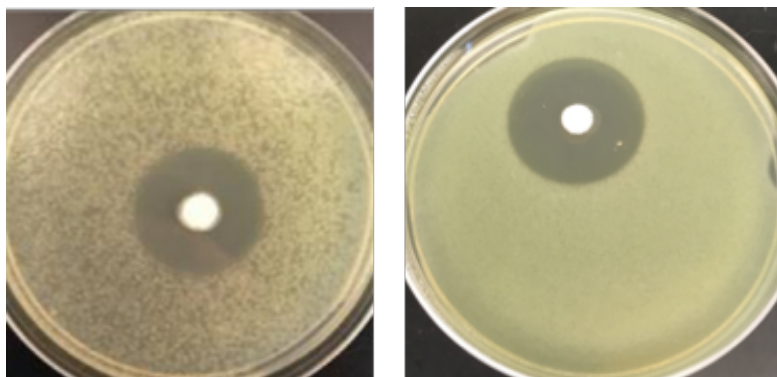


**Figure 5.1.** Comparison of the bacterial rings of clearing from Agqbt (left) and AuPpbt (right) of *P. aeruginosa*.

Another advantage to using pbt or qbt as a ligand is the turn on of fluorescence observed from the ligand exchange around the metal center. In both metal complexes the fluorescence intensity of the pbt and qbt ligands is significantly quenched when bound to the metal center. As the Ag<sup>+</sup> or Au<sup>+</sup> metal centers ligand exchange to bind to biological molecules within bacteria, the pbt or qbt ligands are released from the

coordination environment and the fluorescence of the free ligands appears. This could be particularly advantageous to track the release of the  $\text{Ag}^+$  or  $\text{Au}^+$  as an indication of when all the metal antibiotic in a topical application for a SSTI has been used up. Both silver and gold complexes with pbt and qbt discussed in this work show potent antibacterial activity and could be useful for the treatment of difficult skin and soft tissue infections.

## 5.2 Advantages of Gold(I)PPh<sub>3</sub> Complexes

The applications of gold complexes as therapeutic agents is expanding rapidly and offers a promising route to treat the emerging pathogens. In Chapter 3 (Section 3.2 and 3.3) gold complexes with  $\{\text{Au}(\text{PPh}_3)\}^+$  units were evaluated for their antimicrobial activity. In both cases, potent antimicrobial action was observed and linked to the ability of the gold(I) complexes to ligand exchange with thiol containing biomolecules. This mechanism is further evidenced by the expansive study of other gold phosphine species and their ability to inhibit thiol containing enzyme and proteins like TrxR. Because multiple inhibitory pathways have been identified for these gold complexes, it is likely the combination of multiple targets within the cell (regardless of the identified target) that is responsible for their activity. This helps to overcome the resistance mechanisms present in MDR pathogens; multiple targets would require multiple sites for the bacteria to overcome resistance which is less likely.

One aspect both of these works have in common is the use of bioactive N donor ligands as the second moiety of the  $\{\text{Au}(\text{PPh}_3)\}^+$ . These complexes allow for easy



replacement of the N ligand (and thus release of the free pbt,qbt or pza) and for potential of the free ligand to exert drug action on its own. While in this work's current experimental methodology, this is not strongly observed, there is evidence that synergy between the released ligand and the  $\{\text{Au}(\text{PPh}_3)\}^+$  exist in other cases.  $\{\text{Au}(\text{PPh}_3)\}^+$  complexes with chloroquine, the leading antimalarial drug, show high potency (nM range) towards *Plasmodium falciparum* and the ligation to the lipophilic  $\{\text{Au}(\text{PPh}_3)\}^+$  is able to overcome chloroquine resistance.<sup>2</sup> Regardless of N donor ligand in the antibacterial and antimycobacterial studies done in this work, it seems as though the potent activity arises from the  $\{\text{Au}(\text{PPh}_3)\}^+$ . This suggests that AuPpbt and AuPqbt strongly possess potential to combat skin and wound infections through topical applications and could be utilized in cases of drug resistant infection. For TB treatment, the comparison of the activity of gold(I) phosphine complex AuPpza to the ineffective gold(III) complexes Au<sub>3</sub>pza and Au<sub>3</sub>pzo immediately reveal that the  $\{\text{Au}(\text{PPh}_3)\}^+$  plays a key role in the activity. Current TB treatment regiments require four orally taken drugs (pza, ethambutol, rifampicin and isoniazid) at high dosages for 6 month with the daily dose of pza recommended at 30mg/kg for at least 2 of those months.<sup>3</sup> Much of the difficulty of treating this disease arises from the inherently thick waxy mycomebrane of *M. tuberculosis* that prevents foreign substances from permeation.<sup>4</sup> The  $\{\text{Au}(\text{PPh}_3)\}^+$  moiety in AuPpza could provide enhanced lipophilicity to cross this membrane and exert drug action. Both studies provide valuable insight into the development and treatment of gold phosphine complexes for the treatment MDR pathogens.

### 5.3 Near IR Active photoCORMs

The therapeutic effects of CO have been well examined with much initial success particularly in the anticancer activity observed with light triggered release of CO from transition metal carbonyl photoCORMs. In Chapter 4 (Section 4.2) the release of CO from Mn<sup>pbt</sup> and Mn<sup>qbt</sup> was observed by irradiation of visible light. This was accompanied by the gradual turn on of fluorescence (similarly to Ag and Au structures with pbt and qbt) which provides an efficient means for the tracking of CO release. To further the therapeutic potential of CO, research has shifted to the investigation of photoCORMs that are activated by near IR light (which penetrates further into tissues and with less damage than visible or UV light). This has mainly been observed in Mn(I) systems by the use of TPE which requires the use of high intensity lasers that could potentially damage tissues. In Section 4.3 we examined the CO release properties of MnNIR1 and MnNIR2 which can be activated by SPE with a simple LED source of near IR light. To our knowledge, these are the first examples of Mn(I) systems activated by light in the near IR region that do not require the use of expensive and powerful lasers. We believe that the proper design of ligand frameworks that causes the near IR activity in MnNIR1 and MnNIR2 could be applied to other photoCORM systems and could be beneficial in the development of these systems for clinical use.

### 5.4 Overall Conclusions

Regardless of disease, metal complexes have proven useful in the development of therapeutics. The structural design of the metal complexes used in this work

influences the overall activity of the complexes whether that be to increase the antibacterial activity of silver and gold complexes or to allow for near IR activation of photoCORMs. The specific and careful combination of ligand choice, metal center, and coordination environment can have profound influence on the biological properties of these metal complexes. The tracking capability, increase in lipophilicity and/or photophysical properties are just a few of the aspects governed by this design principle. Thoughtful and careful implementation of these principles into therapeutic applications would be advantageous in drug discovery.

## 5.5 References

- (1) Toner, E.; Adalja, A.; Gronvall, G. K.; Cicero, A.; Inglesby, T. V. Antimicrobial Resistance Is a Global Health Emergency. *Heal. Secur.* **2015**, *13* (3), 153–155.
- (2) Navarro, M.; Castro, W.; Martínez, A.; Sánchez Delgado, R. A. The Mechanism of Antimalarial Action of [Au(CQ)(PPh<sub>3</sub>)]PF<sub>6</sub>: Structural Effects and Increased Drug Lipophilicity Enhance Heme Aggregation Inhibition at Lipid/Water Interfaces. *J. Inorg. Biochem.* **2011**, *105* (2), 276–282.
- (3) Sotgiu, G.; Centis, R.; D'Ambrosio, L.; Battista Migliori, G. Tuberculosis Treatment and Drug Regimens. *Cold Spring Harb. Perspect. Med.* **2015**, *5* (5), 1–12.
- (4) Fenton, M. J.; Vermeulen, M. W. Immunopathology of Tuberculosis: Roles of Macrophages and Monocytes. *Infect. Immun.* **1996**, *64* (3), 683–690.